# Shear-Horizontal Surface Acoustic Wave Microfluidics for Lab-On-Chip Applications

Douglas Stuart Brodie

Submitted for the Degree of Doctor of Philosophy (Ph.D.) on completion of research in the School of Engineering and Physical Sciences,
Heriot-Watt University

July 2014

# Abstract

Surface acoustic wave (SAW) devices based on the piezoelectric principle have been used extensively in telecommunication applications over the last 20 years, but have recently shown promise in the area of biomedical applications due to their efficient micro-fluidic functions and highly sensitive and label-free detection of pathogens, bacteria, cells, DNA and proteins. There are two types of surface acoustic wave modes: i.e., Rayleigh SAW (R-SAW) and shear horizontal SAW (SH-SAW). R-SAW is widely used for microfluidics and sensing in dry conditions, whereas SH-SAW is mainly used for sensing in liquid conditions. This thesis firstly reviewed the current theoretical and research progress related to these devices and application within the biomedical fields to date, and then the SH-SAW was applied into a novel lab-on-chip combining both bio-sensing and micro-fluidic functions.

Simulations of the SH-SAW propagation on $36^{o}$ Y-cut $LiTaO_3$ were undertaken. Results showed a weak vertical wave component, and at a $90^{\circ}$ rotation cut, the crystal was able to support a vertical Rayleigh component showing mixed sensing and streaming possibilities on a single crystal. Experimental investigation of the SH-SAW identified the ability for the shear wave to support mixing, pumping, heating, nebulisation and ejection of sessile droplets on the surface of the crystal with a theoretical explanation for the behaviour presented. A comparison with a standard R-SAW devices made of $128^{o}$ Y-cut $LiNbO_3$ and sputtered ZnO films was performed. This novel behaviour of digital microfludics, i.e., using sessile droplet with the SH-SAW, demonstrated by this work offers the possibility to manufacture a fully integrated micro-fluidic bio-sensing platform using a single crystal to realise a range of micro-fluidic functions.

ACADEMIC REGISTRY

# Research Thesis Submission

| | | | |
|---|---|---|---|
| Name*:* | Douglas Stuart Brodie | | |
| School/PGI: | School of Engineering and Physical Sciences | | |
| Version: *(i.e. First, Resubmission, Final)* | Final | Degree Sought (Award **and** Subject area) | PhD Mechanical Engineering |

## Declaration

In accordance with the appropriate regulations I hereby submit my thesis and I declare that:

1) the thesis embodies the results of my own work and has been composed by myself
2) where appropriate, I have made acknowledgement of the work of others and have made reference to work carried out in collaboration with other persons
3) the thesis is the correct version of the thesis for submission and is the same version as any electronic versions submitted*.
4) my thesis for the award referred to, deposited in the Heriot-Watt University Library, should be made available for loan or photocopying and be available via the Institutional Repository, subject to such conditions as the Librarian may require
5) I understand that as a student of the University I am required to abide by the Regulations of the University and to conform to its discipline.

* *Please note that it is the responsibility of the candidate to ensure that the correct version of the thesis is submitted.*

| | | | |
|---|---|---|---|
| Signature of Candidate*:* |  | Date: | 20/07/2014 |

## Submission

| | |
|---|---|
| Submitted By *(name in capitals):* | DOUGLAS STUART BRODIE |
| Signature of Individual Submitting: |  |
| Date Submitted: | 20/07/2014 |

## For Completion in the Student Service Centre (SSC)

| | | | |
|---|---|---|---|
| Received in the SSC by *(name in capitals):* | | | |
| **Method of Submission** (Handed in to SSC; posted through internal/external mail): | | | |
| E-thesis Submitted (mandatory for final theses*)* | | | |
| Signature: | | Date: | |

## Dedication

# De réir a chéile a thógtar na caisleáin

# Acknowledgements

I would like to thank Dr. Richard Fu for his inspiring supervision during my PhD. His advice, encouragement, time and feedback on the thesis were invaluable. He pushed me to complete this work when I had other distractions and motived me to keep refining the research and to look for new answers.

I am indebted to Prof. Robert Reuben for being my supervisor and giving his advice and guidance.

I gratefully acknowledge the financial support of the Engineering and Physical Sciences Research Council (EPSRC) the Department of Mechanical Engineering and the Royal Society of Edinburgh for the finance afforded to complete this research.

There are many people who have my sincere thanks because they have, sometimes unknowingly, helped, contributed and encouraged this work. I truly acknowledge the contribution of the following key characters: Dr. Yifan Li for all his support at Edinburgh University in the manufacture of all the SAW devices, Dr. Mansour Alghane for his assistance with fluid experiments.

Finally I would like to thank my wife Mairéad and son Ruairi for all their support and encouragement.

# Contents

**ABSTRACT** ..... **I**

**DEDICATION** ..... **III**

**ACKNOWLEDGEMENTS** ..... **IV**

**LIST OF FIGURES** ..... **IX**

**LIST OF TABLES** ..... **XX**

**PUBLICATIONS AND AWARDS** ..... **XXI**

**CHAPTER 1. INTRODUCTION** ..... **1**

1.1 BACKGROUND ..... 1

1.2 AIMS AND OBJECTIVES ..... 3

1.3 THESIS OUTLINE ..... 4

**CHAPTER 2. LITERATURE REVIEW** ..... **6**

2.1 MICROFLUIDICS ..... 6

2.2 SAW PRINCIPLE ..... 6

*2.2.1 Relationship between Stress and Strain for Solids* ..... *7*

*2.2.2 Wave Equation* ..... *8*

*2.2.3 Wave Solutions in Unbounded Anisotropic Media* ..... *9*

*2.2.4 Wave Propagation in a Thin Surface* ..... *10*

*2.2.5 Boundary Conditions:* ..... *11*

*2.2.6 Surface Profile* ..... *12*

*2.2.7 Piezoelectric Materials* ..... *13*

*2.2.8 Excitation and Detection of Surface Waves* ..... *16*

2.3 BIO-SENSORS ..... 17

*2.3.1 Immunosensors* ..... *17*

*2.3.2 DNA Sensor* ..... *19*

*2.3.3 Enzyme Sensors* ..... *19*

2.4 SAW BIOSENSORS ..... 20

*2.4.1 SAW vs. QCM* ..... *20*

*2.4.2 Shear Horizontal SAW Biosensors* ..... *21*

*2.4.3 Love Mode Biosensors* ..... *23*

2.5 FLUID TRANSPORTATION AND MIXING IN SAW DEVICES ..... 24

*2.5.1 Fluid transportation using channels* ..... *24*

*2.5.2 Surface Acoustic Wave Streaming and Pumping* ..... *26*
2.5.2.1 SAW Microfluid Streaming and Mixing ..... 27
2.5.2.2 SAW Microfluidic Pumping ..... 29
2.5.2.3 SAW Microfluidic Jetting and Nebulisation ..... 31
*2.5.3 SAW Liquid Heating* ..... *33*
*2.5.4 Integration of SAW with other technologies* ..... *34*
2.6 SUMMARY ..... 35

**CHAPTER 3. EXPERIMENTAL DETAILS ..... 37**

3.1 MATERIALS AND SAW DEVICE FABRICATION ..... 37
*3.1.1 Fabrication Process* ..... *37*
*3.1.2 Mask Design* ..... *39*
3.2 EXPERIMENTAL SETUP ..... 41
*3.2.1 Signal Measurement* ..... *41*
*3.2.2 Microfluidics testing* ..... *42*
*3.2.3 Thermal Experiments* ..... *45*
*3.2.4 SAW Sensing Experiments Set-Up* ..... *46*
3.2.4.1 Jig Design ..... 46
3.2.4.2 Frequency Shift Measurements with Oscillator Loop ..... 47
3.2.4.3 Frequency Shift Measurements with Phase Shift ..... 49
3.3 BIO-SENSING PROCEDURES ..... 50

**CHAPTER 4. NUMERICAL SIMULATION OF SHEAR WAVE ..... 51**

*4.1.1 Theory* ..... *52*
*4.1.2 Model overview* ..... *53*
4.1.2.1 Simulation parameters ..... 53
*4.1.3 Excitation of Substrate* ..... *55*
*4.1.4 Material Properties* ..... *56*
4.2 RESULTS AND DISCUSSION ..... 57
*4.2.1 Wave Propagation Analysis on 36°YX $LiTaO_3$ SH-SAW Substrate* ..... *57*
*4.2.2 Analysis of Wave Velocity and K Coefficient* ..... *62*
4.2.2.1 Wave Velocity ..... 62
4.2.2.2 Electromechanical coupling coefficient ..... 64
*4.2.3 Analysis of Penetration Depth* ..... *65*
*4.2.4 Analysis of Voltage Variation* ..... *67*
*4.2.5 Analysis of Wavelength Variation* ..... *69*

*4.2.6 Wave Amplitude vs. Spatial Position* ..... *71*
*4.2.7 Rayleigh Wave Propagation Analysis on 36°YX $LiTaO_3$ SH-SAW Substrate* ..... *74*
4.3 ROTATED IDT FOR BIO-SENSING AND ACOUSTIC STREAMING ..... 77
*4.3.1 Introduction* ..... *77*
*4.3.2 Structural Excitation* ..... *78*
*4.3.3 Response to Impulse Excitation* ..... *79*
*4.3.4 Characterisations of Waves on (90,36,0)-cut 36°YX $LiTaO_3$* ..... *80*
4.4 SUMMARY ..... 85

**CHAPTER 5. NUMERICAL AND EXPERIMENTAL INVESTIGATION OF SHEAR WAVE ACOUSTIC MICROFLUIDICS ..... 87**

5.1 SIMULATION OF SHEAR WAVE PROPAGATION IN A FLUID MEDIUM AND ACOUSTIC STEAMING ..... 87
*5.1.1 Numerical Analysis of Shear Displacement Fluid Coupling* ..... *87*
*5.1.2 Analytical Simulation of Shear Wave* ..... *90*
5.1.2.1 Computational Domain ..... 90
5.1.2.2 Theory ..... 91
5.1.2.3 Simulation Parameters ..... 91
5.1.2.4 Excitation of Droplet ..... 92
*5.1.3 Verification of the model* ..... *93*
5.1.3.1 Fluid Oscillation Verification ..... 93
5.1.3.2 Acoustic Wave Propagation ..... 94
*5.1.4 Simulation of SH-SAW Steaming* ..... *96*
5.1.4.1 Fluid Flow Simulations ..... 98
5.2 EXPERIMENTAL RESULTS ON SHEAR WAVE MICROFLUIDICS ..... 102
*5.2.1 Device Characterisation* ..... *102*
*5.2.2 Shear Wave Streaming* ..... *104*
*5.2.3 Effects of Droplet Size and Position on SH-SAW Streaming* ..... *111*
*5.2.4 SH-SAW Pumping* ..... *120*
*5.2.5 SH-SAW Nebulisation* ..... *121*
*5.2.6 SH-SAW Jetting* ..... *124*
5.3 COMPARISON OF RAYLEIGH AND SH-SAW WAVE MICROFLUIDICS. ..... 126
*5.3.1 Rayleigh SAW streaming* ..... *126*
*5.3.2 Rayleigh SAW induced pumping* ..... *129*
*5.3.3 Rayleigh SAW Induced Jetting* ..... *131*

*5.3.4 Rayleigh SAW induced Nebulisation* ..... *132*
5.4 DISCUSSIONS ON THE DIFFERENCES BETWEEN MICROFLUIDICS FROM RAYLEIGH SAW AND SH-SAW ..... 134
5.5 SUMMARY ..... 136
**CHAPTER 6. THERMAL ANALYSIS OF SH-SAW WAVE PROPAGATION ... 138**
*6.1.1 Single Droplet Thermal Analysis* ..... *138*
*6.1.2 Results and Discussion* ..... *139*
6.2 NUMERICAL SIMULATIONS ..... 142
*6.2.1 Theory* ..... *142*
*6.2.2 Simulation Parameters:* ..... *143*
*6.2.3 Quantification of Péclet number Convective Cooling* ..... *144*
6.3 DUAL INLINE DROPLET ANALYSIS ..... 147
6.4 THERMAL ANALYSIS OF DROPLET NEBULISATION AND ATOMISATION ..... 148
6.5 SUMMARY ..... 150
**CHAPTER 7. SH-SAW LAB-ON-CHIP FOR BIO-SENSING ..... 152**
7.1 SH-SAW MASS AND BIO-SENSING ..... 152
*7.1.1 Characterisation of 36°YX $LiTaO_3$ Sensitivity to Mass Loading* ..... *153*
*7.1.2 Shear Wave Bio-Sensing and Streaming* ..... *155*
7.2 DROPLET MANIPULATION INTEGRATION ON SHEAR WAVE SAW SENSOR ..... 157
7.3 SUMMARY ..... 160
**CHAPTER 8. CONCLUSIONS ..... 161**
**CHAPTER 9. FUTURE WORK ..... 164**
**APPENDIX 1: EULER ANGLE TRANSFORMS ..... 166**
**APPENDIX 2: POWER CONVERSION VALUES ..... 168**
**REFERENCES ..... 169**

# List of Figures

Figure 1-1: Range of health monitoring devices [1-3] ..... 1
Figure 1-2: Fabrication of an example μ-TAS system [6] ..... 2
Figure 1-3: (a) SH wave polarized in the Z direction and (b) Rayleigh wave [7] ..... 3
Figure 2-1: Representation of Rayleigh Waves showing elliptical movement [10] ..... 7
Figure 2-2: Coordinate system for surface waves ..... 10
Figure 2-3: Wave propagation vs. depth [28] ..... 13
Figure 2-4: Surface waves on piezoelectric substrates generated by two sets of IDT's ..... 16
Figure 2-5: General principle of biosensors. The chemical target (analyte) is selected by the biological element creating a physical or chemical property change which creates stimulus to the transducer which is then measured ..... 17
Figure 2-6: Antibody to Antigen binding ..... 18
Figure 2-7: QCM Microbalance, gold colour indicates the electrodes, grey indicates the Quartz crystal ..... 21
Figure 2-8: Surface-skimming bulk waves propagate close to the surface with angle θ ..... 22
Figure 2-9: Love wave ..... 22
Figure 2-10: (a) Attenuation of the leaky surface wave on YX-LiTaO3 crystal with different cuts of rotation angles. The minimal attenuation occurs when the angle is 36°. (b) The relative amplitude of surface waves about depth from the free and metalised surface of 36° rot YX-LiTaO3 crystal. The surface wave concentrates closely to the metalised surface, while at free surface the wave is penetrate deep into the substrate. [52] ..... 23
Figure 2-11: Love Mode Biosensor [53] ..... 23
Figure 2-12: Love wave acoustic device with PDMS chip [63] ..... 25
Figure 2-13: Polymer packaged microfluidic chip [64] ..... 25
Figure 2-14: SU-8 Microfluidic cell on SAW device. (a) a general view of the device; (b) cross-section view [65] ..... 26
Figure 2-15: Schematic illustration of interaction between SAW and liquid on surface of SAW [66] ..... 27
Figure 2-16: Side elevation view of SAW induced internal steaming [67] ..... 27
Figure 2-17: Typical Rayleigh wave velocity profiles centred and off centred [70] ..... 28
Figure 2-18: Proposed SAW bioreactor and mixing kinetics [75] ..... 29

Figure 2-19: Sequential top views of droplet displacements. Top: displacement on a substrate without surface treatment. Bottom: displacement on a substrate with OTS treatment. The treatment of the surface with OTS significantly improves the situation [76] .....30
Figure 2-20: Image of assembly of microfluidic device and filling or the water reservoir using the SAW for direct drive and inverse drive [77] .....30
Figure 2-21: (a) laser ablated microchannel (b) viewing planes (c) Particle steamlines in 50μm channel (d) 280μm channel (e) Plane C-C in 280μm channel [25].....31
Figure 2-22 Droplet jetting induced by a single IDT SAW device (a), and droplet jetting induced by a pair of IDT electrodes (b) [61]. .....31
Figure 2-23: Schematic depiction of the SAW-MS interface. The SAW is generated by applying an input RF signal to the interdigitated electrodes patterned onto the device. The analyte solution, delivered to the SAW substrate through a paper wick, is rapidly atomized when in contact with the SAW propagating on the substrate surface. The atomized droplets comprising the target analyte possess an inherent charge and are directed to the MS inlet for detection [80] .....32
Figure 2-24: SAW atomization mechanism and setup for the SAW atomizer using a filter paper [80] .....32
Figure 2-25: (a) micro-channel design for ultrasonic heating (b) Temperate in channel v.s applied power [81] .....33
Figure 2-26: (a) Schematic diagram of set-up for Rayleigh wave thermal measurements (b) Time response of temperature in 10μl droplet excited at 20v p-p. SAW generated from left IDT [70] .....33
Figure 2-27: Visualization of droplet temperature excited by Rayleigh SAW (top view) as a function of time. Top view, $V_{DROPLET}$=10μl, η=13.1 mPa.s with $P_{IDT}$=1.6W [82].....34
Figure 2-28: Movement of droplet on EWOD and SAW structure [86] .....35
Figure 3-1: SAW device fabrication process .....38
Figure 3-2: 4 Inch mask design for SAW experiments.....39
Figure 3-3: Design B Fabricated on 128$^{o}$ YX - black $LiNbO_3$ .....41
Figure 3-4: Insertion loss and Transmission measurements setup.....42
Figure 3-5: Photograph of the experimental apparatus used during experiments of SAW induced streaming .....43
Figure 3-6: Photograph showing a high speed camera experimental setup of a streaming velocity measurement .....44
Figure 3-7: Photograph of an experimental setup used for height effect measurements...44

Figure 3-8: Thermal Camera Set-Up .....45
Figure 3-9: Example Output from Thermal Camera.....45
Figure 3-10: SAW Sensing jig (a) Left image is explode view of components (b) right image is assembled jig .....46
Figure 3-11: SAW sensing oscillator schematic.....47
Figure 3-12: SAW Oscillator Loop Experimental Set-up (inset) magnified view of 36$^{o}$ Y-cut $LiTaO_3$ SAW device with Au plating .....48
Figure 3-13: LabVIEW Interface for Frequency Counter with Temperature Measurement .....48
Figure 3-14: Example of Phase measurement of 36$^{o}$ Y-cut $LiTaO_3$ SAW using $S_{21}$ .....49
Figure 4-1: Three dimensional (3-D) image of typical mesh used for simulation. Inter-digital Transducers (IDT's) are shown on the top surface highlighted in red. Mesh is approx. 50,000 DOF. Grid dimensions are shown in mm. .....55
Figure 4-2: Applied Voltages to IDT's showing 0.3, 1, 2.5 and 5 V peak to peak excitation.....55
Figure 4-3: Rotation of Crystal Cut for 36$^{o}$ Y-cut $LiTaO_3$. .....56
Fig. 4-4: Surface acoustic wave propagation of shear polarised waves on 36ºYX $LiTaO_3$ with 5V peak-to-peak excitation at 100MHz at approx. 50ns. The displacements are shown in nm. The energy of the wave is observed to propagate into the bulk material and along the surface. .....58
Fig. 4-5: Surface acoustic wave propagation of surface normal polarised waves on 36ºYX $LiTaO_3$ with 5V peak to peak excitation at 100MHz at approx. 50ns. The displacements are shown in nm. The vertical wave is observed to be a magnitude small than the shear component with the results in the order of $10^{-9}$ m. .....58
Figure 4-6: Surface acoustic wave propagation of waves on 36ºYX $LiTaO_3$ with 5 V peak-to-peak excitation at 100 MHz at approx. 40 ns. The total displacements are shown in nm. The SAW radiation is observed to "leak" into the bulk material .....59
Fig. 4-7: Displacement of shear horizontal component at 5V peak-to-peak 100 MHz excitation at 6 μm from IDT .....60
Fig. 4-8: Displacement of surface normal component at 5 V peak-to-peak 100 MHz excitation at forward IDT.....60
Fig. 4-9: Displacement of longitudinal component at 5 V peak-to-peak 100 MHz excitation at forward IDT.....61
Figure 4-10: Velocity of three wave components at 5 V peak-to-peak 100 MHz excitation at forward IDT. .....62

Figure 4-11. The displacement as a function of time for 36°YX $LiTaO_3$ at 5 V, 140 μm from IDT. ..... 63
Figure 4-12: Boundary conditions applied to electromechanical coupling coefficient model. ..... 64
Figure 4-13: Shear wave displacement at a point 140 μm from IDT array in the propagation direction for 100 MHz devices at 5 V. ..... 65
Figure 4-14: Displacement image of cross section cut though centre of substrate. The displacement profile is shown at 50 ns when the wave profile had stabilised. ..... 66
Figure 4-15: Mechanical displacements versus normalised distance into substrate for 36°YX $LiTaO_3$. Simulated FEA results are compared to analytical results obtained by Nakamuira et al. [109] ..... 67
Figure 4-16: Plots of Shear Horizontal displacement at 0.5, 3.5 and 7 V (left-right) Peak to Peak excitation modelled on 36°YX $LiTaO_3$ at 100MHz. Displacement show is mm. 68
Figure 4-17: Variation of Shear Horizontal and Surface Normal displacement components with respect to voltage from 0.3 V to 7 V Peak to Peak ..... 69
Figure 4-18: Plots of Shear Horizontal displacement at 50 Hz, 60 Hz and 100 Hz (left-right) modelled on 36°YX $LiTaO_3$ 100MHz. Voltage applied was 5 V, displacement show is nm. ..... 70
Figure 4-19: Variation of Shear Horizontal and Surface Normal displacement components at 50 Hz, 60 Hz and 100 Hz. Voltage applied was 5 V. ..... 70
Figure 4-20: Propagation loss measurement locations shown on plan view of FEA model (Scale is in nm). ..... 71
Figure 4-21: Shear Horizontal displacement across $T_L$ line for 100 MHz 5 V P-P device. The width of the IDT is show schematically for reference ..... 72
Figure 4-22: Surface Normal displacement across $T_L$ line for 100 MHz 5 V P-P devices. The width of the IDT is show schematically for reference ..... 72
Figure 4-23: Shear Horizontal displacement across $P_L$ line for 100 MHz 5 V Peak-to-Peak devices ..... 73
Figure 4-24: Surface Normal displacement across $P_L$ line for 100 MHz 5 V Peak-to-Peak. ..... 74
Figure 4-25: Surface acoustic wave propagation of surface normal polarised waves on 36ºYX $LiTaO_3$ with 5V peak to peak excitation at 79.1 MHz at approx. 50 ns. The displacements are shown in nm. The vertical wave can be seen to be around 0.01 nm at its peak. ..... 75

Figure 4-26: Displacement of shear horizontal component at 5 V peak-to-peak at 79.1 MHz excitation at 6um from IDT. ..... 75
Figure 4-27: Displacement of surface normal component at 5 V peak-to-peak 79.1 MHz excitation at 6 μm from IDT. ..... 76
Figure 4-28. Displacement of longitudinal component at 5 V peak to peak 100 MHz excitation at 6 μm from IDT ..... 76
Figure 4-29: 4 Port IDT array with IDT's in x propagation direction and at Euler angel (90,-36,0)..... 77
Figure 4-30: Impulse Function applied to transmitting IDT's. ..... 78
Figure 4-31: Simulated insertions loss for 90º rotated array and non-rotated array. Experimental transmission measurements for the non-rotated IDT array is also shown. .79
Figure 4-32: Surface acoustic wave propagation of shear horizontal polarised waves on (90,36,0) 36ºYX $LiTaO_3$ with 5 V peak-to-peak excitation at 82 MHz at approximately 50 ns. The displacements are shown in nm. The wave can been seen to be around 0.0092 nm at its peak. ..... 80
Figure 4-33: Surface acoustic wave propagation of shear horizontal polarised waves on (90,36,0) 36ºYX $LiTaO_3$ with 5 V peak-to-peak excitation at 143 MHz at approx. 50 ns. The displacements are shown in nm. The wave amplitude is observed to be approximately 0.014 nm at its peak. ..... 81
Figure 4-34: Surface acoustic wave propagation of surface normal polarised waves on (90,36,0) 36ºYX $LiTaO_3$ with 5 V peak to peak excitation at 82 MHz at approx. 50 ns. The displacements are shown in nm. The wave amplitude is observed to be around 0.0144 nm at its peak. ..... 81
Figure 4-35: Surface acoustic wave propagation of surface normal polarised waves on (90,36,0) 36ºYX $LiTaO_3$ with 5 V peak to peak excitation at 143 MHz at approx. 50 ns. The displacements are shown in nm. The wave amplitude is observed to be approximately 0.0221 nm at its peak. ..... 82
Figure 4-36: Surface acoustic wave propagation of waves on 36ºYX $LiTaO^3$ with 5 V peak to peak excitation at 143 MHz at approx. 40 ns. The total displacement is shown in nm. The SAW radiation is seen to radiate into the bulk material as a BAW..... 82
Figure 4-37: Displacement of three wave components on (90,36,0) 36ºYX LiTaO3 with 5 V peak-to-peak excitation at 82 MHz at 6 μm from IDT. ..... 83
Figure 4-38: Displacement of three wave components on (90,36,0) 36ºYX $LiTaO_3$ with 5 V peak to peak excitation at 143 MHz at 6 μm from IDT. ..... 84

Figure 4-39: Displacement image of cross section cut though centre of substrate. The displacement profile is shown at 30 ns on 82 MHz (90,36,0) 36ºYX $LiTaO_3$ when the wave profile had stabilised.....84
Figure 4-40: Displacement image of cross section cut though centre of substrate. The displacement profile is show at 30 ns 143 MHz (90,36,0) 36ºYX $LiTaO_3$ when the wave profile had stabilised. .....85
Figure 5-1: Numerically calculated viscous fluid layer displacement for infinite volume of water, loaded on oscillating substrate modelled as 36° YX $LiTaO_3$. Vertical direction shows decay of the fluid displacement into the bulk fluid.....89
Figure 5-2: Numerical calculation of evolving fluid displacement of viscous water loaded on 36° YX $LiTaO_3$ oscillating substrate at 150 MHz over 4 ns.....89
Figure 5-3: (left) two dimensional (2-D) image of typical mesh used for simulation. Mesh is approx. 69,181 DOF. (Right) boundary layer refinement shown with 50 layers and 1.2 element growth, bottom seed layer 5 nm thick. .....92
Figure 5-4: Schematic of wave interaction with droplet, superposition principle can be used to idealise interaction to one plane. .....93
Figure 5-5: Decay length of wave vertically into fluid against SAW frequency, analytical solution is compared to FEA solution.....94
Figure 5-6: (a) acoustic pressure wave propagation within 0.2 µl droplet at 40 ns (b) acoustic pressure wave propagation within 0.2 µl droplet at 160 ns (c) acoustic pressure wave propagation within 0.2 µl droplet at 260 ns (d) acoustic pressure wave propagation within 0.2 µl droplet at 0.01 ms. .....95
Figure 5-7: Streaming velocity in increasing droplet sizes vs. steaming velocity at 15 dBm. FEA simulated results are shown compared to experimental data for Rayleigh and Shear waves. .....96
Figure 5-8: (left) Mesh for Fluid Flow Simulation, 4200 Degrees of Freedom, 5 µl droplet. (right) area for force application at boundary.....98
Figure 5-9: (left) Experimental streaming profile for 5µl droplet, SAW direction left to right. (right) CFD simulated droplet flow with reference to IDT position. .....99
Figure 5-10: Flow normalized streaming velocity as a function of normalised RF power for numerical simulation and experimental data using a 5 µl droplet using a 36° YX $LiTaO_3$.....100
Figure 5-11: Streaming velocity distributions across the centre of a 5 µl droplet at Rf powers from 3 W – 50 W. These curves represent numerical results along with y-axis as depicted by the red line through the droplet centre.....101

Figure 5-12: Reflection signal $S_{11}$ of 36° Y-cut $LiTaO_3$ SH-SAW device with 25 μm periodicity, including the Rayleigh SAW, SH-SAW. The insets are the illustrations of the flow patterns for SH-SAW and Rayleigh SAW. ....103
Figure 5-13: Reflection signal $S_{11}$ of 36° Y-cut $LiTaO_3$ SH-SAW device with 16 μm periodicity, including the Rayleigh SAW, SH-SAW. The insets are the illustrations of the flow patterns for SH-SAW and Rayleigh SAW. ....103
Figure 5-14: Illustration of droplet positioning for microfluidic experiments. Multiple droplets are shown to indicate various spatial locations. ....105
Figure 5-15: (a) Streaming patterns in 2.5 μl droplet at ~3 position of IDT with relation to droplet and flow directional vectors. Red dashed lines indicated aperture of IDT. (b) Flow azimuthal changes due to position of droplet with relation to IDT (i) droplet positioned below IDT showing approximately 80° rotation to initial flow (ii) droplet positioned above IDT showing 45° rotation to initial flow. ....106
Figure 5-16: Droplet size vs. mixing velocity for Shear and Rayleigh wave on 36°Y-X $LiTaO_3$. Comparative data is shown for Rayleigh wave on 128° YX- black $LiNbO_3$. All data presented is assumed to be on 36°Y-X $LiTaO_3$ unless otherwise indicated. ....107
Figure 5-17: Reduction in velocity for droplets placed in series on 36°Y-X $LiTaO_3$ and 128° YX- black $LiNbO_3$ with SH-SAW and Rayleigh wave respectively. Droplets of 2 μl were placed at 1mm ($d_i$) and 10mm (do) from IDT. ....109
Figure 5-18. Mixing velocity vs. distance $\Delta_y$ from IDT for 5μl droplet at $P_{IDT}$ = 1 W. Streaming velocity is shown for 36°Y-X $LiTaO_3$ and 128° YX- black $LiNbO_3$ with SH-SAW and Rayleigh wave respectively. Exponential trend-lines are mapped to data. ....110
Figure 5-19: (a-c) Rayleigh wave steaming patterns on 128° YX- black $LiNbO_3$ at various positions from the IDT. (d-f) SH-SAW streaming on 36°Y-X $LiTaO_3$ at various positions from the IDT with a 2.5mm aperture. ....111
Figure 5-20: Location of droplet with reference to IDT structure. ....111
Figure 5-21: Position 1; 5 μl; from 0 to 4 dBm; 36°Y-X $LiTaO_3$. ....112
Figure 5-22: Position 1; 5 μl; from 5 to 7 dBm; 36°Y-X $LiTaO_3$. ....112
Figure 5-23: Position 2; 4 μl; from 0 to 5 dbm; 36°Y-X $LiTaO_3$. ....113
Figure 5-24: Position 2; 3 μl ; from 3 to 5 dbm; 36°Y-X $LiTaO_3$. ....113
Figure 5-25: Position 2; 3 μl; from 8 to 10 dBm; 36°Y-X $LiTaO_3$. ....113
Figure 5-26: Position 2; 3 μl; 12 dBm; 36°Y-X $LiTaO_3$. ....114
Figure 5-27: Position 1; 5 μl; 0 dBm; 36°Y-X $LiTaO_3$; Streaming pattern is unstable with no steady state flow or pattern observed. ....115

Figure 5-28: Position 1; 5 µl; from 1 dBm - 2 dBm; 36°Y-X $LiTaO_3$; Streaming pattern is unstable with two counter rotation streams observed but quickly becoming chaotic.....115
Figure 5-29: Position 1; 10 µl; from 0 dBm - 2 dBm; 36°Y-X $LiTaO_3$. Flow in propagation direction of the SAW observed.....116
Figure 5-30: Position 1; 10 µl; from 1 dBm - 3 dBm; 36°Y-X $LiTaO_3$. Flow starts at opposing side of the droplet to the IDT and develops into two counter flows orthogonal to the IDT.....116
Figure 5-31: Position 3; 4 µl; from 0 dbm - 2 dbm; 36°Y-X LiTaO3; Stream pattern: weak with only minimal fluid displacement at the boundary opposite the IDT observed. .....117
Figure 5-32: Position 3; 4 µl; from 4 dbm - 6 dbm; 36°Y-X LiTaO3; Streaming pattern: weak with only minimal fluid displacement at the boundary opposite the IDT observed. .....117
Figure 5-33: Position 3; 4 µl; from 8 dbm; 36°Y-X LiTaO3; Streaming pattern: weak with flow orthogonal to the IDT observed, streaming was localised to top half of the droplet. .....117
Figure 5-34: Position 3; 4 µl; from 10 dbm; 36°Y-X LiTaO3; flow develops orthogonal to the IDT at the boundary with chaotic mixing developing with no consistent streaming pattern. .....118
Figure 5-35: Position 3; 4 µl; from 12 dbm; 36°Y-X LiTaO3; flow develops orthogonal to the IDT at the boundary with initially chaotic flow developing into counter rotation flow around the boundary. .....118
Figure 5-36: (a) Schematic image (insert) of droplet pumping streaming pattern in 5 µl droplet at 15 dBm on 36°Y-X $LiTaO_3$ (b) (i) 5 µl droplet at initial position (ii) Movement of 5 µl after actuation with 30 dBm power. .....120
Figure 5-37: The top and horizontal views of the SH-SAW atomization driven by an RF signal with the amplitude of 6.7 W from left to right at different durations. The hollow arrow shows the direction of the SH-SAW. The time shows in the form of second/microsecond. .....122
Figure 5-38: (a) Microfluidic phenomena of a 2.5 µl droplet placed on the 36°Y-X $LiTaO_3$ substrate SH-SAW devices vs. aperture of the IDT as a function applied RF power.....122
Figure 5-39: Atomization time as function of droplet size from 3 µl to 6 µl on 36°Y-X $LiTaO_3$ substrate with varying RF power from 2.2W - 6.7W. .....124

Figure 5-40: (a) Jetting process of the droplet of 2 µl under a power of 7.3 W. The SAW direction is from right to left (b) break-up of droplet hitting the side wall, the SAW direction is from right to left. ..... 125
Figure 5-41: Aspect ratio of the jetting as a function of the applied power on the SH-SAW 36°Y-X $LiTaO_3$ device loaded with 2 µl droplets of distilled water. ..... 125
Figure 5-42: The reflection signal of a 128° YX- black LiNbO3 SAW device with IDT's periodicity of 64 µm that measured using the network analyser; the red arrow indicates to the exact resonant frequency of the SAW device. ..... 126
Figure 5-43: Streaming velocity for droplet sizes 5µl and 15µl on 128° YX - Black $LiNbO_3$ substrate excited with Rayleigh wave for varying powers from 2 dBm – 12dBm. ..... 127
Figure 5-44: Numerical 3D illustration showing the droplet SAW interaction leading to 3D complex flow patterns due to SAW energy attenuation and Reynolds stresses formation which in turn produces an effective steady force acting in the fluid body (30 µl droplet at the RF power of 15.98 mW); (a) tilted view, (b) direct view focusing through droplet centre [10]. ..... 128
Figure 5-45: Numerical results showing the progress of flow field after applying the RF power and SAW propagation (30 µl droplet at the RF power of 2.88 mW) [10]. ..... 128
Figure 5-46: Comparison of experimental and numerical modelling for a 30µl droplet positioned at the centre with the SAW propagation direction; the upper row shows pictures of particles trajectories; the bottom row shows the corresponding streaming patterns from numerical simulations. The red arrow indicates the SAW propagation direction. [10] ..... 129
Figure 5-47: Liquid droplet flow on untreated ZnO/diamond surface (the SAW propagates from right to the left) (a) original droplet; (b) droplet deformation and spreading with significant streaming inside. ..... 130
Figure 5-48: Droplet pumping for a droplet of 2 µl at an RF power of 2 W at various durations after applying SAW (a) 0s; (b) 0.08s; (c) 0.16 ..... 130
Figure 5-49: Images captured from a movie taken at 1000 frames s-1 showing the jetting phenomenon for a droplet of 2 µl from the unbalanced force induced by surface acoustic waves on a ZnO substrate (input power of 50 W). The SAW generates from right to left. ..... 132
Figure 5-50: Nebulisation morphology and sequences of the ZnO/Si SAW devices with 0.5µl droplet, IDT power of 12 W; (a) Capillary wave and ejection of droplet after ~0.002 sec; (b) Generation of droplets at ~0.003 sec; (c) Significant nebulisation (mist and

satellite droplets) at ~0.006 sec. Individuate images are also notated with roman numerals for reference. ..... 134
Figure 6-1: Temperature increase from ambient for a 2µl droplet excited with a SH-SAW wave on 36ºYX $LiTaO_3$ crystal ..... 139
Figure 6-2 : Transient plot of increase for a 2µl droplet excited with a SH-SAW wave on 36ºYX $LiTaO_3$ crystal ..... 140
Figure 6-3: Evolution of Péclet number for heat transfer and a function of $P_{IDT}$ (mW) and droplet size (µl) for pure water. Data is shown for thermal heating with SH-SAW wave on 36ºYX $LiTaO_3$ crystal and Rayleigh wave on 128$^o$ YX- black $LiNbO_3$ ..... 141
Figure 6-4: Temperature increase from ambient for varying droplet volumes excited with $P_{IDT}$ =1W. Increase of SH-SAW and Rayleigh wave on 36ºYX $LiTaO_3$ crystal..... 141
Figure 6-5: Three dimensional (3-D) image of typical mesh used for thermal simulation. Mesh is approx. 34,000 DOF. Grid dimensions are shown in mm. ..... 143
Figure 6-6: Evaluation of droplet thermal gradient for increasing Péclet number for 0.2µl with thermal power of 0.23 W at 0.25 s. ..... 144
Figure 6-7: Temperature increase in droplet for increasing Péclet numbers for 0.2 µl droplet with thermal power of 0.23 W. Simulation data is compared to experimental result. ..... 145
Figure 6-8: Efficiency of thermal heating on 36ºYX $LiTaO_3$ with a 2 µl droplet. Calculated input IDT power was varied from 0.2 W – 12 W. ..... 146
Figure 6-9: Temperature increase in two droplets (4 µl) placed in series (a+c) on 36ºYX $LiTaO_3$, (b) temperature in both droplets at t = 0.16 s excited with Rayleigh Wave, (d) temperature in both droplets at t=0.16s excited with SH-SAW wave ..... 147
Figure 6-10: (a) 36ºYX $LiTaO_3$ substrate temperature with no droplet, $P_{IDT}$=4 W (b) 36ºYX $LiTaO_3$ substrate with droplet in situ at start of atomisation process, $P_{IDT}$=4 W. (c) 3 6ºYX $LiTaO_3$ substrate temperature with no droplet, $P_{IDT}$=12 W (d) 36ºYX $LiTaO_3$ substrate with droplet in situ at start of nebulisation process, $P_{IDT}$=12 W ..... 149
Figure 7-1: Mass loading vs. frequency change of various water droplets from 0.1 µl – 16 µl deposited on 36ºYX $LiTaO_3$ substrate ..... 153
Figure 7-2: Radius of Droplet vs. frequency change of various water droplets from 0.1 µl – 16 µl deposited on 36ºYX $LiTaO_3$ substrate ..... 154
Figure 7-3: *In Situ* biosensing and mixing using Euler angle for sensing (0,36,0) and the streaming direction utilised was (90,36,0). Arrow indicates streaming direction. ..... 155
Figure 7-4: Phase angle change for 36ºYX $LiTaO_3$ with and without 1 µl droplet and with acoustic streaming at 23 dBm. ..... 156

Figure 7-5: EWOD lift-off process for integration with SH-SAW.....157
Figure 7-6: (a) Location of droplet with (b) measured frequency when the droplet is located at different positions. 1 & 5 droplet out of SAW propagation path, 2 & 4 at the side of the SAW wave, 3 at the centre of the SAW wave. .....158
Figure 7-7: Insertion Loss Measurement at droplet locations on 36ºYX $LiTaO_3$ Substrate .....159
Figure 9-1: (left) Integrated SH-SAW device (right) Lab-On-USB Shear Wave concept device .....164
Figure 9-2: Loss-Less Acoustic Mixing / Thermal Heating for SH-SAW .....165

# List of Tables

Table 2-1: Properties of Piezoelectric Materials [18] ..... 14
Table 3-1: Frequency of Wave for IDT Designs ..... 40
Table 4-1: Convergence of 36°YX $LiTaO_3$ FEA model ..... 54
Table 4-2: Velocity of wave on 36°YX $LiTaO_3$ substrate for theoretical experimental and simulated results ..... 63
Table 5-1: Parameters for Acoustic Streaming Force ..... 97
Table 6-1: Material Properties used for Thermal Simulations ..... 143

# Publications and Awards

**Awards:**

- Received J.M. Lessels Scholarship from the Royal Society of Edinburgh Research Award to work with Prof. Wixforth at University of Augsburg on the area of research.
- Received University First Year (2009) and Second Year (2010) Research Merit Awards.

**Journal Papers:**

- **D. S. Brodie**, Y. Q. Fu, Y. Li, M. Alghane, R. L. Reuben, and A. J. Walton, "Shear horizontal surface acoustic wave induced microfluidic flow", Appl. Phys. Lett. 99, 153704 (2011), DOI:10.1063/1.3651487.
- Y. Li, Y. Q. Fu, **D. S. Brodie**, M. Alghane, and A. J. Walton, "Integrated microfluidics system using surface acoustic wave and electrowetting on dielectrics technology", Biomicrofluidics, vol. 6, no. 1, pp. 012812–012812–9, Mar. 2012.
- Y. Li, Y. Q. Fu, B. W. Flynn, W. Parkes, Y. Liu, **D. S. Brodie**, J. G. Terry, L. I. Haworth, A. S. Bunting, J. T. M. Stevenson, S. Smith, A. J. Walton; "Test Structures for Characterizing the Integration of EWOD and SAW Technologies for Microfluidics", IEEE Trans. on Semiconductor Manufacturing, 25, 3 (2012) 323 – 330.
- H. F. Pang, **D.S. Brodie**, Y. Q. Fu, X. T. Zu, "Droplet streaming, jetting and nebulisation induced by the shear horizontal surface acoustic wave: high speed observation", Nanotechnology And Precision Engineering, Pts 1 And 2 Editor(s): Jiang, ZY; Kim, YH, Advanced Materials Research, 662 (2013) 580-585.
- **D. S. Brodie**, Y. Q. Fu, Y. Li, and R. L. Reuben, "Numerical analysis and simulation of SH-SAW microfluidics", (in preparation).

**Conference Papers:**

- Y. Li, Y.Q. Fu, B.W. Flynn, W. Parkes, Y. Liu, **D. S. Brodie**, J.G. Terry, L.I. Haworth, A. Bunting, J.T.M. Stevenson, S. Smith, A.J. Walton; "Test structures for characterising the integration of EWOD and SAW technologies for microfluidics", IEEE International Conference on Microelectronics Test Structures, pp. 52-57, March 2010.
- **S. Brodie**, Y.Q. Fu, Luis Garcia-Gancedo, S. Porro, J. Wilson, A.J. Flewitt, W.I. Milne, "Characterization of ZnO/nanocrystalline diamond based surface acoustic wave devices". The 5th International Conference on Technological Advances of Thin Films & Surface Coatings, Harbin, 2010.
- Li Yifan, **Brodie Stuart**, Fu Y.Q., Garcia-Gancedo Luis, Flewitt A.J. Walton A.J., "Integrating digital microfluidics based on ZnO thin films". The 5th International Conference on Technological Advances of Thin Films & Surface Coatings, Harbin, 2010.

- Y.Q. Fu, Y. Li, **S. Brodie**, A.J. Walton; "Integrated Digital Microfluidics based on Surface Acoustic Wave and Electrowetting on Dielectrics", Asia-Pacific International Symposium on Lab on a Chip - AMN-APLOC 2011, pTBD, Jan 2011.
- Y. Li, R. Fu, **D. S. Brodie**, M. Alghane, A.J. Walton; "Enhanced Micro-droplet Splitting, Concentration, Sensing and Ejection by Integrating Electrowetting-on-Dielectrics and Surface Acoustic Wave Technologies", Transducers 11, pp. 2936-2939, 5-9 June 2011.

# Chapter 1. Introduction

## 1.1 Background

The revolution in the biotechnology field has shown the possibility of changing the way we think about healthcare, with emerging sensor technologies opening up the possibilities for new treatments and detection of diseases. With the average age of the population increasing across the world, there is a significant requirement to reduce healthcare costs while still maintaining a high level of care [1].

Remote monitoring is a promising area where patients can use a range of sensors and diagnostic systems to monitor their own health whilst giving them the ability to communicate information with medical professionals. Recent studies have shown that this remote monitoring can significantly reduce hospitalization rates as well as emergency care [2], [3].

Current technologies are mainly single test systems, e.g. blood glucose monitoring, oxiometry, blood pressure and heart rate [1-3]. Limited systems exist for any advanced blood chemistry analysis of pathogens such as virus, bacteria or fungal materials.


**Figure 1-1: Range of health monitoring devices [1-3]**

The growth of microfluidic technology, specifically the *"lab-on-chip"* systems since the 1990's, has given raises to the possibility of developing an integrated a bio-sensing system for home monitoring. Recent technologies such as micro total analysis system (μTAS) show the most promise for developing such a system as they integrate key technologies required, including sample preparation, injection, fluid handling, mixing, separation and detection [4]. Typical μTAS systems generally integrate several technologies [5].

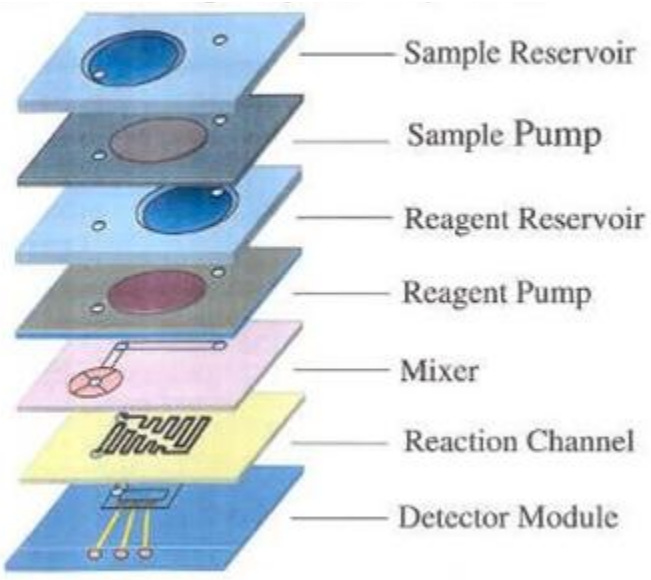


**Figure 1-2: Fabrication of an example µ-TAS system [6]**

Whilst the current µ-TAS systems offer the promise for the future development of tele-monitoring pathogen detection, major challenges still exist before it is likely to have any wide spread adoption. The significant challenges are as follows:

- Multiple process steps and materials are required for manufacture as technologies use different processes such as magneto-hydro-dynamic (MHD) micropumps, CMOS fluoresce detectors and polydimethylsiloxane (PDMS) channels.
- Technologies used for manufacture are generally specialised, expensive and can results in a low yield making devices uneconomical.
- Devices are non-configurable and are designed for a single purpose which negates the possibility for reconfiguration at point of use.
- Devices are typically not used at point of care.

Surface Acoustic Wave (SAW) technology offers possibility to develop a device that can be used for fluid transportation, mixing, jetting, nebulisation and bio-sensing on a single platform and one manufacturing process step.

Surface acoustic wave devices can be characterised by the two main waves that propagate within the medium, the Rayleigh (R-SAW) wave mode and the Shear Horizontal (SH-SAW) wave mode. The Rayleigh wave mode is the propagation of an acoustic wave near to the surface of the elastic medium that travels in a longitudinal direction with a vertical component causing an elliptical motion of a particle at the surface. The shear

wave mode is a propagation of an oscillatory shearing motion that propagates in the longitudinal direction.

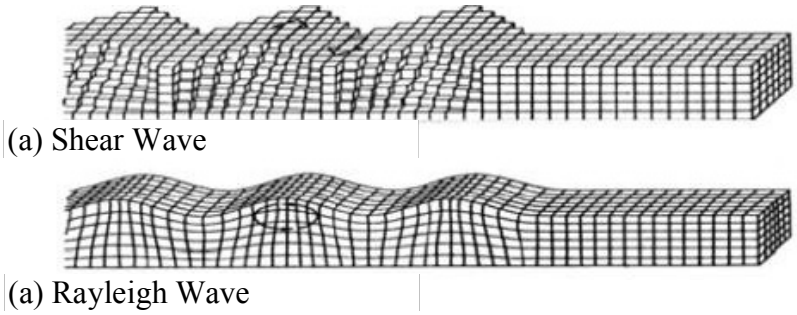


**Figure 1-3: (a) SH wave polarized in the Z direction and (b) Rayleigh wave [7]**

To date, the Rayleigh wave mode has been utilised for dry sensing where a mass loading will change the frequency of the wave propagation [8], [9]. Additionally, the Rayleigh mode has been found to support a wide range of fluidic functions though the mechanism of acoustic streaming, which can be used for streaming, pumping, and ejection of sessile droplets [10]–[17].

The SH-SAW mode has been utilised as an effective fluid biosensors, with sensitivities of 1 ng/cm$^2$ achieved [18], but it is generally accepted that due to minimal fluid coupling, the SH-SAW is inefficient for fluid manipulation [19]. Therefore, while both fluidic and sensing functions have been realised effectively on various crystal cuts, no reports on integration of acoustic streaming and liquid sensing on an SH-SAW device are available.

## 1.2 Aims and Objectives

The main aim of this research is to investigate the feasibility of developing a novel shear horizontal SAW (SH-SAW) bio-sensing platform, with sensing technology integrated with fluid control and advance the understanding of piezoelectric microfluidic systems.

The objectives of the research work include:

- Literature review of SAW technology for bio-sensing and fluid transportation and mixing, and construction of theoretical numerical simulation of SAW device to investigate crystal orientation and optimise the device layout;

- Simulation and characterisation of SH-SAW induced microfluidics, and comparison with the conventional R-SAWs;
- Characterisation of SH-SAW bio-sensing, and comparison with the conventional R-SAW in liquid conditions;
- Evaluation of the integration of microfluidic and biosensing in liquid conditions.

## 1.3 Thesis Outline

This thesis comprises of nine chapters, the contents of which are described below:

Chapter 1 gives a brief introduction of the project outlining the main goals and objective of the thesis.

In Chapter 2, the literature review assesses the development of the research field and discusses microfluidics, biosensors and SAW materials whilst examines the current "state of the art" work.

Chapter 3 covers the MEMS fabrication processes used to manufacture the SAW devices, as well as experimental procedures and apparatus for all work in this thesis.

Chapter 4 outlines basic numerical theory and models for the simulation of the shear wave acoustic fluidics describing the mechanism for the observed fluidic behaviour. This chapter also details the numerical simulation work carried out using Finite Element Analysis of the wave propagation for both the SH-SAW and R-SAW.

Chapter 5 describes all the experimental work and results undertaken analysing the microfluidic behaviour of sessile droplets on both the SH-SAW and R-SAW substrates (including SAWs based on $LiNbO_3$ and ZnO films).

Chapter 6 presents an analysis of acoustic heating generated using the SH-SAW wave and a numerical analysis of the diffusion mechanism.

Chapter 7 outlines the bio-sensing and mass sensing experiments undertaken with the fabricated devices and integration with other technologies.

Chapter 8 summarises the main results with reference to the objectives outlined in chapter one and draws the main conclusions from the work.

Chapter 9 outlines future work that may be undertaken based on the research in this thesis, including novel bio-medical devices that may be realised with the SH-SAW wave.

## 1.4 Contribution to Knowledge:

The author claims two contributions to the existing knowledge with this thesis. The first contribution is the numerical analysis of SH-SAW wave that demonstrates the mechanism where an acoustic wave may be generated and propagated leading to acoustic streaming. The second contribution is the analysis of microfluidic function using the SH-SAW wave and demonstration of key microfluidic functions such as streaming, pumping, nebulisation, ejection and heating.

# Chapter 2. Literature Review

## 2.1 Microfluidics

The concept of microfluidics can be dated back to the late 1970s, when research work was carried out at Stanford and IBM on the development of gas chromatograph and inkjet nozzles producing the first microfluidic devices [20]. Microfluidic devices essentially enable the analysis of small volumes of liquid ranging from the micro to nano litre scale. For the liquid to be analysed, there are several components which are required for a simple systems. They include a method for transportation of the liquid and a structure for which the liquid can travel though. The channel geometry and size can generally be varied to obtain different functions including altering the mass transportation and thermal gradient of any fluid passing through the system. Typically the microchips used have a size of sub-centimetre or a few cm, and materials such as borosilicate, quartz, silicon and piezeoelectric are used for manufacture of the devices [21]. For the fluidic transportation, typically different pumping techniques are used. These vary from mechanical techniques such as diaphragm displacement pumps, electroosmotic, magento-hydrodynamic and electrokinetic [22].

Microfluidic chips have the advantages over the existing systems that they can use tiny volume of liquids over traditional chemical methods of mixing large volumes in beakers and similar standard chemical equipment. The micro volume allows the decrease in reaction time thus allowing for an increased performance of the system.

## 2.2 SAW Principle

As we are interested in the application of the surface acoustic wave (SAW) for microfluidics applications, we will firstly cover the principle of the SAW and the method of wave excitation and fluid coupling.

With the work of Wixforth in the early 1990s, the application of the surface acoustic wave technology has become an interesting area of development for microfluidics [23]. The SAW principle was first described be Lord Rayleigh in 1885, when he observed that during an earthquake, a longitudinal surface wave was produced when the ground began to oscillate. In his paper to the London Mathematical on November 12$^{th}$ 1885, he discussed the mathematical theory and proposed that for wave propagation on

homogenous isotropic elastic solids, their amplitude is confined to a thickness comparable to their wavelength [24]. As a consequence, it has been found that for solid materials, waveforms consisting of traverse and longitudinal components can propagate though the material; these are known as Rayleigh waves (Figure 2-1).

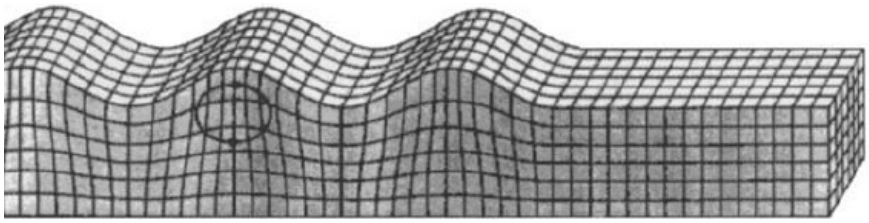

**Figure 2-1: Representation of Rayleigh Waves showing elliptical movement [10]**

A particle in a solid influenced by Rayleigh waves can move in an elliptical path with surface-normal and surface parallel components. The energy is dissipated within a wavelength of the free surface [25] deceasing exponentially below the free surface of the substrate [26].

### 2.2.1 Relationship between Stress and Strain for Solids

Before the use of piezoelectric materials for the SAW devices is discussed, it is advantageous to look at the relationship between stress and strain in standard solid materials.

When a force is applied to a solid material, there is a displacement induced in the material due to the realignment of the atoms. This displacement is dependant on the stiffness of the material as described by the principles of Hooks Law.

For this study, a 3D solid object will be considered but will be simplified by assuming the material has isotropic and homogenous properties. The forces which will be considered are acting on the surface of the object, and for simplicity of the model all body forces such as gravity will be neglected. In order to describe the deformation of an object by forces, the gradient of the displacement is introduced.

$$(\nabla\vec{u})_y = \frac{\partial u_i}{\partial x_j} \qquad 2\text{-}1$$

where $i$ is the component of the displacement, and $j$ is the spatial coordinate. Therefore, the rigid body of a solid undergoes a displacement which is the sum of the displacement gradient and its transpose called a strain tensor:

$$S_{ij} = \frac{1}{2}\left[(\nabla\vec{u})_y + (\nabla\vec{u})_\mu\right] = \frac{1}{2}\left(\frac{\partial u_i}{\partial x_j}\right) + \left(\frac{\partial u_j}{\partial x_i}\right) \quad 2\text{-}2$$

A strain is defined as the change in length per unit length in the solid equilibrium. The diagonal strain term $S_{ij}$ represents the axial strain, while the off diagonal terms, $S_{ij}$ with $i=j$ are shear strains. An application of force results in a strain to a unit volume $dV$ of a solid. The forces which give rise to the deformation and act on a unit volume element $dV$ can be represented as:

$$dF_i = f_i dV = \sum \frac{\partial T_{ij}}{\partial x_j} dV = \sum T_{ij} ds_j \quad 2\text{-}3$$

Both the strain tensor $S_{kl}$ and the stress tensor $T_{ij}$ are made up of 3x3 matrices corresponding to the nine combinations available. An equation to correlate these two components is called a constitutive equation. The form of the constitutive equation depends on whether the material is a fluid, purely elastic or viscoelastic. In a purely elastic deformation, the stress is independent only on the strain $S_{kl}=C_{ijkl}T_{ij}$. This equation is generalized to the 1D spring, but it accounts for the forces and deformation in all three directions. The quantity is the modulus tensor of elastic coefficients and is the equivalent of the spring constant k, used to describe the deformation of a spring. The four subscripts indicate the four sets of a 3-D coordinate system, which are required for a general description of the relation between the strain and stress tensors, and the stiffness coefficient $C_{ijkl}$ has 81 components. In most materials, the stress and strain tensors are symmetric and therefore each contains at most six independent components. Therefore, the modulus tensor for infinitesimal elastic deformation is also symmetrical and contains at most 36 independent components. By assuming a material to be completely isotropic, it can be shown that the number of elastic coefficients can be reduced to two.

### 2.2.2 Wave Equation

Before the analysis of the piezoelectric medium, the basic wave equation for an elastic medium will be discussed.

The basic wave equation is based on the fundamental law of dynamics given by,

$$F = \frac{\partial T_{ij}}{\partial X_j} \quad 2\text{-}4$$

where $F$ is the force density per unit volume, $T_{ij}$ is the stress tensor and $X_j$ are the axes of three co-ordinate direction ($X_x = X$, $X_y = Y$, $X_z = Z$). Thus the wave equation for displacements in an elastic, homogeneous, anisotropic as well as isotropic medium is expressed as,

$$\rho \frac{\partial^2 U_i}{\partial t^2} = \frac{\partial T_{ij}}{\partial X_j} \quad 2\text{-}5$$

Where ρ is the mass density of the elastic medium and $U_i$ are the displacements in respective coordinate directions. Equation 2-5 can also be written as [27],

$$T_{ij} = C_{ijkl} \frac{\partial U_l}{\partial U X_k} \quad 2\text{-}6$$

integrated over indices , the full wave equation is given by,

$$\rho \frac{\partial^2 U_i}{\partial t^2} = C_{ijkl} \frac{\partial^2 U_l}{\partial U_j \partial U X_k} \quad 2\text{-}7$$

Equation 2-7 is a set of 3 equations for displacements $U_x, U_y, U_z$ in 3 co-ordinate directions. The *ijkl* takes all possible combinations of *X, Y, Z* values and are repeatedly summed in the right-hand side of the equation. The size of the wave equation depends on the number of stiffness constants existing for a particular material. For instance, many entries are zero for materials that are isotropic or cubic (symmetry) and the equations are smaller, whereas for general piezoelectric materials fewer entries are zero and the equation can be lengthy. The other important thing to note in Equation 2-7 is that it represents wave propagation in a non-piezoelectric medium as noted before, but provides useful information about wave propagation in media and can be directly extended to piezoelectric case.

### 2.2.3 Wave Solutions in Unbounded Anisotropic Media

An unbounded medium is one which is infinite in all directions (of three co-ordinate axes) and the simplest solution for the wave equations in such media can be plane waves is given by,

$$u_i = A_i \exp\left[jk(l_i x_i - vt)\right] \quad 2\text{-}8$$

where $A_i$ is the amplitude of displacement, $k.l_i$ is the wave vector ($l_i$ describes the direction cosines of wave vector) and v is the velocity of wave [28].

Equation 2-8 represents three waves with different polarizations propagating in a given direction, i.e., a wave with displacement component only in the wave vector direction, a wave with displacement component in direction perpendicular to the wave vector direction and a wave with displacement component in the direction perpendicular to the plane in which the wave vector exists. The three waves are one quasi-longitudinal and two quasi-shear waves, categorized according to the polarization of the displacement of the corresponding waves. They are called quasi-waves because of the fact that almost none (except for certain propagation directions at which modes become pure) of them have displacement components either in the direction of wave propagation or perpendicular to it but rather make a small angle to the propagation vector and its normals. Nevertheless, the polarizations of the three waves are always mutually perpendicular to each other. The velocity of the quasi-longitudinal wave is always higher than that of quasi-shear waves and also the shear waves have different velocities which are in turn classified as fast and slow shear waves depending on their velocities. This kind of wave propagation is true only for unbounded media and all these modes propagate at all frequencies. But once the medium is bounded or finite, mechanical boundary conditions should be satisfied and these waves cannot propagate independently. This prompts a look into surface wave solutions for bounded finite media [27].

### 2.2.4 Wave Propagation in a Thin Surface

A co-ordinate system shown in Figure 2-2 is assumed for surface wave solutions with the surface at Z = 0, extending to infinity. It is assumed the wave vector is to be in the XY plane, i.e., parallel to the surface of the medium which is unbounded in the X and Y directions.

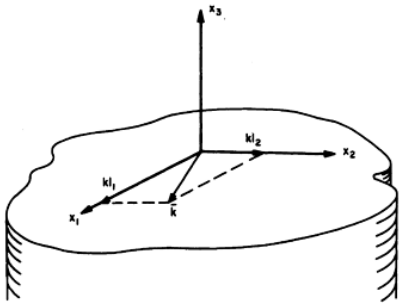


**Figure 2-2: Coordinate system for surface waves**

Surface wave solutions are those in which displacements decay with depth below the substrate surface and are straightly crested, i.e., there is no dependence of the displacement at any depth on the distance measured perpendicular to the sagittal plane [23] (plane containing wave vector and normal to the surface as shown in Figure 2-2). Such a solution can be written in the form in which the Z dependence is treated as part of the amplitude term and wave-like properties depending on the X and Y components and is given by,

$$U_i = A_i \exp(jkl_3 z) \exp\left[jk(l_1 x + l_2 y - vt)\right] \quad 2\text{-}9$$

These solutions (with $l_1$ and $l_2$) can be substituted into the Equation 2-9 and a 3×3 matrix is formed which when equated to zero, results in a sixth order equation in $l_3$ with $v$ as a parameter. A sixth order equation has six roots with three complex conjugate pairs. For surface wave solutions, the value of $l_3$ must lead to displacement components vanishing as $z \rightarrow \infty$. The roots in the upper half of the complex planes leads to solutions which makes displacements increased to infinity at $z = \infty$. Contrastingly, the other three roots on the lower half complex plane lead to surface wave solutions for which the displacements vanish at an infinite depth. The phase velocity is the same for each value of $l_3$ and is determined from the boundary condition matrix. A linear combination of the solutions in Equation 2-9 for each $l_3$ value in the lower half complex plane forms the assumed solution and is given by,

$$U_i = \sum_{r=1}^{3} A_i \exp(jkl_3 z) \exp\left[jk(l_1 x + l_2 y - vt)\right] \quad 2\text{-}10$$

From Equation 2-10, it can be seen that there are 3 displacement amplitudes for each root and for 3 displacements there are totally 9 amplitudes. To determine these amplitudes and the phase velocity of the surface wave, the boundary conditions should be satisfied at the surface.

### 2.2.5 Boundary Conditions:

The boundary condition that should be satisfied for the surface wave solution is that the surface at z = 0 should be stress free, i.e., no surface forces should be acting on it. The stress free condition can be written from Equation 2.9 for stress as,

$$T_{i3} = C_{i3kl} \frac{\partial u_l}{\partial u_k} = 0, at\ z = 0\ for\ i = 1,2,3 \quad 2\text{-}11$$

which can be further written as follows,

$$T_{13} = T_{23} = T_{33} = 0, at\ z = 0 \quad 2\text{-}12$$

Substituting the assumed solution (Equation 2-10) into the set of boundary conditions gives rise to another set of three homogeneous equations in terms of unknown displacement amplitudes. A 3 × 3 boundary condition matrix is formed and for non-trivial solutions to exist, the determinant must be equal to zero. The displacement amplitudes that ought to be found may be a complex and as a consequence the boundary matrix determinant is also a complex. For any particular value of *v* (in the $l_3$ component), it is almost improbable to give a determinant value equal to zero. The equation can be algebraically very complicated to give an explicit analytic expression for the amplitudes. Instead, a set of successive values of velocities were substituted in the equation to find a particular value for which the determinant vanishes (both the real and imaginary parts should vanish). Nevertheless, explicit relations can be found out in certain special cases such as in isotropic media as reported by Farnell [25].

The velocity of surface waves remains s constant in the case of an isotropic media, whereas it is a function of propagation direction in the anisotropic case. For each direction, a set of velocities should be successively checked for the boundary condition to vanish in order to find out the correct velocity.

### 2.2.6 Surface Profile

The homogeneity of the wave solution equations and boundary condition equations allows only for solutions of amplitudes to be found in terms of other amplitude(s). Also, the choice of displacement component to divide through, to find others in terms of it, is compounded by the fact that for certain special directions, some displacement components are zero. Effectively, there are only two displacement components, which are confined to the sagittal plane.

In isotropic media, the roots or the values of $l_3$ are always on the imaginary axis, giving rise to a purely exponential decay of displacements in the negative z direction. Thus an ellipse and the shape of the ellipse changes describe the particle displacement at any depth with the depth due to the change in relative magnitudes of *Uz* and *Ux* with depth (see Fig 2-3). This is given by the following equations:

$$u_1 = \hat{u}_1 cosk(x_1 - vt) \quad 2\text{-}13$$

$$u_3 = \hat{u}_3 sink(x_1 - vt) \quad 2\text{-}14$$

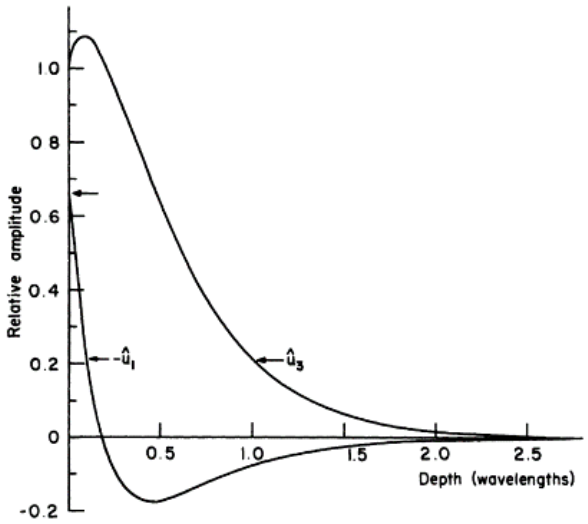


**Figure 2-3: Wave propagation vs. depth [28]**

### 2.2.7 Piezoelectric Materials

Pierre and Jacques Curie first discovered the piezo-electric effect in 1880 when they observed that quartz crystals would be electrically polarised when deformed by an applied force [29]. For typical solid materials, the structure of the atoms is such that there is no net dipole moment, therefore, the atoms have no differential charge. In piezoelectric materials, when equal and opposite forces are applied, the deformation of the crystal lattice will produce a separation of the centre of gravity of positive and negative charges. If we use the piezoelectric tensors for the solution of the wave propagation model, $p_{ijkl}$, then this results in a modified elastic tensor of $c'_{ijkl}=c_{ijkl}(1+K^2_{ijkl})$, where $K^2_{ijkl}$ is the electro-mechanical coupling coefficient of the piezoelectric material. The electromechanical coupling coefficient is essential for the measure of the efficiency of the material to convert mechanical energy into electrical energy in an acoustic material. Since the $K^2_{ijkl}$ is always positive and the piezoelectric tensors $c'_{ijkl}$ is by its nature greater than $c_{ijkl}$, the material will become stiffer and the sound velocity will increase.

SAW devices are typically fabricated using bulk materials that remain dominant in industry today. The disadvantage of bulk technologies is that they are expensive, and they cannot be integrated with Si-electronics on the same substrate for signal processing and control, and with other microfluidics and sensors for microfluidics and LOCs applications.

**Table 2-1: Properties of Piezoelectric Materials [30]**

| Materials | ZnO | AlN | PZT | Quartz | 128° cut $LiNbO_3$ | 36° cut $LiTaO_3$ | PVDF |
|---|---|---|---|---|---|---|---|
| Density ($g/cm^3$) | 5.61 | 3.3 | 7.8 | 2.64 | 4.64 | 7.45 | 1.79 |
| Moulus (GPa) | 110-140 | 300-350 | 61 | 71.7 | 202 | 225 | 0.16 |
| Hardness | 4-5 GPa | 15 GPa | 7-18 GPa | Moh's 7 | Moh's 5<br>Knoop 800-1000 | 70-110<br>Knoop 700-1200 | Shore D75-85 |
| refractive index | 1.9 to 2.0 | 1.96 | 2.40 | 1.46 | 2.29 | 2.18 | 1.42 |
| Piezo-constant d33 (pC/N) | 12 | 4.5, 6.4 | 289-380, 117 | 2.3(d11) | 19-27 | -21 | -35 |
| Coupling coefficient, k | 0.15-0.33 | 0.17-0.5 | 0.49 | 0.0014 | 0.23 | 0.2 | 0.12-0.2 |
| Effective coupling coefficient, $k^2$ (%) | 1.5-1.7 | 3.1-8 | 20-35 | 8.8-16 | 2-11.3 | 0.66-0.77 | 2.9 |
| Acoustic velocity by transverse (m/s) | 6336<br>(2650) | 11050 (6090) | 4500<br>(2200) | 5960<br>(3310) | 3970 | 3230-3295 | 2600 |
| Shear wave velocity (m/s) | - | - | - | - | - | 4117 | - |
| Shear coupling coefficient, k | - | - | - | - | - | 4.7 | - |
| Dielectric constant | 8.66 | 8.5-10 | 380 | 4.3 | 85 (29) | 54 (43) | 6-8 |
| Coefficient of thermal expansion (CTE, $x10^{-6}$) | 4 | 5.2 | 1.75 | 5.5 | 15 | -16.5 | 42-75 |

The most common bulk piezoelectric materials are lead zirconate titanate ($Pb[Zr(x),Ti(1-x)]O_3$), PZT blocks for ultrasonic transducers, quartz ($SiO_2$) for QCMs, and quartz,

lithium tantalite ($LiTaO_3$) and lithium niobate ($LiNbO_3$) for SAW devices. Table 2-1 lists common piezoelectric materials which have been used in SAW devices.

Various piezoelectric thin film technologies have been developed for ultrasonic and acoustic wave device applications. Piezoelectric thin films PZT, ZnO and AlN have good piezoelectric properties and high electro-mechanical coupling coefficient, $k^2$, thus they have been studied intensively for this purpose. They can be grown in thin film form on a variety of substrates, including silicon, making these materials very promising for integration with electronic circuitry, particularly for devices aimed at low-cost and mass production for one-time use. PZT has the highest piezoelectric constant and $k^2$, but PZT films have very high acoustic attenuation, lower sound wave velocities, poor biocompatibility and worst of all, the requirement for extremely high temperature sintering and high electric field polarization, making them unsuitable for integration with electronics. PZT has been limited to ultrasonic devices, but not for the acoustic wave devices even though some research has been conducted.

AlN and ZnO are the most common thin films used for SAW devices, FBARs and FPW devices. AlN material is chemically inert and stable, with high acoustic velocity, but AlN thin films are relatively difficult to deposit, requiring a much stringent optimization process to obtain high quality thin films with smooth surfaces. On the other hand, ZnO PE films with a high PE quality are much easier to obtain using various deposition technologies such as sputtering, laser-ablation, chemical vapour deposition (CVD) and molecular beam epitaxy (MBE) etc, therefore, it is the most widely used PE thin film for thin film ultrasonic and acoustic wave devices. For better precision applications, high operating frequency ZnO SAW devices have been developed by using non-piezoelectric supporting thin films with high acoustic velocity such as sapphire and diamonds [31]–[34]. Acoustic waves generated by ZnO SAW travel inside the supporting layer with high velocity, resulting in high frequencies. Besides PZT, AlN, and ZnO, many other PE thin films have been developed, mostly for SAW device application. Gallium arsenide (GaAs), gallium nitrides (GaN), polyvinylidene fluoride (PVDF) and its copolymers are a few of them being investigated for piezoelectric applications.

The apparent advantages for thin film based ultrasonic transducers are their potential for integration with other technology to form LOCs for better functions and applications. Thin film technology is considered to be the technology for future of the microfluidics and lab-on-chips, as it uses less materials and energy during fabrication, with advantages

of low cost, easy for disposal etc. Currently, there are a several studies using the thin film SAWs to realise both microfluidics and sensing functions [14], [17].

### 2.2.8 Excitation and Detection of Surface Waves

For excitation and detection of the surface waves, a structure is required to both transmit and receive the signals. Typically a pair of interdigitated transducers are used for this purpose which is illustrated in Figure 2-4. An oscillatory voltage is applied to the input transducer which is then converted into mechanical energy by the inverse piezoelectric effect with a wavelength of 2p, where p is the spacing of adjacent electrodes. If the output transducer is patterned with the same wavelength, an electrical signal will be produced using the direct piezoelectric effect from the mechanical vibrations which can be measured using standard apparatus such as a network analyser.

To calculate the resonate frequency of such a device the following relationship can be used [35].

$$f = \frac{v_r}{\lambda_r} \qquad 2\text{-}15$$

Where $v_r$ is the velocity of the wave in the piezoelectric substrate and the $\lambda_r$ is the wavelength which is 2p.

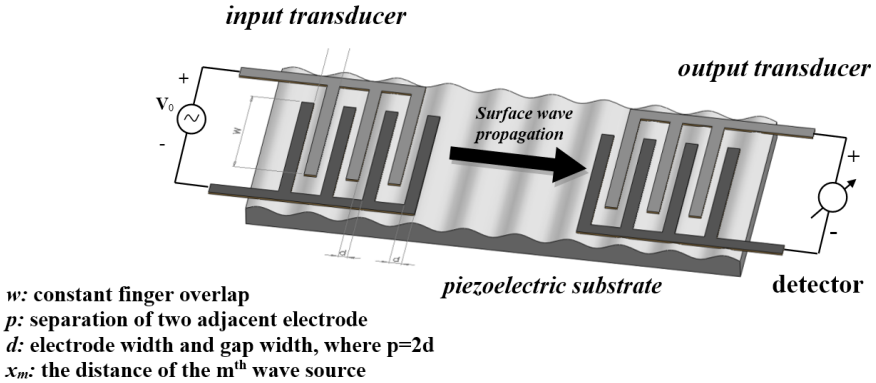


**Figure 2-4: Surface waves on piezoelectric substrates generated by two sets of IDT's**

The signal generated by the IDT will propagate in both directions thus only half the power transmitted will be received by the output IDT set.

## 2.3 Bio-Sensors

Biosensors can be defined as a device containing a biological sensing material or a biological-derived sensing element such as enzymes, antibodies, nucleic acids, receptors, cell etc. [36]. The initial biosensors were called enzyme electrodes and were firstly described in a paper by Clark and Lyons in 1962 for the continuous measurement of glucose during cardiovascular surgery [37]. A biosensor typically consists of three elements: an analyte which is the substance to be measured, a biological element which will react with the analyte producing a response, a transducer which will detect the optical, electrical or mechanical change and a signal processor which can be used to analyse the response, with one example shown in Figure 2-5 [38].

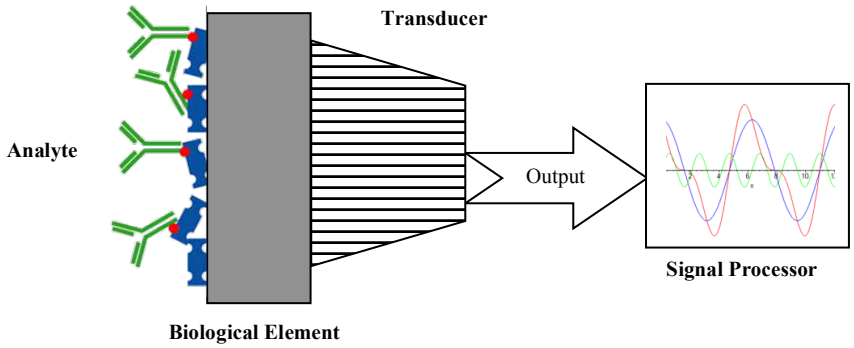


**Figure 2-5: General principle of biosensors. The chemical target (analyte) is selected by the biological element creating a physical or chemical property change which creates stimulus to the transducer which is then measured**

Most transducers are based on electrical measurements due to the ubiquity of electrical technology. The common transducers include: electrochemical, optical and piezoelectric [38].

### 2.3.1 Immunosensors

With the focus on point of care testing, an immosensor, where the antibody serves as the biological components of the biosensors, provides one of the most interesting areas for detection of diseases.

Immunsensors are based on measuring the bonding between antibodies and antigens. When the immune system is exposed to a pathogen, a reaction is started to eradicate it which includes the production of antibodies and then bonds to the antigens of the disease (see Figure 2-6).

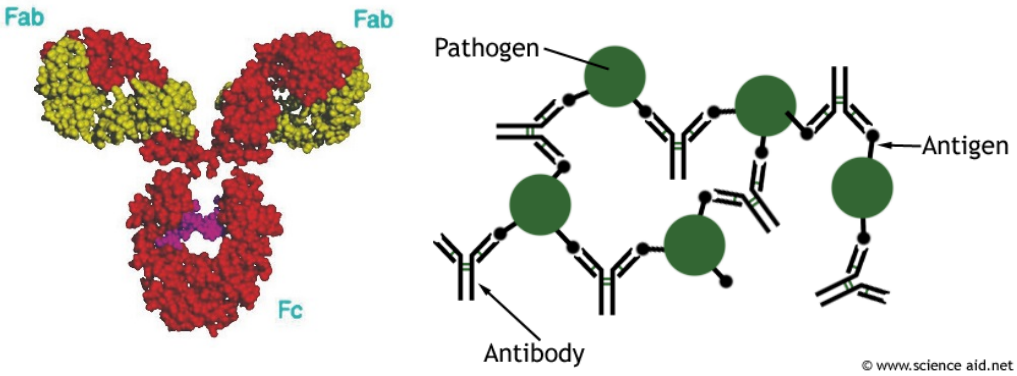


**Figure 2-6: Antibody to Antigen binding**

For the manufacture of an effective immosensors, the antibody or antigen must be bonded to the surface by a process of immobilisation. Several methods of immobilisation which are common as follows:

- Adsorption: Simplest method suitable for a short scale bonding;
- Microencapsulation: Material is placed closely to the biosensor using a membrane;
- Entrapment: Biomaterial is mixed with monomer solution and then polymerise into a gel;
- Cross-Linking: Biomaterial is chemically bonded to a biomaterial to solid supports;
- Covalent-Bonding: Biomaterial is bonded to a specifically designed bond in the support matrix.

For the development of biosensors, adsorption is the simplest process where a material such as gold adsorbs the enzyme on its surface. There are two types of adsorption: physical adsorption and chemical adsorption. Physical adsorption is where a weak bond occurs via the formation of van der Waals forces. Chemical adsorption is the process where a covalent bond forms between the two components. Typically the lifetime of the bond is around 24 hours meaning it is only suitable for short term biosensors. Numerous papers have been published to discuss the procedure of immobilisation using adsorption for biosensors onto a monolayer such as gold or PMMA and the method are well documented [39].

### 2.3.2 DNA Sensor

With the importance of diagnosis of genetic disease, DNA sensors are of intense interest as an area of research. There have been various types of DNA sensors developed over the years. Methods used for DNA detection in those sensors have been reported to be based on radiochemical, enzymatic, fluorescent, electrochemical, optical, and acoustic wave techniques [40].

SAW DNA biosensors have been successfully developed by Hur [25], who developed a technique for developing DNA sensors with a complementary DNA binding achieved by the DNA oligonucleotide target layer deposited on the Au coated delay line of a transverse SAW device. The probe DNA immobilization on the Au coated delay line and the probe-target DNA hybridization on the delay line caused a corresponding shift in the oscillation frequency of the SAW sensor [41].

### 2.3.3 Enzyme Sensors

Another interesting biosensor is an enzyme sensor which consists of a transducer and a thin enzymatic layer, which measures the concentration of a substrate. The enzymatic reaction transforms the substrate under analysis into a reaction product which is detectable by a traducer.

This detection may occur using various methods:

- Enzyme electrode;
- Enzyme thermistor;
- Enzyme transistor;
- Enzyme photodiode.

The critical steps during the operation of an enzyme sensor are as follows:

- Transportation of the substrate under analysis in the bulk solution towards the enzymatic layer;
- Diffusion of the substrate within this layer, accompanied by the enzymatic transformation of the substrate into a reaction product;
- Migration of the product towards the transducer;
- Conversion of the product into an electrical signal by the associated transducer.

SAW sensors have been used effectively as enzyme sensors with the first SAW enzyme sensors being developed in the early 1990 using SH SAW devices based on $LiTaO_3$ [26]. They used the pH change associated with an enzyme substrate reaction. Inoue et al. coupled glucose oxidase for the detection of glucose, while Kondoh et al. coupled urease for the detection of ureas on the SAW device [42]. Furthermore, Kondoh et al. coupled cholinesterase to the sensor surface and investigated the reaction with butyrylcholine. This enzyme reaction could be inhibited by adding fenitrothion, an organophos-phorus pesticide substrate.

## 2.4 SAW Biosensors

SAW devices have a long history of being used as sensors with the first SAW sensors being presented by Wohltjen et al. in 1979 [43]–[45]. They showed that a sensor supporting a "Rayleigh Wave" could be used as a chemical sensor for gas detection by coating the surface with a polymer layer and detecting the mass change due to the absorption of the gas. SAW devices act as excellent sensors due to the acoustic energy being confined to several wavelengths near the surface. Due to this, they are very sensitive to any change on the surface such as mass loading or viscosity changes [46].

Initial work for development of biosensors for the detection of proteins was less successful with a poor sensitivity observed [47]. Reasons for poor sensitivity in detection were mainly due to proteins or substances being in a liquid such as phosphate buffered saline (PBS) which dampened the Rayleigh SAWs due to the displacement of the wave being perpendicular to the surface.

### 2.4.1 SAW vs. QCM

Due to the dampening of the Rayleigh wave, initial research was therefore undertaken into bulk acoustic wave devices (BAW) that use thickness shear mode (TSM), typically known as quartz crystal micro balances (QCM as shown in Figure 2-7). QCM operates at relatively low frequencies usually in the range of a few MHz. Higher frequencies are desirable due to increased sensitivity but require thinner substrate making the devices impossible to manufacture and impractical [48].

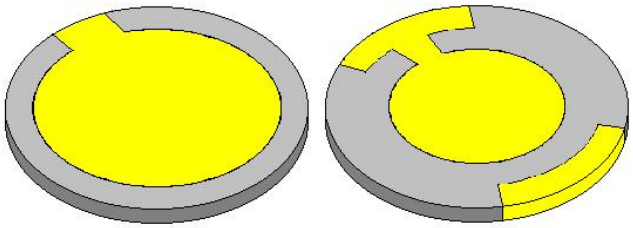

**Figure 2-7: QCM Microbalance, gold colour indicates the electrodes, grey indicates the Quartz crystal**

The QCM is a bulk wave device with the waves propagating through the entire piezoelectric material. The displacement is maximised in the upper and lower surfaces making the device highly sensitive to surface changes such as mass and viscosity. Current research is focused on BAW based biosensors using QCM and SAW based biosensors. SAW sensors have been shown to be advantageous to QCM devices due to the following reasons:

- Higher operating frequency resulting in higher mass sensitivity [24-27];
- Ability to realise microfluidic function using SAW

### 2.4.2 Shear Horizontal SAW Biosensors

As discussed, the limitation of the initial SAW sensors was the loss of energy due to the damping effects of a fluid medium used as a buffer on the piezoelectric surface [8]. The first successful approach using SAW for biosensing was with shear horizontal (SH) waves devices by Shiokawa and Moriizumi [49]. They investigated the use of materials lithium niobate ($LiNbO_3$) and lithium tantalate ($LiTaO_3$) at different crystal orientations. The work showed that the $LiTaO_3$ SAW device was found to have the highest sensitivity in a water medium. The wave was called a shear horizontal wave and in this substrate it was titled a "leaky wave" since small amounts of acoustic energy propagates into the crystal. The authors did not evaluate the biosensing application but suggested its use as a biosensor.

The shear wave in a SAW device causes displacement of particles vertical to the propagation direction and also perpendicular to the sagittal plane. Surface shear horizontal waves can be roughly classified into three distinct groups:

### 1. Surface Skimming Bulk Wave (SSBW)

A surface skimming bulk wave travels close to or just under the surface of the surface with small angle θ in relation to the surface of the substrate as shown in Figure 2-8.

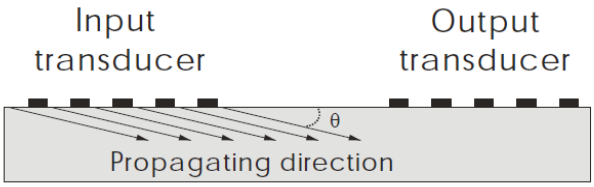


**Figure 2-8: Surface-skimming bulk waves propagate close to the surface with angle θ**

The SSBW energy is localised very near to the surface with a slow decay into the bulk material. It has a dominant shear horizontal polarisation similar to the transverse wave.

### 2. Leaky Wave

As described for a certain crystal orientation, a special wave called the "leaky wave" can exist. The wave is very similar to the real surface wave but there is some small attenuation into the bulk material.

### 3. Love Wave

Love waves are characterised as shear horizontal waves that propagate into a thin layer lying on a semi-infinite solid [50]. As shown in Figure 2-9, the wave is guided though the top layer if the acoustic velocity of this is lower than the wave velocity in the bulk material. The top layer of the Love mode devices with lower shear velocities have been shown to significantly improve the sensitivity of the sensor [51]. The first SAW devices to be used as biosensors were based on 36°YX $LiTaO_3$ and work was first published on their use in the 1990's [33-34]. The 36°YX $LiTaO_3$ is known to have the lowest attenuation at 36° which means there is a minimum energy loss into the substrate, thus maximising the sensitivity of the layer for sensing as shown below in Figure 2-10.

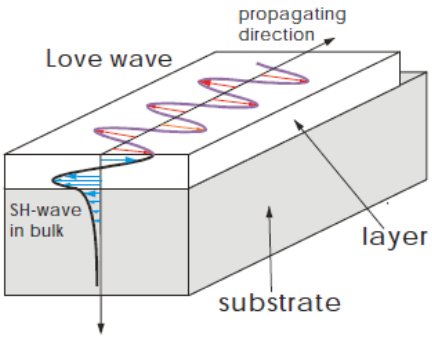


**Figure 2-9: Love wave**

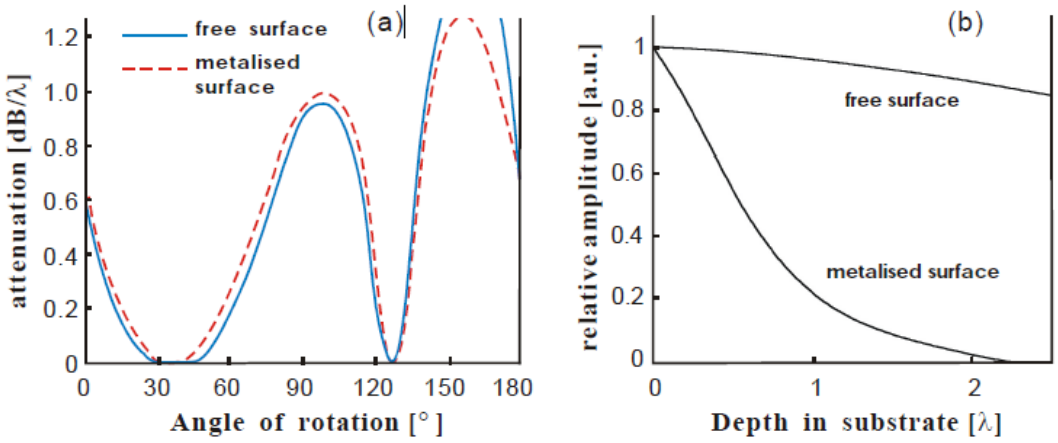


**Figure 2-10: (a) Attenuation of the leaky surface wave on YX-LiTaO3 crystal with different cuts of rotation angles. The minimal attenuation occurs when the angle is 36°. (b) The relative amplitude of surface waves about depth from the free and metalised surface of 36° rot YX-LiTaO3 crystal. The surface wave concentrates closely to the metalised surface, while at free surface the wave is penetrate deep into the substrate. [52]**

### 2.4.3 Love Mode Biosensors

With work being undertaken on pure shear wave biosensors for several years, new research was published on a novel type of biosensor in 1992 using the Love mode shear wave [53] . A typical Love mode biosensor is shown below in Figure 2-11.

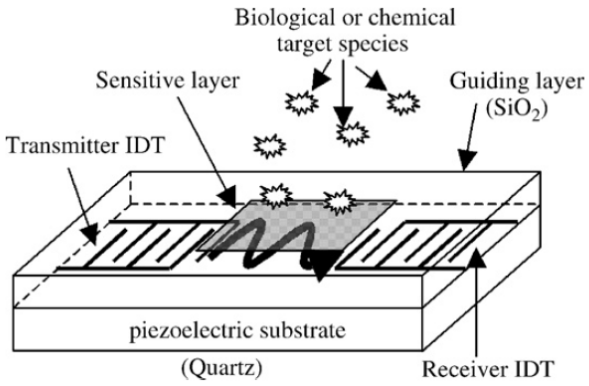


**Figure 2-11: Love Mode Biosensor [53]**

Gizeli et al. reported that the application of a polymer (PMMA) layer (commonly called a waveguide) on a quartz substrate supporting a shear horizontal wave resulted in increased sensitivity of the device [54]. Sensitivity was seen to be increased by 19 times with a 1.6 µm PMMA layer and a phase change was measured for the binding of Human IgG and ant-human IgG adsorbed onto the surface. Also in the same year, an alternative Love mode fabrication method was developed by Kovacs et al.[55]. The authors reported that

the Love mode could be supported by a sputtered $SiO_2$ layer though only photoresist was used for mass loading.

In addition to PMMA and $SiO_2$ waveguide layers, additional materials have been tested for their suitability. Kalantar-Zadeh et al. tested the adsorption of rat immunoglobulin onto ZnO layers sputtered onto ST-cut quartz. Their results showed that the ZnO layer was able to detect 500 pg·ml IgG for a thickness equal to 0.12 of the wavelength and with mass sensitivity of 0.95 cm²/ng [56]. Brach et al. investigated the use of polyimide and polystyrene waves guides spun coated on 36ºYX $LiTaO_3$ substrates [18]. They used bovine serum albumin (BSA) for saturation of the device to improve mass sensitivity. With a polymide layer of 0.6 μm, a mass of 0.815ng was detected with a sensitivity of 4.08 ng/cm². The polystyrene layer of 0.75μm was seen to be an optimum with a sensitivity of 2.62 ng/cm². Polymer waveguides were shown to be highly chemical resistant, exhibited less swelling and are easier to apply than comparable $SiO_2$ waveguides [57].

## 2.5 Fluid Transportation and Mixing in SAW Devices

For development of a cost effective point of care system using SAW technology, it is important that not only biosensing can be performed, but also mixing and transportation can be undertaken as well. A review of the current technology related to fluid mixing and movement will now be discussed together with the current integration technologies.

### 2.5.1 Fluid transportation using channels

For fluid transportation of an analyte across the sensor surface, the most reported method used is by means of a fluid channel and capillary tubes. One embodiment of the setup includes a polydimethylsiloxane (PDMS) channel formed from soft lithography techniques [58] using an SU-8 spun coated master which is then poured with the PDMS mixture (see Figure 2-12). The desired channels are then bonded to the SAW device using a UV plasma treatment which creates covalent bonds between the two surfaces. Capillary tubes are used to connect the PDMS channel to a syringe pump for a continual flow of the solution. A typical set-up for a love mode SAW device is shown below and also reported in the following sources [59]–[62].

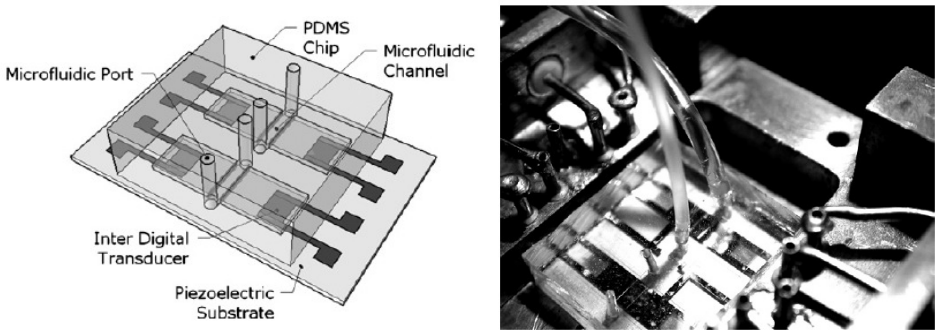


**Figure 2-12: Love wave acoustic device with PDMS chip [63]**

Whist this method provides a highly accuracy geometry and flow system, there are multiple fabrication steps required and bonding of the analyte to the PDMS channel can occur limiting any reuse of the system.

Lange et al. proposed a similar system with the SAW $LiTaO_3$ biosensor packaged in a microfluidic polymer chip [64]. The polymer layers were manufactured using a photopolymer which was exposed to successive masks and bonded in layers to form the channel. The chip was then inserted into a carrier with conductive pogo pins for contact and the capillaries were sealed using O-rings to the device. Figure 2-13 shows the set-up used by Lange et al. with the polymer channel and carrier [57].

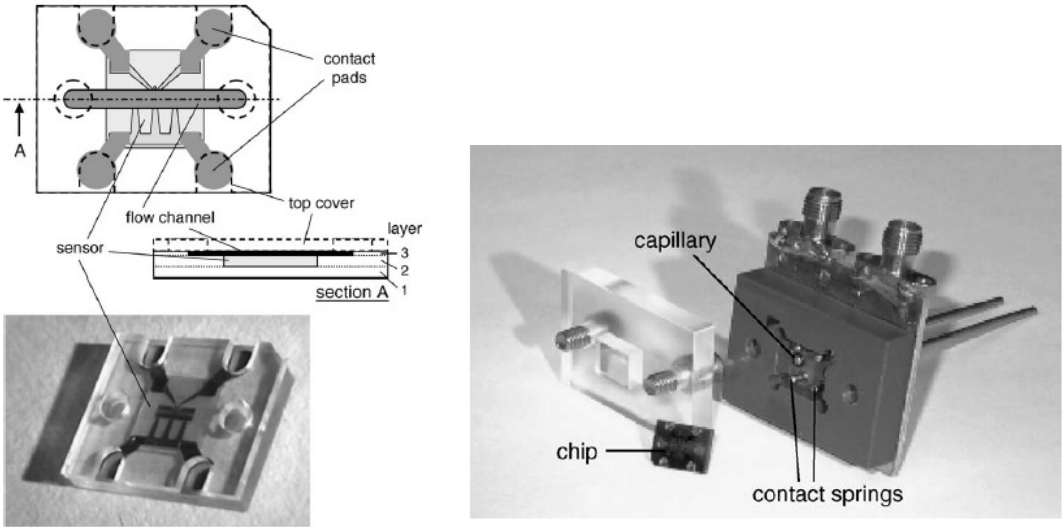


**Figure 2-13: Polymer packaged microfluidic chip [64]**

This method again has the limitation of complex assembly and manufacture but the polymer is more robust than the PDMS channel and is suitable for rigorous washing and

cleaning after analysis and encapsulation, thus significantly enhances the mechanical robustness of the package.

The final method to be discussed is the formation of a SU-8 liquid cell reported by Francis et al. [65]. The SU-8 was patterned on Quartz at the SAW fabrication step with 150 µm walls and then a 500 µm quartz cap was placed manually after dicing of the SAW wafer as shown in Figure 2-14.

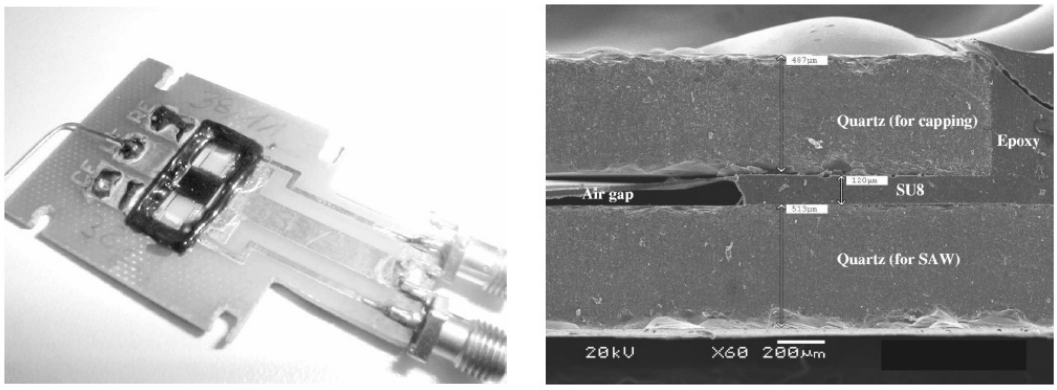


**Figure 2-14: SU-8 Microfluidic cell on SAW device. (a) a general view of the device; (b) cross-section view [65]**

The advantages of this method over PDMS include: stiffer material leading to lower adsorption of acoustic signal, chemical resistance to organic solvents and low thermal dissipation with high adhesion.

Whist this method is an improvement over the PDMS system in terms of process steps, it is still limited by external syringe pumps being required for fluid movement.

### 2.5.2 Surface Acoustic Wave Streaming and Pumping

As it has been shown, micro syringe and pumps provide suitable flow systems for biosensing platform. For development of a point of care testing; miniaturisation is critical. Integrating the mixing and pumping technology directly onto the SAW device would allow this critical reduction in scale.

As previously discussed, when a Rayleigh wave is induced in a piezoelectric material, a wave propagates along the substrate causing nanometre displacement on the surface of the material. If any material is placed on the surface, it will naturally absorb the energy from the wave propagation and if a viscous material such is a liquid is placed on the device then a large amount of the energy is absorbed. In the case of a liquid the wave is

launched into the fluid under the Rayleigh diffraction angle given by the relationship [23]:

$$\boldsymbol{\theta_r = arcsin\left(\frac{v_s}{v_f}\right)} \qquad 2\text{-}16$$

Where $v_s$ and $v_f$ are the sound velocities of the substrate and the fluid [23]. A schematic illustration of the acoustic wave propagation into a droplet is shown in Figure 2-15.

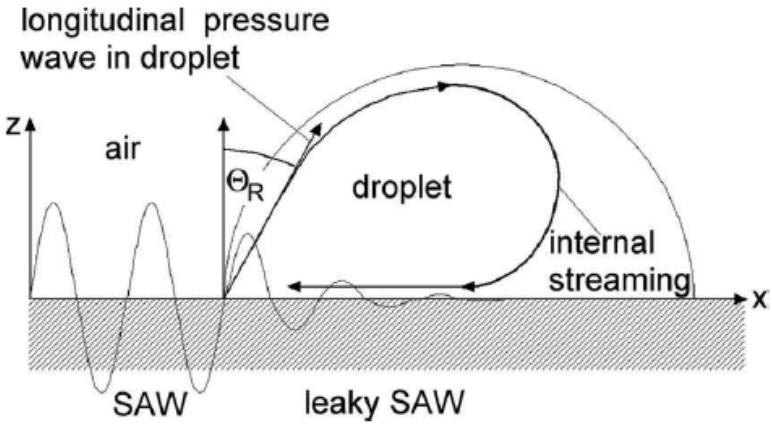


**Figure 2-15: Schematic illustration of interaction between SAW and liquid on surface of SAW [66]**

### *2.5.2.1 SAW Microfluid Streaming and Mixing*

Wixforth et al. showed that at low powers internal streaming within the droplet could happen and if fluorescent die was introduced it would quickly dissipated as shown in Figure 2-16 [67].

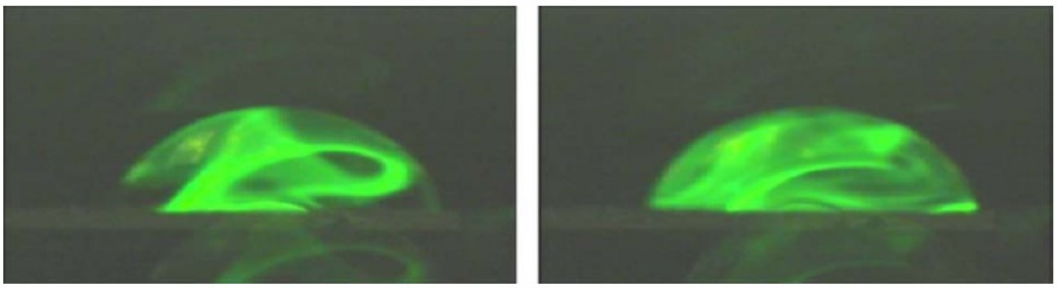

**Figure 2-16: Side elevation view of SAW induced internal steaming [67]**

Several papers have shown that the SAW device supporting a Rayleigh wave can act as an effective micromixer [68], [69]. Ito et al. showed that varying the position of the droplet with respect to the IDT would result in different mixing vortex within the droplet [70] as can be seen from Figure 2-17.

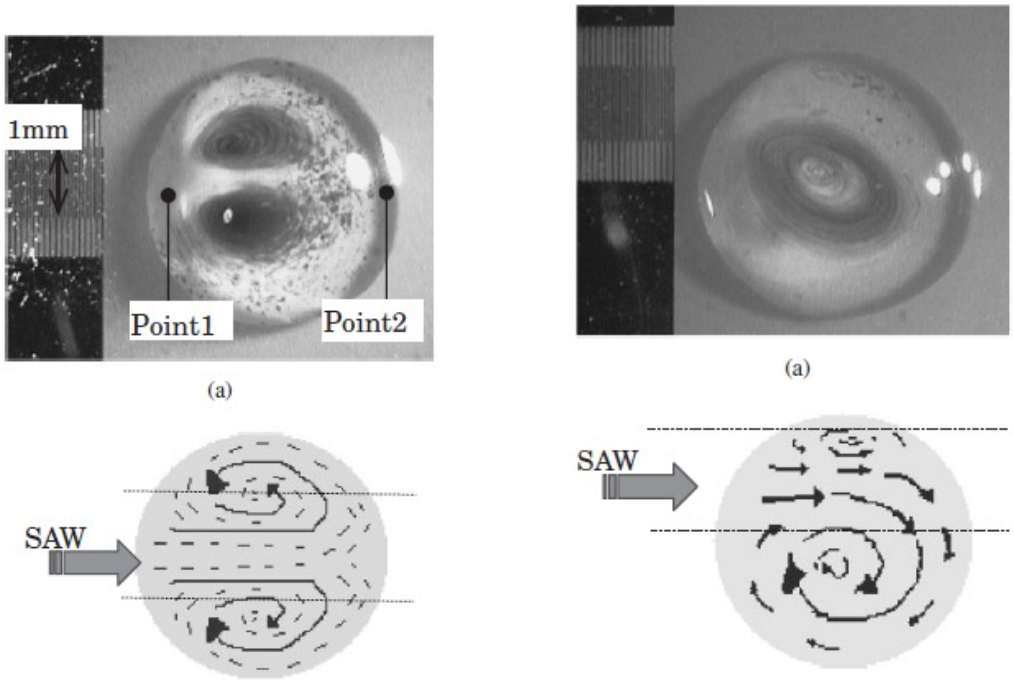


**Figure 2-17: Typical Rayleigh wave velocity profiles centred and off centred [70]**

Shilton et al. used the positional variation of the droplet to show that rapid concentration of particle mixing using polystyrene could occur within 1 second [71]. Similarly they used the same set-up to quantify mixing and diffusion of a food die within glycerine which was shown to have been diffused in around 1s. In later papers they also proposed that this concentration method could be used for the separation of blood plasma for red blood cells for point of care devices but no work on this has been presented to date [72]. Tseng et al. also demonstrated a SAW driven micromixer with a 9.6 MHz SAW device with a U shape PDMS channel bonded onto the surface [73]. They found that for micro-mixing, an induced streaming vortex is more important than a uniform flow in the channel. Sritharan et al. developed a hybrid system by placing a 146 MHz SAW device underneath a substrate with a micro-channel fabricated into it [74]. The SAW device was positioned such that wave propagation wave propagated transversely to the flow inducing mixing.

One critical issue for development of a micro sensing platform is the in situ mixing during biosensing for improved reaction kinetics and stable results. Ducloux et al. presented a method for inducing SAW microstirring during a bio-reaction [75]. They developed a theoretical model based on measured data showing that the mean concentration of the binding analyte can be increased from 0.02 nM/mm to 0.14 nM/mm

when the analyte is stirred at a velocity of 0.01mm/s. The set-up discussed is shown along with the mean concentration over time in Figure 2-18. Whilst providing a theoretical framework for this process, however, no experimental results of the process were presented in their paper.

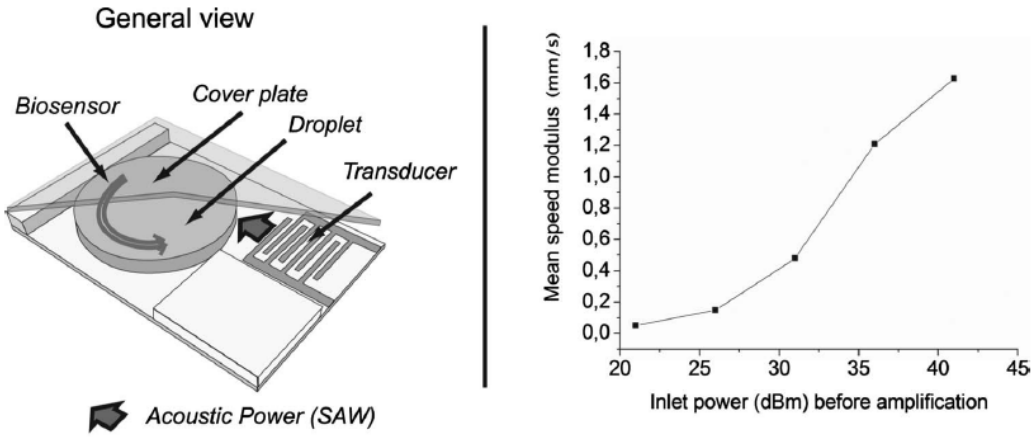


**Figure 2-18: Proposed SAW bioreactor and mixing kinetics [75]**

### *2.5.2.2 SAW Microfluidic Pumping*

Whilst at low SAW powers, it has been shown that streaming occurs in the droplet. At higher powers, movement of the droplet can be induced as initially described by Wixforth [23]. Renaudin et al. showed that for droplet movement on an untreated hydrophilic surface that a minimum power of 32 dBm was required for a 2 µl droplet [76]. With the treatment of a hydrophobic coating of octadecyltrichloro-silane (OTS), the power was seen to drop to 27.5 dBm for droplet movement and the droplet was seen to maintain in geometric form during movement. Figure 2-19 shows the droplet movement before and after a hydrophobic treatment [76].

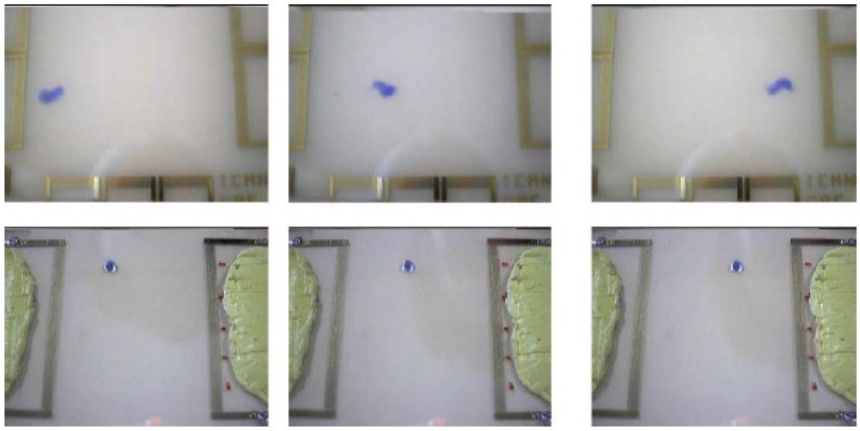

**Figure 2-19: Sequential top views of droplet displacements. Top: displacement on a substrate without surface treatment. Bottom: displacement on a substrate with OTS treatment. The treatment of the surface with OTS significantly improves the situation [76]**

In addition to droplet flow, SAW has been shown to induce streaming in micro channels. Cecchini et al. have shown that SAW streaming within a channel can be induced when a SAW wave is excited [77]. Streaming was observed within the PDMS channel fabricated over the SAW device. When driven directly with the SAW wave propagating along the direction of flow, atomisation and break-up of the droplets quickly occurred at 20 dBm. Driving the SAW device from the two opposite sides, it was observed that a fast liquid transfer from the reservoir into the micro-channel with 20 dBm was observed resulting in a flow velocity of 1.24 mm/s. Unfortunately, no theoretical explanation was suggested in the paper for this behaviour. Figure 2-20 shows the experimental set-up used for the channel design and the pumping of the liquid in the channel [77].

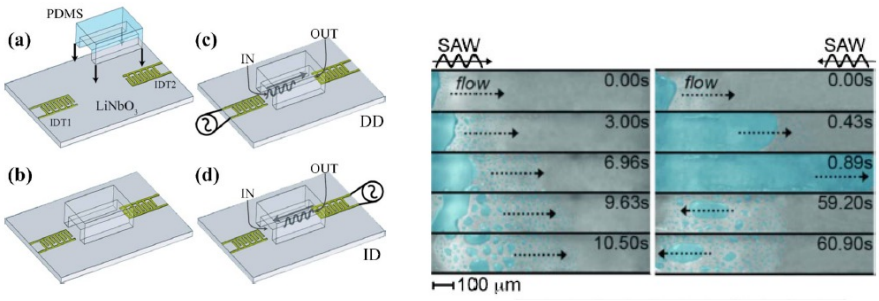


**Figure 2-20: Image of assembly of microfluidic device and filling or the water reservoir using the SAW for direct drive and inverse drive [77]**

Another method of cell flow was investigated by Tan et al. using a laser ablated groove micro-channel with a rectangular cross-section [25]. Flow velocities of up to 10 mm/s were observed in the 50 µm channel and up to 55 mm/s were observed in the 280 µm channel. It was shown that for channels smaller than the SAW wavelength, the flow was unidirectional. However, with a wavelength close to the SAW device, a higher vortex was introduced forming a chaotic flow. This means that the device is suitable for a micropump only for small wavelengths but may act as an efficient micromixer at higher wavelengths. The manufactured device and flow profiles are shown below in Figure 2-21.

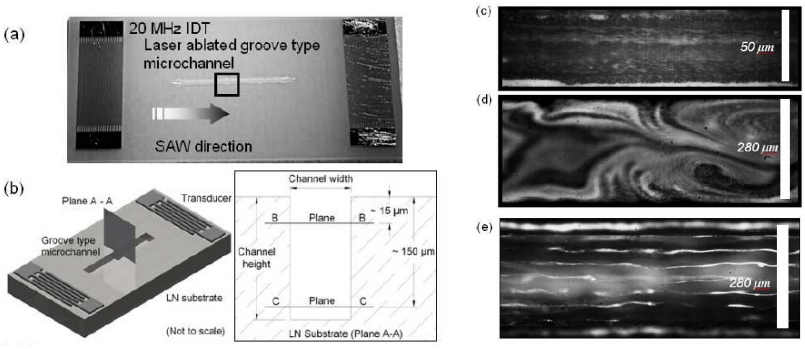


**Figure 2-21: (a) laser ablated microchannel (b) viewing planes (c) Particle steamlines in 50µm channel (d) 280µm channel (e) Plane C-C in 280µm channel [25]**

### *2.5.2.3 SAW Microfluidic Jetting and Nebulisation*

For SAW devices if RF power, with sufficient magnitude, is applied to the liquid on a hydrophobic surface, the droplet can be ejected from the device surface based on the Rayleigh wave angle (see Figure 2-22(a)). If the SAWs are excited from a pair of IDT electrodes then a vertical jetting may be realised (see Figure 2-22(b)) [78].

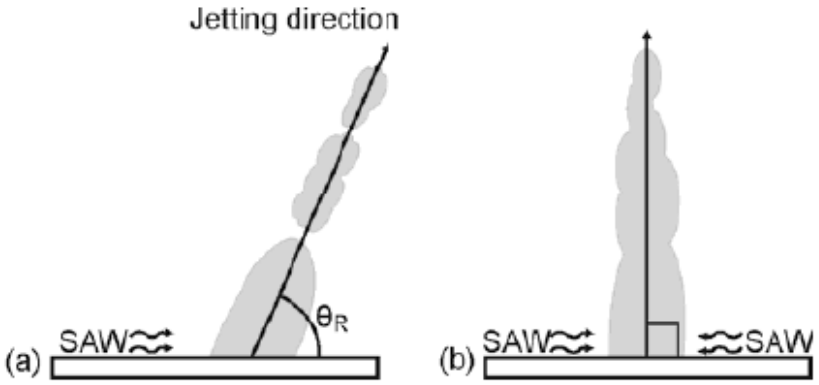


**Figure 2-22 Droplet jetting induced by a single IDT SAW device (a), and droplet jetting induced by a pair of IDT electrodes (b) [61].**

If the RF power applied to the liquid on a hydrophilic surface is sufficiently large, tiny droplets with volumes in range of a few femitolitres to a picolitre can be generated and escape from the surface of a liquid reservoir, forming a continuous mist of droplets as shown in Figure 2-23. This is called atomisation or nebulisation [79].

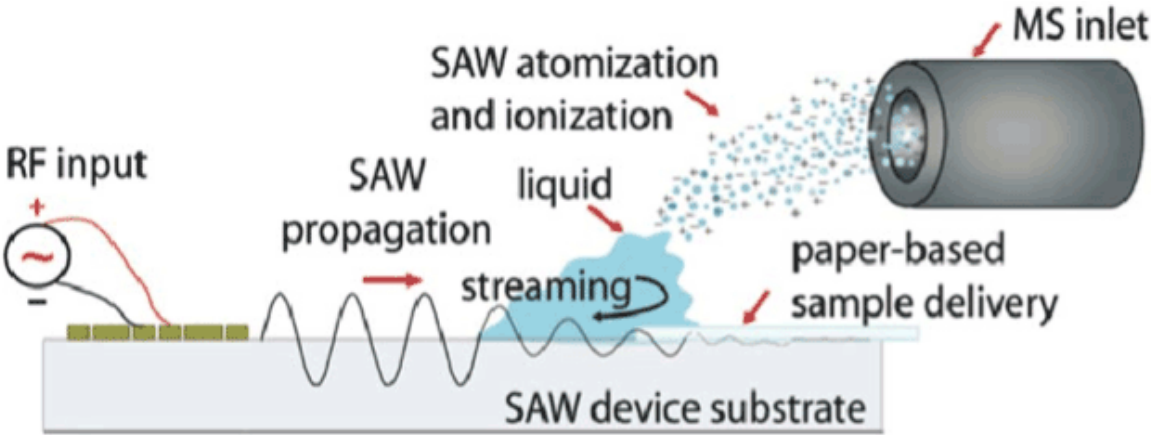


**Figure 2-23: Schematic depiction of the SAW-MS interface. The SAW is generated by applying an input RF signal to the interdigitated electrodes patterned onto the device. The analyte solution, delivered to the SAW substrate through a paper wick, is rapidly atomized when in contact with the SAW propagating on the substrate surface. The atomized droplets comprising the target analyte possess an inherent charge and are directed to the MS inlet for detection [80]**

Nebulisation of small particles and liquids has many applications ranging from inkjet printing, fuel and oil injection sprayer and propeller. The height of the mist is dependent of the RF power applied, up to tens of cm observed. In order to generate a continuous mist on demand, there must be a continuous supply of liquid. A continuous mist can be realized by using porous structure such as filter paper that is linked to a large liquid reservoir as shown in Figure 2-24 [80].

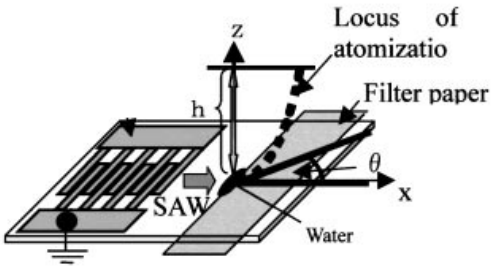


**Figure 2-24: SAW atomization mechanism and setup for the SAW atomizer using a filter paper [80]**

### 2.5.3 SAW Liquid Heating

Acoustic heating has been used in a wide range of biomedical application such as physiotherapy for treating pain and inflammation and is termed diathermy. Using a Piezoelectric ZnO substrate, an effective heating of micro-fluid encapsulated in a channel can be realized using a two electrode structure with a single drive frequency as shown in Figure 2-25.

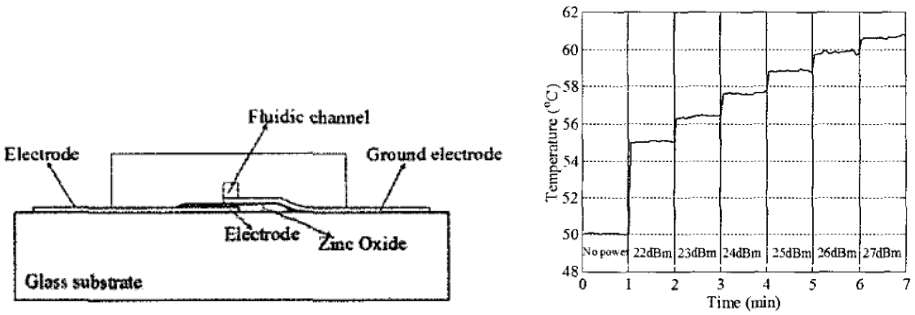


**Figure 2-25: (a) micro-channel design for ultrasonic heating (b) Temperate in channel v.s applied power [81]**

Jagannathan et al. reported a power of 100 mW was found to be required to heat the temperature within the SU8 channel by 4ºC, with a power of 500mW required to increase the temperature by 10 ºC [81].

Utilizing the Rayleigh wave SAW devices, heating of sessile droplets has been observed by Ito et al. Using a 128º rotated Y-cut X-propagating $LiNbO_3$ single crystal a 10 µl droplet increased by 15ºC when driven at 20 v p-p (1W). The droplet was heating using only a single IDT aligned with the sessile droplet as show in Figure 2-26. As noted the constraint of the SAW droplet nebulising at 70$^{o}$C and movement of the droplet limited the ability to heat the droplet with varying condition with a fluidic chamber required for more accurate measurements [70].

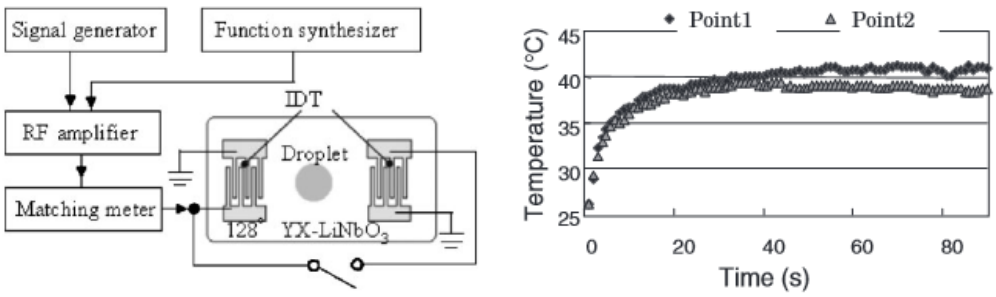


**Figure 2-26: (a) Schematic diagram of set-up for Rayleigh wave thermal measurements (b) Time response of temperature in 10µl droplet excited at 20v p-p. SAW generated from left IDT [70]**

Thermal charachterisation of SAW devices has been analysed to invesitigate nebulisation behavious of SAW liquid films. Kondoh et al. studied atomization behaviour using filter paper alinged with a IDT on 128º rotated Y-cut X-propagating $LiNbO_3$ substrate. Using a thermocouple it was observed that atomization occurred at 70ºC and 30 v p-p (2.5W), concluding that atomization is not occurring at the boiling temperature. Temperature rises of 5 ºC were observed at powers of 0.25 W and rises of 20 ºC at 1 W.

Further investigation of the Rayleigh wave SAW heating by Beyssen et al. highlighted the non-homogeneity of the Rayleigh wave heating with all the energy dissipated in the interface of the IDT as shown in Figure 1-1 [82]. Noted in their analysis was the streaming behaviours allows the heat transfer in the droplet with the steady state equilibrium time related to the streaming velocity.

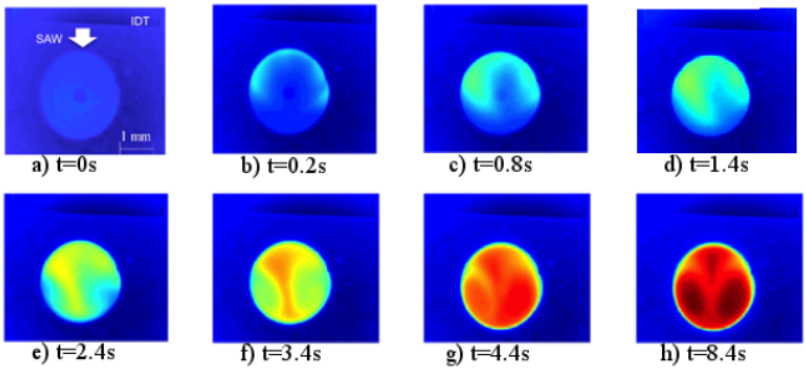


**Figure 2-27: Visualization of droplet temperature excited by Rayleigh SAW (top view) as a function of time. Top view, $V_{DROPLET}$=10µl, η=13.1 mPa.s with $P_{IDT}$=1.6W [82]**

Due to this dependency of forced convection and the dissipation of the Rayleigh wave with the inlet area of the droplet this showed weakness which would make it unsuitable for Polymerase Chain Reaction.

### 2.5.4 Integration of SAW with other technologies

Whilst standard fluid channels and SAW fluid manipulation provide interesting opportunities for the development of a point of care system, other technologies have been investigated which can be integrated with the SAW devices. These include many microfluidic techniques, such as electro-wetting-on dielectric (EWOD), dielectrophoresis, phononic structures, etc; as well as some common micro-scale bio-sensing techniques, such as surface plasma resonance (SPR), surface enhanced Raman Spectrscopy (SERS) [16], [83]. One promising area of integration with SAW device is EWOD which consists

of electrode array covered by a dielectric insulation and coated with a hydrophobic surface. When a DC voltage is applied to the electrode, the surface the hydrophobic surface is changed to hydrophilic attracting the droplets. The use of EWOD in lab-on-chip devices has been widely reported [84], [85].

For example, Li et al. has published work showing the EWOD can be used for fluid movement in a SAW system when patterned onto a $LiNbO_3$ wafer with the IDT structure [86]. They were able to demonstrate movement of a 2.5µl droplet using the EWOD structure and subsequent combination and then mixing using the SAW device. Movement of a droplet using EWOD on the SAW substrate is shown below in Figure 2-28.

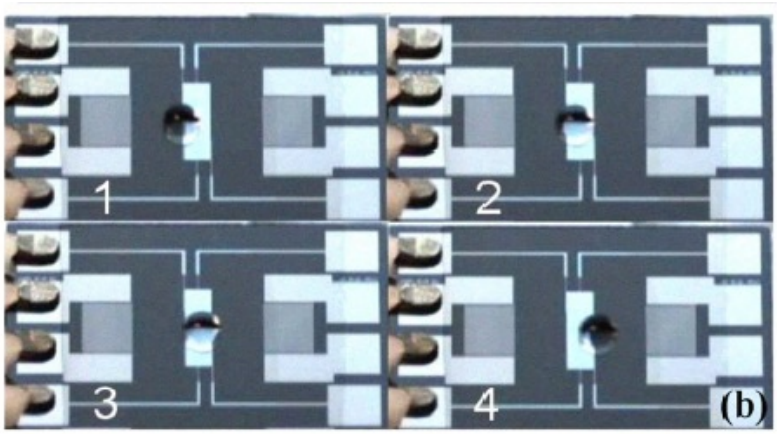


**Figure 2-28: Movement of droplet on EWOD and SAW structure [86]**

## 2.6 Summary

With the purpose of this research being to develop an integrated SAW bio-sensing platform with fluid handling, the literature review has shown the following:

1. Biosensors capable of acting as effective immounosensors, enzyme and DNA sensors have been developed using Love mode SAW sensors utilising $LiTaO_3$ substrates and polymer wave guide layers.
2. Fluid transportation using PDMS channels has been show to integrate effectively with a biosensing platform and provide adequate results.
3. Rayleigh wave modes on SAW substrates have been used to induce streaming in droplets placed on substrates and have been shown to be effective micromixers and particles concentrators.

4. Droplet transportation has been shown with high power Rayleigh waves and improvements have been seen with a hydrophobic treatment of the surface. Velocities of up to 1.24mm/s have been observed.
5. Droplet jetting and nebulisation have been realised using Rayleigh mode SAWs.
6. SAW streaming in fluid channels has been observed both within PDMS channels and micro-machined channels.
7. Thermal heating of liquids with Rayleigh wave SAW is possible enabling PCR on a substrate
8. SAW has been successfully integrated with other technologies on the same substrate such as SPR, SERS, DEP and EWOD.

Whilst all the effective components of a lab-on-chip system have been developed, no integration of these technologies on a single chip has been found in the literature survey. The following areas that currently limit the development of a system are:

- Bio-sensing uses a shear wave as where fluid transportation utilise a Rayleigh mode which is difficult to be realised on the same bulk material substrate
- SAW fluid stream and transportation has primarily been realised using digital droplet microfluidic stems where it is advantageous to have fluid channels for assay analysis in bio-sensing systems

With these inherent gaps in the knowledge to date, this research will investigate the integration of the bio-sensing and fluid transportation on a single substrate. The novelty of the work is to apply a shear horizontal SAWs to realise both microfluidic and bio-sensing in a liquid environment. The mechanisms and phenomena for microfluidics and bio-sensing using the SH-SAWs will be investigated in detail.

# Chapter 3. Experimental Details

This chapter introduces the manufacturing and experimental method and apparatus procedures used for this investigation. Firstly, the manufacturing methods of the SAW devices used for all experiments are described, then the experimental set-up for used for all SAW sensing work is discussed. Finally, the experimental set-up used for acoustic streaming work is introduced. Custom lithography masks with distinct electrode structures were designed for analysis of the wave propagation which will be discussed in detail. For sensing work, test fixtures designed to reduce any signal noise and provide a unique micro-fluidic test platform will be discussed. Several high speed image capture set-ups were utilised to characterise the sessile drop behaviour on the piezoelectric surface. Experimental procedures for thermal characterisation of droplets will also be discussed.

## 3.1 Materials and SAW device fabrication

Devices were fabricated using 128$^{o}$ YX- black $LiNbO_3$ and 36$^{o}$ Y-cut $LiTaO_3$ devices 4 inch wafers of 500 μm thick. A contact angle of 49$^{o}$ for a water droplet on the untreated hydrophilic surface was measured for both wafers. For Rayleigh wave based microfluidic of streaming at lower RF power range, SAW devices made of 128$^{o}$ YX- black $LiNbO_3$ were used. With the increase of RF power, due to its ceramic nature, the 128$^{o}$ YX- black $LiNbO_3$ SAW devices were often cracked during testing. Therefore, for high power pumping, jetting and nebulisation process, ZnO based SAW devices were generally used, attributing to the good thermal and mechanical properties of the silicon substrates. ZnO films of ~4.5 μm thick were deposited on silicon (100) substrate using a standard DC magnetron sputtering from a Zn (99.99%) target at a power of 400 W and an $Ar/O_2$ flow ratio of 30/45 SCCM (standard cubic centimetre per minute) without intentional substrate heating. During deposition, the gas pressure was ~5 mTorr. The film has a strong texture along (0002) orientation and has a thickness is ~4.5 μm.

### 3.1.1 Fabrication Process

An image reversal process was used for fabrication of the devices. The substrates were cleaned with acetone and then isopropyl alcohol to remove any residue before spin

coating. Photoresist AZ5124E (AZ electronics materials) was used for the lithography process and was spin-coated onto the wafer with a thickness of between 1.5 µm -1.8 µm. Once the coating had been deposited the devices were soft-baked by being placed directly on a hotplate at 110ºC for 50 s then removed and allowed to cool for 10 min on a copper plate at room temperature for rehydration. Using a Karl Suss MA8 mask aligner the photo resist was exposed for 7 s using a hard contact with a UV power of 4 mW/cm$^2$. Wafers were allowed to rest for 30 minutes after UV exposure to allow for $N_2$ outgassing, and then were again baked at 120ºC for 2 minutes on a direct contact hot plate and a flood exposes was performed on the Karl Suss MA8 for 45 s at a UV power of 4 mW/cm$^2$. They were then developed with AZ726 developer for 90 s. After that, 150 nm of aluminium was sputtered onto the wafers which were finally cleaned using acetone for 60 seconds whist being agitated until all photoresist was removed. This process is shown in Figure 3-1.

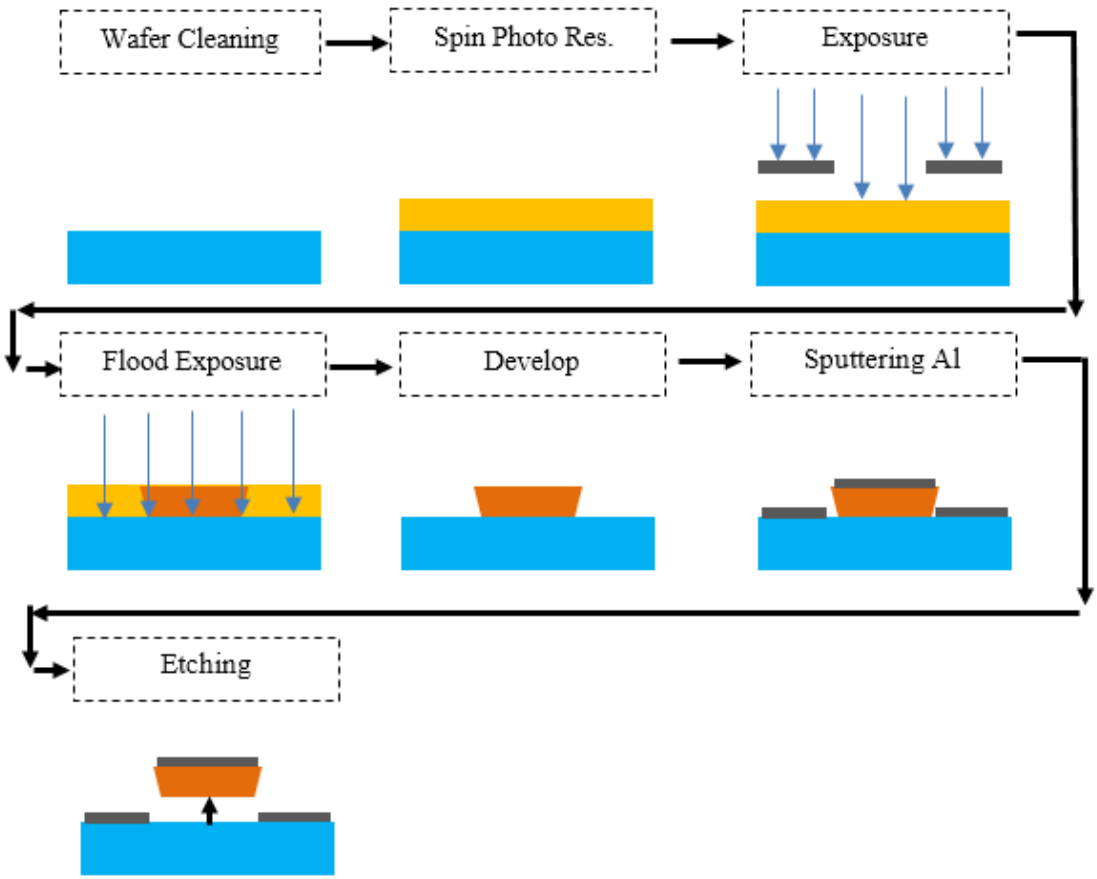


**Figure 3-1: SAW device fabrication process**

For the microfluidic experiments, devices were treated with a hydrophobic coating of CYTOP™ (Asahi Glass Co., Ltd.). For application of CYTop™ (1,3,5,7-tetramethyl-2,4,8-trioxa-6-phenyl-6-phosphaadamantane) a spin coater was used to deposit it to a thickness of 5µm and baked with direct contact hotplate for 60 s at 100 ºC.

### 3.1.2 Mask Design

A lithography mask (Figure 3-2) was designed for the experiments with a range of IDT structures for various experiments. The spatial periodic of the IDT's used were 16 µm and 10 µm and the aluminium IDT's of 150 nm thick consisted of 30 pairs of fingers with a wavelength of 100 µm and aperture sizes of 0.2, 0.5, 1.5 and 2.5 mm.

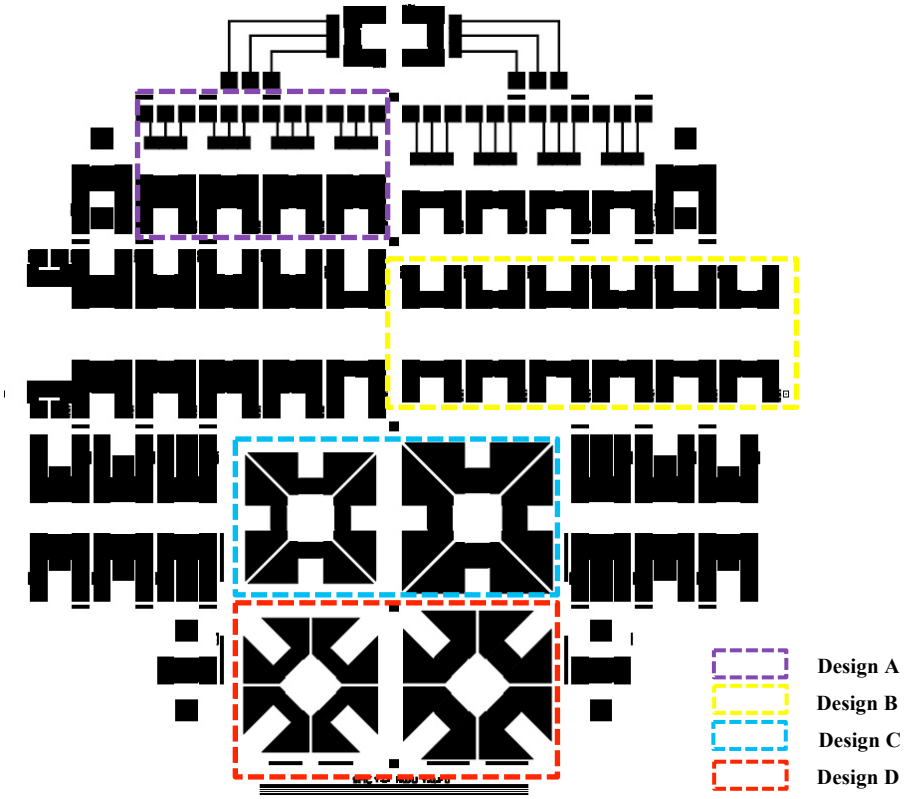


**Figure 3-2: 4 Inch mask design for SAW experiments**

The mask design can be categorised into various structures which were used for the experiments:

- Design A consists of 4 IDT's with 16 µm spacing and 2.5 mm aperture. On the opposite side, there are 3 electrodes which were used for EWOD + SAW experiments
- Design B contains 6 pairs of IDT's with 16 µm spacing and apertures varying from 0.5 mm to 3.0 mm aperture each with 30 IDT's. This design was used for mixing, pumping, nebulisation, thermal heating and jetting experiments.
- Design C contains 4 IDT's with two pairs aligned orthogonally. The left IDT's contain 30 pairs with spacing of 16 µm and an aperture of 2.5 mm. The right IDT's contains 30 pairs with a spacing of 25 µm and an aperture of 2.5 mm.
- Design D contains 4 IDT's, aligned orthogonally but with a rotation of 45º to the propagation direction. The left IDT's contain 30 pairs with spacing of 16 µm and an aperture of 2.5 mm. The right IDT's contained 30 pairs with spacing of 25 µm and an aperture of 2.5 mm.

Summarizing the designs, the following expected frequency for predominate waves for each design was calculated using the following equation $f = \frac{v_r}{\lambda_r}$, and the results are listed in Table 3-1.

**Table 3-1: Frequency of Wave for IDT Designs**

| Design | IDT Spacing (µm) | Frequency (MHz) $128^o$ YX- black $LiNbO_3$ | Frequency (MHz) $36^o$ Y-cut $LiTaO_3$ |
|---|---|---|---|
| **Design A** | 16 | 62.34 | 64.33 |
| **Design B** | 16 | 62.34 | 64.33 |
| **Design C Left** | 16 | 62.34 | 64.33 |
| **Design C Right** | 25 | 39.90 | 41.17 |
| **Design D Left** | 16 | 62.34 | 64.33 |
| **Design D Right** | 25 | 39.90 | 41.17 |

An example of one of the fabricated SAW device is show in Figure 3-3.

**Figure 3-3: Design B Fabricated on 128° YX - black $LiNbO_3$**

## 3.2 Experimental setup

Characterisation and testing of SAW devices were undertaken using various experimental setups and hardware which will be described.

### 3.2.1 Signal Measurement

For characterisation of the fabricated SAW devices, the reflection signal insertion loss ($S_{11}$) was characterized using an HP8752A network analyser. For forward transmission measurements ($S_{21}$), two pairs of IDT's were utilised and connected to the network analyser. The GPIB interface LabView (National Instruments Corporation) was used to capture the data form the network analyser for further analysis. The set-up used is shown in Figure 3-4.

For the measurements insertion loss was characterized as follows:

$$S_{11} = Inertion\ Loss(dB) = 20log\left|\frac{V_{reflected}}{V_{incidet}}\right| \quad 3\text{-}1$$

Forward transmission was characterized as follows:

$$S_{21} = Inertion\ Loss(dB) = 20log\left|\frac{V_{transmitted}}{V_{incidet}}\right| \quad 3\text{-}2$$

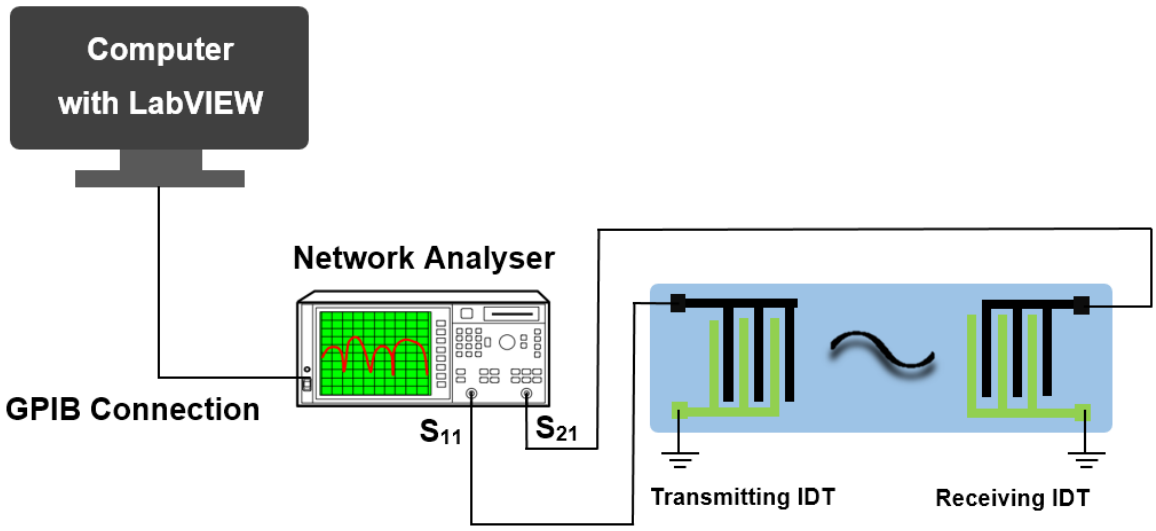


**Figure 3-4: Insertion loss and Transmission measurements setup**

Measurements of $S_{11}$ and $S_{22}$ were used to characterise the SAW devices assessing the manufacturing quality, detect wave velocities and frequencies. Box scanning modes were utilised for high resolution data.

### 3.2.2 Microfluidics testing

Water droplets were loaded at the centre of the SAW propagation path by using a Micro-Volume Kit micropipette. To agitate the liquid droplets, the SAW was generated on the surface by applying an RF signal to the IDT's using a standard signal generator Marconi Instruments 2019A. The signal was amplified using an MI TF2175 RF power amplifier, which delivered a 27 dB gain up to 0.4 W. In order to calculate the exact RF powers that were applied to the SAW device, the output readings of an Marconi Instruments TF2175 RF power amplifier were calibrated using a Racal 9104 RF power metre, where the output readings, $P_{out}$, were captured at a moderate rang of excitation frequencies ranged from 20 to 100 MHz, and with variable input powers, $P_{in}$, from a Marconi Instruments 2019A signal generator. The resulting flow patterns within the liquid droplet were captured using a standard digital CCD camera, as illustrated in Figure 3-5.

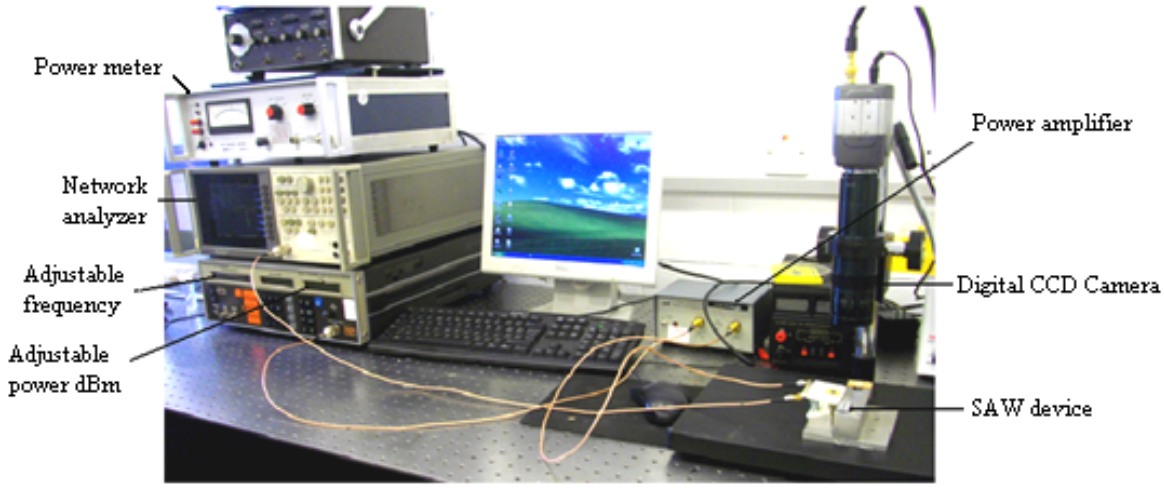


**Figure 3-5: Photograph of the experimental apparatus used during experiments of SAW induced streaming**

In order to measure the time variation of a SAW streaming velocity, polystyrene particles with average diameters of 6 μm were placed inside the water droplets and their motion was recorded using a high speed camera (Kodak Motion Corder Analyzer with a capability to record 600 frames per second)**.** These particles were treated as passive objects that move with the same streaming velocity and follow the stream paths of fluid flow, in a similar to that assumed in ref. [22, 67]. In order to visualize the particle motions inside the droplets, a source of AmScope 150 W Haloids Light Microscope Illuminator was used. The movements of the particles at the top centre of droplets were captured at different time periods using the high speed camera. In order to get the average particle velocity, the process was repeated between ten to fifteen times at the same droplet position, as shown in Figure 3-7. Therefore, the streaming velocities were calculated using $U = \frac{\Delta x}{\Delta t}$, where x denotes the particle position and Δx the distance that particle travelling during time period Δt. For wave propagation visualisation, starch was added into the fluid and mixed vigorously for 30 s to create a uniform solution.

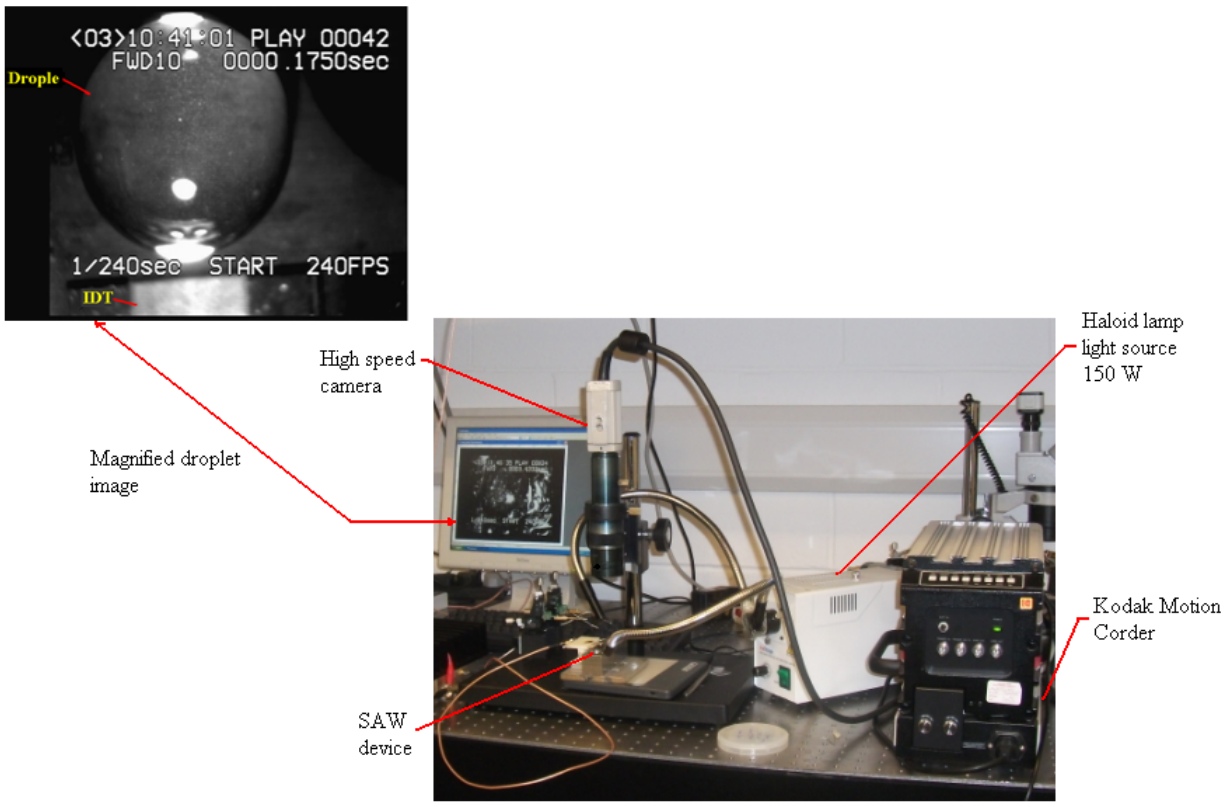


**Figure 3-6: Photograph showing a high speed camera experimental setup of a streaming velocity measurement**

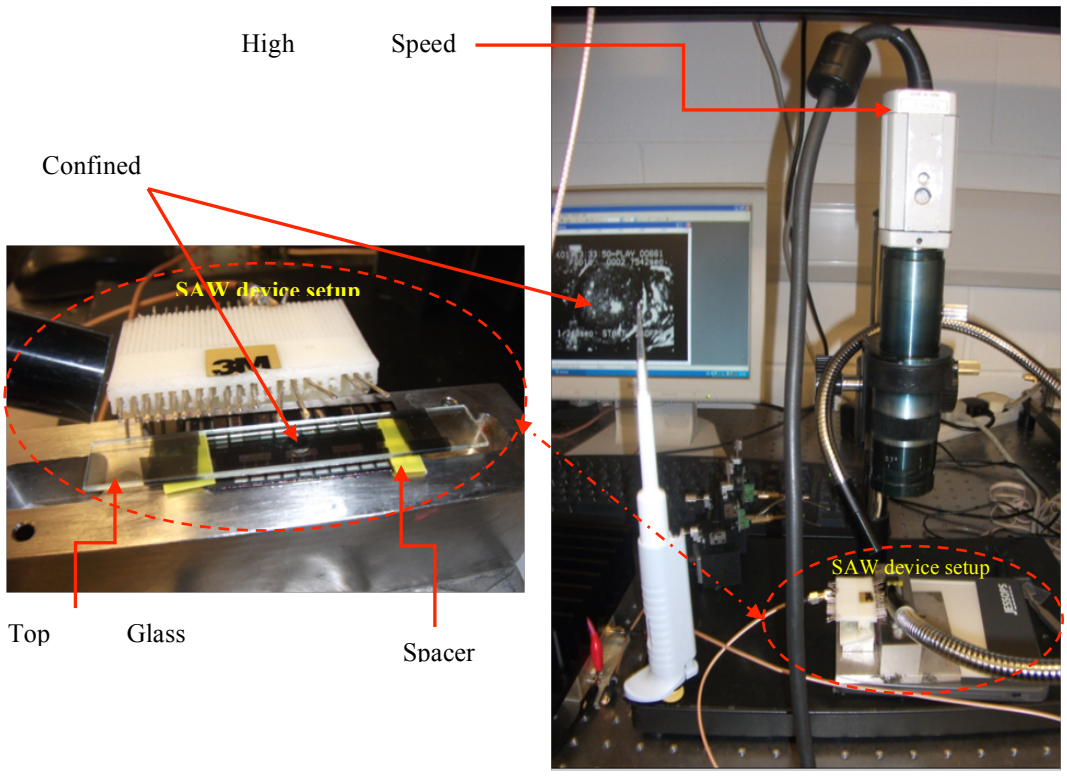


**Figure 3-7: Photograph of an experimental setup used for height effect measurements**

### 3.2.3 Thermal Experiments

For thermal measurements a Fluke TiRx thermal imager with 160 x 120 pixel resolution was used to capture thermal data with a 9 Hz refresh rate. For data analysis movies were recorded of the screen using a Logitech Quickcam with 640 x 480 resolution. SAW devices were connected to a standard signal generator Marconi Instruments 2019A and a high power RF amplifier Mini-Circuits ZHL-5W with a 44 dBm gain was used to observe the temperature effects in the droplet. An example of the captured data is shown in Figure 3-9.

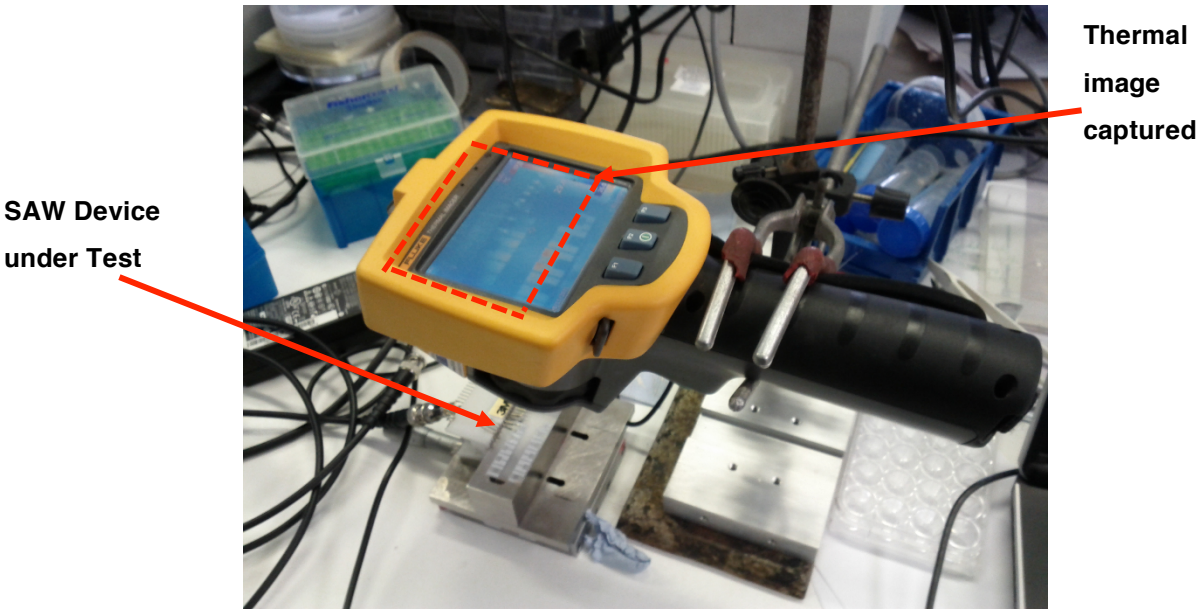


**Figure 3-8: Thermal Camera Set-Up**

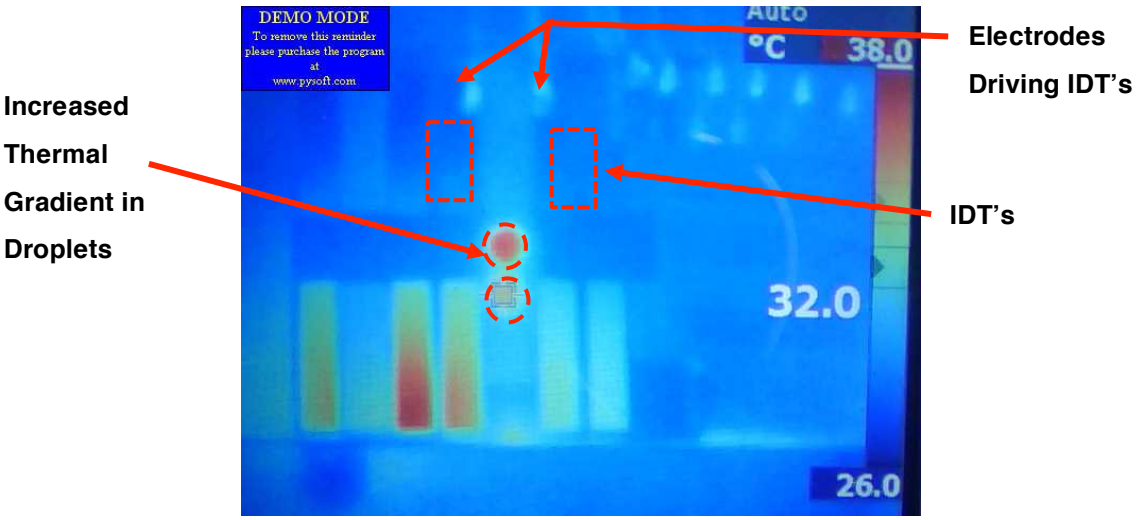


**Figure 3-9: Example Output from Thermal Camera**

### 3.2.4 SAW Sensing Experiments Set-Up

For sensing experiments, a range of experiments were undertaken utilizing several set up which will be described.

#### *3.2.4.1 Jig Design*

For sensing experiments using a SAW device at a high frequency (MHz -GHz) range, it is critical to have a low noise set-up therefore a custom jig was designed to hold the SAW device under test and reduce any external interference. The jig design is shown below in Figure 3-10.

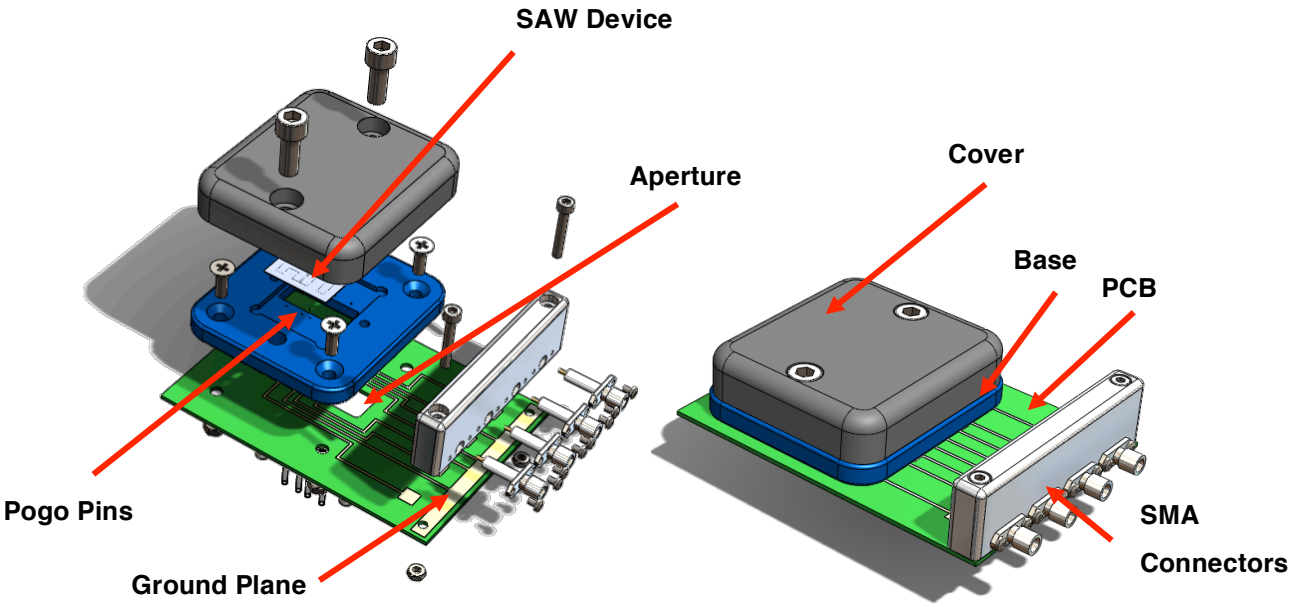


**Figure 3-10: SAW Sensing jig (a) Left image is explode view of components (b) right image is assembled jig**

The design was able to measure two SAW devices simultaneously with 4 channels, in which 2 channels being utilised for transmission, and another 2 for receiving. SMA connectors were used as a connection method with a large common ground being utilised for a low noise floor. To contact to the SAW device, high frequency (6 GHz) pogo pins (SCP-080ZJ) were utilised with a 43 g contact force. An aperture was exposed through the PCB to allow access to the SAW device for dispensing of droplets and access to the surface.

### *3.2.4.2 Frequency Shift Measurements with Oscillator Loop*

For SAW sensing experiments, the frequency change of the SAW device, when either mass loading occurs or a temperature changes, was measured in these experiments. As presented by Avramov et al., an optimal measurement method for SAW devices is when they are used as active frequency control elements in an oscillator circuit [87]. Oscillation will be sustained, provided the gain of the RF amplifiers exceeds the insertion loss of the resonator.

To measure frequency shift of the SAW device with mass loading, an oscillator loop was designed as show in Figure 3-11.

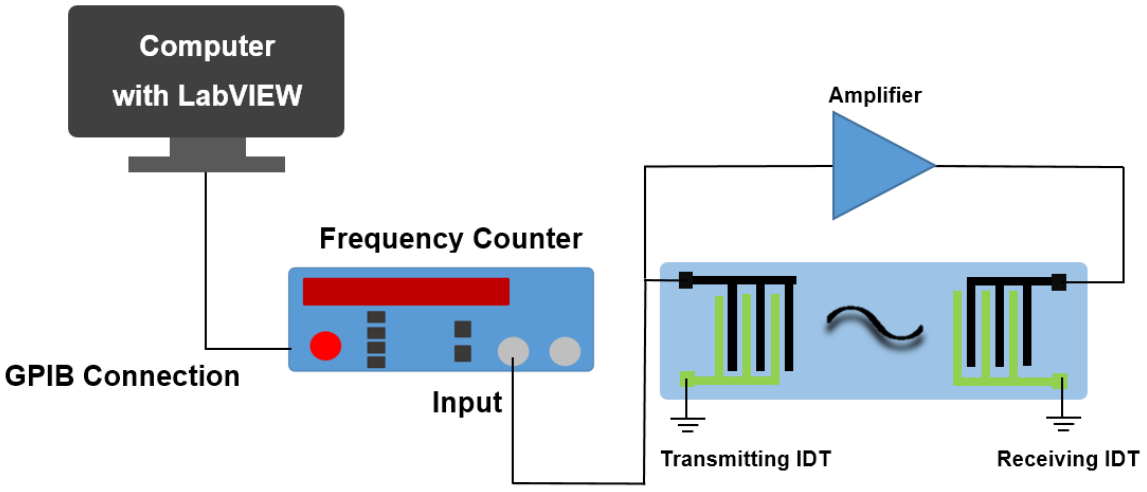


**Figure 3-11: SAW sensing oscillator schematic**

For the oscillator loop to function correctly, it must satisfy the Barkhausen's gain condition where:

$$G_{\text{delay line}} + G_{\text{amplifier}} + G_{\text{other elements}} = 0 \text{ dB} + \qquad 3\text{-}3$$

and phase condition, where:

$$2\pi f_0 L_{cc}/V_p + 2\Phi IDT + \Phi_{\text{amplifier loop}} = 2n\pi \qquad 3\text{-}4$$

The SAW device was connected to a Marconi Instruments TF2175 RF amplifier with the frequency counter, RACAL DANA 1998 (with 10 Hz precision), connected to a SMA splitter to configure the feedback loop. The set-up with the custom designed jig is shown in Figure 3-12.

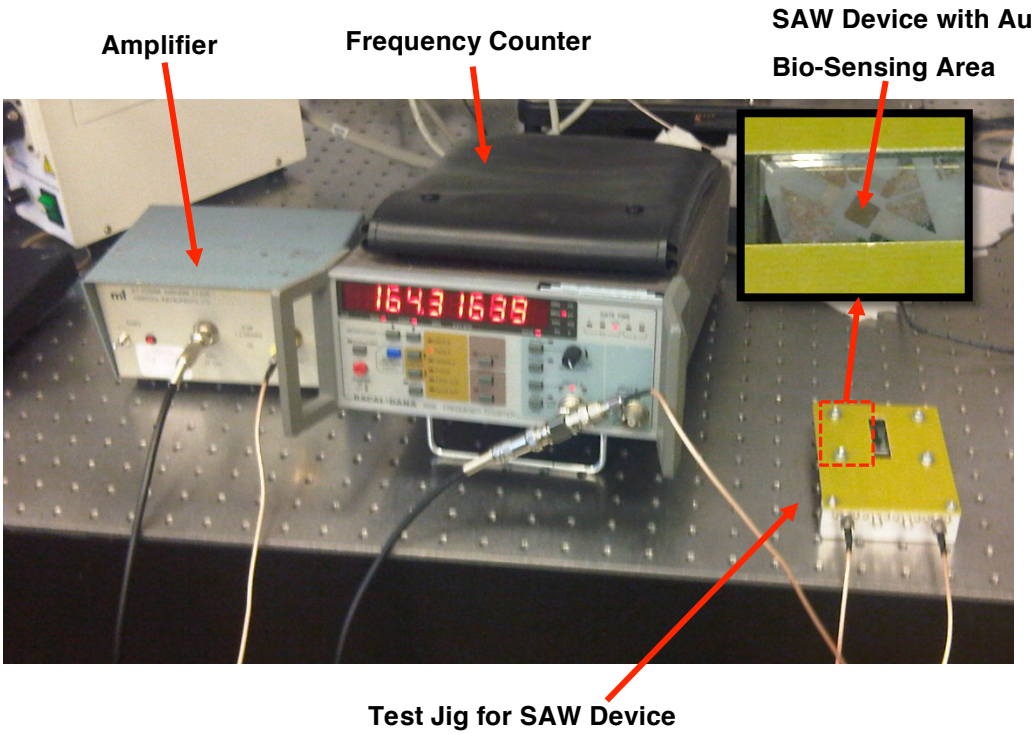


**Figure 3-12: SAW Oscillator Loop Experimental Set-up (inset) magnified view of 36° Y-cut $LiTaO_3$ SAW device with Au plating**

For analysis and capture of the data from the frequency counter, a custom LabVIEW program was written to interface with the GPIB connection on the frequency counter. The sampling rate used was 10 Hz with data being captured in real time and recorded to an external spreadsheet for further data analysis. The interface of the data capture is shown in Figure 3-13.

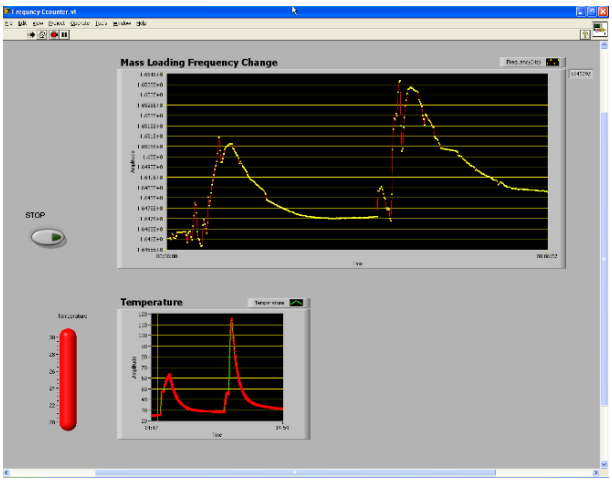


**Figure 3-13: LabVIEW Interface for Frequency Counter with Temperature Measurement**

### *3.2.4.3 Frequency Shift Measurements with Phase Shift*

In addition to using the feedback oscillator loop for frequency shift measurements, the network analyser was also utilised for some experiments to measure the frequency shift of the devices during bio-sensing experiments.

The SAW device under test was connected directly to the network analyser as outlined in Figure 3-4 and $S_{21}$ transmission measurements were made using the phase setting on the LabVIEW software. The data was magnified to the primary resonance peak of the SAW device under investigation with a 0.4 MHz range for either side the peak of interest and the data was recorded to an external spreadsheet. A typical measurement is shown in Figure 3-14 where a 10 µl droplet was pipetted onto 36° Y-cut $LiTaO_3$ SAW device and the frequency shift was recorded before and after.

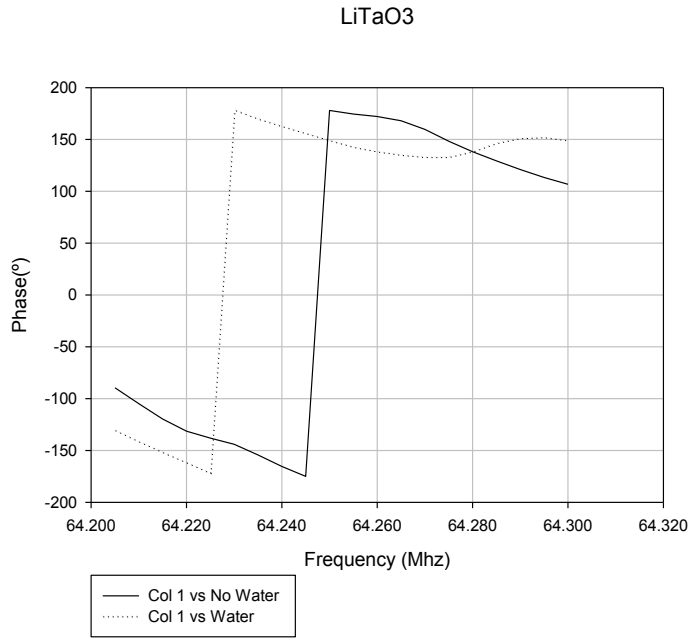


**Figure 3-14: Example of Phase measurement of 36° Y-cut $LiTaO_3$ SAW using $S_{21}$**

Due to ease of analysis, phase measurement was chosen over insertion loss due to difficult of accurately detecting the peak of the resonance mode. The disadvantage over the oscillator loop was the difficulty in obtaining real time frequency changes and this method was better suited for measurements where a refresh frequency was less than 0.5 Hz.

## 3.3 Bio-sensing Procedures

Bio-sensing experiments were undertaken using the 36° Y-cut $LiTaO_3$ substrate which was prepared by depositing a 3 nm layer of chromium and a 50 nm layer of gold coated between the IDT's (Figure 3-12 inset) using e-beam evaporation. Thicknesses were checked with a ZYGO white light interferometer. The substrate was washed with deionised water and ethanol after processing and ultrasonically agitated for 5 minutes to remove any residue. Strepavadin beads (purchased from Bangs Laboratories Inc., USA) were centrifuged at 0.9 g for 1 minute to separate beads from suspension solution. The suspension solution was removed using a micro pipette to leave only the beads, and then 5 µl Phosphate Buffered Saline (PBS) was added to the beads. The solution was then centrifuged again and the PBS solution removed and replaced with the PBS, this was repeated once more. Once the final washing was complete 5 µl of PBS was added and the mixture was shaken vigorously for 30 s.

The strepavadin beads were pipetted onto the 36° Y-cut $LiTaO_3$ coated Au surface and incubated for various durations up to 60 minutes. The samples were analysed using a Nikon light microscope to measure the binding coverage.

# Chapter 4. Numerical Simulation of Shear Wave

Flow behaviour driven by Rayleigh waves has been well documented using both experimental and numerical methods, [56,57,58,59] based on the theory of the acoustic pressure wave propagation of a leaky wave into the droplet. SH-SAW to date has only been investigated for the purpose of bio-sensing, with a limited number of numerical models having been constructed to analyse the detailed 3D wave propagation [92]. The Rayleigh wave contains both a longitudinal and a surface transverse waves, whereas the SH-SAW is described by three components, the shear horizontal, surface normal and longitudinal components. To understand the mechanism behind the SH-SAW streaming, the amplitudes of the three components and their propagation in the substrate are required to be quantified before a simulation, and thus the understanding, of the motion can be developed.

To simulate the piezoelectric substrate, it is required that the complete set of fundamental equations relating mechanical and electrical quantities to be solved. To identify the wave propagation modes in a surface acoustic wave device, it is necessary to obtain solutions of the coupled wave equations derived from the mechanical equations of motion and Maxwell's equation for electrical behaviour. The coupling between the electrical and mechanical parameters can be obtained by means of the piezoelectric constitutive equations. There are several methods that can be used to solve the coupled wave equations and identify wave propagation characteristics. The models commonly used to simulate the mechanical and electrical behaviour of piezoelectric transducers are based on perturbation theories or methods such as Campbell-Jones in which numerical solutions to the complex characteristic equations for wave velocity are sought [93]. These generally introduce simplified assumptions that are often invalid for actual designs [92]. The geometries of practical transducers are often two dimensional (2-D) or three dimensional (3-D) [94]. The finite element technique has been a preferred method for modelling acoustic wave propagation in piezoelectric devices such as SAW [92], [95]–[97]. The main advantage lies in its ability to handle complicated transducer geometries [98]. A 3-dimensional finite element model is able to concurrently consider second order effects such as back scattering, bulk wave interference, harmonic responses as well as electromagnetic feed-through.

For the initial investigation, a standard substrate based on 36°YX $LiTaO_3$ was modelled using the Finite Element Analysis (FEA) method. COMSOL software was chosen as the finite element software for the simulation as it has successfully been used to model Rayleigh SAW wave propagation by numerous researchers [62,63,64,65]. Subramanian et al. have shown some limited modelling of the shear wave propagation on 36°YX $LiTaO_3$, although their paper was focused on hexagonal patterns for bio-sensing without reference to propagation of the wave into a fluid. Sing et al. investigated fluid interaction on a Rayleigh wave substrate using a coupled FEA fluid model, which is the most promising method proposed for this type of study [102].

The developed model was comprised of anisotropic piezoelectric material properties with the 3D tensors. The wave propagation was modelled along with reference to the following variables: number of IDT's, frequency and voltage. The particle displacement and velocities were then obtained at relevant points to measure the wave propagation. The results were then compared to those obtained through perturbation theories to validate the FEA model.

### 4.1.1 Theory

The propagation behaviour for piezoelectric materials is governed by Newton's mechanical equations of motion and Maxwell's equations for electric behaviour [98], [103]. Therefore the following equations are solved for the piezoelectric substrate:

$$T = C^E : S - e \cdot E \tag{4-1}$$

$$D = e : S + \varepsilon^s \cdot E \tag{4-2}$$

$$\nabla \cdot [e \cdot \nabla\varphi] + \nabla \cdot [C^E : \nabla_s u] - \rho\ddot{u} = 0 \tag{4-3}$$

$$\nabla \cdot [e \cdot \nabla\varphi] = \nabla \cdot [\varepsilon^s \cdot (\nabla\varphi)] \tag{4-4}$$

where $T$ is the stress tensors, $C^E$ is the elasticity matrix , $S$ is the strain tensor, $e$ is the piezoelectric coupling matrix, $E$ is the electric field vector, $D$ is the electrical displacement, $\varepsilon^s$ the permittivity matrix, $\varphi$ the electric potential, $u$ is the particle displacement and $\ddot{u}$ the particle acceleration.

The mechanical wave propagation is an order of approximately 5 magnitudes smaller than that of electromagnetic waves; therefore Maxwell's equations can be reduced as follows:

$$\left(\frac{\partial D_i}{\partial x_j}\right) = 0 \text{ and } E_i = -\left(\frac{\partial \emptyset}{\partial x_j}\right)$$

Where $\Phi$ represents the electrical potential.

The components of strain are defined by:

$$S_{ij} = \frac{1}{2}\left(\frac{\partial u_i}{\partial x_j}\right) + \left(\frac{\partial u_j}{\partial x_i}\right) \quad 4\text{-}5$$

The equation of motion disregarding any internal body forces is:

$$\left(\frac{\partial T_{ij}}{\partial x_j}\right) - \rho\left(\frac{\partial^2 u_i}{\partial t^2}\right) = 0 \quad 4\text{-}6$$

where $\rho$ is the density and $u_i$ represent the components of displacement. Rearranging the above set of equations leads to a system of four coupled wave equations for the electric potential and the three components of displacement in piezoelectric material, which are solved for the piezoelectric solid domain.

$$-\rho\frac{\partial^2 u_i}{\partial t^2} + c^E_{ijkl}\frac{\partial^2 u_k}{\partial x_j\,\partial x_i} + e_{kij}\frac{\partial \emptyset}{\partial x_k\,\partial x_j} = 0 \quad 4\text{-}7$$

$$e_{ikl}\frac{\partial^2 u_k}{\partial x_i\,\partial x_l} - \varepsilon^s_{ik}\frac{\partial^2 \emptyset}{\partial x_i\,\partial x_j} = 0 \quad 4\text{-}8$$

These equations can be solved using the FEA method with the voltage and the three displacement fields being obtained as the outputs at any element or node.

### 4.1.2 Model overview

A transient model was simulated to characterise the shear wave propagation on the 36° YX $LiTaO_3$ substrate. The 3D FEA model was simulated for a total of 50 ns with a time step of 0.05 ns with varying IDT delay line structures. This section describes the finite element models for the simulations and the analysis of the structure as well as the model boundary conditions, electrical and mechanical results.

#### *4.1.2.1 Simulation parameters*

The finite element simulation model consists of a single delay line configuration with varying number of pairs of IDT's. The IDT's are defined as mass-less electrodes on the

surface of the piezoelectric material, thus mass loading and reflection effects have not been considered in order to simplify the computation and reduce any second order effects. The standard computational domain of the simulation was defined as a substrate of 300 μm in length, 150 μm wide and a substrate thickness of 150 μm. The periodicity of the finger pairs was varied for the simulation to the following values of 40, 64 and 80 μm with an aperture width of 40 μm. For a second simulation, the periodicity was set at 40 μm and the aperture width was varied from 40, 80 and 120 μm wide. For the third simulation, the voltage input was varied from 0.5, 1 and 2 V peak to peak on a substrate with a periodicity of 40 μm. For selection of the mesh parameters, a number of 5 elements per wavelength were chosen which equates to 8 μm. For the time steps, the CFL method was used where CFL = $c*\Delta t/h$, $c$ is the local speed of sound, $\Delta t$ is the time step, $h$ is the mesh size. Using an optimum CFL value of 0.2, a step size of 0.04 ns was chosen. To verify the settings, a convergence analysis was carried out to find the optimum mesh size. The results are listed in Table 4-1.

**Table 4-1: Convergence of 36°YX $LiTaO_3$ FEA model**

| Mesh size (mm) | 0.004 | 0.006 | 0.008 | 0.009 | 0.01 | 0.02 | 0.04 |
|---|---|---|---|---|---|---|---|
| Degress of Freedom(DOF) | 295,756 | 89,564 | 58,436 | 47,892 | 31,472 | 12,156 | 7,108 |
| Shear Horizontal Z Displacement (m) | 8.98E-08 | 8.98E-08 | 9.27E-08 | 8.84E-08 | 9.17E-08 | 1.04E-07 | 9.54E-08 |
| Surface Normal Displacement (m) | 4.48E-08 | 4.48E-08 | 4.60E-08 | 4.74E-08 | 6.43E-08 | 6.84E-08 | 4.36E-08 |

Using this convergence analysis and the pre-calculated values, an element size of 8 μm was selected near the surface and IDT's with a lower density into the substrate resulting in approximately 60,000 DOFs, which include three displacements and one voltage. The 3D finite element mesh is shown in Figure 4-1 for the simulation with the IDT's highlighted in red/blue. For the electrical boundary conditions, the alternating electrodes were grounded as well as the base of the substrate to remove any electromagnetic feed-though effect. For the mechanical constraints, a single node at the bottom corner of the substrate was fixed to satisfy the equilibrium conditions.

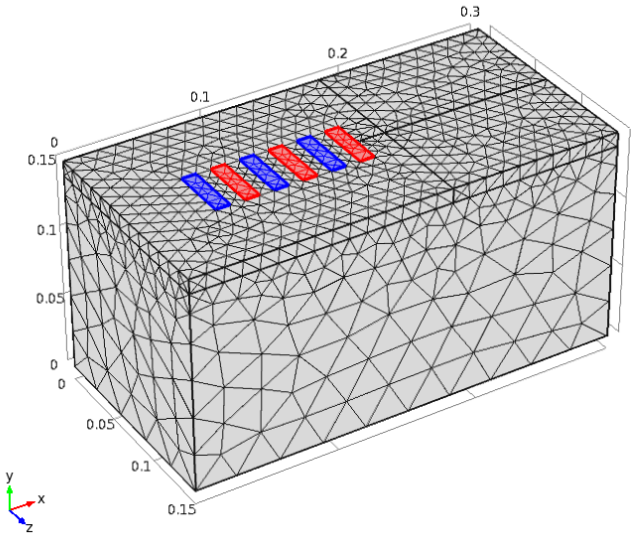


**Figure 4-1: Three dimensional (3-D) image of typical mesh used for simulation. Inter-digital Transducers (IDT's) are shown on the top surface highlighted in red. Mesh is approx. 50,000 DOF. Grid dimensions are shown in mm.**

### 4.1.3 Excitation of Substrate

Using the known velocities for the substrates, sinusoidal voltage signals were applied to alternating IDT's. The varying voltages for 0.3, 0.5, 1.25 and 2.5 V are shown in Figure 4-2.

For the sinusoidal functions generated from the SAW device, the following function was applied:

$$V_i = 1 \times sin(2\pi \times f \times t);\ f = center\ frequency\ MHz;\quad t = 50ns \qquad (4\text{-}10)$$

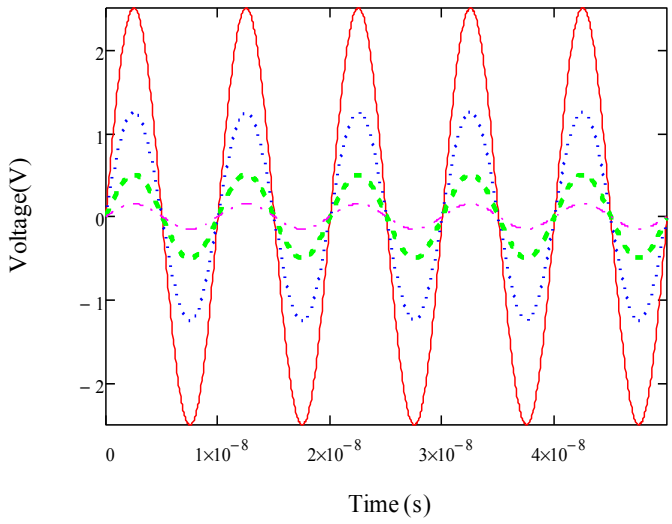


**Figure 4-2: Applied Voltages to IDT's showing 0.3, 1, 2.5 and 5 V peak to peak excitation.**

### 4.1.4 Material Properties

For modelling, the 36º Y-Cut $LiTaO_3$ [104] was investigated; which is orientated to the standard crystal axis as shown in Figure 4-3.

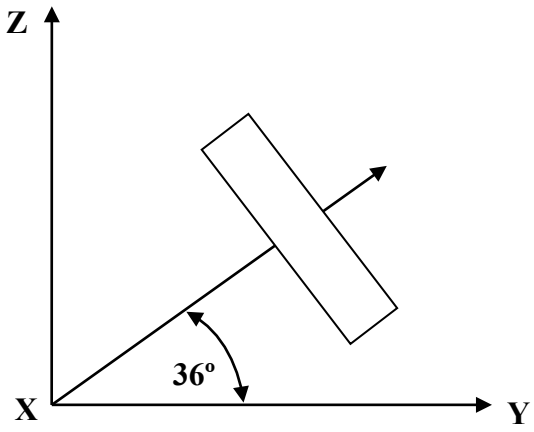


**Figure 4-3: Rotation of Crystal Cut for 36º Y-cut $LiTaO_3$.**

The elastic matrix of $LiTaO_3$ can be expressed as follows:

$$C^{\varepsilon} = \begin{pmatrix} C_{11} & C_{12} & C_{13} & C_{14} & 0 & 0 \\ C_{12} & C_{11} & C_{13} & -C_{14} & 0 & 0 \\ C_{13} & C_{13} & C_{33} & 0 & 0 & 0 \\ C_{14} & -C_{14} & 0 & C_{44} & 0 & 0 \\ 0 & 0 & 0 & 0 & C_{44} & C_{14} \\ 0 & 0 & 0 & 0 & C_{14} & (C_{11} - C_{12})/2 \end{pmatrix} \quad 4\text{-}9$$

The permittivity and piezoelectric coupling matrix can be expressed as follows:

$$\varepsilon^{S} = \begin{pmatrix} \varepsilon_{11} & 0 & 0 \\ 0 & \varepsilon_{11} & 0 \\ 0 & 0 & \varepsilon_{33} \end{pmatrix} \quad 4\text{-}10$$

$$e = \begin{pmatrix} 0 & 0 & 0 & 0 & e_{15} & e_{-22} \\ -e_{22} & e_{22} & 0 & e_{15} & 0 & 0 \\ e_{31} & e_{31} & e_{33} & 0 & 0 & 0 \end{pmatrix} \quad 4\text{-}11$$

For the 36ºYX $LiTaO_3$, it is necessary to rotate the piezoelectric parameters as only material data for bulk $LiTaO_3$ is published [69,70]. To achieve this, a MathCAD program was written based on the method described by Fahmy et al. [106]. The transformation formulations used are shown in Appendix 1. The transformed material properties were used in the FEA model.

## 4.2 Results and Discussion

The results of the transient simulation of the shear wave propagation are presented in this section. The simulated displacement and voltage response, as well as the corresponding calculated results, were analysed for four different simulation scenarios:

- Analysis of wave propagation on substrate
- Analysis of frequency
- Analysis of voltage variation
- Analysis of rotated cut of crystals

### 4.2.1 Wave Propagation Analysis on 36°YX $LiTaO_3$ SH-SAW Substrate

In order to understand the wave propagation on the 36ºYX $LiTaO_3$, a transient analysis using the AC signals was undertaken. A 5 V peak-peak sinusoidal signal was applied to alternating IDT's as shown in Figure 4-2 for approximately 100 ns at a frequency of 100 MHz, corresponding to the excitation frequency of the SH-SAW. The application of the voltage results in a mechanical wave, which propagates away from both IDT fingers along the substrate. The piezoelectric FEA model is able to capture the wave propagation on the 36ºYX $LiTaO_3$ including the shear and vertical polarised waves. Examples of the displacement outputs of the shear and surface normal components are shown in Figure 4-1 and Figure 4-2.

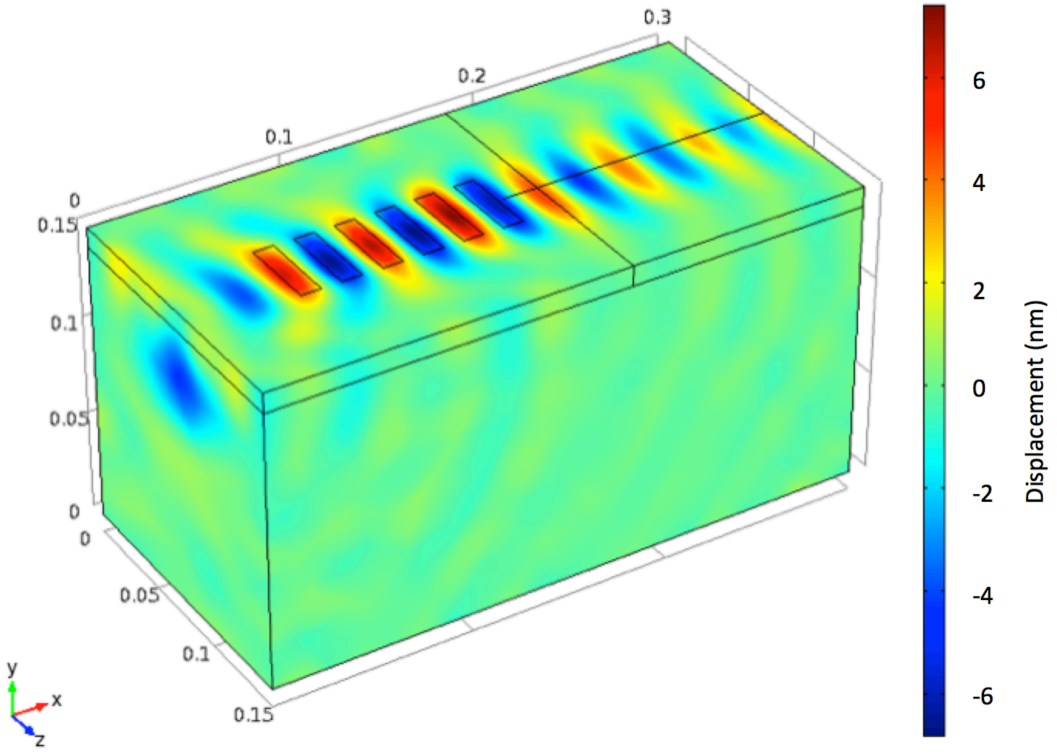


**Fig. 4-4: Surface acoustic wave propagation of shear polarised waves on 36°YX $LiTaO_3$ with 5V peak-to-peak excitation at 100MHz at approx. 50ns. The displacements are shown in nm. The energy of the wave is observed to propagate into the bulk material and along the surface.**

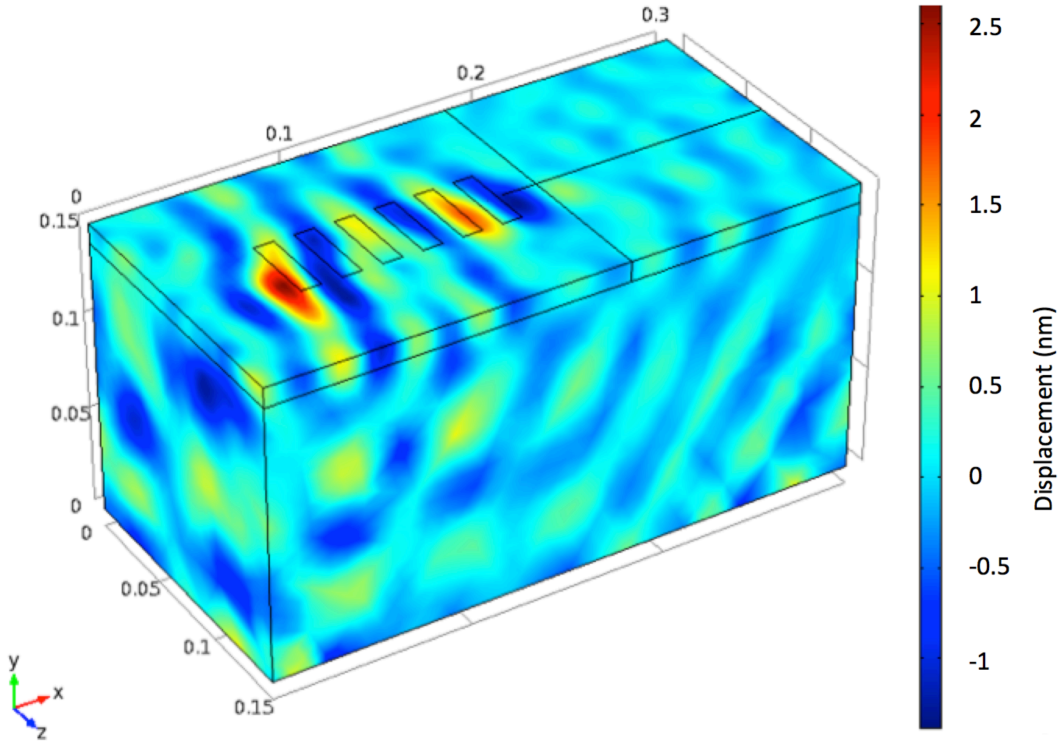


**Fig. 4-5: Surface acoustic wave propagation of surface normal polarised waves on 36°YX $LiTaO_3$ with 5V peak to peak excitation at 100MHz at approx. 50ns. The displacements are shown in nm. The vertical wave is observed to be a magnitude small than the shear component with the results in the order of $10^{-9}$ m.**

When the IDT's are exited, a series of constructive waves are generated from the alternating IDT's, which build up in phase to create a maximum displacement at the end of the array. The displacements recorded are typically in the nm range as shown in Figure 4-1 and Figure 4-2. The generated wave travels outside of the aperture and also into the bulk of the substrate, showing the dissipation of the energy. The generated wave also travels in the forward and traverse directions, and reflections are observed when it reaches the edge of the substrate.

Looking at a cross section of the wave propagation in Figure 4-6, we can see that the acoustic energy is "leaking" into the bulk substrate from the surface. This is in contrast to the Rayleigh wave, which is confined mostly to the surface of the substrate. This correlates well with published data, which shows the Leaky SAW (LSAW) is the dominant wave mode on the 36ºYX $LiTaO_3$ substrate. Also noted is that the Rayleigh wave component is visible only within the IDT area and dissipates quickly outside the array in both directions.

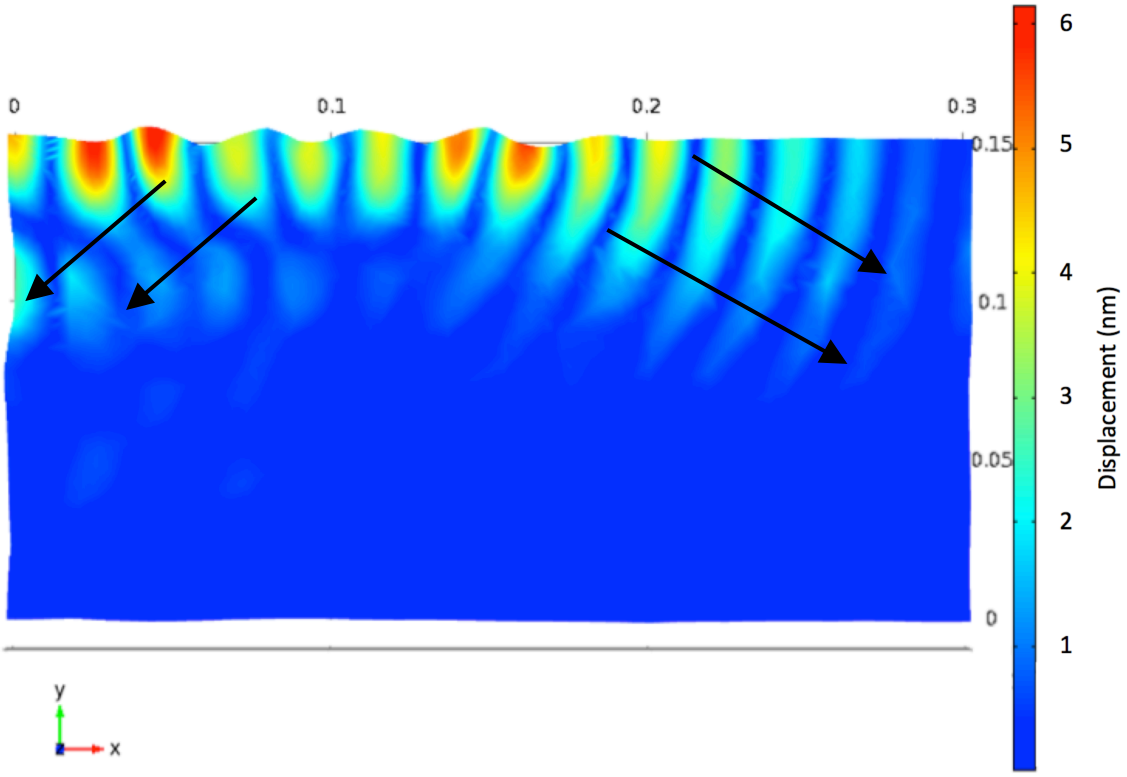


**Figure 4-6: Surface acoustic wave propagation of waves on 36ºYX $LiTaO_3$ with 5 V peak-to-peak excitation at 100 MHz at approx. 40 ns. The total displacements are shown in nm. The SAW radiation is observed to "leak" into the bulk material**

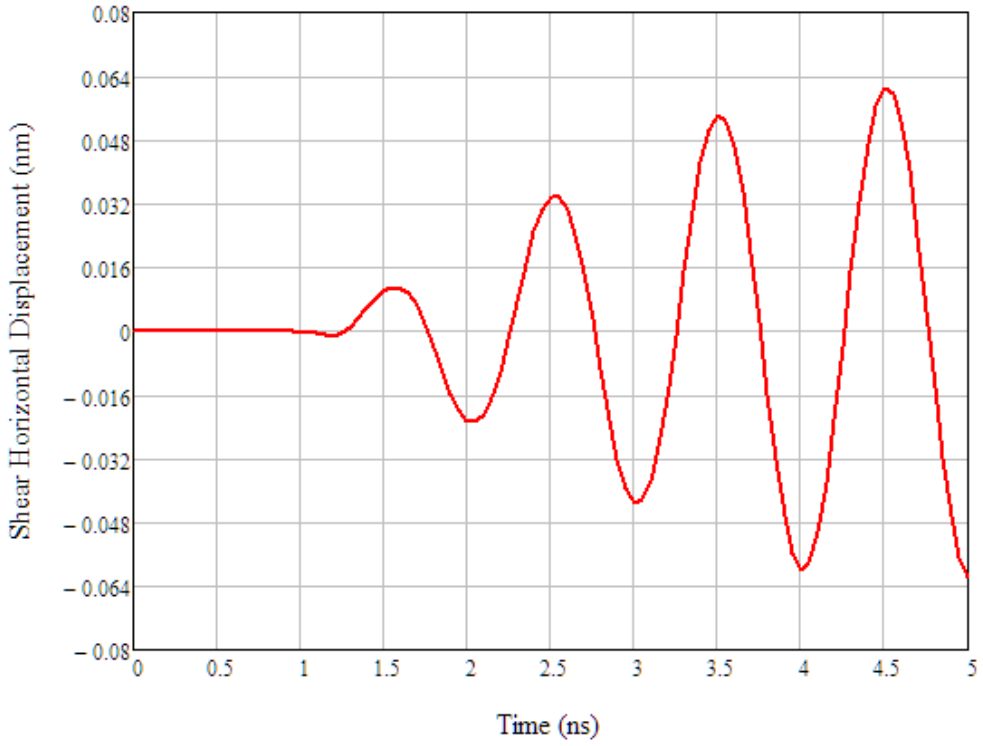


**Fig. 4-7: Displacement of shear horizontal component at 5V peak-to-peak 100 MHz excitation at 6 µm from IDT**

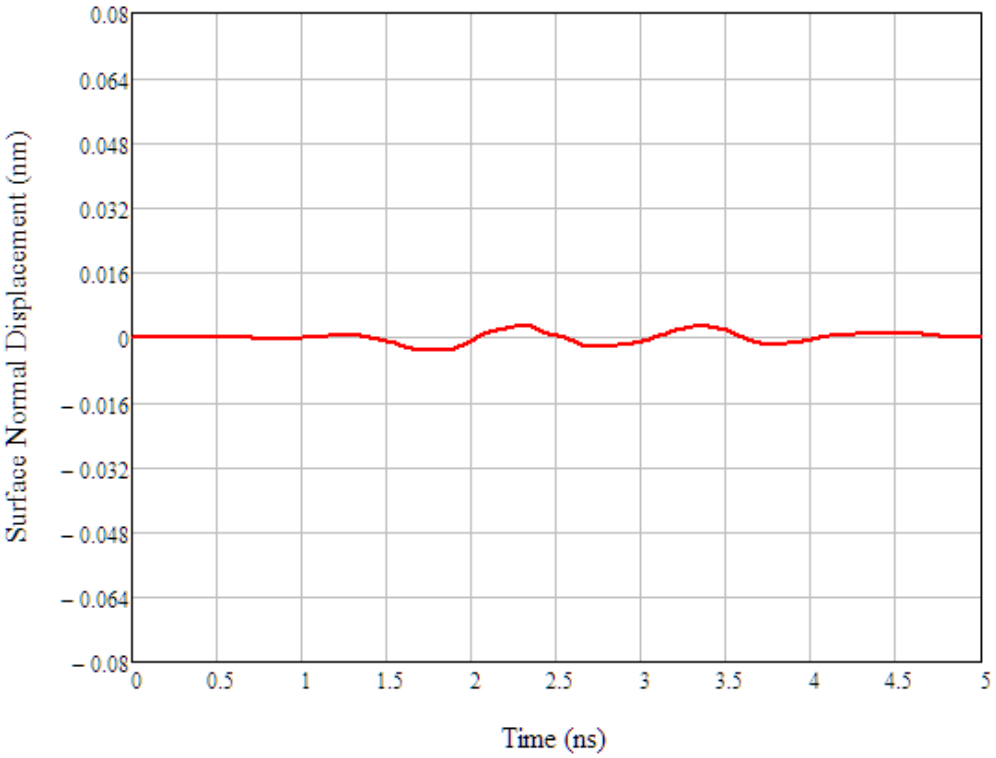


**Fig. 4-8: Displacement of surface normal component at 5 V peak-to-peak 100 MHz excitation at forward IDT**

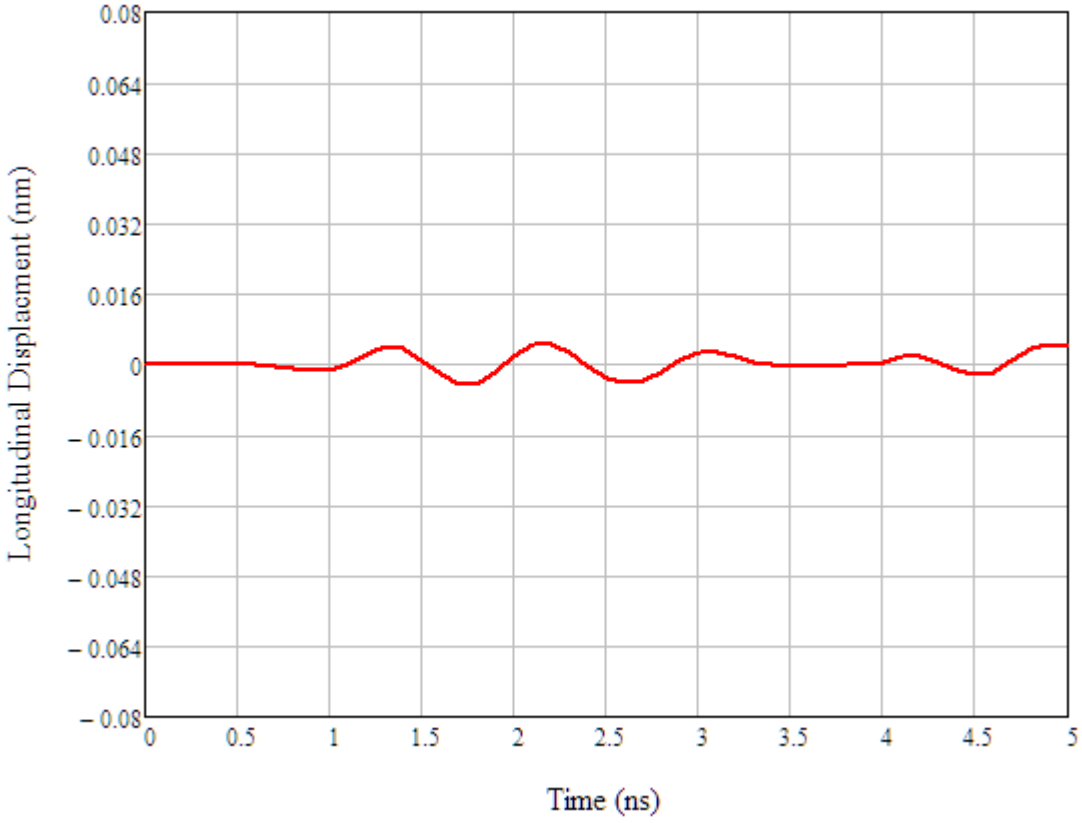


**Fig. 4-9: Displacement of longitudinal component at 5 V peak-to-peak 100 MHz excitation at forward IDT.**

Figures Fig. 4-7 to Fig. 4-9 show the displacement outputs of the substrate obtained at the forward IDT's. The indicated displacements show that the shear wave component was the highest at around 0.064 nm with the surface normal and longitudinal components with around 0.003 nm. This represents a surface normal or vertical Rayleigh wave component at around 4% of the shear wave component showing the shear wave is the dominant wave on the substrate. Data on 36°YX $LiTaO_3$ to date has shown that the surface normal component could be negligible though no definitive value has been put on the vertical displacement during laser vibrometer measurements, due to the weak amplitude [75,76]. Analysing the vertical components on the 3D displacement output, we can see they are generated at the outer edges of the IDT fingers where the shear displacement reverse with the application of the voltage. These vertical components appear as an artefact of the distortion of the piezoelectric matrix for the shear wave. Due to the stiffness of the material, some material must be displaced vertically for the horizontal motion to occur. In addition to the three displacement components, the velocity of a point on the surface, that may represent a particle, was calculated. This was achieved by differentiating the

distance with respect to time, thus giving us the instantaneous velocity at each point for the three components. The results are shown in Figure 4-10.

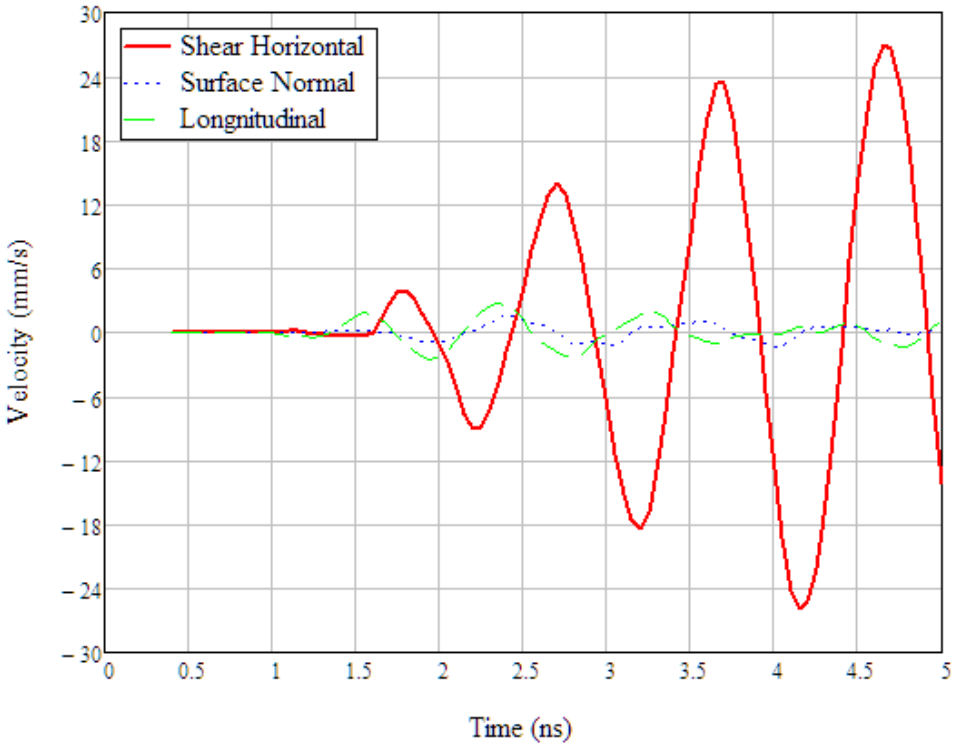


**Figure 4-10: Velocity of three wave components at 5 V peak-to-peak 100 MHz excitation at forward IDT.**

As the velocity is the differential function of each of the three components, they show similar behaviours as the displacement but the maximum particle velocity for the shear horizontal wave was seen to be approximately 26 mm/s whereas the vertical and longitudinal components had a velocity of around 2 mm/s.

### 4.2.2 Analysis of Wave Velocity and K Coefficient

For verification of the FEA model, the electro-mechanical coupling coefficient and the wave velocities were compared against analytical and experimental results.

#### *4.2.2.1 Wave Velocity*

For the calculation of the wave velocity, a point was chosen, ~140 µm away from the IDT arrays and the vertical and horizontal components were measured. The shear horizontal wave takes approximately 34.1 ns to reach the measuring point from the array, which

corresponds to a wave velocity of 4105 m/s. The value compares well to the published values of 4112 m/s for the LSAW wave and to the measured value of 4128 m/s.

The 36°YX $LiTaO_3$ substrate is also known to support a Rayleigh wave, [109] which has a weak coupling coefficient of $2\Delta v/v$ of 0.00046. This coupling coefficient is extremely small and hence the amplitudes observed of the Rayleigh wave are also small. To analyse this Rayleigh propagation, the surface normal component was again measured at 140 µm away from the IDT array and was shown to take approximately 44.6 ns to reach the measurement point. This corresponds to a wave velocity of 3135 m/s, which compares well to the published value of 3116 m/s and to the measured value of 3000 m/s of the Rayleigh wave.

The corresponding wave velocity curves obtained from the simulation are shown in Figure 4-11 with the summarised values listed in Table 4-2.

**Table 4-2: Velocity of wave on 36°YX $LiTaO_3$ substrate for theoretical experimental and simulated results.**

| Wave Mode | Theoretical (m/s) [109] | Experimental (m/s) | FEA Simulation (m/s) |
|---|---|---|---|
| Leaky SAW | 4112 | 4128 | 4105 |
| Rayleigh | 3116 | 3000 | 3135 |

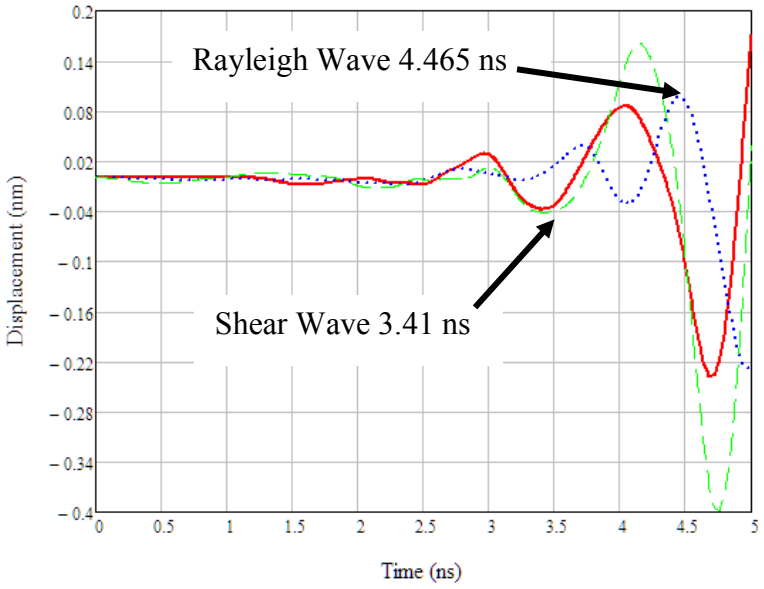


**Figure 4-11. The displacement as a function of time for 36°YX $LiTaO_3$ at 5 V, 140 µm from IDT.**

#### 4.2.2.2 *Electromechanical coupling coefficient*

For the second verification of the model, the electromechanical coupling coefficient was simulated. The electromechanical coupling coefficient or $K^2$ can be derived theoretically using the relationship [30]:

$$K^2 = \frac{e^2}{c\varepsilon} \qquad 4\text{-}12$$

Where $e$ is piezoelectric coefficient, $c$ is the elastic constant and $\varepsilon$ is the dielectric permittivity.

Alternatively $K^2$ can also be derived experimentally using the following relationship:

$$K^2 = \frac{2\Delta v}{v} \qquad 4\text{-}13$$

Where $\Delta v$ is the velocity of the SAW wave, when the free surface of the device is shorted by a thin highly conductive metal film, and $v$ is the un-perturbed SAW signal [30].

To calculate the electromechanical coupling coefficient, the surface of the FEA model was shorted using a ground boundary condition as shown in Figure 4-12.

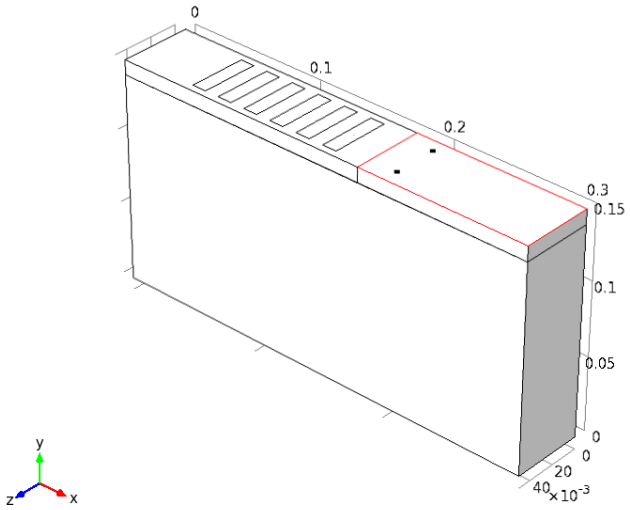


**Figure 4-12: Boundary conditions applied to electromechanical coupling coefficient model.**

The shear wave amplitude was then measured at a point 140 µm from the IDT array for both the unperturbed and perturbed signals. These measurements are shown in Figure 4-13.

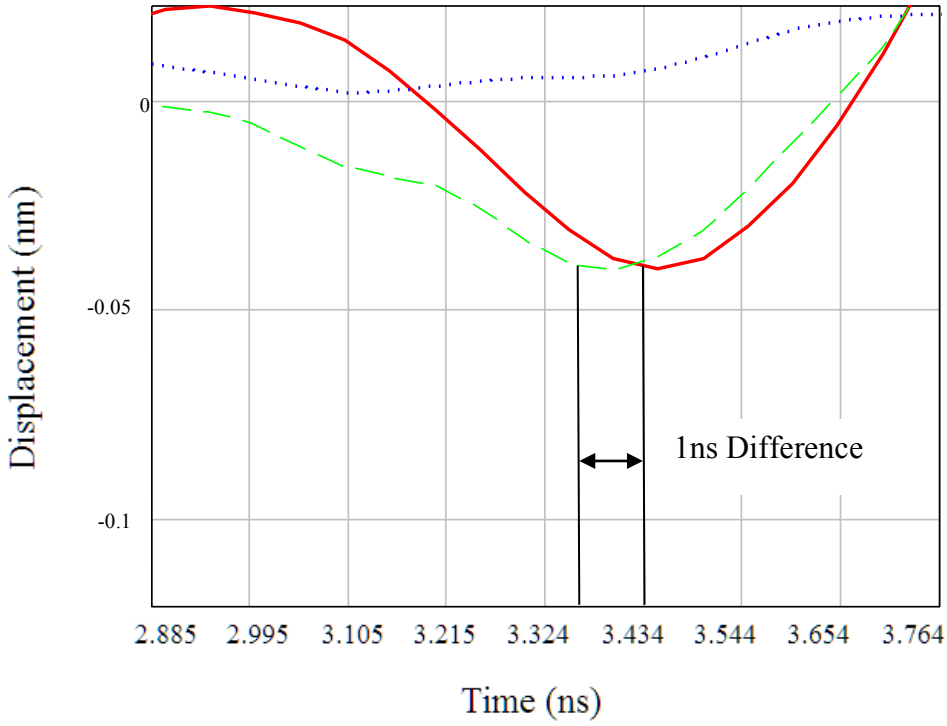


**Figure 4-13: Shear wave displacement at a point 140 µm from IDT array in the propagation direction for 100 MHz devices at 5 V.**

The delay between the signals was found to be 1 ns which corresponds to a velocity change of approximately 124 m/s. The above calculated value shows a $K^2$ value of 5.8%, which compares well to the published values of 4.7%, showing an error of around 20%, which is reasonable considering the inaccuracies in the wave measurement method.

### 4.2.3 Analysis of Penetration Depth

The generation of mechanical waves on the surface of the SAW surface results in propagation of an associated electric field into the bulk substrate. The penetration depth of the wave is of particular interest in determining the wave mode and analysing the energy loss into the bulk material. Analysis of three displacement components (including surface normal, shear horizontal and longitudinal) was undertaken along tangential line through the centre of the substrate at 50 ns. The location of the measurement point is shown in Figure 4-14.

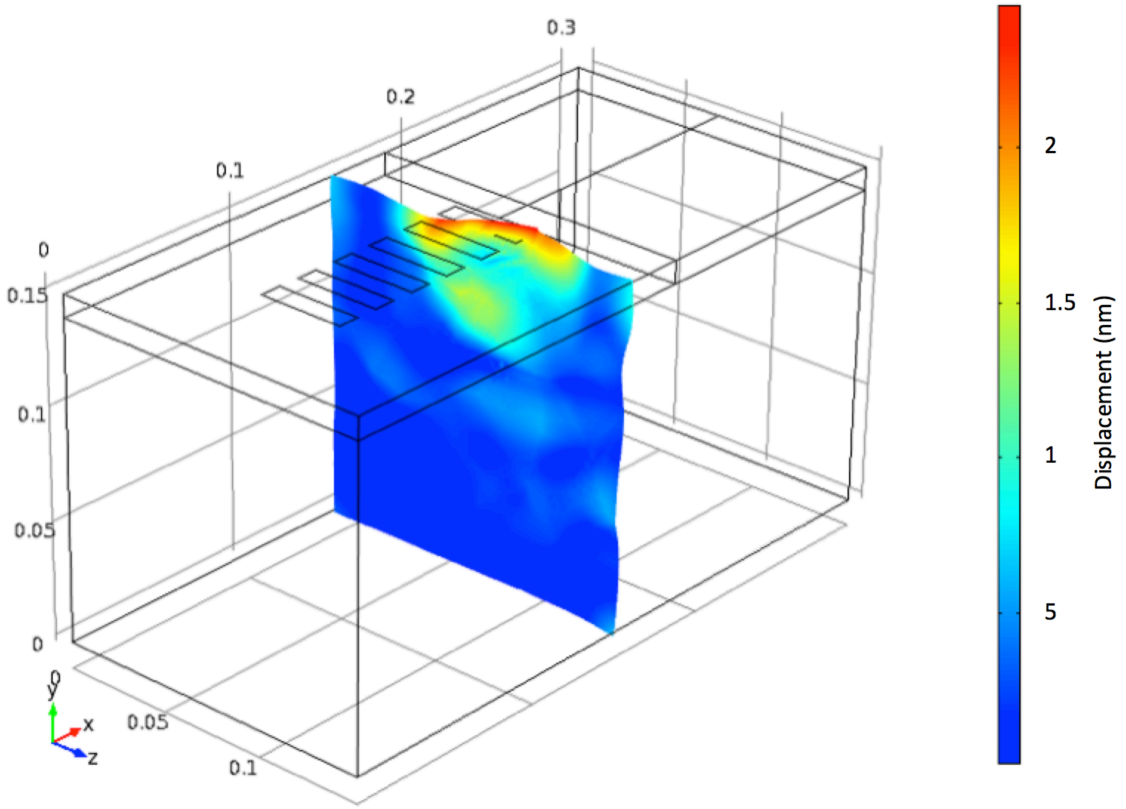


**Figure 4-14: Displacement image of cross section cut though centre of substrate. The displacement profile is shown at 50 ns when the wave profile had stabilised.**

The analysis of the three components was compared to analytical results calculated by Nakamuira et al. for the 36°YX $LiTaO_3$ substrate [109]. The propagation of the SAW leaky wave can be described by the following relationships [93]:

$$u_i = \sum_{n=1}^{4} A_n \, \alpha_{in} e^{jk[\beta_n \; x_2 + (1-\delta)x_1 - vt]} \qquad 4\text{-}14$$

$$\Phi = \sum_{n=1}^{4} A_n \, \alpha_{4n} e^{jk[\beta_n \; x_2 + (1-\delta)x_1 - vt]} \qquad 4\text{-}15$$

Where $v$ is the propagation velocity, $k$ is the wave number and $\delta$ is the decay constant along the propagation direction. The three displacement components are represented by $u_i = (u_1, u_2, u_3)$.

The results obtained for the three displacement components and the analytical results are shown in Figure 4-15.

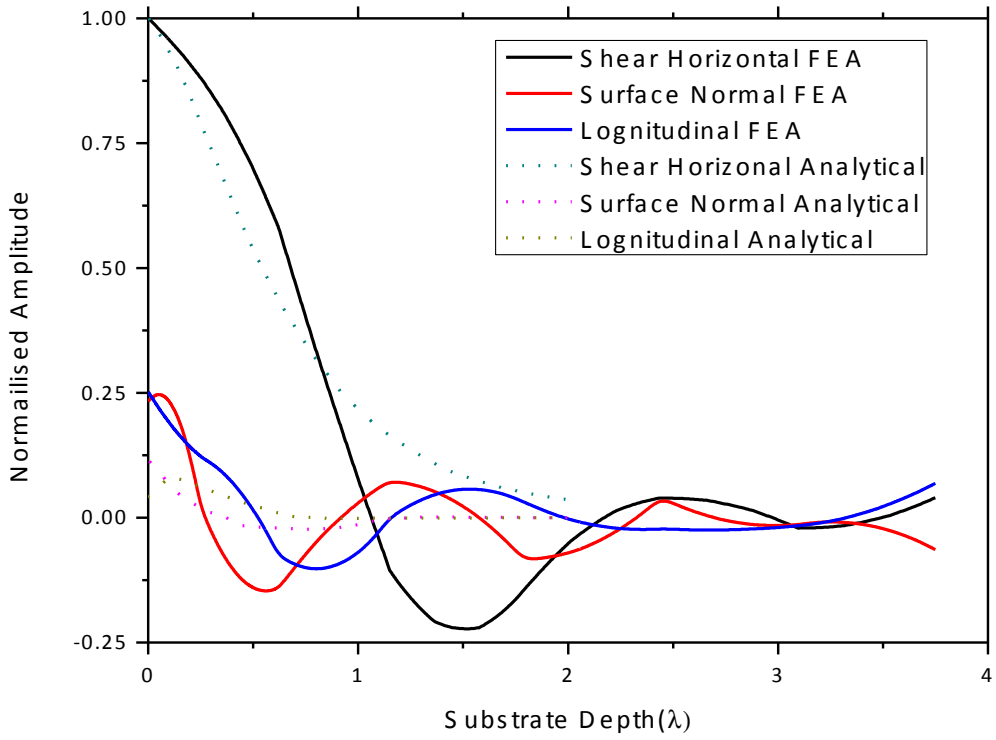


**Figure 4-15: Mechanical displacements versus normalised distance into substrate for 36°YX $LiTaO_3$. Simulated FEA results are compared to analytical results obtained by Nakamuira et al. [109]**

The numerical FEA solution shows that the shear horizontal wave has the highest amplitude on the surface, as expected, and decays quickly into the bulk material with the wave amplitude of zero at around 2λ, which is a similar magnitude to Rayleigh waves [109]. This shows that the substantial portion of the SAW waves propagated near the surface with minimal dissipation into the bulk substrate. The major components of the surface normal and longitudinal waves decay within 1λ of the surface with some residual amplitude decaying by 2λ. Comparing these results with the analytical results, a good correlation is found confirming the accuracy of the FEA simulation.

### 4.2.4 Analysis of Voltage Variation

After verification of the model, different parameters were investigated in order to understand the relationship of the wave displacements *vs.* design variations for the SH-SAW devices.

For the initial investigation, the voltage was varied, because for microfluidic applications, increasing wave displacements are related to streaming and pumping characteristics. For

the initial investigation, the voltage was varied in intensity from 0.1 V up to 7 V with the device operated at 100 MHz with 40 µm periodicity. The displacement measurements were taken 6 µm from the IDT to simulate a droplet positioned directly in front of the IDT. Plots of the relative displacements are shown schematically in Figure 4-16.

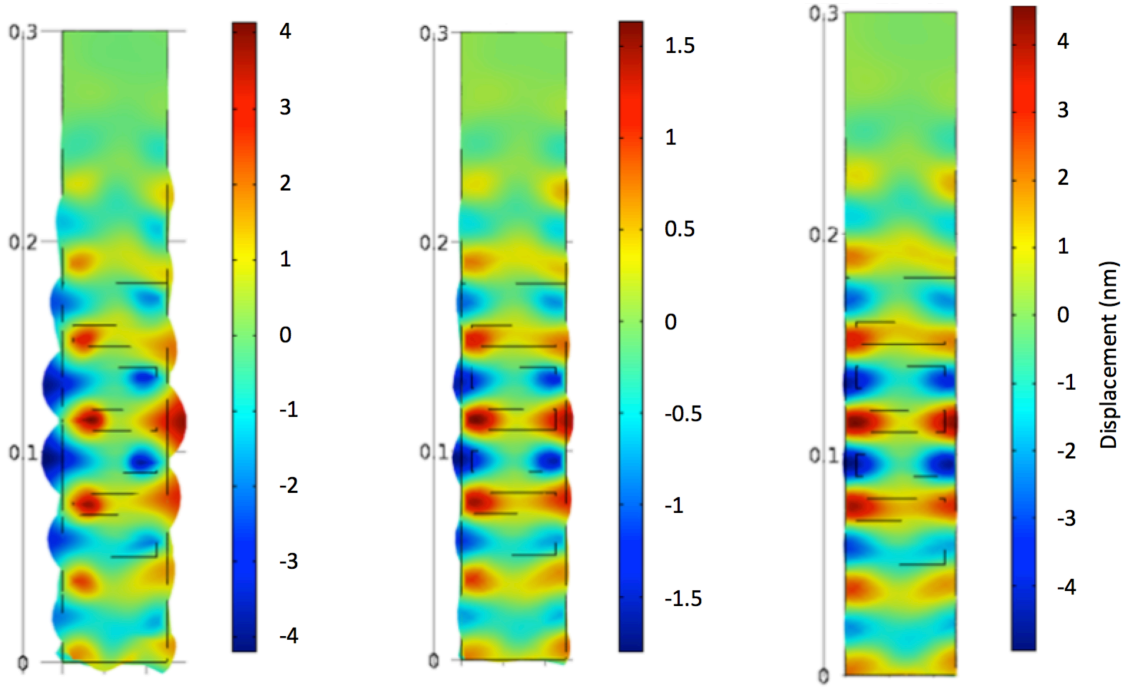


**Figure 4-16: Plots of Shear Horizontal displacement at 0.5, 3.5 and 7 V (left-right) Peak-to-Peak excitation modelled on 36°YX $LiTaO_3$ at 100MHz. Displacement show is mm.**

The shear horizontal and surface normal components were plotted to analyse the behaviour as show in Figure 4-17.

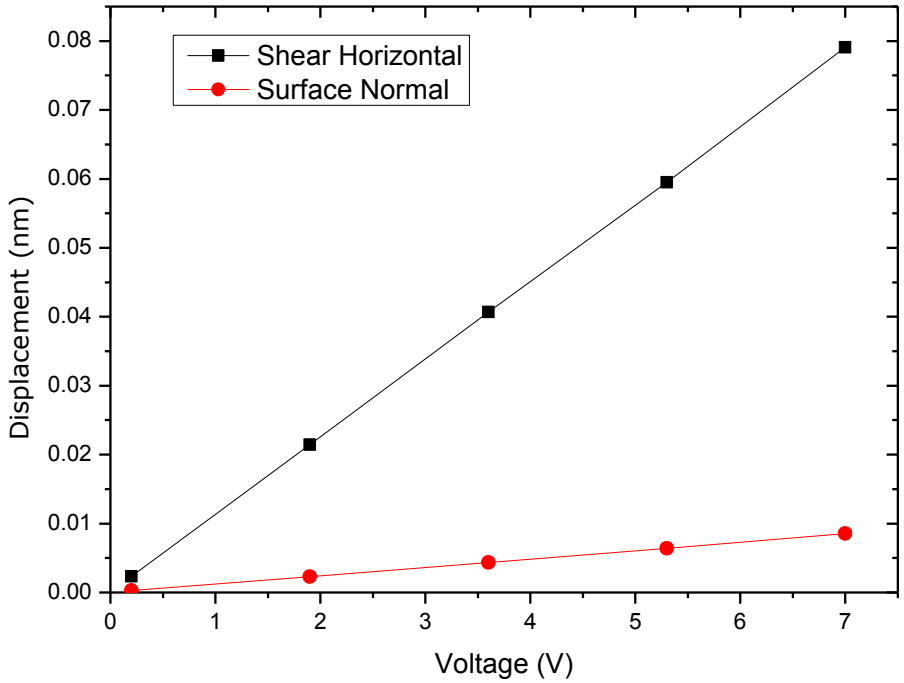


**Figure 4-17: Variation of Shear Horizontal and Surface Normal displacement components with respect to voltage from 0.3 V to 7 V Peak to Peak**

The shear horizontal and surface normal displacements were seen to vary linearly with the voltage from 0.3 V to 7 V. Calculated percentage of the vertical component to the shear component was seen to vary from around 12% at 0.3 V down to 10.5% at 7 V. This indicates that the amplitude of the vertical wave is reduced as the voltage increases. These results show the applicability of the SH-SAW device for microfluidics as an increasing power results in an increased displacement.

### 4.2.5 Analysis of Wavelength Variation

The second design parameter investigated is the variation of the wavelength or frequency of the devices.

The periodicity of the IDT's was varied to achieve a frequency of 50 Hz, 60 Hz and 100 Hz. A constant voltage of 5 V was applied for all simulations; the shear displacements plots are show in

Figure 4-18.

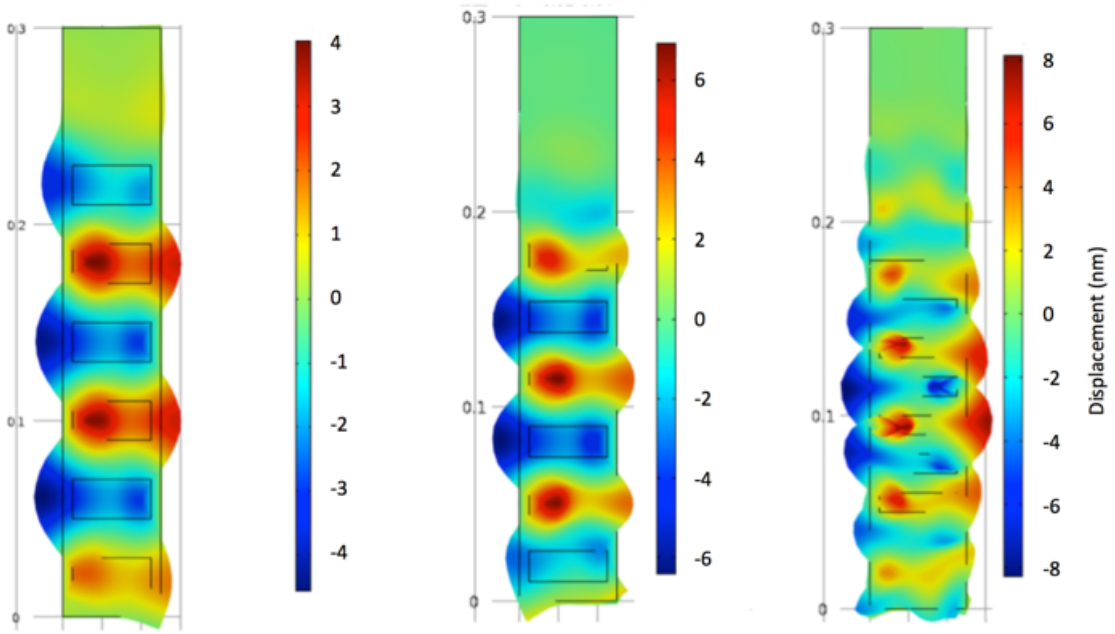


**Figure 4-18: Plots of Shear Horizontal displacement at 50 Hz, 60 Hz and 100 Hz (left-right) modelled on 36°YX $LiTaO_3$ 100MHz. Voltage applied was 5 V, displacement show is nm.**

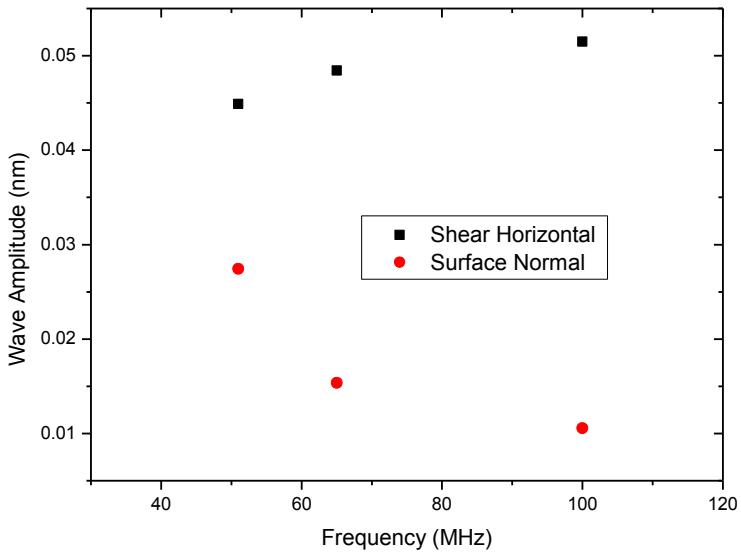


**Figure 4-19: Variation of Shear Horizontal and Surface Normal displacement components at 50 Hz, 60 Hz and 100 Hz. Voltage applied was 5 V.**

A non-linear behaviour was observed as the frequency was increased with the observed amplitude of the SH-SAW increasing from 0.045 nm to 0.05 nm and the vertical

component of the wave decreasing from 0.03 nm to 0.01 nm. The relatively flat response of the SH-SAW wave to frequency would be expected due to the constant voltage input but the vertical response may be an artefact of the mesh variation between the models.

### 4.2.6 Wave Amplitude vs. Spatial Position

One critical parameter for micro-fluidic functions is the decay of a wave along the propagation and tangential direction to the propagation. A wave with a large decay will alter the ability to place droplets at any given spatial location on the substrate and thus reduce the versatility of the device and possible micro-fluidic functions.

To investigate this, a 100 MHz modelled substrate with a 5 V peak-to-peak input voltage was investigated. The wave decay was probed at different positions on the simulated model at 50 ns. Two locations were seen to be critical: the propagation direction and the tangential direction as shown in Figure 4-20. The tangential direction is interesting to study, as we know that the off-centre mixing was observed on the Rayleigh wave devices [110]. The shear horizontal and vertical waves were probed at these locations to determine the variation of the waves.

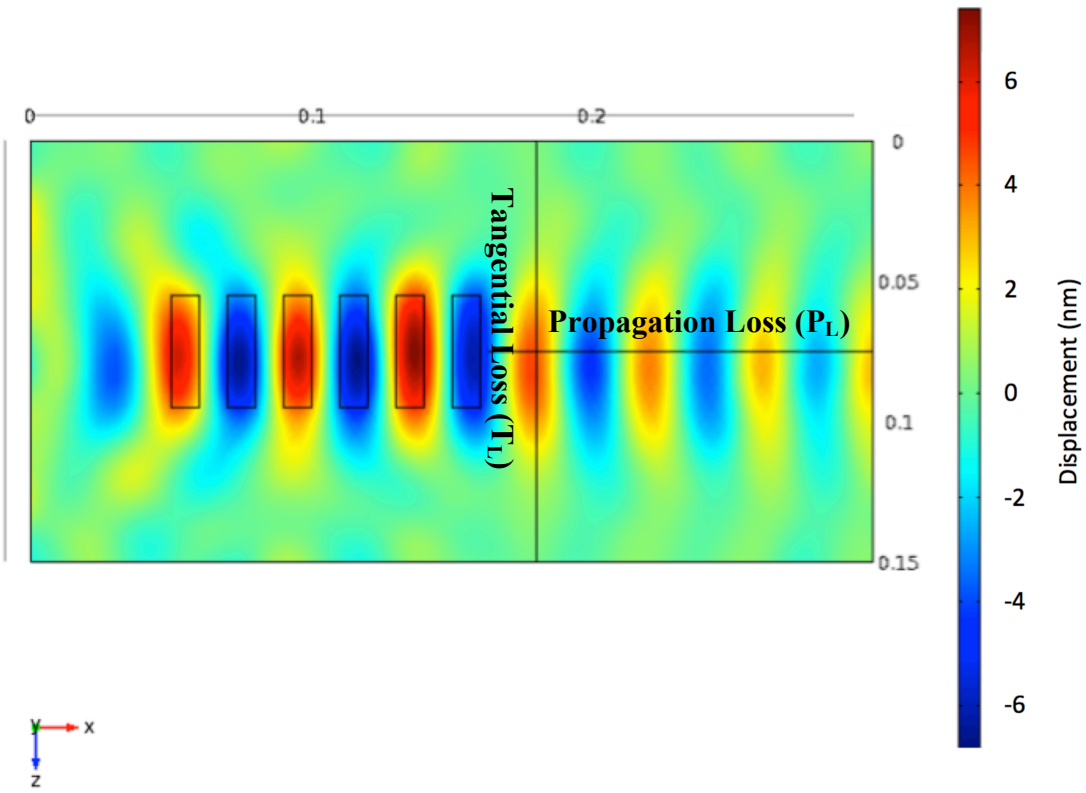


**Figure 4-20: Propagation loss measurement locations shown on plan view of FEA model (Scale is in nm).**

The shear wave was investigated initially across the $T_L$ axis; the plot of the shear displacement is shown in Figure 4-21.

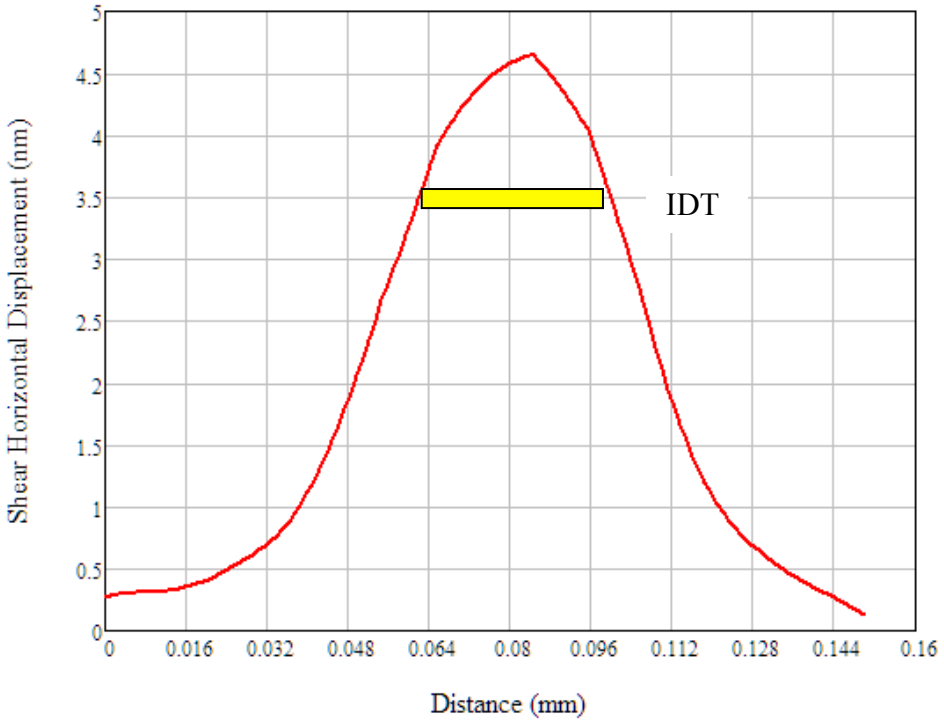


**Figure 4-21: Shear Horizontal displacement across $T_L$ line for 100 MHz 5 V P-P device. The width of the IDT is show schematically for reference**

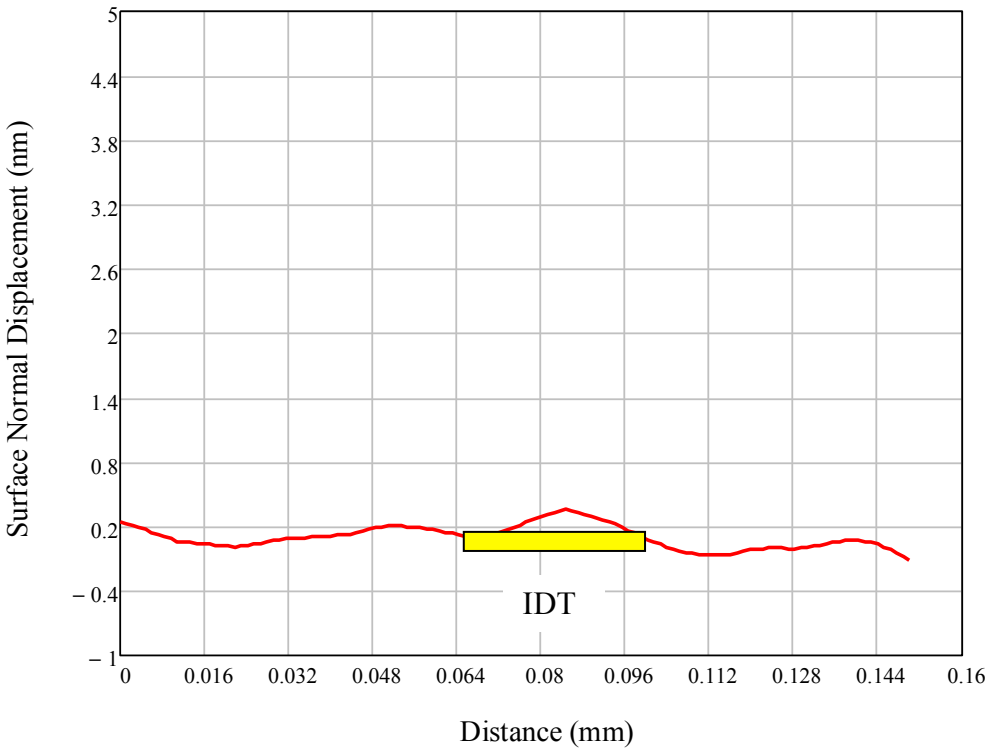


**Figure 4-22: Surface Normal displacement across $T_L$ line for 100 MHz 5 V P-P devices. The width of the IDT is show schematically for reference**

For the shear horizontal component, the highest displacement was seen across the IDT's with the wave dissipating from 3.5 nm to 0.3 nm within 1 width of the IDT. The decay function was seen to be exponential on both sides of the IDT's. This pattern shows that the optimal micro-fluidic and sensing functions should occur within the propagation path, with the areas outside this region showing decaying wave amplitudes with high attenuation within the substrate.

The surface normal component across the $T_L$ axis was investigated with the displacement plot shown in Figure 4-22. The pattern for the vertical component shows that the maximum amplitude of the wave occurs within the IDT aperture but no characteristic pattern of decay is observed. This correlates well with the low amplitude of the wave which shows there is little propagation of the vertical wave though the substrate due to the dominate shear component and hence the chaotic pattern.

Examination of the $P_L$ component of the shear horizontal wave showed a sinusoidal decay pattern with the wave function, representing the direction changes of the shear wave polarisation along the propagation path (see Figure 4-23). The wave amplitude was seen to decay by 15% over a distance of 0.1 mm.

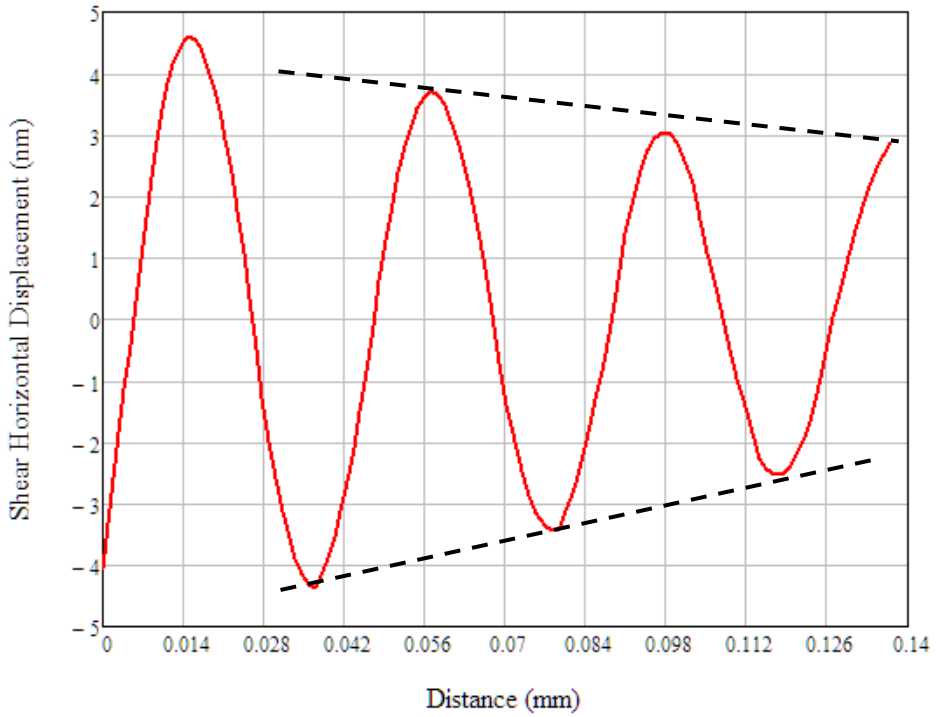


**Figure 4-23: Shear Horizontal displacement across $P_L$ line for 100 MHz 5 V Peak-to-Peak devices.**

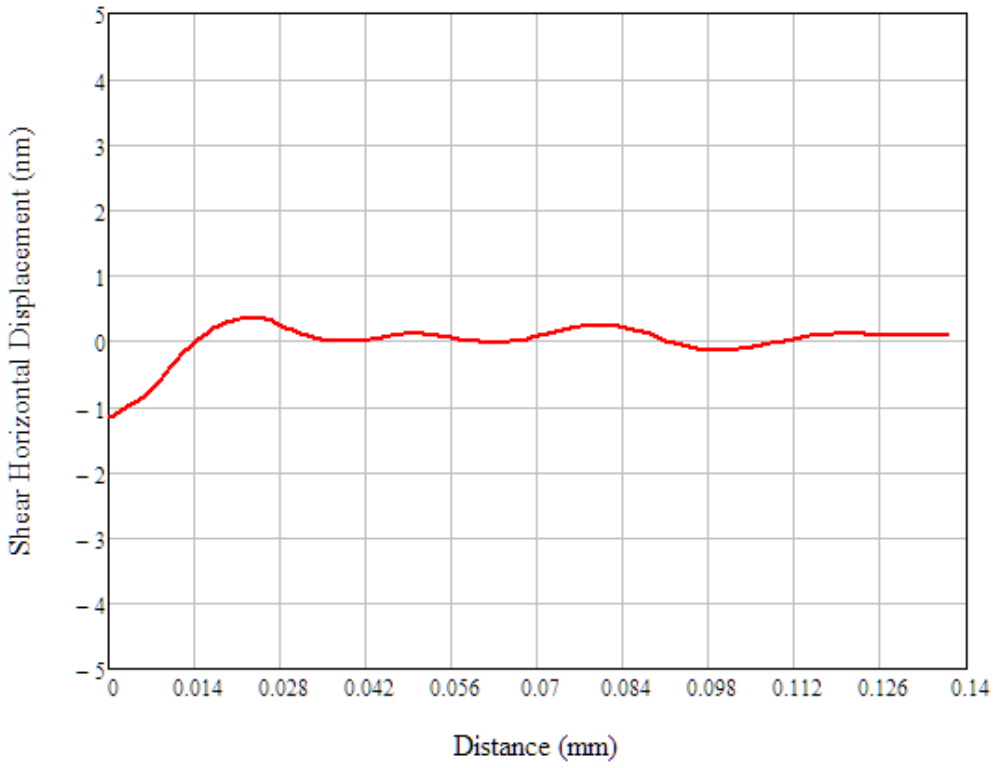


**Figure 4-24: Surface Normal displacement across $P_L$ line for 100 MHz 5 V Peak-to-Peak.**

The surface normal wave along $P_L$ exhibited an almost instant decay with the wave decaying to around zero amplitude within 15 µm of the IDT array. This indicates that there is little vertical wave propagation on the 36°YX $LiTaO_3$ substrate.

### 4.2.7 Rayleigh Wave Propagation Analysis on 36°YX $LiTaO_3$ SH-SAW Substrate

In addition to supporting the SH-SAW polarised wave at 4112 m/s, the 36°YX $LiTaO_3$ crystal cut is known to also support Rayleigh wave at a lower velocity of 3116 m/s [111]. This wave is known to have a weak coupling coefficient of $2\Delta v/v$ of 0.00046 and is expected to have a lower amplitude and propagation in comparison to the SH-SAW. To investigate the Rayleigh wave propagation, the pulse frequency was adjusted to 79.1 MHz to excite the vertical mode. The simulation was run with an input of 5 V peak-to-peak excitation and a total time of 50 ns. The vertical wave displacement at approximately 30 ns is shown in Figure 4-25.

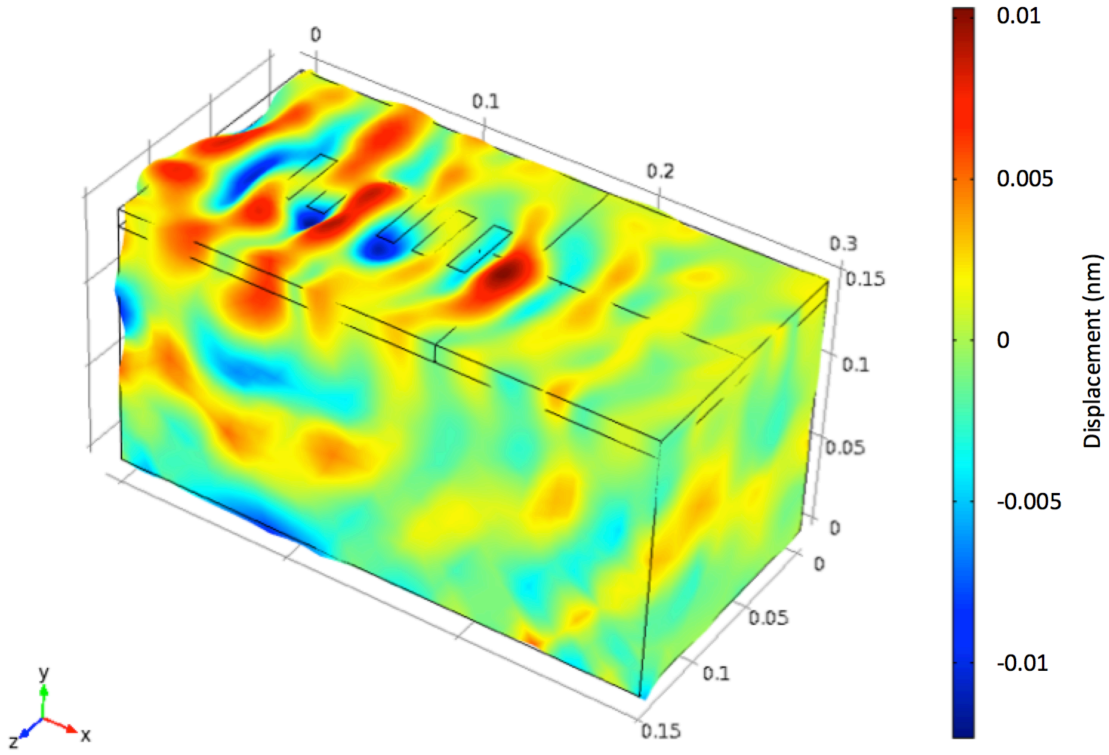


**Figure 4-25: Surface acoustic wave propagation of surface normal polarised waves on 36°YX $LiTaO_3$ with 5V peak to peak excitation at 79.1 MHz at approx. 50 ns. The displacements are shown in nm. The vertical wave can be seen to be around 0.01 nm at its peak.**

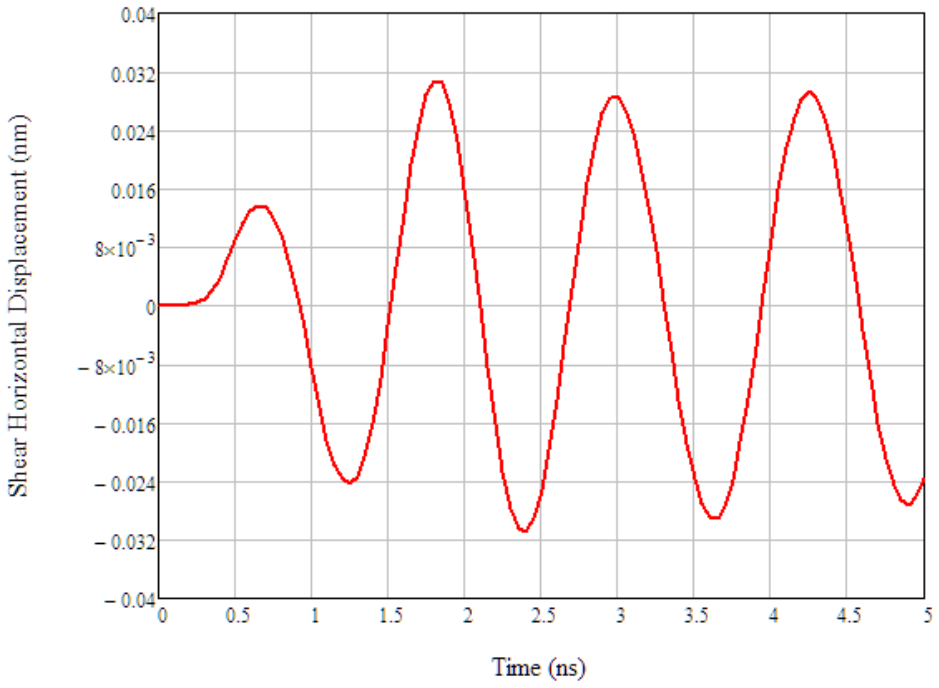


**Figure 4-26: Displacement of shear horizontal component at 5 V peak-to-peak at 79.1 MHz excitation at 6um from IDT.**

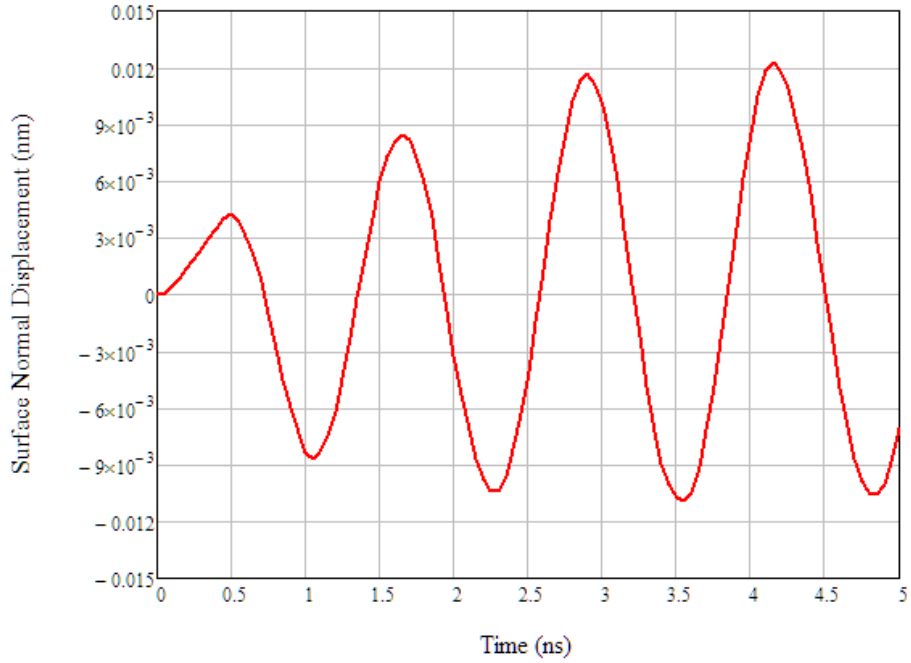


**Figure 4-27: Displacement of surface normal component at 5 V peak-to-peak 79.1 MHz excitation at 6 µm from IDT.**

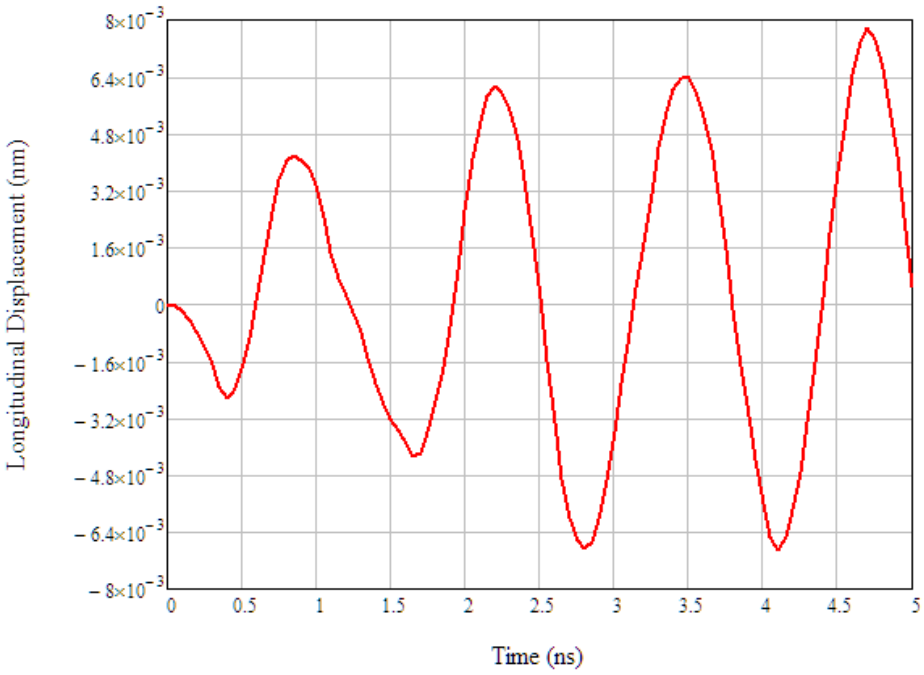


**Figure 4-28. Displacement of longitudinal component at 5 V peak to peak 100 MHz excitation at 6 µm from IDT**

Figure 4-26 to Figure 4-28 show the displacement outputs of the substrate obtained at 6 µm from the forward IDT. The indicated displacements show that the shear wave component was the highest at around 0.03 nm with the surface normal and component at

0.012 nm and the longitudinal component at 0.0064 nm. In contrast to the 100 MHz devices, the Rayleigh wave is now 40% of the shear wave component.

These results show that the wave propagation is still a mixed shear and Rayleigh mode, which is possible due to its mechanical coupling coefficient.

## 4.3 Rotated IDT for Bio-sensing and Acoustic Streaming

### 4.3.1 Introduction

For the integration of micro-fluidic functions on a single substrate, it is critical that multiple functions can be realised in as small domain as possible. To date it is known that the X propagation direction of the 36°YX $LiTaO_3$ crystal cut can support both a weak Rayleigh wave and a SH-SAW leaky wave. To investigate if different micro-fluidic functions can be realised on a single substrate, it was decided to investigate the wave polarisation in different Euler angels on the 36°YX $LiTaO_3$ crystal. As the material is anisotropic, different waves can be realised at different angles of crystal cut.

The 36°YX $LiTaO_3$ has been shown to be a highly accurate biosensor when used in the X propagation direction with detection levels of 1 ng/cm$^2$ [41], [54], [112]–[114]. Micro-stirring during bio-reaction has been shown by Ducloux et al. [75] that both the concentration of the binding analyte and speed of reaction can be improved if stirring takes place during the sensing. To investigate if micro-stirring and sensing can be integrated on a single crystal cut, it was decided to investigate the wave propagation from an IDT array at 90 degrees to the main X propagation direction to determine if the wave will support any micro-fluidic functions. The proposed device is shown schematically in Figure 4-29.

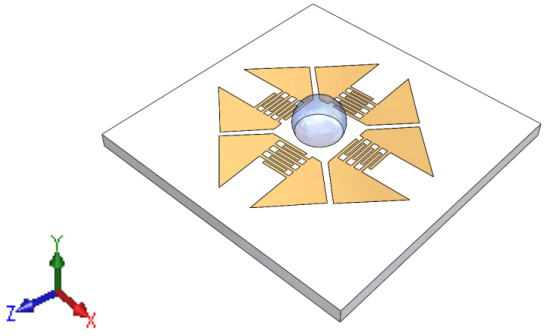


**Figure 4-29: 4 Port IDT array with IDT's in x propagation direction and at Euler angel (90,-36,0)**

As there is no published data to date of the wave characteristics or velocity for the 90 degree rotated 36°YX $LiTaO_3$, it was decided an impulse response simulation would be undertaken to determine the insertions loss for the $S_{12}$ parameters of the devices. The simulation model was the same as outlined previously in this chapter except for the changes to the voltage excitation of the IDT's.

### 4.3.2 Structural Excitation

For the excitation of the substrate by the wave, the following impulse function was applied to the transmitting IDT's:

$$V_{i^+} = \begin{cases} +0.5V, t \leq 1ns \\ 0V, t \geq 1ns \end{cases}, V_{i^-} = \begin{cases} -0.5V, t \leq 1ns \\ 0V, t \geq 1ns \end{cases}$$

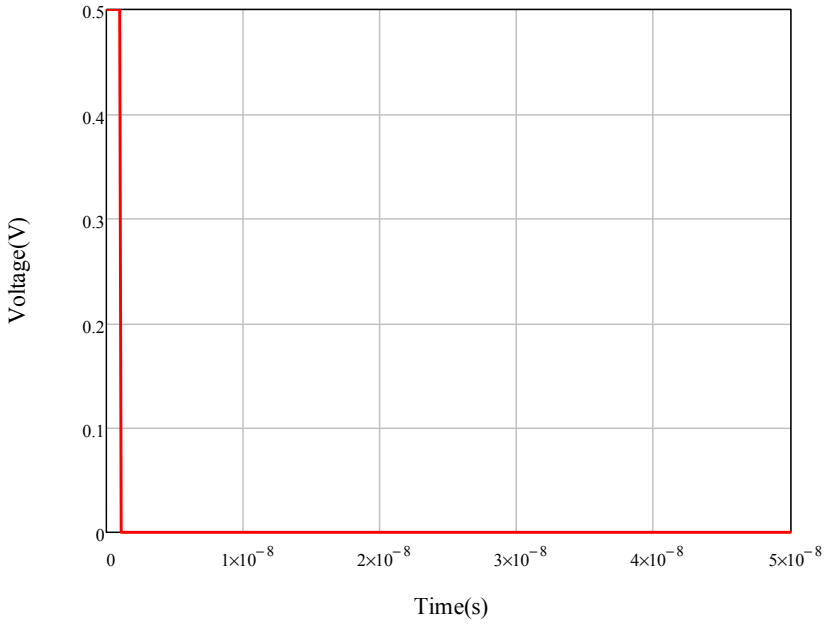


**Figure 4-30: Impulse Function applied to transmitting IDT's.**

The impulse function was used to measure the frequency response of the signal, which was measured in the form of the voltage response over time at a point 40 µm from the input IDT array to represent the output IDT array.

To obtain the frequency response, a Fourier transform was used to deconvolve the signal into a frequency response [115]:

$$H(f) = \int_{-\infty}^{+\infty} h(t) e^{-2\pi f t}\, dt. \qquad 4\text{-}16$$

As the reflection of the substrate may have effects on the frequency response, the signal was cut off at the point before any reflection could occur.

### 4.3.3 Response to Impulse Excitation

The insertion loss was simulated for both the standard 36°YX $LiTaO_3$ along Euler angle cut (0,36,0) and the 90 degree rotated cut (90,36,0). The full spectrum was simulated but the results were limited to the 600 MHz range. The results for the standard cut were compared to the experimental results for a sample device. These are shown in Figure 4-31.

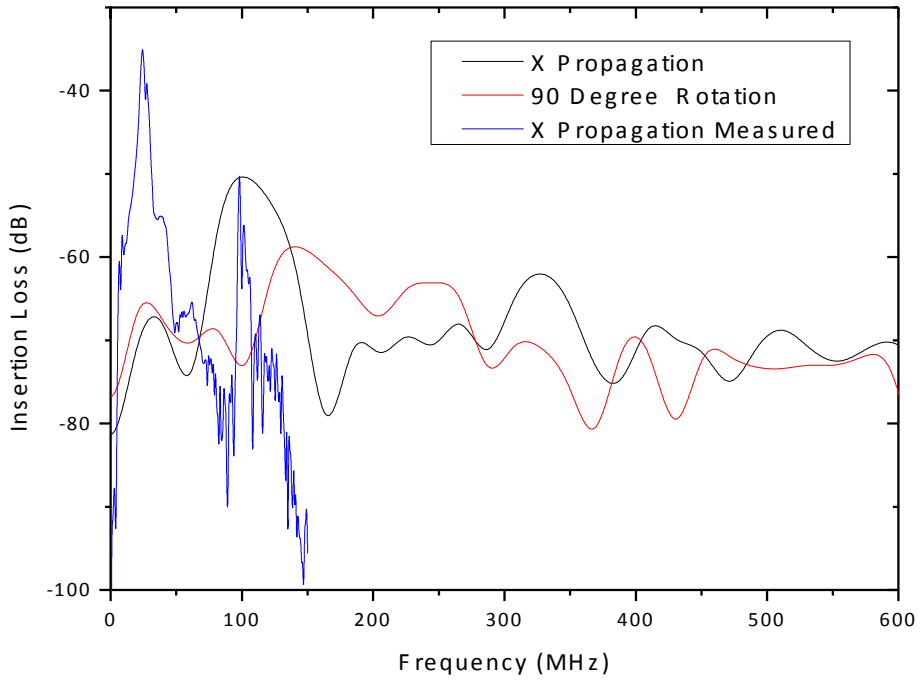


**Figure 4-31: Simulated insertions loss for 90° rotated array and non-rotated array. Experimental transmission measurements for the non-rotated IDT array is also shown.**

The standard (0,36,0)-cut device had the lowest insertion loss at 102 MHz, which correlates well to the published and experimental values of the peak frequency for the SH-SAW wave. A lower calculated insertion loss was observed for the (90,36,0)-cut rotation with two peaks visible at 82 MHz and 143 MHz. These frequencies correspond to wave velocities of approximately 3500 m/s and 5700 m/s, respectively. This correlates well with numerical modelling by Slobodink et al. using the Campbell-Jones method

which showed that the YX $LiTaO_3$ supports the maximum velocity SAW wave at 90 degree rotation [111] at around 3200 m/s.

### 4.3.4 Characterisations of Waves on (90,36,0)-cut 36°YX $LiTaO_3$

With two wave velocities identified, the wave type was analysed using the standard sinusoidal excitation described previously with a 5 V peak-to-peak signal. The substrate was excited at the input IDT's with the frequencies of 82 MHz and 143 MHz.

Analysing the observed displacements plots in Figure 4-32 and Figure 4-33, it can be seen that at 82 MHz, there is a very low displacement in the shear horizontal direction at 0.0092 nm, which increase by 80% to 0.014 nm at 142 MHz. No clear SH-SAW pattern can be observed in either of the images with the wave decaying rapidly.

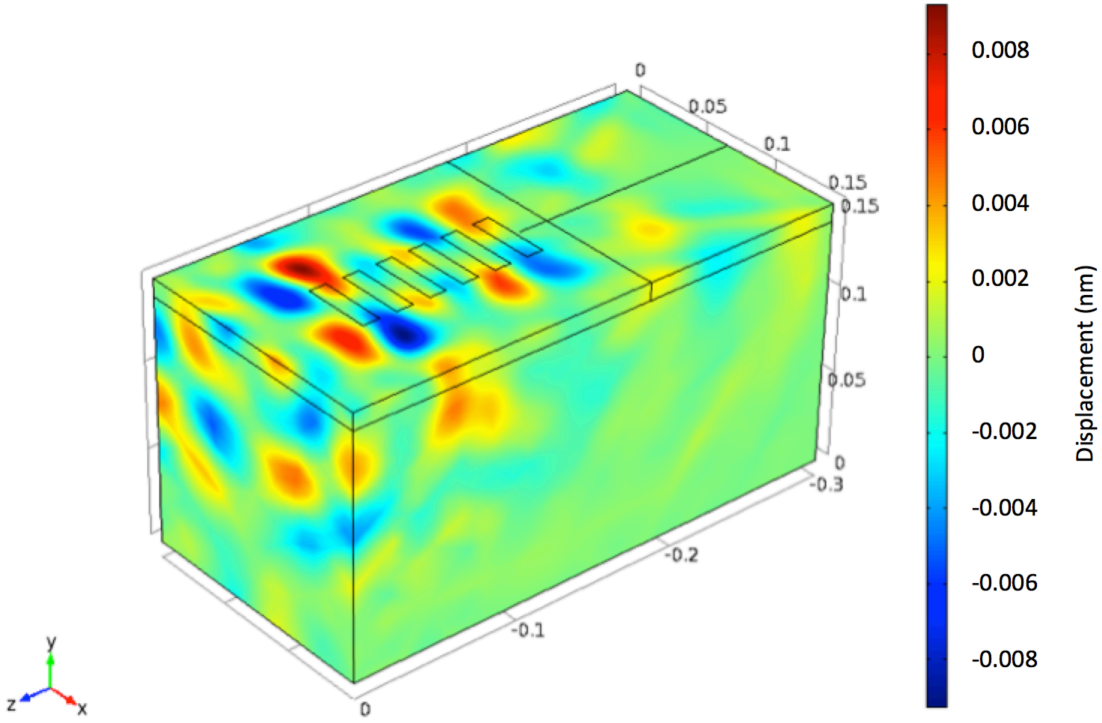


**Figure 4-32: Surface acoustic wave propagation of shear horizontal polarised waves on (90,36,0) 36°YX $LiTaO_3$ with 5 V peak-to-peak excitation at 82 MHz at approximately 50 ns. The displacements are shown in nm. The wave can been seen to be around 0.0092 nm at its peak.**

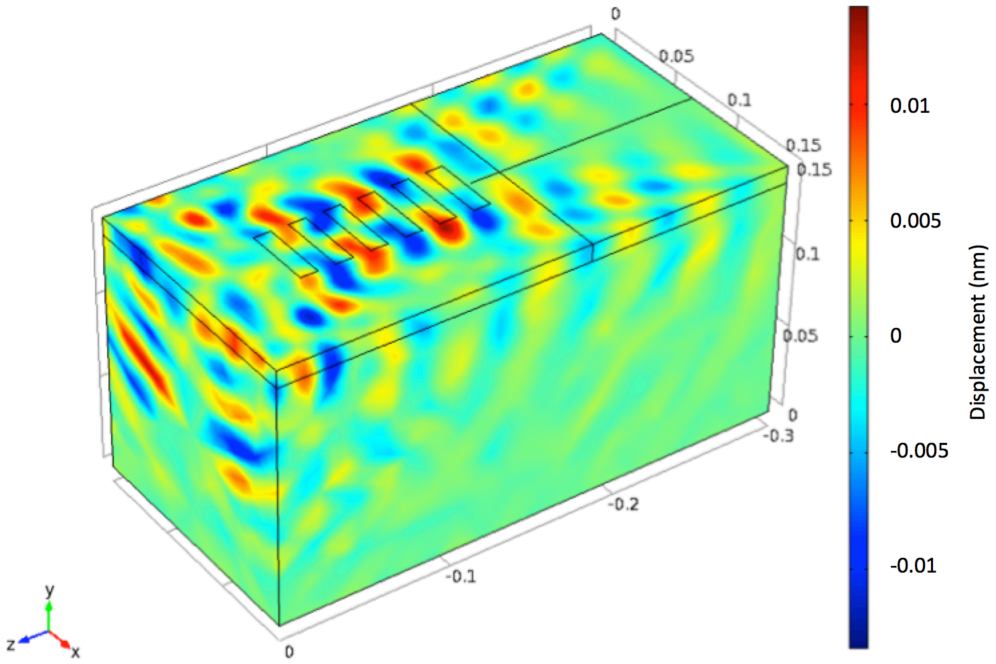


**Figure 4-33: Surface acoustic wave propagation of shear horizontal polarised waves on (90,36,0) 36°YX $LiTaO_3$ with 5 V peak-to-peak excitation at 143 MHz at approx. 50 ns. The displacements are shown in nm. The wave amplitude is observed to be approximately 0.014 nm at its peak.**

The vertical component was shown to have a displacement of 0.0144 nm at 82 MHz and 0.0221 nm at 143 MHz. A clear vertical component of constant amplitude across the substrate can be observed in Figure 4-34 and Figure 4-35.

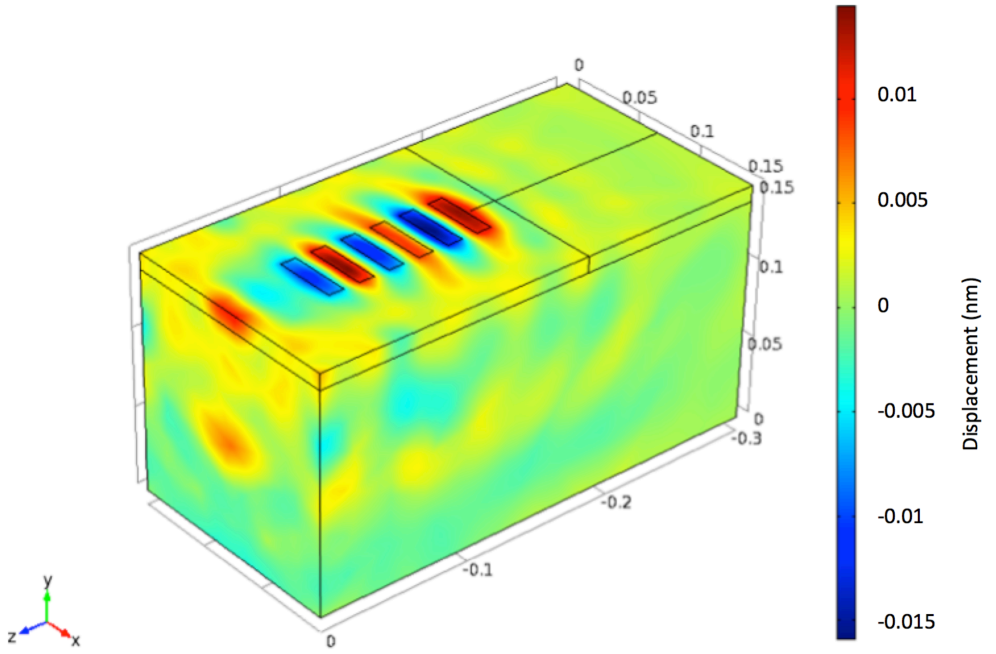


**Figure 4-34: Surface acoustic wave propagation of surface normal polarised waves on (90,36,0) 36°YX $LiTaO_3$ with 5 V peak to peak excitation at 82 MHz at approx. 50 ns. The displacements are shown in nm. The wave amplitude is observed to be around 0.0144 nm at its peak.**

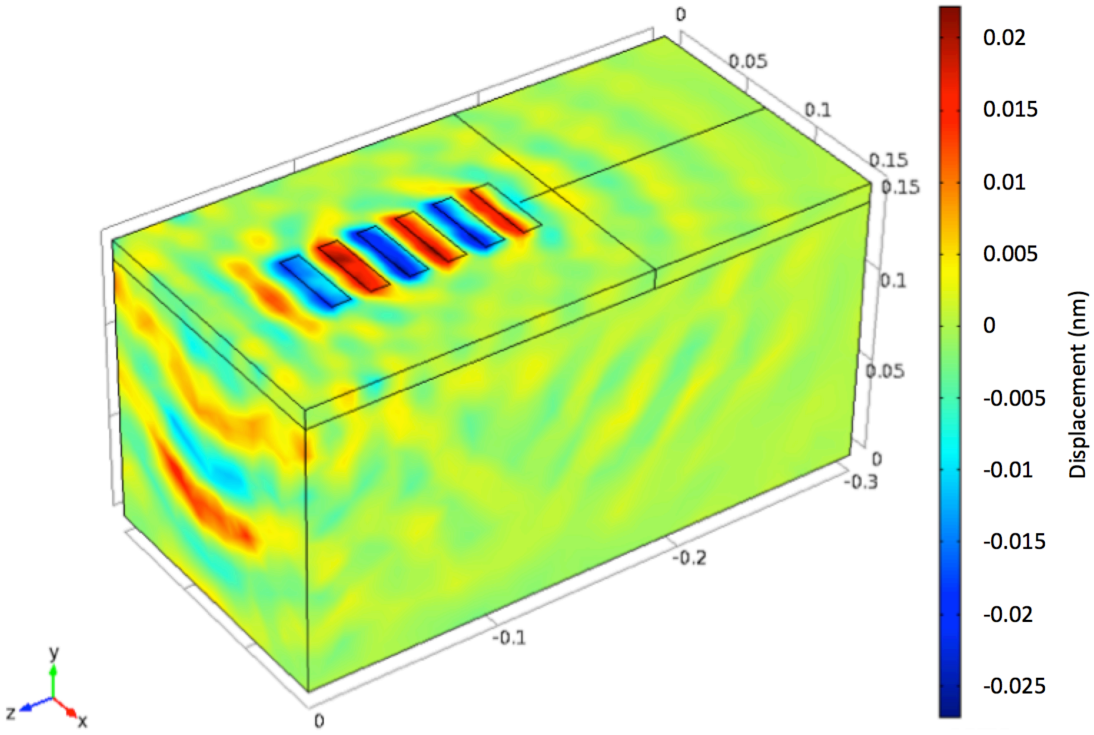


**Figure 4-35: Surface acoustic wave propagation of surface normal polarised waves on (90,36,0) 36°YX $LiTaO_3$ with 5 V peak to peak excitation at 143 MHz at approx. 50 ns. The displacements are shown in nm. The wave amplitude is observed to be approximately 0.0221 nm at its peak.**

Observing that stronger coupling was apparent at 143 MHz, a cross-section though the model was created to analyse the behaviour in Figure 4-36.

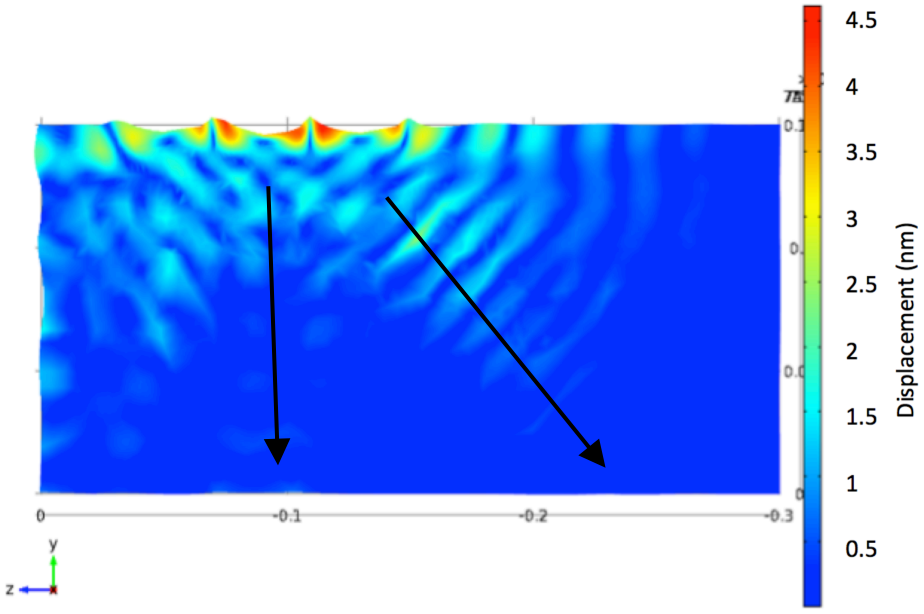


**Figure 4-36: Surface acoustic wave propagation of waves on 36°YX $LiTaO^3$ with 5 V peak to peak excitation at 143 MHz at approx. 40 ns. The total displacement is shown in nm. The SAW radiation is seen to radiate into the bulk material as a BAW.**

With the improved coupling a large surface displacement is observed. This displacement results in a large amount of energy dissipated into the bulk material both vertically and at a downward propagation vector. This demonstrates a significant energy loss and inefficiency of the excited mode. A mixed mode of Rayleigh and SH-SAW was observed without any dominate mode observed at either 83 MHz or at 143 MHz.

To analyse the possibility of using the (90,36,0) 36ºYX $LiTaO_3$ rotation cut for microfluidic applications, the displacement at 6 µm from IDT was plotted to analyse the vectors in the propagation direction at the approximate location of a fluid. The three components were plotted to enable the comparison of the wave propagation vectors. The results are shown in Figure 4-37 & Figure 4-38.

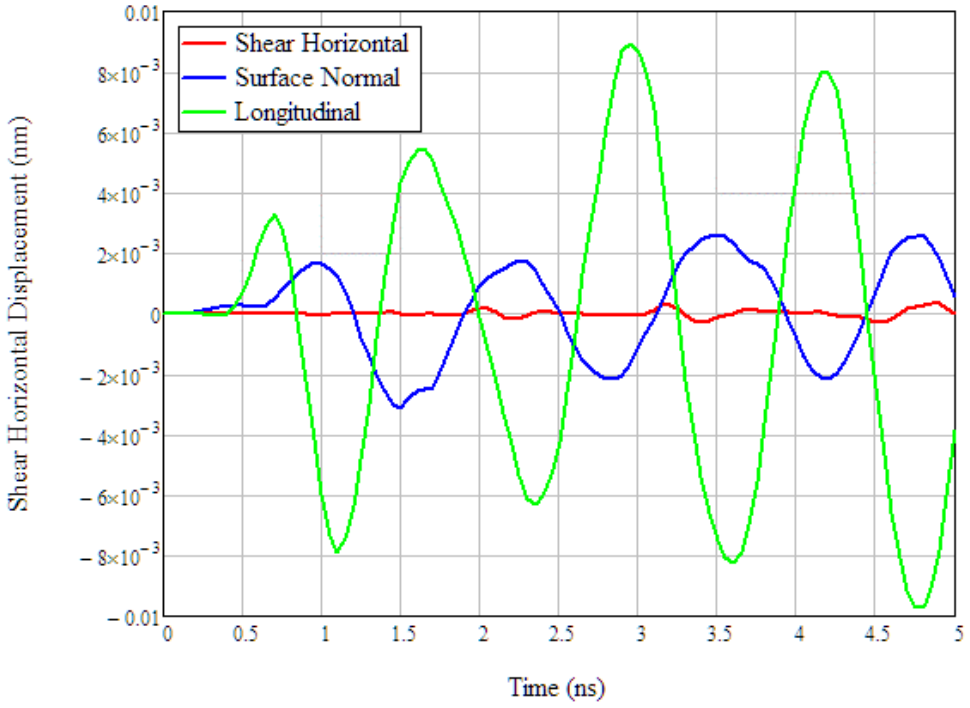


**Figure 4-37: Displacement of three wave components on (90,36,0) 36ºYX LiTaO3 with 5 V peak-to-peak excitation at 82 MHz at 6 µm from IDT.**

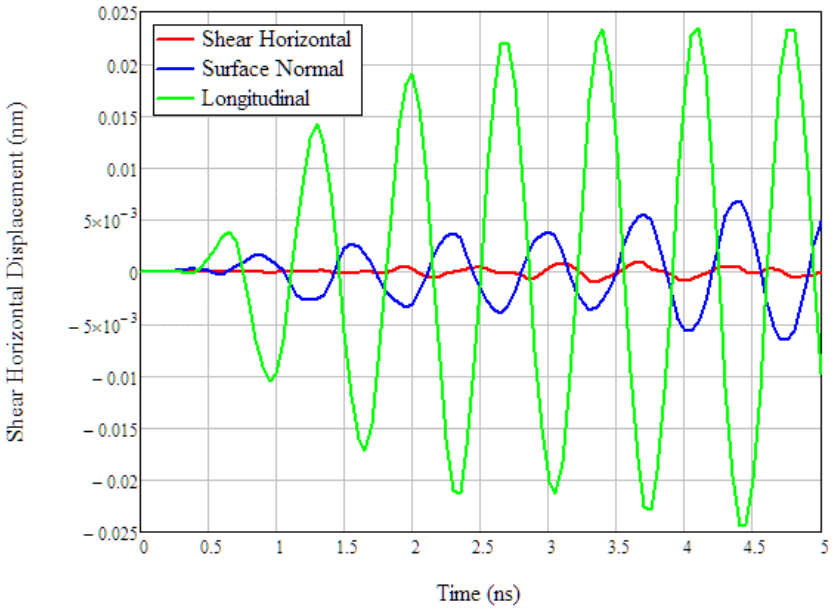


**Figure 4-38: Displacement of three wave components on (90,36,0) 36ºYX $LiTaO_3$ with 5 V peak to peak excitation at 143 MHz at 6 µm from IDT.**

Observing the displacements of the surface normal for both 82 MHz and 143 MHz revealed that the surface normal component is dominate at both frequencies, minimal amplitudes were observed for the shear horizontal component. For the 82 MHz devices, a surface normal component of 0.002 nm was observed, whereas doubled this value was obtained for the 143 MHz devices at 0.005 nm; indicating the improved coupling of this mode.

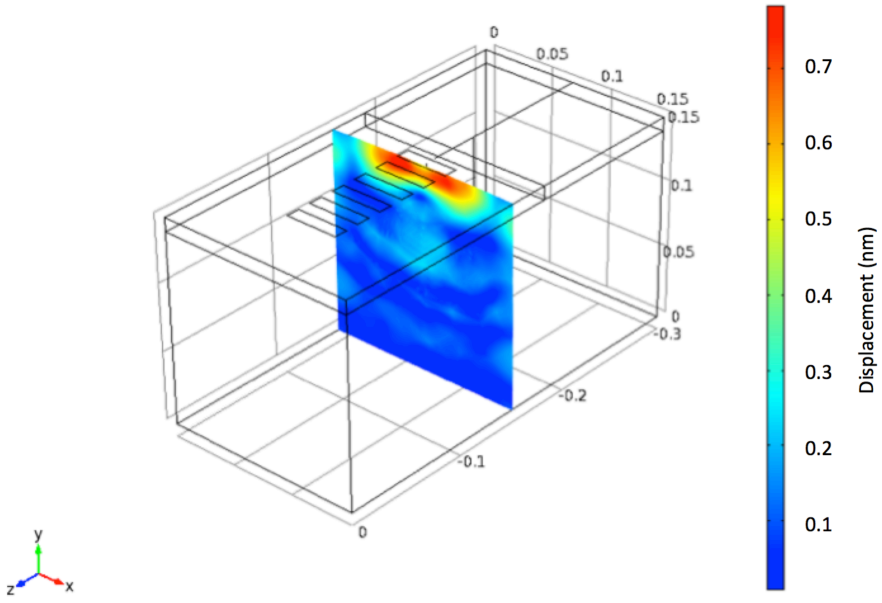


**Figure 4-39: Displacement image of cross section cut though centre of substrate. The displacement profile is shown at 30 ns on 82 MHz (90,36,0) 36ºYX $LiTaO_3$ when the wave profile had stabilised.**

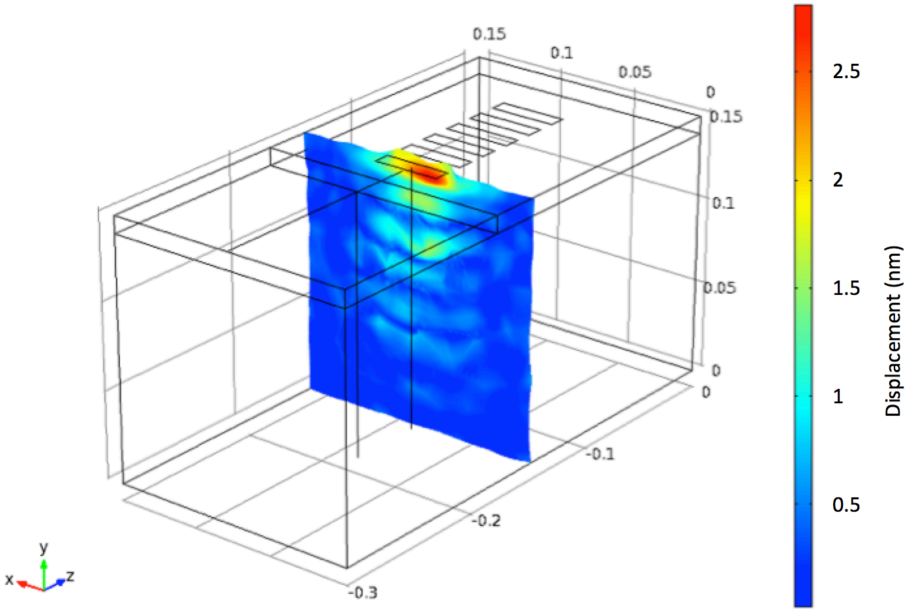


**Figure 4-40: Displacement image of cross section cut though centre of substrate. The displacement profile is show at 30 ns 143 MHz (90,36,0) 36ºYX $LiTaO_3$ when the wave profile had stabilised.**

Cross-sections were created though the vertical axis to analyse the energy dissipated from the IDT's as shown in Figure **4-39** & Figure 4-40. As can be seen at 82 MHz, a wide energy loss is observed though the substrate shows a weak attenuation of the mode at 143 MHz. The wave energy is confined within the IDT's and radiated with a high attenuation vertically downwards, showing the improved coupling of the 143 MHz mode.

Reviewing the displacement results, it is clear for the 143 MHz device a Rayleigh wave mode is dominate, which would enable the device to be a suitable substrate for microfluidic applications.

## 4.4 Summary

Reviewing the finite element analysis of the Y cut 36ºYX $LiTaO_3$ crystal, the results can be summarized as follows:

- FEA model of the Y cut 36ºYX $LiTaO_3$ crystal showed the surface normal or vertical Rayleigh wave component at around 4% of the shear wave component, demonstrating the shear wave is the dominant wave on the substrate.
- Wave velocities of both Rayleigh and Shear waves were compared against experimental devices with values within 1% of published data and 5% of experimental values.

- Electromechanical coupling coefficient ($K^2$) was found to be 5.8%, which compares well to the published values of 4.7%, showing an error of around 20%.
- Propagation depth of the SH-SAW wave compares well to theoretical calculations.

With the accuracy of the FEA model correlated the results of the simulations of the SH-SAW wave for microfluidics can be summarized as follows:

- Variation of voltage from 0.3 V to 7 V peak-to-peak showed a linear relationship; indicating the applicability of the Y cut 36ºYX $LiTaO_3$ for microfluidic applications.
- Analysis of wave decay outside the IDT's showed the highest displacement was seen across the IDT's with the wave dissipating from 3.5 nm to 0.3 nm within 1 width of the IDT. The decay function was seen to be exponential on both sides of the IDT.
- Shear wave propagation was shown to have minimal losses in the propagation direction of 15% over a distance of 0.1 mm compared to the Rayleigh wave which decayed within 15 μm of the IDT's, this demonstrates the suitability of the shear wave for microfluidic applications due to minimal losses.
- Simulation of the Rayleigh wave mode at 3116 m/s on the Y cut 36ºYX $LiTaO_3$ showed that a mixed Rayleigh/Shear wave mode exists with Rayleigh wave 40% of the shear wave component.

The investigation of the applicability of the SH-SAW for bio-sensing with simultaneous fluid streaming can be summarized as follows:

- Simulation of insertion loss showed the optimum direction of 36°YX $LiTaO_3$ substrate along Euler angle cut (0,36,0) for bio-sensing.
- For the 90 degree rotated cut (90,36,0), a dominant surface normal component or Rayleigh wave mode was observed at 83 MHz and 143 MHz.
- At 5 V and 6 μm from the IDT, a surface normal displacement of 0.002 nm was observed for 83 MHz device, and 0.005 nm for 143 MHz device, indicating that the high frequency mode is preferred for fluidic applications.
- Results showed that on a single substrate mixing whilst sensing is achievable.

# Chapter 5. Numerical and Experimental Investigation of Shear Wave Acoustic Microfluidics

With a SH-SAW wave shown to exist on the 36°YX $LiTaO_3$ substrate in Chapter 4, this chapter will analyse the fluidic application of the SH-SAW wave. A basic theoretical background of the fluid displacement, when subjected to a shear wave, will be presented with preliminary acoustic streaming simulations. A full experimental analysis of the SH-SAW device will be undertaken using the fabricated devices and experimental methods described in Chapter 3.

## 5.1 Simulation of Shear Wave Propagation in a Fluid Medium and Acoustic Steaming

It is known that Rayleigh wave devices with a normal displacement component, when in contact with a liquid, couple strongly with the liquid and leak ultrasonic power into the fluid in the form of acoustic waves called leaky SAWs. For SH-SAW devices, a mechanism to generate acoustic energy in a liquid medium has not been investigated to date.

From the FEA simulation in Chapter 4, it was shown that when a SH-SAW device is excited with a time varying voltage through IDT's, a shear wave is generated on the surface of the SAW device. For a fluid layer on this surface we can numerically analyse the behaviour of the fluid assuming the surface is excited in pure shear with minimal surface normal attenuation as confirmed by modelling in Chapter 4.

### 5.1.1 Numerical Analysis of Shear Displacement Fluid Coupling

The velocity field, $U_x$, generated by this in-plane shear oscillation is determined by solving the Navier-Stokes equation for one-dimensional plane-parallel flow [116]:

$$\eta_1 \left(\frac{\partial^2 U_x}{\partial^2 y^2}\right) = \rho_1 \dot{U}_x \qquad 5\text{-}1$$

where $\rho_l$ and $\eta_l$ are the liquid density and shear viscosity respectively. The solution will be [117] :

$$U_x(y,t) = U_{xo}e^{-y\gamma}e^{i\omega t} \quad 5\text{-}2$$

Equation 5-2 represents a damped shear wave radiated into the fluid by the oscillating device surface; $y$ is the distance from the surface and $\gamma$ is the complex propagation factor for the acoustic wave:

$$\gamma = \sqrt{\frac{\omega\rho_1}{2\eta_1}}\,(1+i) \quad 5\text{-}3$$

Subsisting equation 5-3 into 5-2 and only taking the real part we get the following:

$$U_x(y,t) = U_{xo}e^{\frac{-y}{\delta}}\cos\left(\frac{y}{\delta}\right)e^{i\omega t} \quad 5\text{-}4$$

where $U_x$ is the velocity of the fluid, $\delta$ is the decay length, $y$ is the distance from the surface, $\omega$ is the angular frequency and $t$ is the time. The decay length of wave, $\delta$, is defined as follows:

$$\delta = \sqrt{\frac{2\eta_1}{\omega\rho}} \quad 5\text{-}5$$

where $\eta_l$ is the shear viscosity of the liquid and $\rho$ is the density of the liquid [118].

Substituting the properties of the 36° YX $LiTaO_3$ crystal into equation 5-4 we get the flow pattern as shown in Figure 5-1.

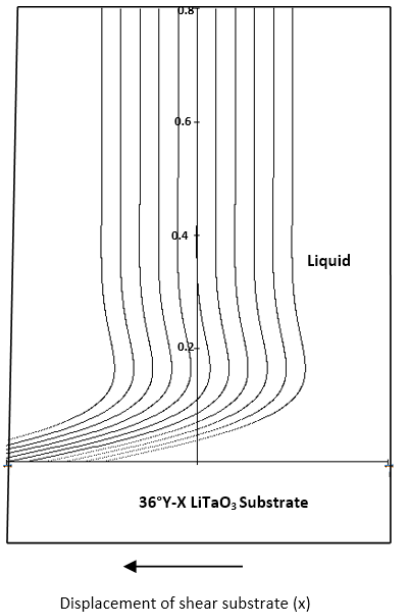


**Figure 5-1: Numerically calculated viscous fluid layer displacement for infinite volume of water, loaded on oscillating substrate modelled as 36° YX $LiTaO_3$. Vertical direction shows decay of the fluid displacement into the bulk fluid.**

Solving Equation 5-1 over a varying time domain, the behaviour of the fluid layer can be observed as shown in Figure 5-2.

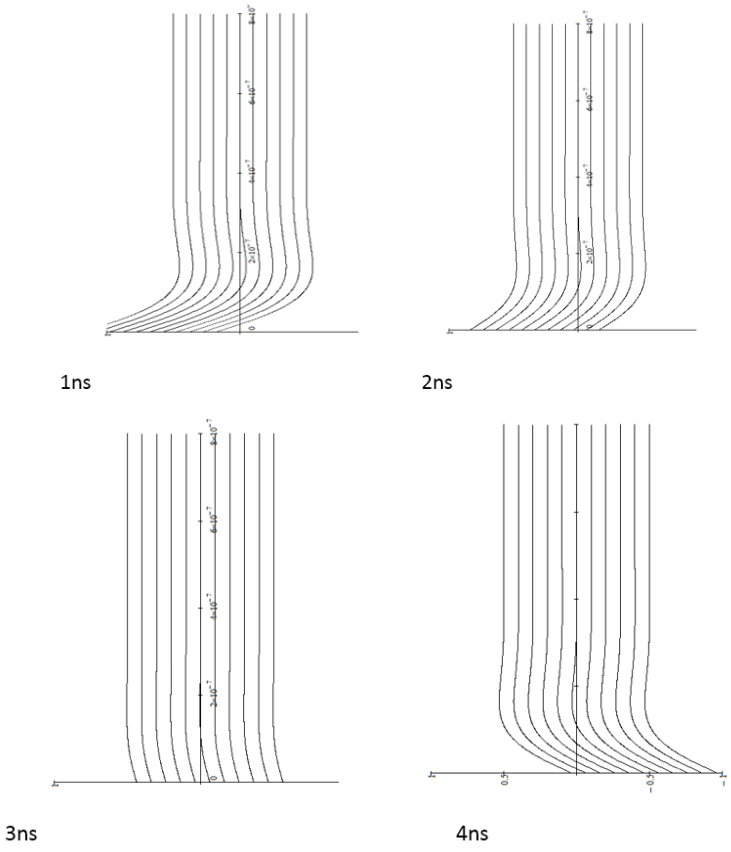


**Figure 5-2: Numerical calculation of evolving fluid displacement of viscous water loaded on 36° YX $LiTaO_3$ oscillating substrate at 150 MHz over 4 ns.**

For the 150 MHz devices, the wave has dissipated within 30 nm of the surface of the acoustic device, showing that no net flow will be generated from the oscillation of the fluid layer at the boundary.

### 5.1.2 Analytical Simulation of Shear Wave

Whilst numerical techniques are able to analyse simple liquid velocity, a more complex analysis of the coupled acoustic wave behaviour with the liquid oscillation is beyond the scope of these techniques. For analysis of the complex coupling between viscous fluid oscillation and pressure acoustics, a coupled field analysis using FEA analysis must be solved to determine the wave propagation behaviour. To date, no known coupled fluid acoustic analysis has been undertaken using the finite element method.

For this case we are required to solve the generalised Navier-Stokes equations for fluid oscillation and the complete acoustic wave propagation equations resulting from the pressure change in the fluid. By analysing the SH-SAW wave propagation, we can generalise the behaviour in a 2D dimension to a boundary oscillation problem. Boundary oscillation in this case is described as a Stoke Second Flow problem [116] which has modelled in FEA with a high degrees of accuracy [119].

#### *5.1.2.1 Computational Domain*

Comsol multi-physics software was chosen to model the coupled fluid acoustic simulation. Previously it has been shown to be able to accurately model stokes second flow problem [119]. Brunet et al. showed that Comsol could be used for analysing acoustic wave propagation demonstrating the attenuation of various acoustic wavelengths in a sessile droplet with correlation to experimental results [120].

In this study, the developed model was comprised of a 2D fluid domain with boundary layers. The viscous flow of the fluid was modelled with the associated acoustic wave propagation in the medium. The decay length of the wave was compared to numerical data for validation of the model. The pressure field was measured for various volumes of droplets and compared to experimental results.

#### *5.1.2.2 Theory*

The fluid is assumed as a compressible, viscous, Newtonian one using the Navier-Stokes and continuity equation in the Lagrange frame of reference, which can be given by:

$$\rho\left(\frac{\partial v_f}{\partial t}\right) + v_f \cdot \nabla v_f + \nabla P - 2\eta\nabla \cdot \mathrm{D} = 0 \quad 5\text{-}6$$

$$\nabla \cdot v_f = 0 \quad 5\text{-}7$$

Here, $v_f$, $P$, $\rho$ and $\eta$ denote the fluid velocity, pressure, density, and viscosity, respectively. $D$ is the rate of deformation tensor given by:

$$D = \frac{1}{2}\left(\nabla v_f + \left(\nabla v_f\right)^t\right) \quad 5\text{-}8$$

The acoustic field was modeled as a Lagrangian frame of reference using the acoustic pressure equation given below:

$$\frac{1}{\rho c^2} \cdot \frac{\partial^2 p_t}{\partial t^2} + \nabla \cdot -\frac{1}{\rho}(\nabla p_t) = Q \quad 5\text{-}9$$

Here, $\rho$, $c$, $p_t$, $t$ and $Q$ denote the fluid density, speed of sound, pressure, time, and Monopole source, respectively. $P_t$ is the pressure with respect to time given by the following:

$$p_t = p + p_b \quad 5\text{-}10$$

To couple the two models, the pressure field ($p$) was assumed as a share variable between the respective partial differential equations.

#### *5.1.2.3 Simulation Parameters*

A transient model was used in the simulation to characterise the wave and acoustic propagation within the droplet. The 2D FEA model was simulated for a total of 100 ns with a time step of 1 ns with varying oscillation velocities and frequencies. This section describes the finite element model for the simulation and the analysis of the structure as well as the model boundary conditions, acoustic and flow results.

Droplet of 0.5 mm in diameter (or 0.1 µl) was modelled with a wetting angle of 85° as the computation environment. Water was used at the fluid volume for all simulations. For the fluidic boundary, a slip condition was applied to the outer surface to model the fluid-air boundary. An excitation was applied to the base of the droplet to simulate the time-varying SH-SAW wave interfacial displacement. The acoustic boundary was defined as sound soft where the boundary pressure is zero, which is valid for a liquid-gas interface. The base of the droplet was modelled as a sound hard boundary to simulate the substrate. For selection of the mesh fluid elements, a general mesh size of 8 µm was chosen using a convergence analysis. For the boundary layer, with the oscillation of the fluid, equation 5-2 was used to calculate the decay length. A boundary layer was assumed with a 5 nm thickness, 100 layers thick and with an element growth of 1.2. The meshed droplet is shown in Figure 5-3 with an enlarged boundary layer shown in the right image.

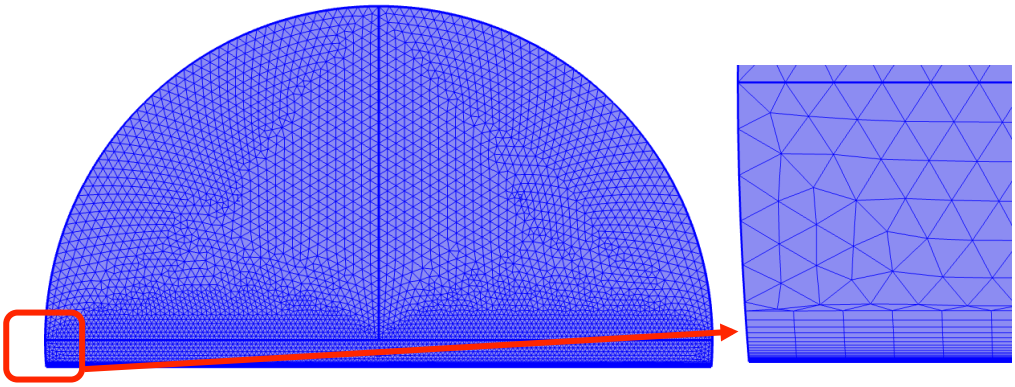

**Figure 5-3: (left) two dimensional (2-D) image of typical mesh used for simulation. Mesh is approx. 69,181 DOF. (Right) boundary layer refinement shown with 50 layers and 1.2 element growth, bottom seed layer 5 nm thick.**

#### *5.1.2.4 Excitation of Droplet*

For excitation of the droplet, a time varying oscillation was applied to the base of the droplet. From chapter 4, we know that the SH-SAW wave propagates in a sinusoidal time varying wave at the interface; therefore, the following equation was applied as a boundary condition at the base of the droplet:

$$U_x(t) = U_i \times sin(2\pi \times f \times t) \qquad 5\text{-}11$$

Where $U_x$ is the time varying velocity of the substrate and $U_i$ is the velocity obtained. Whilst $U_i$ may be numerically derived by equation 4-14, FEA simulated results for the substrate velocity were used as discussed in Chapter 4.

Due to the simplification of the model to 2D in order to reduce computation time and aid analysis of the pressure behaviour, the boundary condition must account for this simplification. As the SH-SAW wave will interact with the boundary of the droplet at multiple positions along the propagation length (as shown in Figure 5-4), the principle of superposition can be used to determine the summation of the pressure.

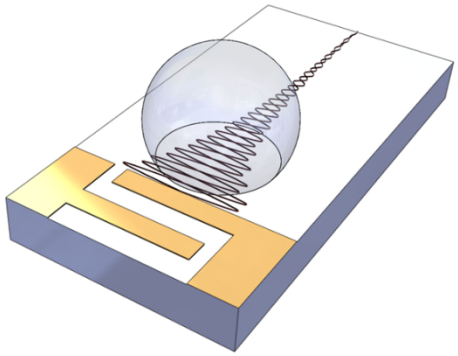

**Figure 5-4: Schematic of wave interaction with droplet, superposition principle can be used to idealise interaction to one plane.**

For the wave velocity, the boundary length of the droplet was calculated for each size and divided by the wavelength to calculate the multiplication factor for the superposition calculation. Using this method, a relative approximation can be made for the overall pressure and streaming velocity in the droplet.

### 5.1.3 Verification of the model

To verify the accuracy of the model, experimental results of the flow oscillation and acoustic wave propagation were compared.

#### *5.1.3.1 Fluid Oscillation Verification*

FEA simulation with a variance of the base oscillation frequency was undertaken to analyse the decay length of fluid, where the x component of the velocity of the fluid drag due the oscillation decays to zero. The base oscillation was simulated for 10 ns at 1, 5, 10, 50, 100, 500, 1000 MHz and 10 ns with the decay length measured at the peak of the first oscillation. This decay length was compared to the numerical calculation using Equation 5-5, and the results are shown in Figure 5-5.

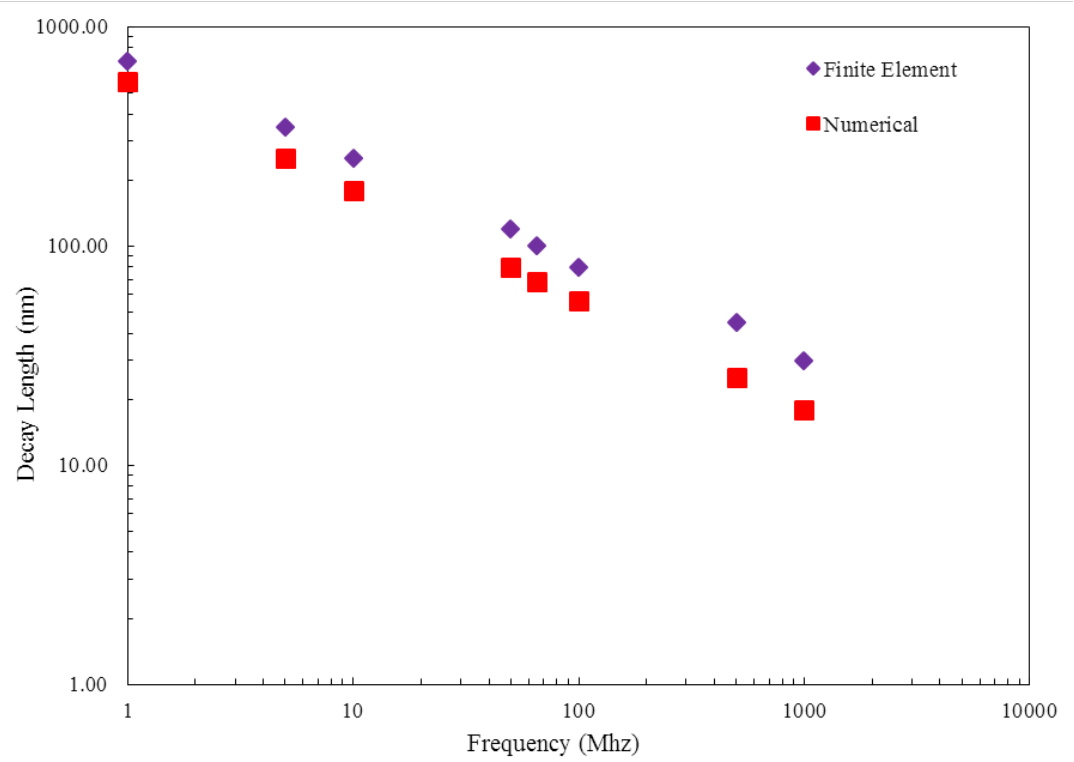


**Figure 5-5: Decay length of wave vertically into fluid against SAW frequency, analytical solution is compared to FEA solution.**

Analysing the data, it can be observed that as the frequency increases, the decay length decreases as a root squared quadratic function. Comparisons of the numerical and FEA simulated data reveal a good correlation with the FEA data showing the same trend but the FEA results are constantly higher at about 20%. This difference may be accounted for by the mesh density used. These results correlate with similar data presented by Sin et al. who showed results from the Comsol simulation matched with theoretical Stoke second flow derivations [119]. The results confirm that the model can accurately predict the fluid flow at the boundary layer.

### *5.1.3.2 Acoustic Wave Propagation*

The acoustic wave propagation was simulated for a droplet with a given size of 2 µl actuated by a 65 MHz SH-SAW for 0.01 ms, the plot of the pressure acoustic wave propagation over time is shown in Figure 5-6.

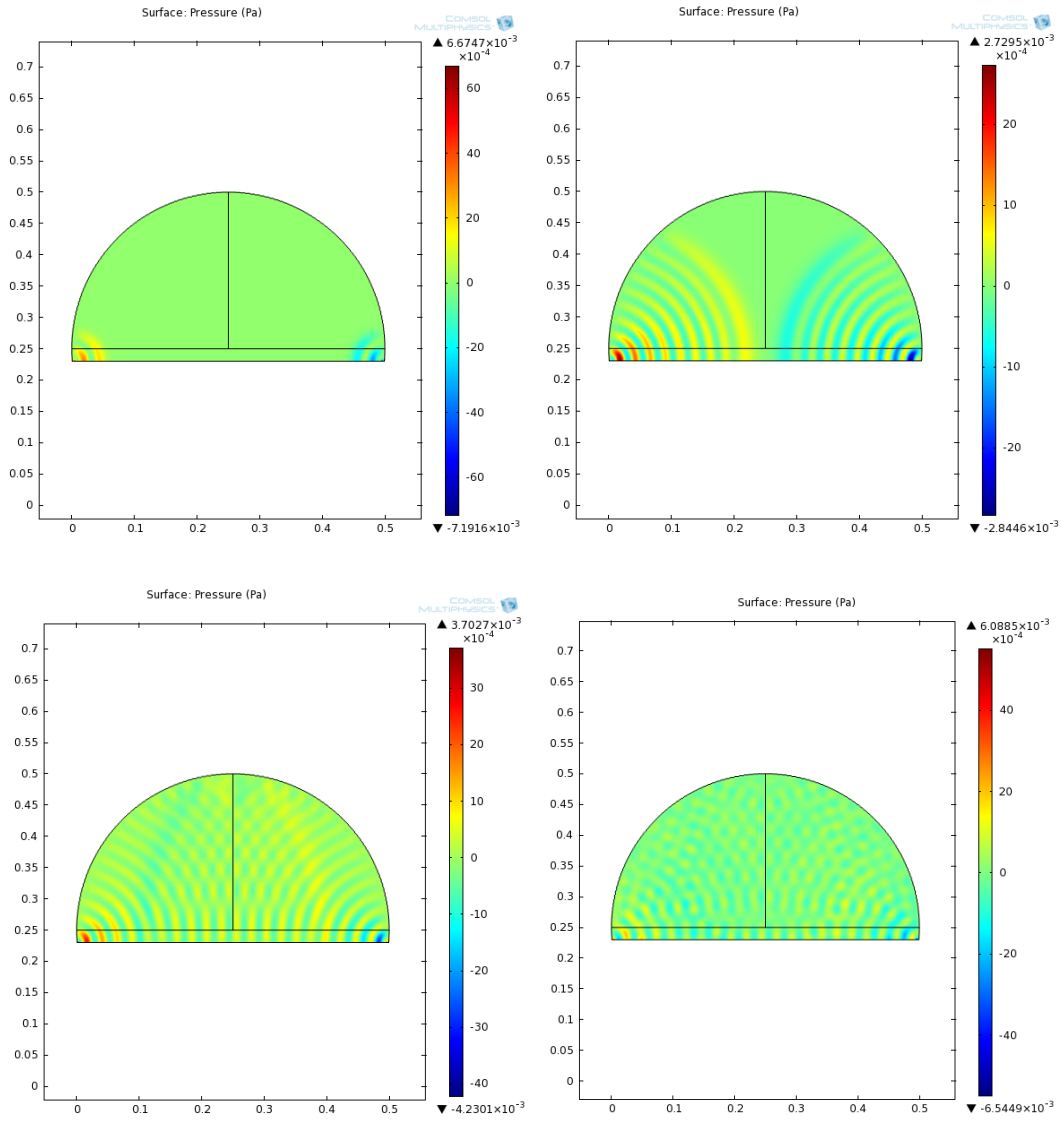


**Figure 5-6: (a) acoustic pressure wave propagation within 0.2 µl droplet at 40 ns (b) acoustic pressure wave propagation within 0.2 µl droplet at 160 ns (c) acoustic pressure wave propagation within 0.2 µl droplet at 260 ns (d) acoustic pressure wave propagation within 0.2 µl droplet at 0.01 ms.**

At 40 ns, the start of the acoustic wave propagation can be observed with the wavelength determined by the attenuation of the base excitation frequency with the water. The pressure wave is being created by compression of the liquid due to the viscous drag resulting in a time varying pressure at the liquid to air boundary. At 160 ns, we can see that the wave has propagated almost to the boundary, and at 260 ns, we can see the refection of the wave pattern from the boundary. At 0.01 ms, we observe that the wave has reached a steady state where no more changes are occurring.

With SAW streaming typically taking the order of micro seconds to develop, which is beyond the scope of this model, an approximation was made using the maximum pressure from the FEA simulation and Bernoulli equation to estimate a steady state flow velocity as an approximation. The pressure was simulated at varying droplet volumes from 2 µl to

15 µl and the final pressure was calculated and compared with experimental values. The results are shown in Figure 5-7.

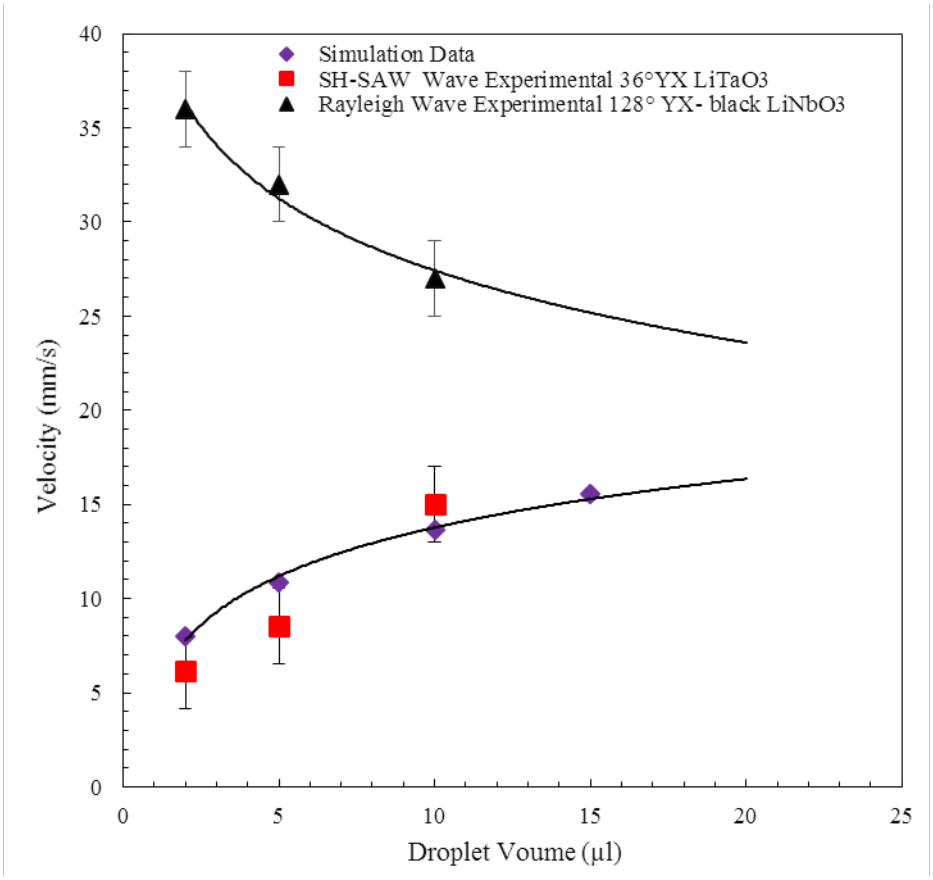


**Figure 5-7: Streaming velocity in increasing droplet sizes vs. steaming velocity at 15 dBm. FEA simulated results are shown compared to experimental data for Rayleigh and Shear waves.**

The simulated data of the streaming velocity was seen to vary from 8 to 15 mm/s with the velocity increasing with the droplet size. This correlates well to the experimental data which shows the same trend of flow increasing with droplet size and the magnitude of flow matches within the error of the experimental data. Whereas for the simulated Rayleigh wave data shown in Figure 5-7, we can see that with increasing droplet volume, the velocity of streaming decreases which has the opposite trend observed for the SH-SAW.

### 5.1.4 Simulation of SH-SAW Steaming

Numerical simulation of acoustic streaming for Rayleigh wave propagation has been well documented by pervious researchers [88], [121]–[128]. No investigation of SH-SAW streaming has been undertaken to date.

The governing equations for acoustic streaming were derived by Nyborg and are defined as follows [129]:

$$-F \equiv \rho_0 \langle (u_1 \cdot \nabla) u_1 + u_1 (\nabla \cdot u_1) \rangle \quad 5\text{-}12$$

$$-\mu \nabla \times \nabla \times u_2 = \mu \nabla^2 u_2 = \nabla p_2 - F \quad 5\text{-}13$$

In the above equations, $\mu$ is dynamic shear viscosity coefficient, $\rho_0$ is the constant equilibrium density, $u_1$ is the oscillatory particle velocity, $u_2$ is the acoustic streaming velocity, $p_2$ is the steady state "dc" pressure, $F$ is the effective force term, and the angular brackets denote the time averaging over a number of sonic cycles [130].

For a shear wave propagating in the $y$ direction the displacement is mainly in the $x$ direction defined by Eqn. 5-4:

$$U_x(y,t) = Ae^{\frac{-y}{\delta}} \cos\left(\frac{y}{\delta}\right) e^{i\omega t} \quad 5\text{-}14$$

Where $U_x$ is the component of displacement, $A$ is the displacement amplitude. Letting particle displacement of Eqn. 5-14 be replaced by particle velocity using $u = dv/dt$ we get the following equation:

$$u_x = A\omega \cos\left(\frac{y}{\delta}\right) e^{\frac{-y}{\delta}} e^{\omega t i} \cdot i \quad 5\text{-}15$$

Substituting Eqn. into 5-15 into Eqn. 5-12 we can obtain an expression for force:

$$F = \frac{A^2 \omega^2 e^{\frac{-2y}{\delta}} (\rho_0 + 1)(\cos(\frac{2y}{\delta} + 1)}{2} \quad 5\text{-}16$$

We can assume at maximum fluid displacement at $y = 0$. The force was calculated using the parameters in Table 5-1.

**Table 5-1: Parameters for Acoustic Streaming Force**

| Crystal Orientation | Displacement Amplitude (Å) | Frequency (MHz) | SAW Streaming Force ($N/m^3$) |
|---|---|---|---|
| 36° YX $LiTaO_3$ | 1 | 100 | 394 |

The amplitude of the SH-SAW was derived from the FEA data in Chapter 4 for a 100 MHz device at 7V (0.126 W).

To simulate the fluid flow within a droplet Comsol was again used with a 2D domain for the fluid simulations.

#### *5.1.4.1 Fluid Flow Simulations*

A steady state Navier Stokes compressible model was used to simulate the fluid propagation. The equation can be re-written in the following terms to allow for the application of the force vector:

$$\rho\left(\frac{\partial v_f}{\partial t}\right) + \rho(v_f \cdot \nabla)v_f = \nabla\left[-\rho l + \mu(\nabla v_f \cdot (\nabla v_f)^T - \frac{2}{3}\mu(\nabla \cdot v_f)l\right] + \boldsymbol{F} \qquad 5\text{-}17$$

where $^T$ is the viscous stress tensor and $F$ is the force in N/m$^3$.

A droplet of 3 mm in diameter (or 5 µl) was modelled with a wetting angle of 85° as the computation environment. The IDT's were assumed to have an aperture wider than the droplet so as no second order effects of wave loss across the droplet is considered. Water was used at the fluid volume for all simulations, and the force was applied as a volume force to the boundary areas as indicated in Figure 5-8. A mesh of 2660 triangular elements was used with 4200 degrees of freedom.

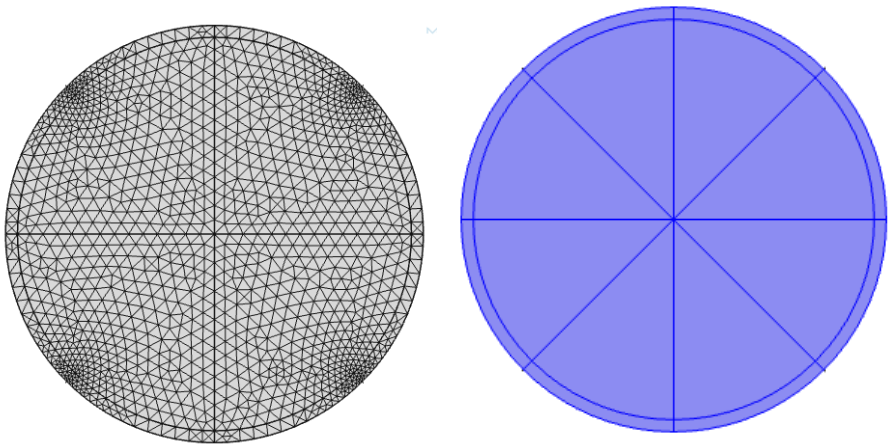

**Figure 5-8: (left) Mesh for Fluid Flow Simulation, 4200 Degrees of Freedom, 5 µl droplet. (right) area for force application at boundary.**

Due to limitation of a 2D model a dimensionless analysis was undertaken to predict if a boundary flow pressure wave could accurately simulate the observed flow behaviour. For the acoustic wave force an area was defined at the boundary as shown in Figure 5-8, additionally this was divided into eight sectors for a vectors force definition.

(a) -8dBm

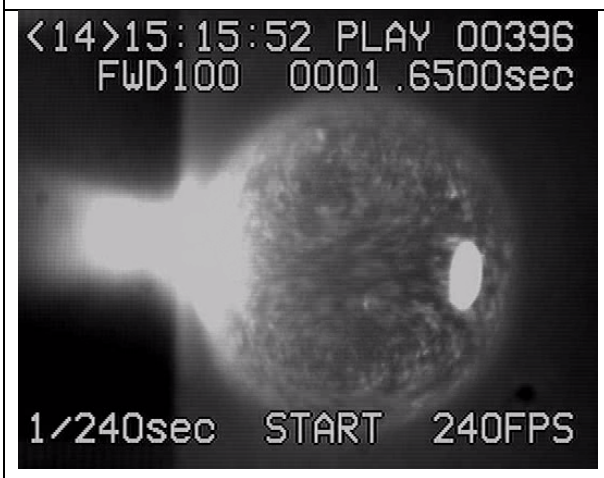


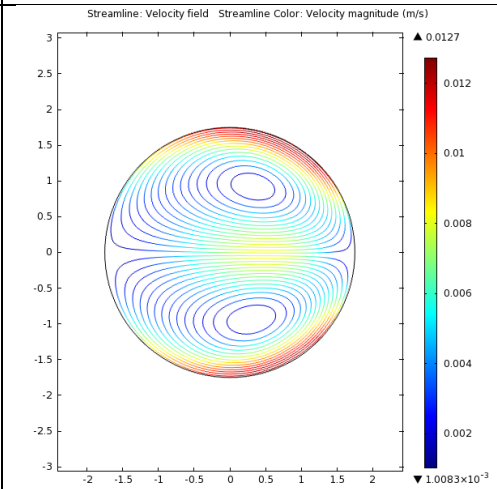


(b) 13 dBm


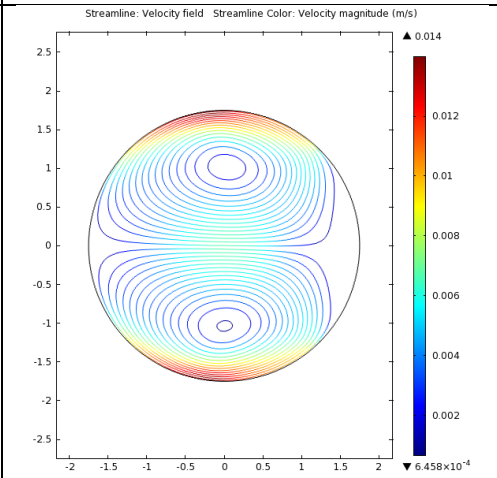


(c) 18 dBm


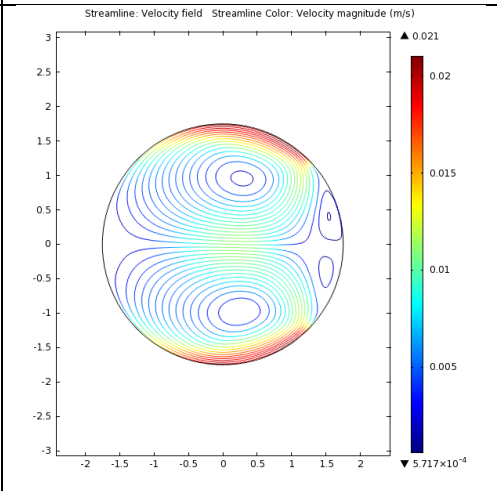


**Figure 5-9: (left) Experimental streaming profile for 5µl droplet, SAW direction left to right. (right) CFD simulated droplet flow with reference to IDT position.**

From the pressure wave distribution, we can assume the compression of the fluid at the boundary to act as a net force in the acoustic wave propagation vector coupled with the wave velocity.

Whilst the force amplitude can be calculated using FEA, as shown in Figure 4-17, the computation time to simulate the IDT structure and piezoelectric substrate size is substantial. For the initial dimensional analysis the value of $A$ in Eqn. 5-16 was evaluated empirically with experimental results using the method outlined by Alghane et al. [131]. Powers, and hence amplitude, were increased from -8dBm to 23dBm and the flow patterns compared against experimental results. Figure 5-9 shows that at increasing powers the streaming counter flow areas are reduced in overall size and a stagnant pressure zone appears behind the main streaming area.

Comparing to experimental result we can see good correlation of the 2D flow patterns with increasing powers showing a stagnant pressure zone at the opposite end to the SAW propagation. Noted in the simulated results is the high velocity at the boundary of the droplet and the centre flow region.

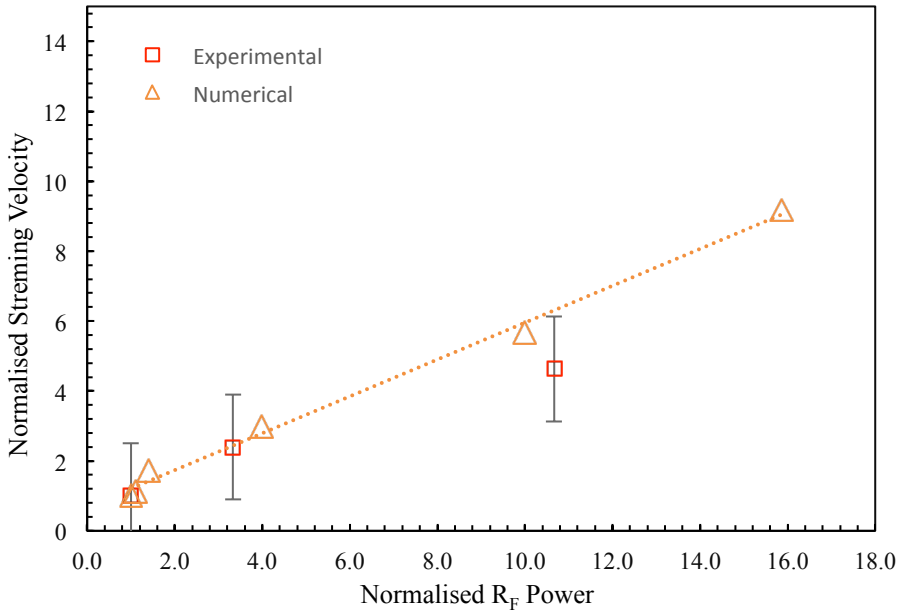


**Figure 5-10: Flow normalized streaming velocity as a function of normalised RF power for numerical simulation and experimental data using a 5 µl droplet using a 36° YX $LiTaO_3$.**

A dimensionless analysis of the streaming velocity from simulation was compared to experimental data to determine the validly of the derived SAW force equation (Eqn. 5-16). The experimental and simulated data showed good correlation with some deviation

at higher powers outside of the calculated error bars. This demonstrates the validly of the derived SH-SAW calculation and enables the possibility of calculating the SH-SAW streaming velocity given the substrate displacement amplitude.

Figure 5-11 shows the streaming velocities through a cross section of a 5 µl droplet for powers varying from 3W to 50 W. The highest velocity flow can be observed at the droplet boundary and central position of the reverse streaming; this correlates with observed flow patterns from experimental data using a high-speed camera. The flow velocity was also not observed to be uniform for increasing powers with the centre velocity showing large increases for the increase in the streaming velocities indicating a non-linear behaviour.

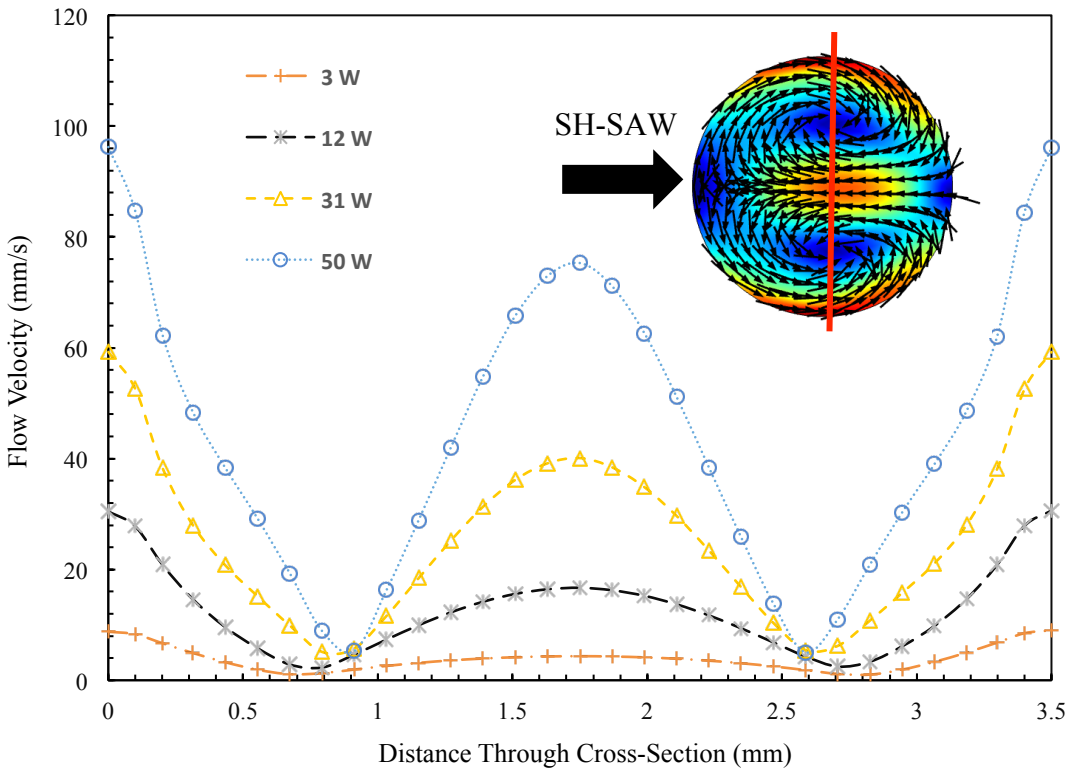


**Figure 5-11: Streaming velocity distributions across the centre of a 5 µl droplet at Rf powers from 3 W – 50 W. These curves represent numerical results along with y-axis as depicted by the red line through the droplet centre.**

This initial analysis shows good correlation with experimental results for a simple case of the droplet inline with the IDT. For a more complex case the exponential energy loss outside of the IDT must be considered to calculate the streaming profiles at offset distances. This analysis is beyond the scope of this thesis and should be undertaken with 3D CFD analysis.

## 5.2 Experimental Results on Shear Wave Microfluidics

This section presents the results obtained from the experimental work of the 36º YX $LiTaO_3$ crystal and the ZnO/Si SAW devices using the methods outlined in Chapter 3. Experimental characterisation was undertaken of various microfluidic function with the SH-SAW wave and a comparison is made to the Rayleigh wave leaky SAW.

### 5.2.1 Device Characterisation

Characterisation of the velocity of the wave propagate on the 36º YX $LiTaO_3$ was undertaken using a network analyser to measure the insertion loss as outlined in Chapter 3. Two fabricated SAW devices were characterised with a 16 μm and 25 μm periodicity. Figure **5-12** shows the insertion loss of the reflection spectrum of the 16 μm SH-SAW device. The sharp peak at 41.17 MHz (corresponding to a phase velocity of 4117 m/s) was assigned to the fundamental SH-SAW wave based on microfluidic observation [132]. The small peak at 31.20 MHz (corresponding to a phase velocity of 3120 m/s) as well as smaller peaks at 26.63 and 33.67 MHz were identified as the Rayleigh based SAWs. Comparing to literature values the peak with highest attenuation correlates well the Rayleigh SAW wave (3116 m/s) [133]. Higher harmonic peaks of both the Rayleigh and SH-SAWs were identified as shown in Figure **5-12**. The insertion loss ($S_{11}$) of the second SAW device was measured and two peaks were observed at 44.5 MHz (3000 m/s) and 64.5 MHz (4212 m/s) as shown in Figure 5-13. These values compare well to literature values obtained for the two wave velocities.

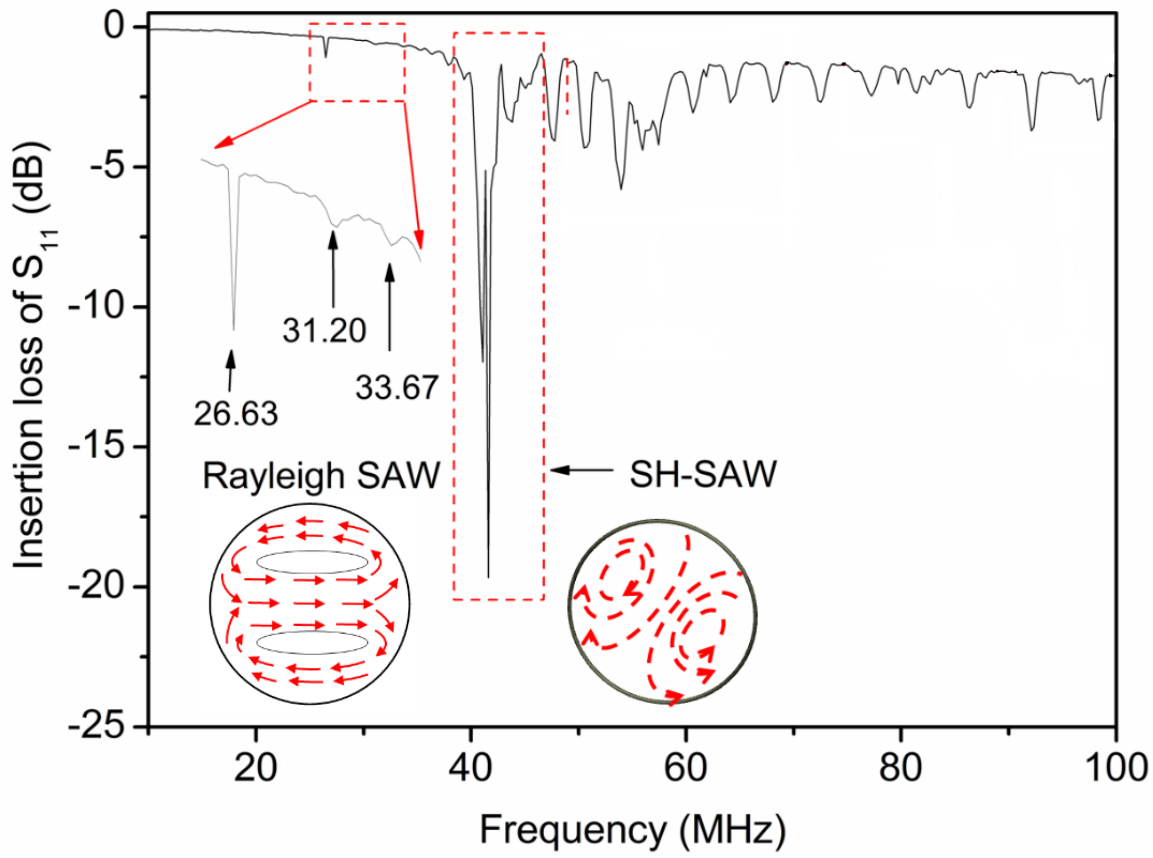


**Figure 5-12: Reflection signal $S_{11}$ of 36° Y-cut $LiTaO_3$ SH-SAW device with 25 µm periodicity, including the Rayleigh SAW, SH-SAW. The insets are the illustrations of the flow patterns for SH-SAW and Rayleigh SAW.**

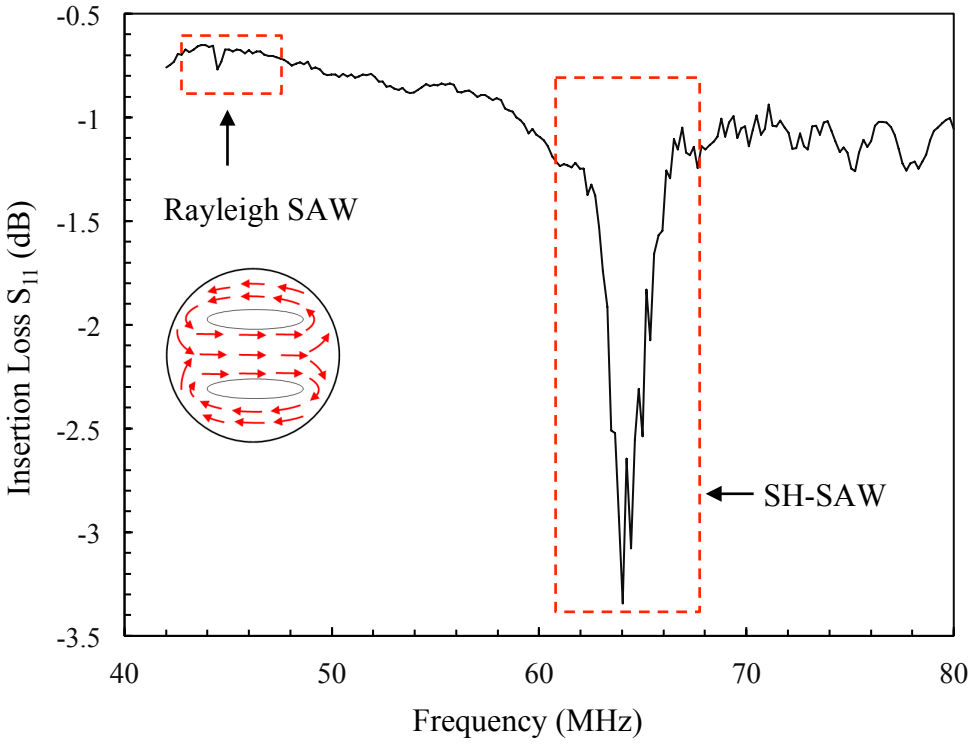


**Figure 5-13: Reflection signal $S_{11}$ of 36° Y-cut $LiTaO_3$ SH-SAW device with 16 µm periodicity, including the Rayleigh SAW, SH-SAW. The insets are the illustrations of the flow patterns for SH-SAW and Rayleigh SAW.**

For the 25 μm periodicity device a second order resonance mode can be observed for the Rayleigh wave between 45 MHz – 65 MHz and the third order observable at 90 MHz – 100 MHz Figure 5-13.

### 5.2.2 Shear Wave Streaming

Rayleigh mode devices are known to support liquid micro-mixing and streaming with the longitudinal waves propagating into the droplet at the Rayleigh angle and the damping of the fluid resulting in liquid streaming [134]–[137].

Although Rayleigh wave mode streaming has been well characterised no analysis of SH-SAW streaming has been undertaken to date. The following section will detail the experimental analysis of the SH-SAW streaming phenomenon.

The experimental set-up used for the fluid experiments was described in Chapter 3 section 3.2. The $36^{o}$ Y-cut $LiTaO_3$ substrate was used with the IDT's having a periodicity of 16 μm, with the wave being launched in the X propagation direction. For the initial streaming experiments the SAWs were excited using a power below 10 dBm to minimise any second order effects from high velocity streaming. For the fluidic experiments, water droplets of up to 10 μl were micro-pipetted onto the surface at 1 mm from the IDT aperture. A solution of distilled water and homogeneous polystyrene particles with 6 μm mean diameter were used for flow visualisation and velocity calculation experiments. For the damping experiments, droplets were applied to the surface at varying displacements from the IDT denoted by $\Delta_x$ in Figure 5-12. For spatial location experiments, the droplets were positioned at locations denoted by $\Delta_y$ from the IDT of up to 30 mm from the central axis and the steaming velocity was observed (Figure 5-14).

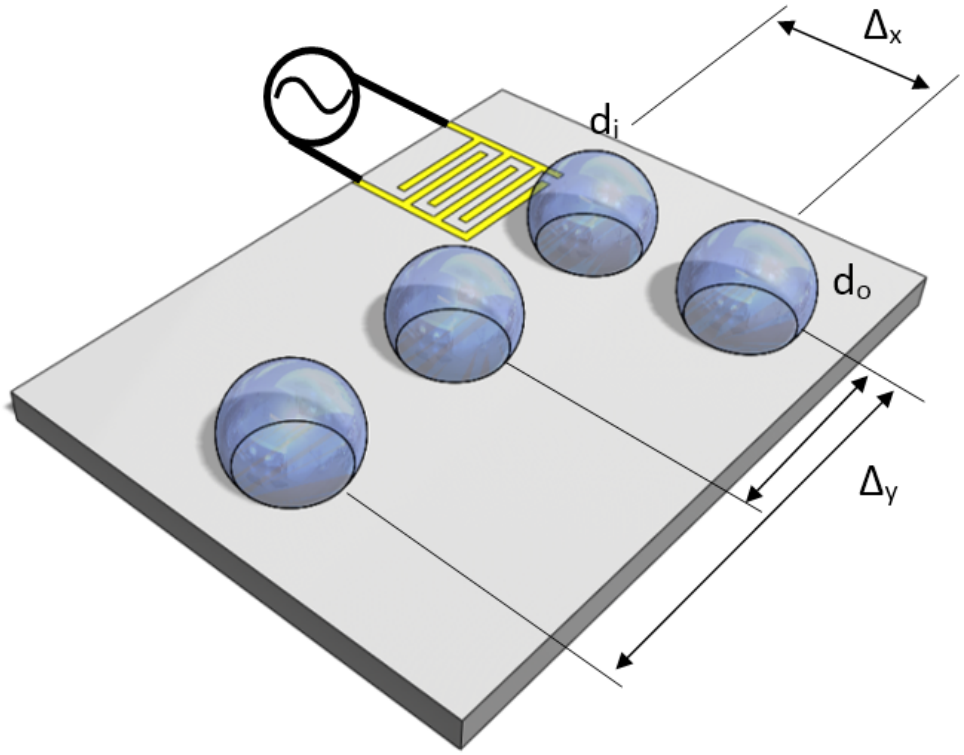


**Figure 5-14: Illustration of droplet positioning for microfluidic experiments. Multiple droplets are shown to indicate various spatial locations.**

Initially, the first resonant frequency (44.5 MHz) streaming was observed with the characteristic Rayleigh wave pattern using a 5 µl droplet. This flow showed fluid streaming at the centre axis of the droplet in the wave propagation direction with two counter butterfly shape flows. This is depicted schematically in Figure **5-12**.

Exciting the SH-SAW at a frequency of 66 MHz (4212 m/s), resulted in the streaming patterns shown in Figure 5-15(a). It can be observed that shear wave / liquid interaction formed two vortexes in a counter rotation that were aligned in the droplet along the SAW propagation axis. The flow was observed to form initially near the droplet centre, with a steady butterfly flow dominating after ~ 0.5 s. The SH-SAW streaming was observed with the dominant flow largely in the direction opposing the SAW wave propagation as shown in Figure 5-15(a). Streaming patterns were seen to depend upon the asymmetrical placement of the droplet in relation to the IDT aperture, resulting in azimuthal changes of the streaming up to 90° as shown in Figure 5-15 (b).

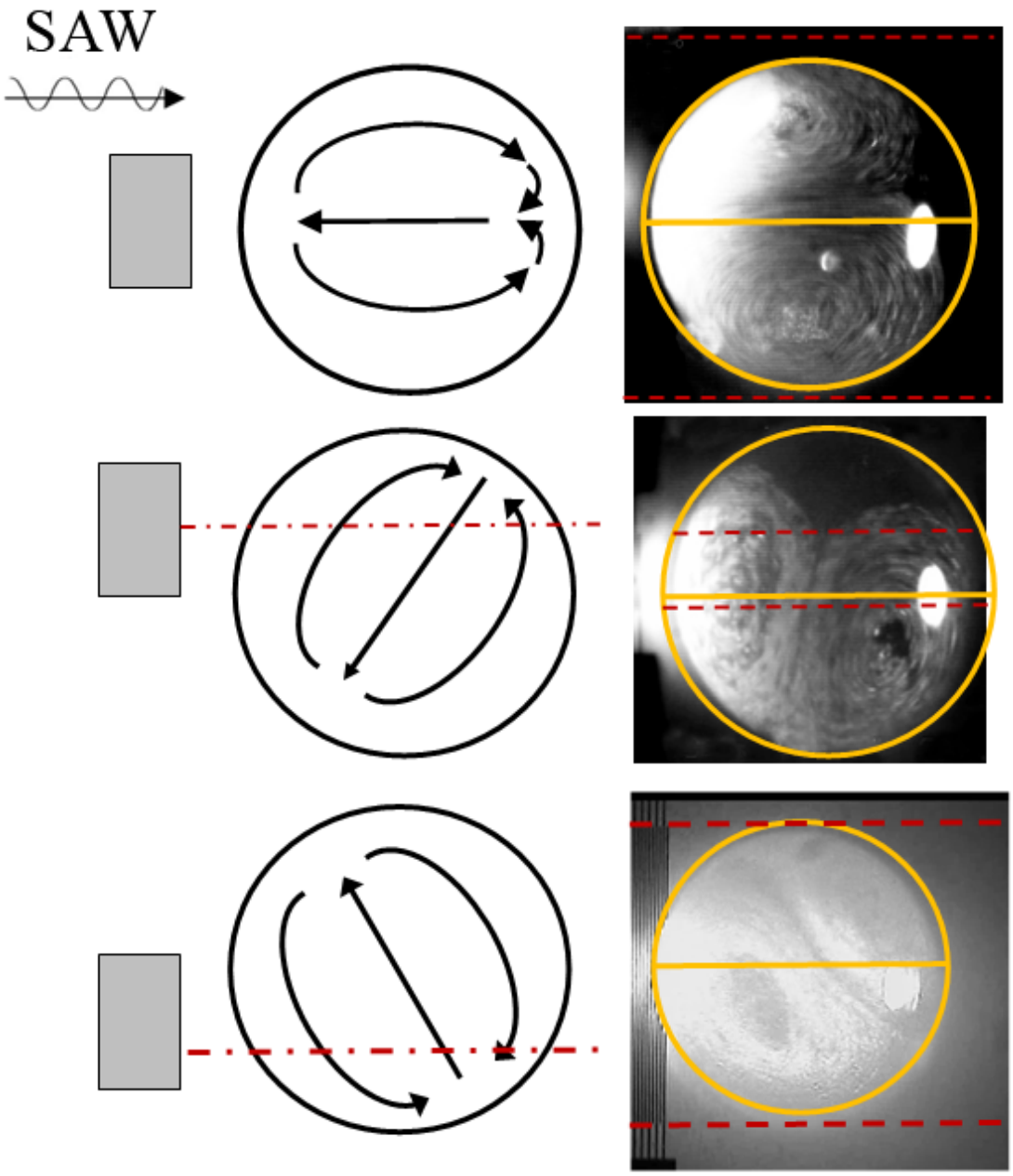


**Figure 5-15: (a) Streaming patterns in 2.5 µl droplet at ~3 position of IDT with relation to droplet and flow directional vectors. Red dashed lines indicated aperture of IDT. (b) Flow azimuthal changes due to position of droplet with relation to IDT (i) droplet positioned below IDT showing approximately 80° rotation to initial flow (ii) droplet positioned above IDT showing 45° rotation to initial flow.**

With a IDT width of 5 mm the spatial location of the droplet was still observed to results in azimuth changes of the droplet though only a 45° rotation is noted (Figure 5-15 (c)). These results indicated that the energy balance for the SH-SAW wave is position dependant and any imbalance will result in a change in streaming angle.

The streaming velocity was characterised next using the high speed camera to quantify velocity. Analysis of the velocity data shows that the velocity of the streaming, induced by the shear wave component in the 36° Y-X $LiTaO_3$ substrate, is of a similar magnitude to that observed on standard Rayleigh wave substrates (128° Y-cut $LiNbO_3$), with a similar droplet size and RF source power [131]. Figure 5-16 shows that the streaming velocity proportionally increases from 5 mm/s at 2 µl to 10 mm/s as the droplet size increases up to 10 µl. Also shown in Figure 5-16 is the velocity of the Rayleigh wave (44.5 MHz) streaming induced on the same 36° Y-X $LiTaO_3$ substrate. This shows a maximum velocity of 2 mm/s for a droplet size of 2 µl, which is a much lower value due to the minimal return loss of the Rayleigh wave measured on the 36° Y-X $LiTaO_3$ substrate.

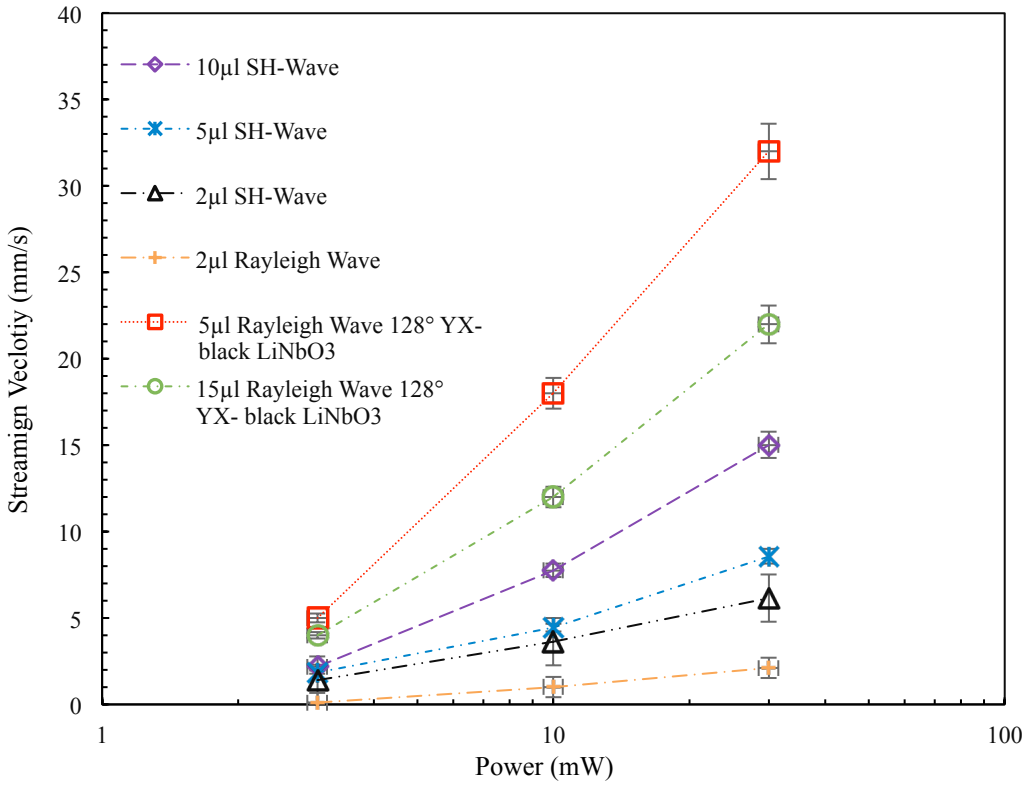


**Figure 5-16: Droplet size vs. mixing velocity for Shear and Rayleigh wave on 36°Y-X $LiTaO_3$. Comparative data is shown for Rayleigh wave on 128° YX- black $LiNbO_3$. All data presented is assumed to be on 36°Y-X $LiTaO_3$ unless otherwise indicated.**

Comparing the SH-SAW steaming to the Rayleigh wave streaming observed on the 128°YX- black $LiNbO_3$, it is observed that the streaming velocity of the Rayleigh wave decreases with droplet volume. The SH-SAW streaming is seen to have increasing velocity with droplet size, with the highest obtained for the 10 µl droplet. Comparing the mechanical coupling coefficient of the SH-SAW wave on the 36°Y-X $LiTaO_3$ (4.7) with

the Rayleigh wave coupling coefficient on the 128°YX- black $LiNbO_3$ (0.23), we can see a weak attenuation of the SH-SAW wave as shown by modelling.

The observed SH-SAW streaming on the 36° Y-X $LiTaO_3$ is indeed unexpected due to the minimal attenuation of the fluid layer. Numerical modelling in Chapter 4 has shown a weak vertically polarised component of the wave velocity and it is therefore unlikely that this alone explains the observed streaming velocities and opposing patterns observed. As previously shown with numerical modelling in this chapter the entrapment of a thin visco-elastic fluid layer which has a decay length of $\delta = \sqrt{((2\eta)/\omega\rho)}$ , where $\eta$ is the shear viscosity of the liquid and $\rho$ is the density of the liquid and $\omega$ is the angular frequency [118], [138], [139]. Oscillation of this layer will result in small pressure differences due to the compression wave formed at the droplet boundary. The oscillation of this boundary pressure will radiate as acoustic waves with a vertical component and a longitudinal component due to the SAW propagation direction. This will cause a net flow around the boundary of the droplet resulting in the reverse streaming observed as the fluid is dragged along the boundary of the droplet.

Further investigation of this phenomenon was undertaken to examine the damping within the droplets. It is already known that the SH-SAW causes minimal attenuation in comparison to the Rayleigh wave, although some attenuation has been shown to exist due to both in-plane, normal and parallel surface components [140]. For the SH-SAW, and therefore the boundary layer oscillation to be responsible for the streaming, minimal damping would be expected as compared to the Rayleigh wave. Droplets of 2 µl with fixed distances ($d_0$ of 10 mm and $d_i$ of 1 mm) from the IDT's were placed on the substrate (see Figure 5-14), firstly separately and then at the same time, and the maximum streaming velocities in the droplets was measured for all conditions. Large energy losses of approximately 70% were observed in droplet $d_0$ when droplet $d_i$ was present and a range of RF powers were applied using the Rayleigh wave component at 44.5 MHz (Figure 5-17). For the SH-SAW component at 66 MHz, the experiment was repeated with a 30% reduction in velocity being observed in droplet $d_0$, when $d_i$ was present with a power up to 5 dBm. No apparent velocity reduction was observed with powers above 10 dBm. These results clearly indicate that a damping effect exists with the SH-SAW component, although it is significantly smaller than the Rayleigh wave component, in line with the expected behaviour for the boundary layer oscillation theory. This results leads to the interesting possibility of a single IDT being used as a multi-drop mixing system resulting in more cost effective mixing systems.

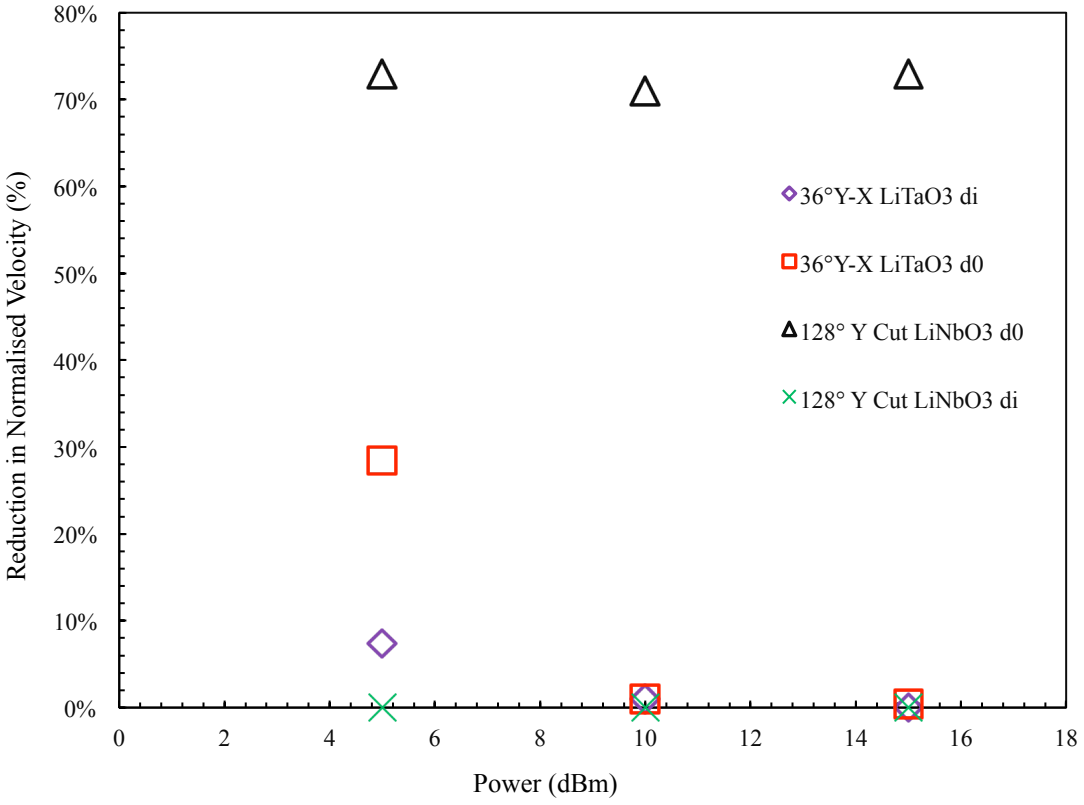


**Figure 5-17: Reduction in velocity for droplets placed in series on 36°Y-X $LiTaO_3$ and 128° YX- black $LiNbO_3$ with SH-SAW and Rayleigh wave respectively. Droplets of 2 µl were placed at 1mm ($d_i$) and 10mm (do) from IDT.**

Numerical modelling in Chapter 4 showed that at a spatial distance from the IDT, the tangential attenuation losses followed an exponential function (Figure 4-21). To validate the numerical model and identify if fluid function can be realised at a spatial distance from the IDT, droplets were placed at varying distances and the velocity was characterised. Droplets of 5 µl were placed at 1 mm in the $\Delta_x$ direction from the IDT and at varying positions of 5 mm – 25 mm in the $\Delta_y$ direction. Using a $P_{IDT}$ of 1 W, the SH-SAW wave was excited on the 36°Y-X $LiTaO_3$ substrate, the Rayleigh wave was also excited on the 128° YX $LiNbO_3$. For the SH-SAW wave the velocity was seen to drop from 100 mm/s to 1mm/s at 42 mm from the IDT. For the Rayleigh wave the velocity changed from 60 mm/s to around 1 mm/s at 42 mm from the IDT. These results are shown in Figure 5-18.

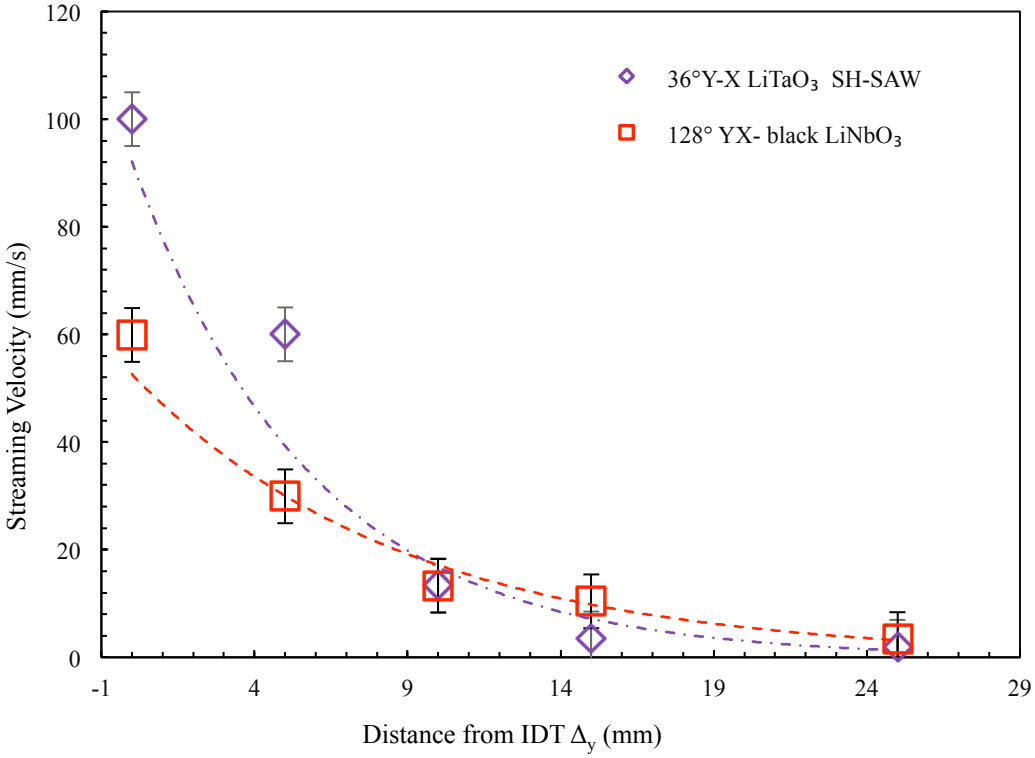


**Figure 5-18. Mixing velocity vs. distance $\Delta_y$ from IDT for 5µl droplet at $P_{IDT}$ = 1 W. Streaming velocity is shown for 36°Y-X $LiTaO_3$ and 128° YX- black $LiNbO_3$ with SH-SAW and Rayleigh wave respectively. Exponential trend-lines are mapped to data.**

Fitting a trend line to the data, we can see the velocity reduction fits an exponential function for both the SH-SAW and Rayleigh wave with both showing the same trend. This data correlates well with numerical simulation which showed that the amplitude of the SH-SAW wave decays exponentially outside of the active IDT area. For realising microfluidic functions, it is interesting to note that mixing velocity can be determined accurately from the IDT position enabling multiple streaming velocities for a single substrate. Observing the flow patterns, it was apparent that the streaming vectors changed with increasing distances from the IDT's. For the Rayleigh wave devices, the flow varied as a rotational vector which correlates well with the wave propagation for a point source. At 10 mm from the IDT, the flow was approximately at a 45° angle with the flow at 25 mm at approximately 90° (Figure 5-19). For the SH-SAW wave, the flow was seen to change with location to the IDT with the flow rotating through 90° at 5 mm from the IDT and an angular rotation at 10 mm and again a 90° rotation at 25 mm. As previously observed, the flow was in the reverse direction to the Rayleigh wave streaming.

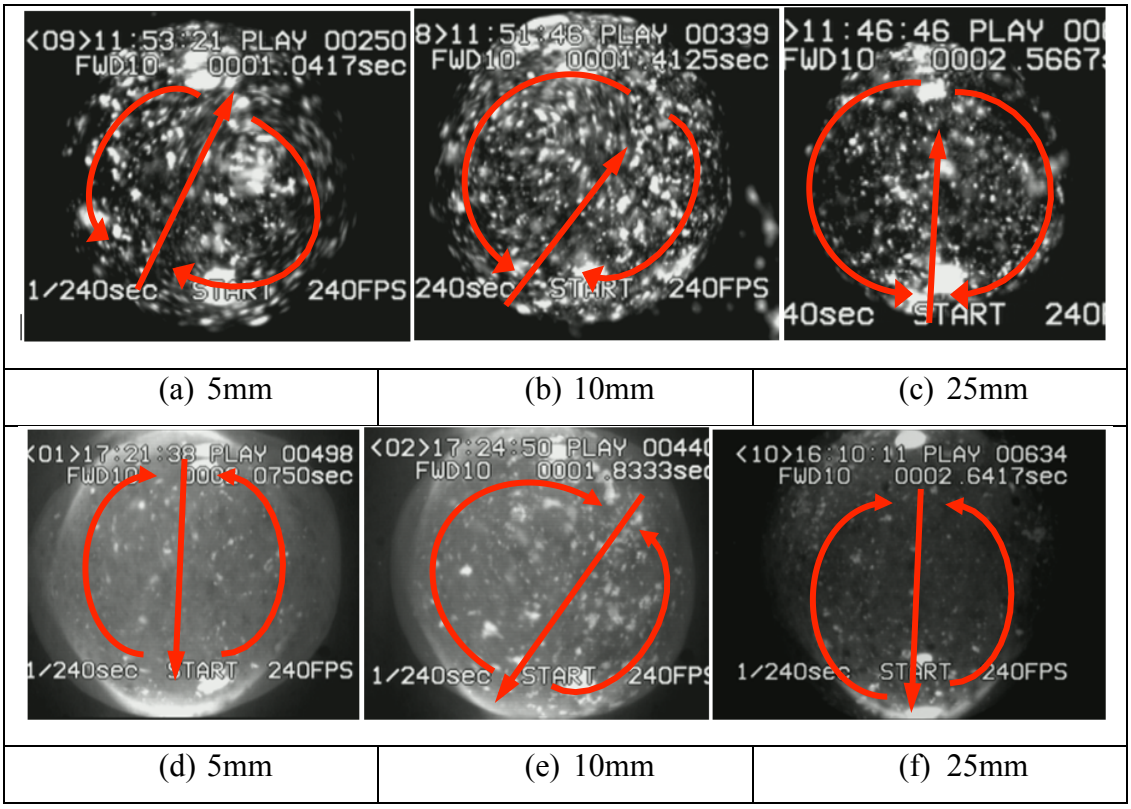


**Figure 5-19: (a-c) Rayleigh wave steaming patterns on 128° YX- black $LiNbO_3$ at various positions from the IDT. (d-f) SH-SAW streaming on 36°Y-X $LiTaO_3$ at various positions from the IDT with a 2.5mm aperture.**

### 5.2.3 Effects of Droplet Size and Position on SH-SAW Streaming

With a preliminary analysis of droplet position to IDT investigated, a more comprehensive study was undertaken using droplets with starch solution, to analyse particle concentration and flow patterns as a function of droplet size and positions.

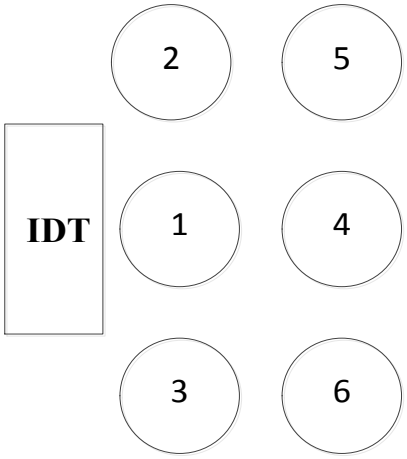


**Figure 5-20: Location of droplet with reference to IDT structure.**

Droplets with various volumes were put into varying spatial positions relative to the IDT's as shown in Figure 5-21 - Figure 5-35, the detailed streaming patterns as functions of RF powers were recorded using the high speed video camera. The SAW frequency used was 66.3 MHz with an IDT aperture of 1 mm.

For position 1, 5 µl droplets were excited with SH-SAW at powers from 0 to 7dBm, the flow was seen to start near the centre of the droplet towards the IDT side, Figure 5-21 - Figure 5-22. At low powers, the flow was observed with strong outer vector and with a centre flow in the propagation of the SAW wave. For these devises, the IDT was approximately half the width of the droplet diameter. With a narrow IDT, it is expected that the liquid in the centre attenuated by the shear wave will compress against the static fluid due to the difference in SAW amplitude, and this effect will lead to different flow patterns which are shown in Figure 5-15. With the increase in power from 4 dBm to 7 dBm, the flow was seen to form two vortexes with a reverse flow. Apparently, instability of the SH-SAW flow with an increase in power results in a change in the streaming behaviour.

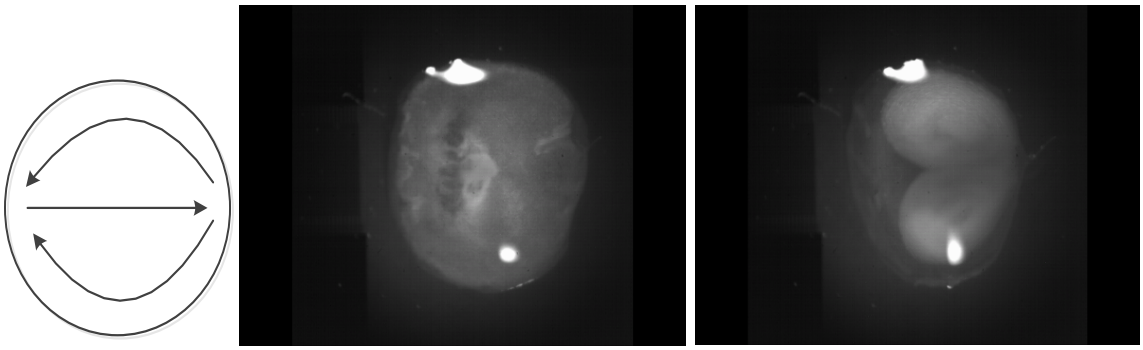

**Figure 5-21: Position 1; 5 µl; from 0 to 4 dBm; 36°Y-X $LiTaO_3$.**

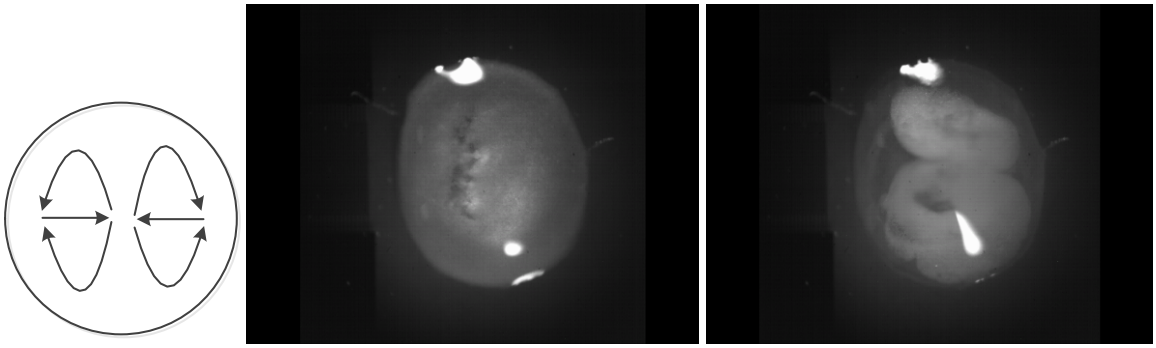

**Figure 5-22: Position 1; 5 µl; from 5 to 7 dBm; 36°Y-X $LiTaO_3$.**

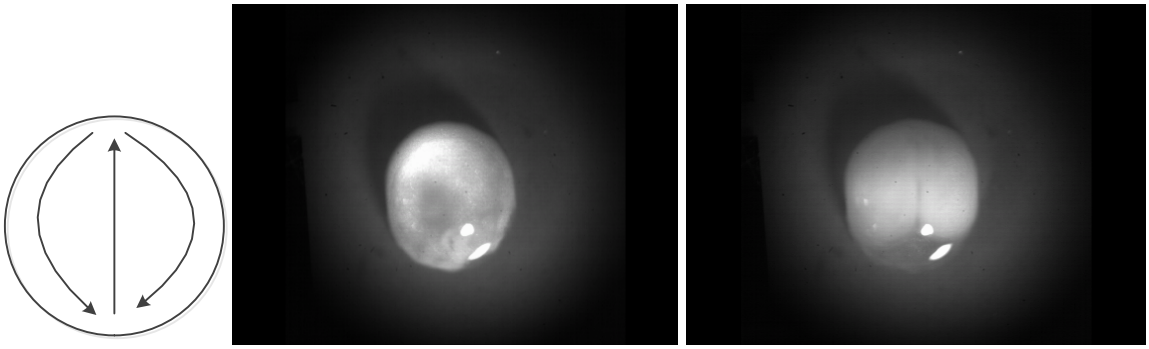

**Figure 5-23: Position 2; 4 µl; from 0 to 5 dbm; 36°Y-X $LiTaO_3$.**

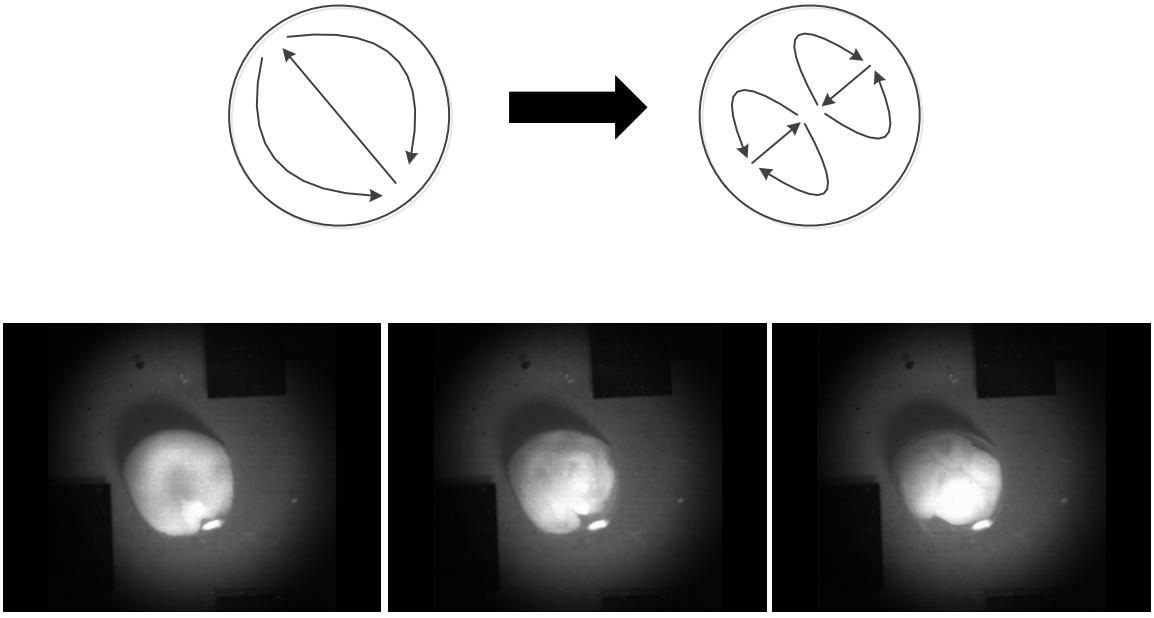

**Figure 5-24: Position 2; 3 µl ; from 3 to 5 dbm; 36°Y-X $LiTaO_3$.**

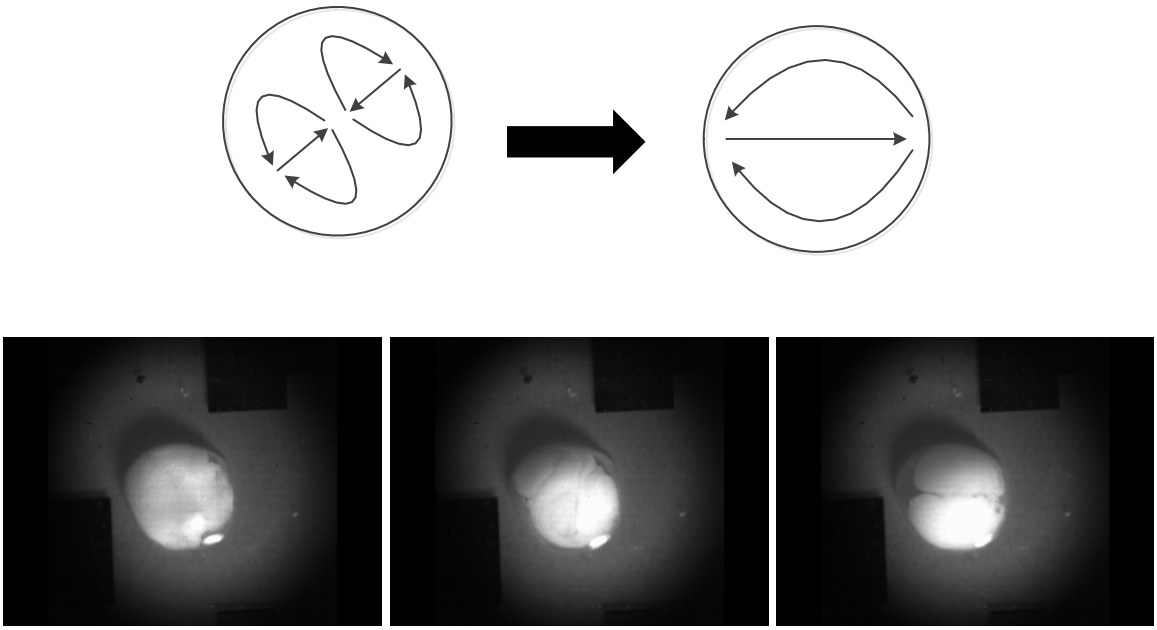

**Figure 5-25: Position 2; 3 µl; from 8 to 10 dBm; 36°Y-X $LiTaO_3$.**

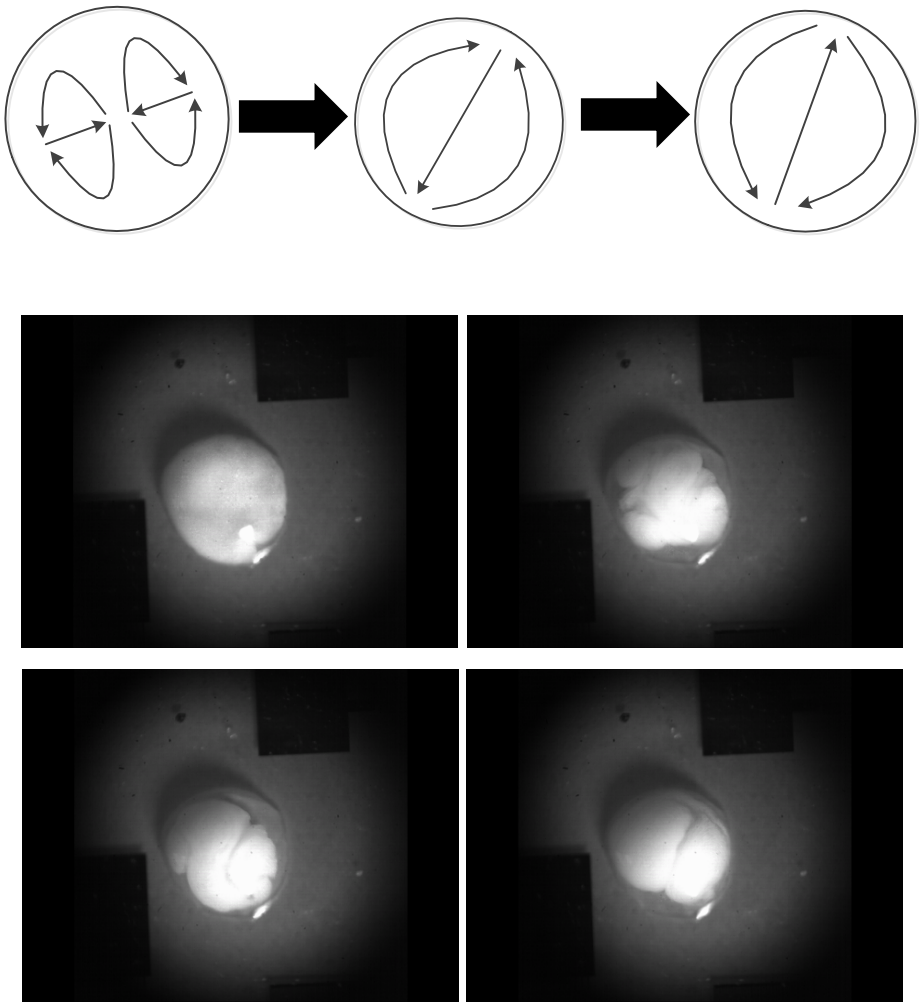

**Figure 5-26: Position 2; 3 µl; 12 dBm; 36°Y-X $LiTaO_3$.**

For position 2, 4 µl and 3µl droplets were excited at different powers as shown in Figure 5-23 - Figure 5-26. At 4 µl at position 2, a vertical flow was observed at 90° to the IDT with a strong boundary reverse flow. With reduction of droplet size to 3 µl, a 45° streaming was observed which split into two distinct counter vortexes at 1s. Increasing powers at 3 µl from 3 dBm to 10 dBm resulted in a strong horizontal flow which started initially at two vortices. At powers of 12 dBm, the streaming transitioned from two vortices initially to a 70° streaming with the flow towards the IDT's then finally transitioning to a flow with the same angle but with the streaming away from the IDT. Droplet volume, spatial location and streaming power all have influences on the flow patterns. No clearly defined patterns for the 4 µl and 3 µl droplets was observed for the different flow regimens. The only observable change was from position 1 to 2 where the flow is mainly orthogonal to the IDT at position 2 as where at position 1 is was aligned with the SH-SAW wave propagation direction.

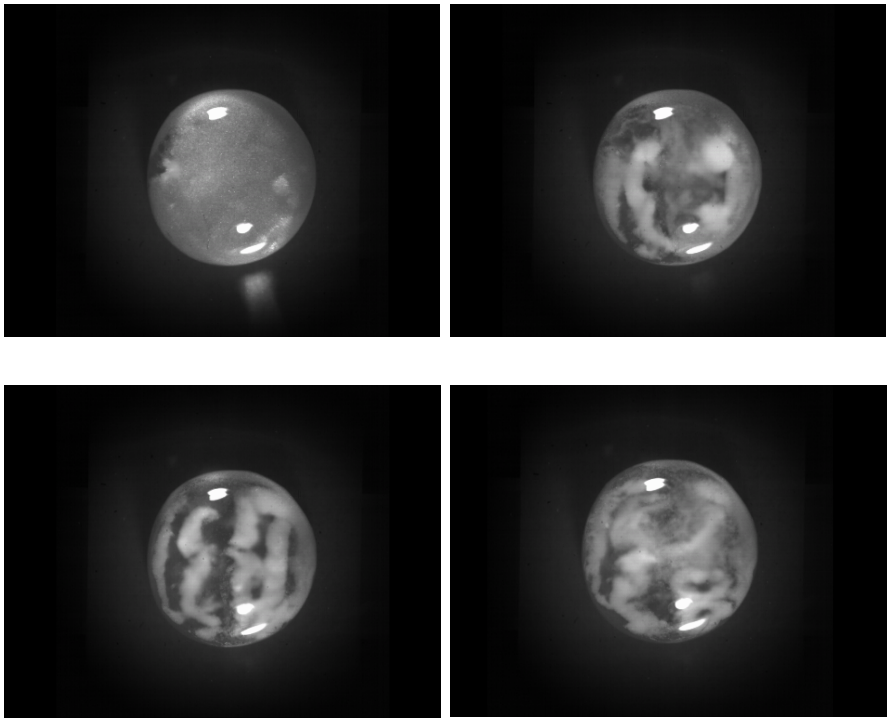

**Figure 5-27: Position 1; 5 µl; 0 dBm; 36°Y-X $LiTaO_3$; Streaming pattern is unstable with no steady state flow or pattern observed.**

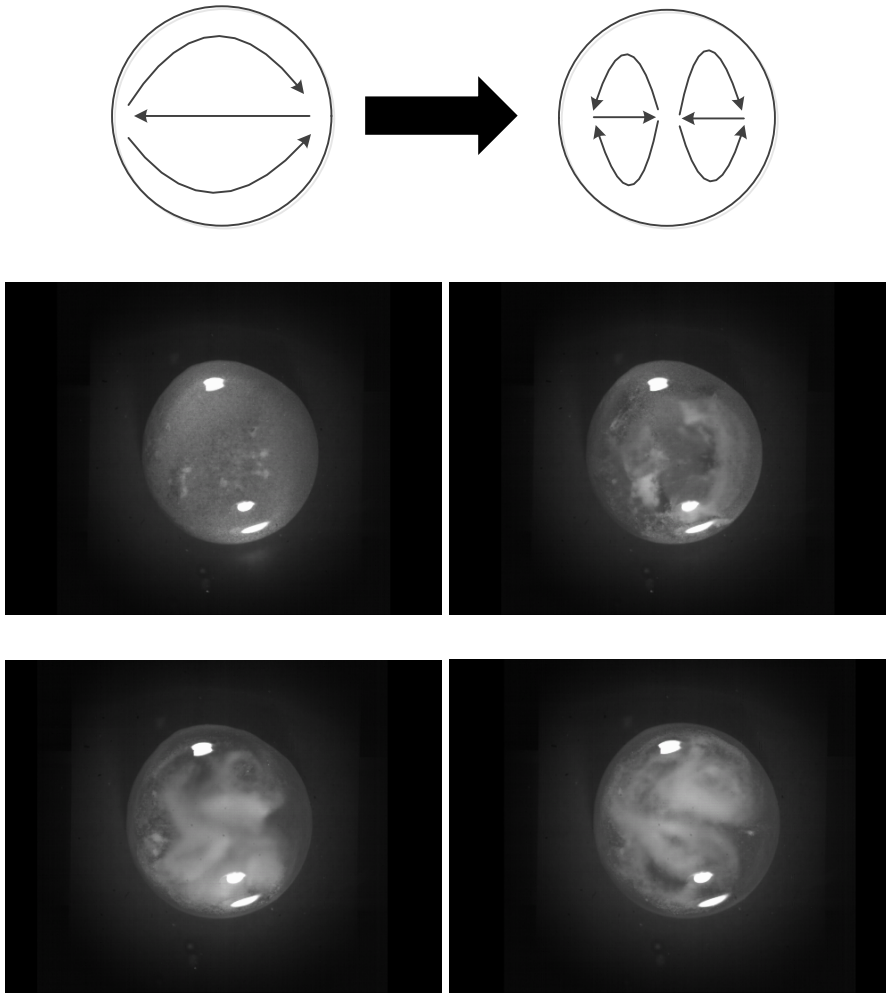

**Figure** 5-28**: Position 1; 5 µl; from 1 dBm - 2 dBm; 36°Y-X $LiTaO_3$; Streaming pattern is unstable with two counter rotation streams observed but quickly becoming chaotic.**

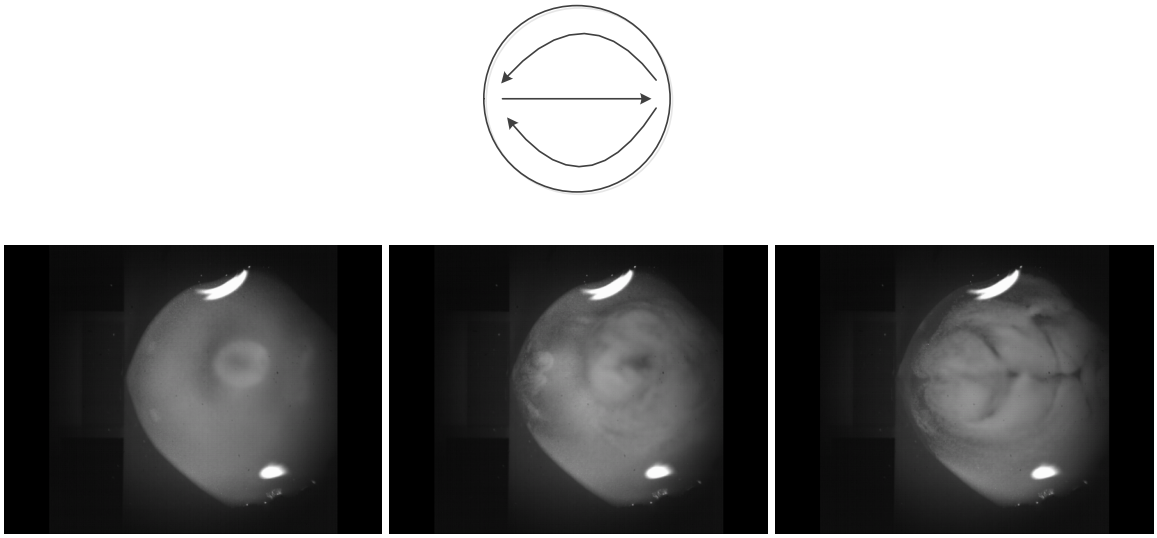

**Figure 5-29: Position 1; 10 µl; from 0 dBm - 2 dBm; 36°Y-X $LiTaO_3$. Flow in propagation direction of the SAW observed.**

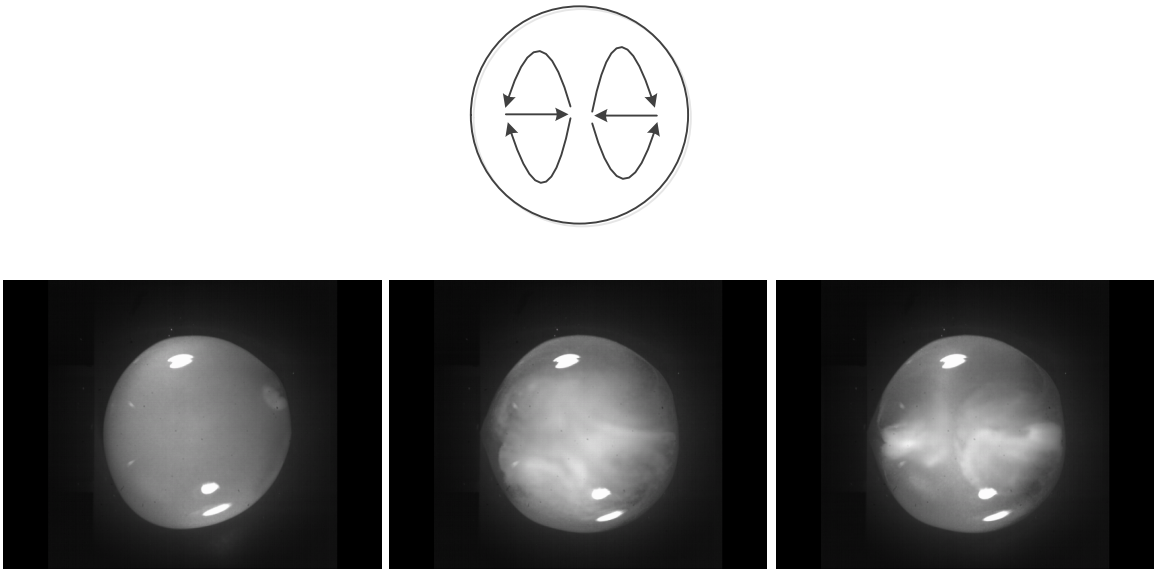

**Figure 5-30: Position 1; 10 µl; from 1 dBm - 3 dBm; 36°Y-X $LiTaO_3$. Flow starts at opposing side of the droplet to the IDT and develops into two counter flows orthogonal to the IDT.**

When the droplet size was increased to 5 µl, position 1 at 0 dBm, no stable streaming pattern was observable with only chaotic vortices formed in the droplet (Figure 5-27). Increasing the power to 2 dBm, no steady state streaming was reached but more concentration of particles was observed as shown in Figure **5-28**. With the droplet size of 10 µl, the IDT aperture was approximately half the width of the droplet diameter. At 0 dBm, the streaming can be observed at the IDT width with scallop shapes forming showing the wave propagation, and the flow is in the propagation direction of the SH-SAW wave (Figure 5-29). At 3 dBm, two counter vortexes were seen to develop with the two opposed flow directions (see Figure 5-30).

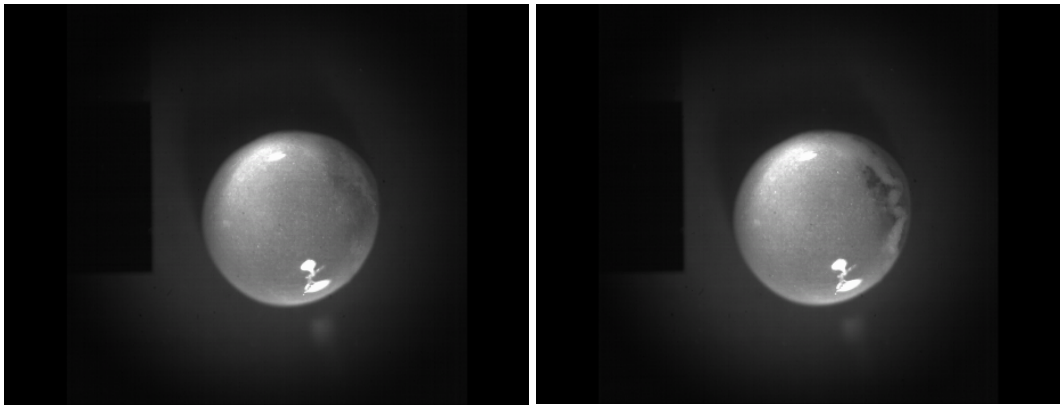

**Figure 5-31: Position 3; 4 µl; from 0 dbm - 2 dbm; 36°Y-X LiTaO3; Stream pattern: weak with only minimal fluid displacement at the boundary opposite the IDT observed.**

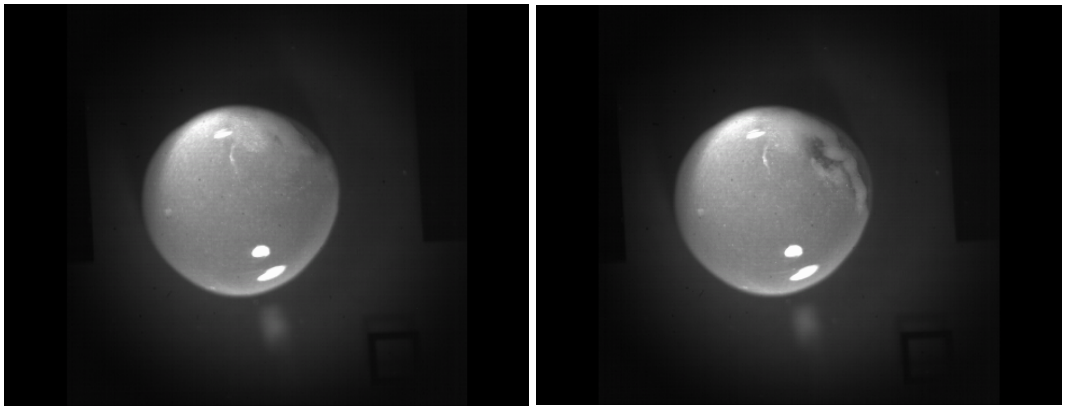

**Figure 5-32: Position 3; 4 µl; from 4 dbm - 6 dbm; 36°Y-X LiTaO3; Streaming pattern: weak with only minimal fluid displacement at the boundary opposite the IDT observed.**

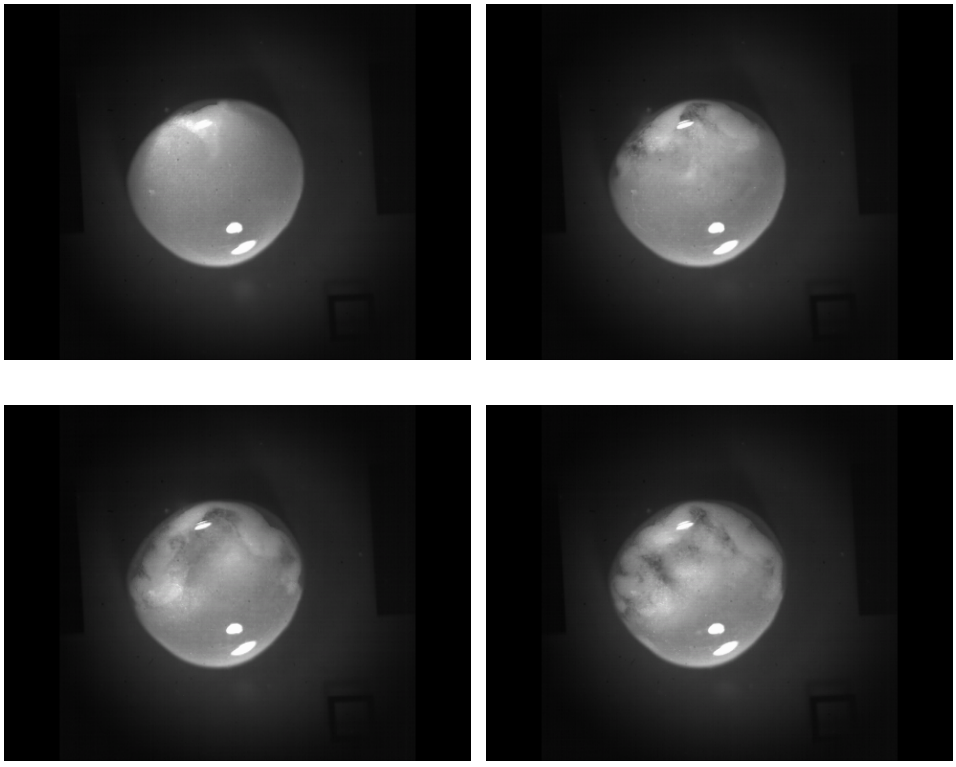

**Figure** 5-33**: Position 3; 4 µl; from 8 dbm; 36°Y-X LiTaO3; Streaming pattern: weak with flow orthogonal to the IDT observed, streaming was localised to top half of the droplet.**

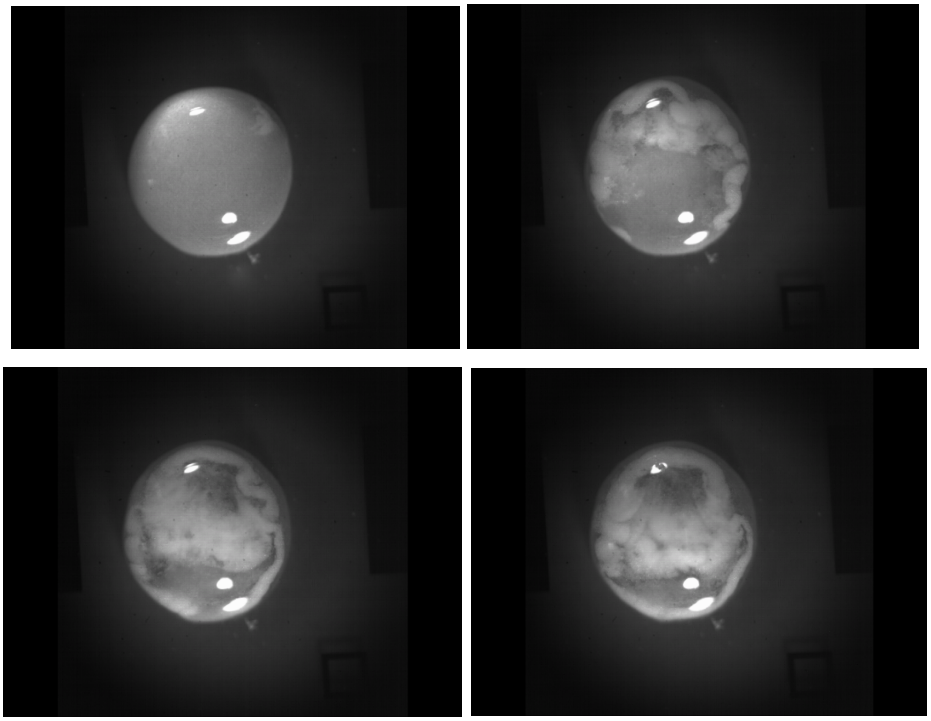

**Figure 5-34: Position 3; 4 µl; from 10 dbm; 36°Y-X LiTaO3; flow develops orthogonal to the IDT at the boundary with chaotic mixing developing with no consistent streaming pattern.**

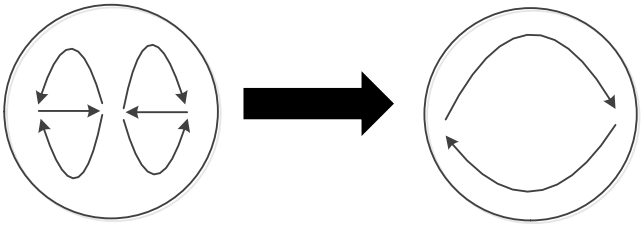

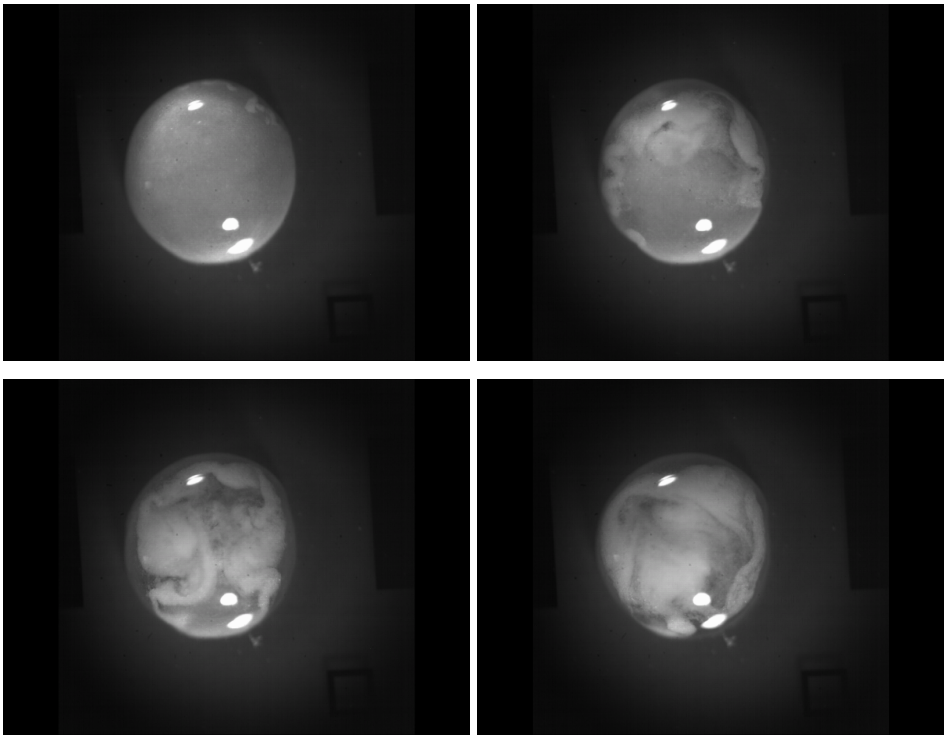

**Figure 5-35: Position 3; 4 µl; from 12 dbm; 36°Y-X LiTaO3; flow develops orthogonal to the IDT at the boundary with initially chaotic flow developing into counter rotation flow around the boundary.**

Locating a droplet of 4 µl at position 3 with 0 dBm, only weak streaming was observed at a 45° on the boundary of the droplet at the opposite to the IDT as shown in Figure 5-31. With the power increased to 6 dBm, the same pattern was observed as shown in Figure 5-32. At 8 dBm, the streaming characteristics were seen to change with the streaming observed at 125° to the SH-SAW propagation direction (see Figure **5-33**). The flow for both powers of 6 dBm and 8dBm was observed at the boundary again showing the SH-SAW acoustic pressure wave is compressing at the boundary of the droplet, thus creating the streaming effects. At powers of 10 dBm and 12 dBm, more pronounced streaming was observed with some rotational flow, again the flow was observed mainly at the boundary of the droplet (see Figure 5-34 and Figure 5-35).

With starch particles introduced into the sessile droplets, the streaming behaviour is indeed surprising. Rayleigh wave flow has been shown to follow a consistent streaming (butterfly) pattern across a range of droplets volumes, IDT sizes and fluidic viscosities. For the SH-SAW wave fluidics with water droplets with only die particles added, the flow was seen to be consistent when the IDT aperture was larger than the droplet resulting in flow in the counter direction to the SAW propagation (Figure 5-15). With the higher viscosity of the starch particles, no consistent flow was observed for the varying droplet volumes, positions and IDT power. The viscosity of the droplet is likely to effect the propagation of the acoustic pressure wave as compared to the water. Comparing the viscosity of water (0.001002 Pa·s) to the starch mixture (1 Pa·s), we can see that the viscosity will have large influence. With the low viscosity of water the maxwellian relaxation rate will be high, meaning the flow is only likely to be compressed at the boundary for large IDT sizes. With the higher viscosity starch mixture, the SH-SAW pressure wave is likely to compress internally in the droplet, thus creating complex pressure differentials dependant on the particle distribution and local viscosity of the fluid. An observation of the wave compression is visible in Figure 5-29 where the wave compression is apparent at the IDT aperture width creating scallop flow lines.

The SH-SAW streaming is clearly driven by a complex combination of the various physical boundary conditions including, droplet size, viscosity, spatial location, SAW power and wavelength.

### 5.2.4 SH-SAW Pumping

It is know that streaming and pumping can be generated within sessile droplets from the Rayleigh wave [23]. It was decided to investigate if pumping could be realised using the SH-SAW wave for fluidics manipulation. No know reports of the SH-SAW pumping have been published to date.

Droplets of 0.1 µl to 2 µl were placed on the 36°Y-X $LiTaO_3$ substrate coated with a CYTop hydrophobic layer (500 nm thick) and actuated using an SH-SAW power of 1 W. Droplet movement was observed with a threshold IDT aperture of 0.2 times the droplet diameter or less, with droplet pumping velocities of up to 20 mm/s. With an aperture size above this threshold value, a negligible droplet pumping displacement was observed. This effect could be linked to the wave energy interaction with the droplets. In all cases, the droplet motion observed was in the direction of propagation of the SH-SAW, with a rotational velocity in one direction (as shown in Figure 5-36). At a narrow IDT aperture such as 1 mm, any asymmetry in the spatial location of the droplet results in a large rotational vector of the flow within the droplet as shown in Figure 5-36 . Insertion of dye particles further highlighted the concentration of an acoustic pressure field within the droplet. This pressure field thus results in a flow at the width of the IDT aperture, with the velocity near the IDT being high and reducing when moving away from the IDT. Pumping of the droplet can thus be explained in that a concentrated acoustic pressure field with a defined propagation direction away from the IDT will result in droplet movement, as observed with Rayleigh wave acoustic pressure fields.

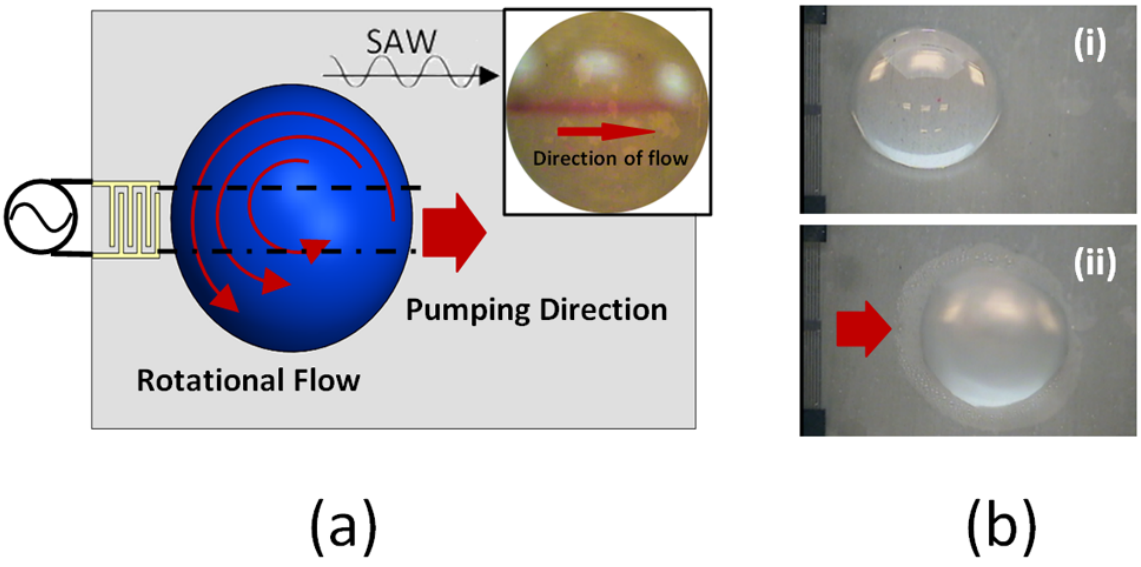


**Figure 5-36: (a) Schematic image (insert) of droplet pumping streaming pattern in 5 µl droplet at 15 dBm on 36°Y-X $LiTaO_3$ (b) (i) 5 µl droplet at initial position (ii) Movement of 5 µl after actuation with 30 dBm power.**

From this analysis, we can conclude that for the SH-SAW pumping narrow IDT apertures are required. Rayleigh wave pumping is observable for a large range of IDT apertures and indeed for pumping and jetting two IDT configurations are required to apply larger powers to the droplet without pumping occurring [141]. Due to the narrow conditions required for the SH-SAW pumping, it is a suitable candidate for high power microfluidic nebulisation and jetting using a single IDT structure.

### 5.2.5 SH-SAW Nebulisation

With streaming and pumping realised with the SH-SAW, nebulisation was investigated. Nebulisation has been shown to exist with Rayleigh wave devices with numerous papers characterising the process [79], [142]–[145].

When the power was larger than 5 W, the nebulisation of the droplet appeared along with the droplet pumping process. The SH-SAW generated from the IDT with the aperture larger than 0.5 mm resulted in the nebulisation under the relative high power as shown in Figure 5-37 (c-e). The mist was generated from both sides of droplet along the propagation direction. This indicates that a narrower aperture of the IDT is beneficial to the formation of a large force along the propagation direction, whereas a wider aperture results in a larger drag force perpendicular to the propagation direction in the droplet.

To obtain a dynamic view of the nebulisation, an RF signal with a power of ~6.7 W was applied to the IDT with an aperture of 2.5 mm, and the droplet was deformed dramatically under the SAW actuation as shown in Figure 5-37 c and d. Two vortex patterns can be formed and the droplet was stretched along the direction of the SH-SAW. The streaming became so significant that it caused instability of the streaming pattern at the interface of the liquid, air and the substrate. A mist was clearly observed emanating from both sides of the stretched droplet as shown in Figure 5-37 e and f, which is perpendicular to the designed SAW propagation direction. The mist quickly spread horizontally to both sides of the deformed droplet as shown in Figure 5-37 g and h. Along with the significant atomization, the droplet was found to be driven back towards the IDT's as shown in Figure 5-37 i and j. In the final stage of the nebulisation process, the remaining droplet quickly broke up into many tiny droplets.

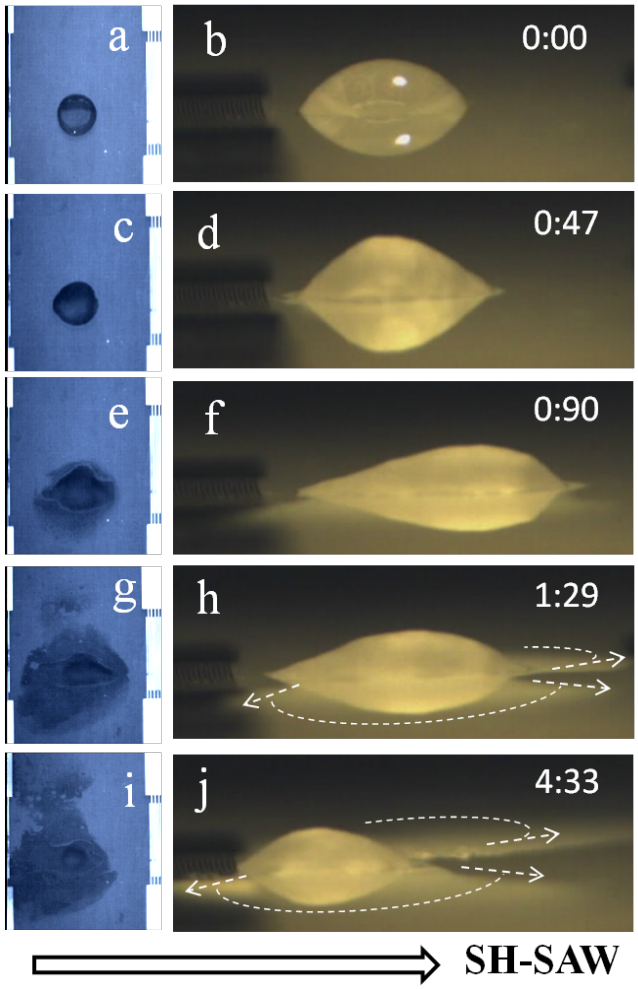


**Figure 5-37: The top and horizontal views of the SH-SAW atomization driven by an RF signal with the amplitude of 6.7 W from left to right at different durations. The hollow arrow shows the direction of the SH-SAW. The time shows in the form of second/microsecond.**

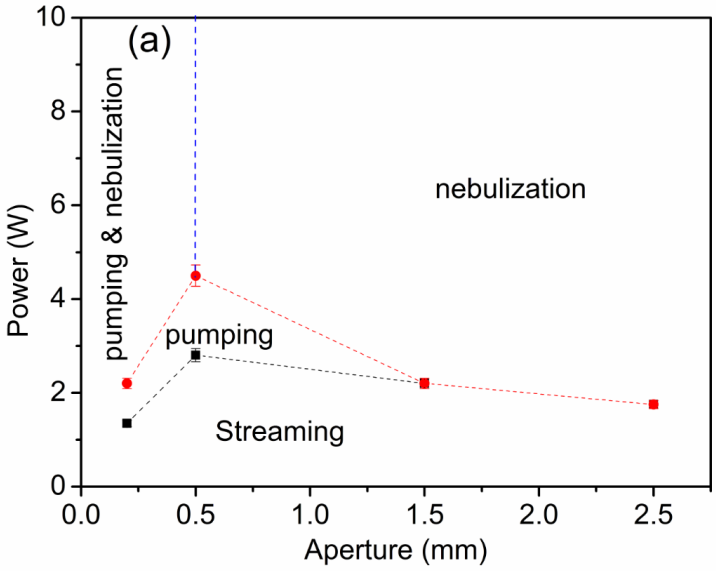


**Figure 5-38: (a) Microfluidic phenomena of a 2.5 µl droplet placed on the 36°Y-X $LiTaO_3$ substrate SH-SAW devices vs. aperture of the IDT as a function applied RF power.**

The different regimes, with reference to the aperture width and powers, can be characterised as shown in Figure 5-38. Noted is that pumping can only occur within a narrow window with an aperture less than 1.5 mm. Only nebulisation was seen to occur with powers over 2 W with a large aperture though powers of 4 W were required for an aperture size of 0.5 mm below this threshold nebulisation and pumping occurred.

Further experiments showed that by putting the water droplets at different lateral positions surrounding the IDT electrode (not on the IDT path), nebulisation could still be realised, although was significantly weaker and the power required was much higher outside of the IDT direction or further apart from the IDT's. The phenomena are substantially different from those caused by the Rayleigh wave: i.e., the nebulisation could only occur along the propagation route of the Rayleigh SAW. In the nebulisation process induced by the Rayleigh mode SAW, the strong interaction of large leaky Rayleigh SAW and the capillary wave leads to significant atomization and mist generation of the water droplet along the SAW propagation direction. Whereas for the nebulisation process induced by the SH-SAW device, the SH-SAW is coupled into the droplet which is within a thin layer of a few μm near the bottom of the water droplet. An acoustic radiation pressure is generated at the interface of solid and liquid, and a pressure gradient between a near point and a far point apart from the source of the SH-SAW results in the streaming. The fluid is observed to swirl along the surface layer from the edge to the top, forming double vortexes in the droplet. Meanwhile, the contact area of the droplet with the solid surface is increased due to the push and stretch of the droplet originated from the longitude component of the leaky SH-SAW. With the continuous application of the large SAW power, the angular velocity of the fluid in the edge of the droplet is significantly increased. The action of the drag force from the shear horizontal component of the leaky SH-SAW results in the dynamical instability in horizontal direction of the droplet. Many tiny droplets were broken up at the edge of the droplet and horizontally jetted because of the appearance of the strongest interactions among the drag force, acoustic radiation force and surface tension. If the droplet is departed from the central line of the propagation, a mist at one side of the droplet are formed and spread while only many tiny droplets appear at another side of the droplet. However, when the droplet is placed on the central line of the propagation from IDT's, a mist can be generated at both sides of the droplet due to the nearly equal intensities of the interaction among different forces from both sides.

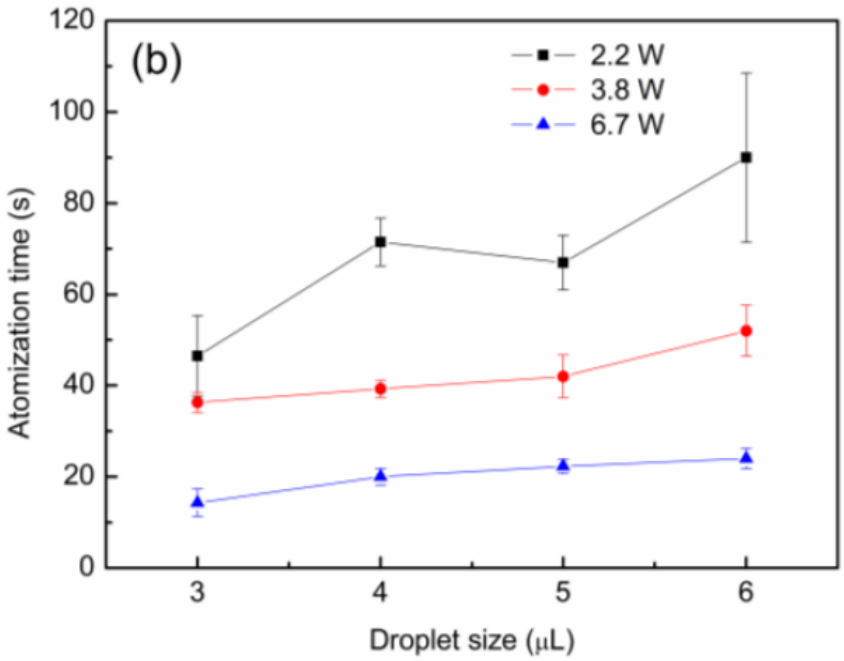


**Figure 5-39: Atomization time as function of droplet size from 3 µl to 6 µl on 36°Y-X $LiTaO_3$ substrate with varying RF power from 2.2W - 6.7W.**

Summarised in Figure 5-39 is the duration for the nebulisation process, i.e., the time for all the liquid to have been atomized, as functions of the droplet volume and RF power. The atomization duration increases with the droplet size, while it decreases at a given droplet size when the power is increased. The maximum rate of the droplet atomization is about 0.2 µl /s at a power of 6.7 W.

### 5.2.6 SH-SAW Jetting

Jetting was the final fluid function investigated using the SH-SAW wave. It is known that for the Rayleigh wave droplets may be ejected from the surface using high powers [78], [146]. No investigation has been undertaken to date using the SH-SAW wave.

For the hydrophobically treated SH-SAW device, when the RF power was increased to 5.2 W, the large inertial pressure inside the droplet induced by the SAW overcomes the surface tension force, resulting in jetting of a coherent liquid beam. The maximum height for the 2 µl drop is up to 4.3 mm before breaking up. Finally the liquid beam broke up and a small droplet was pinched off when the input power was increased to 7.3 W as shown in Figure 5-40a. Figure 5-40b shows that at a high power of 11 W, the break-up droplet was ejected onto the surface of the side wall, indicating that the jetting is not vertically forward, but has a certain angle towards one side of the IDT's (i.e., laterally).

The lateral-jetting phenomena agrees well with the nebulisation phenomena, which are caused by the streaming patterns induced by the shear horizontal waves. In contrast, a typical Rayleigh-type SAW device will result in jetting with a Rayleigh angle of 22.6$^{o}$ towards the SAW propagation direction. The jetting was evaluated by measuring the aspect ratio of the liquid jet, i.e., ratio between the jet length and the radius of the liquid beam. The aspect ratio was found to be proportional to the applied RF power before pinching off a single drop as shown in Figure 5-41.

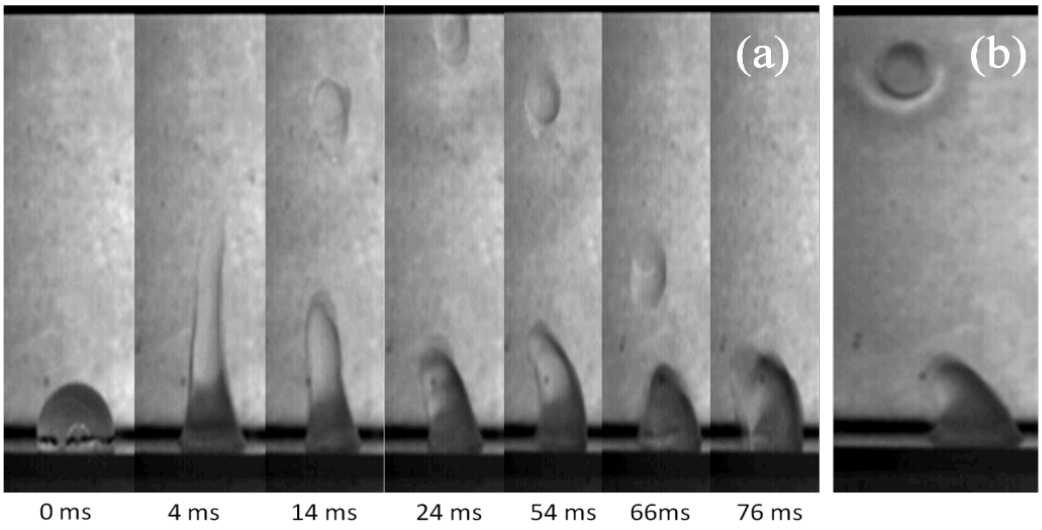


**Figure 5-40: (a) Jetting process of the droplet of 2 µl under a power of 7.3 W. The SAW direction is from right to left (b) break-up of droplet hitting the side wall, the SAW direction is from right to left.**

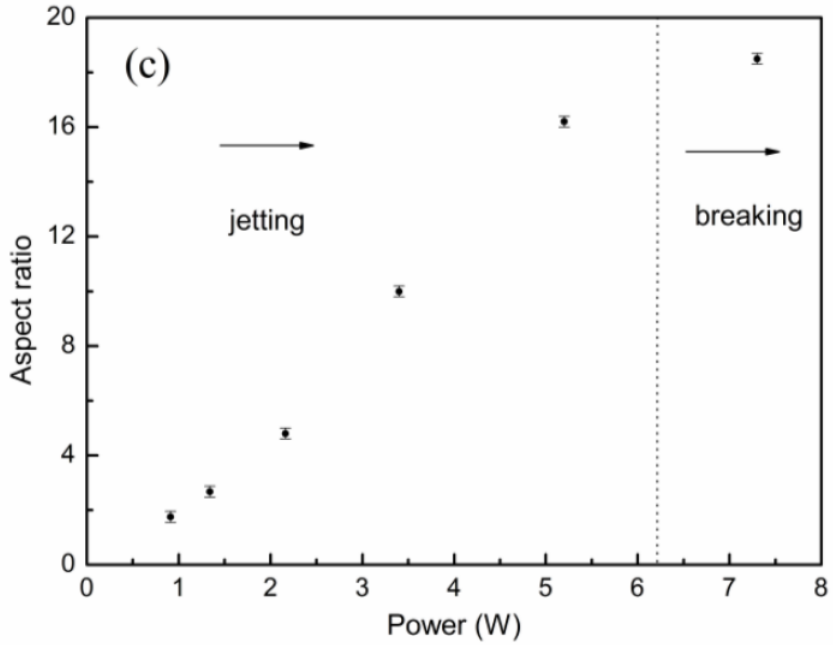


**Figure 5-41: Aspect ratio of the jetting as a function of the applied power on the SH-SAW 36°Y-X $LiTaO_3$ device loaded with 2 µl droplets of distilled water.**

## 5.3 Comparison of Rayleigh and SH-SAW Wave Microfluidics.

For a comparison of microfluidics from SH-SAW, we also studied those of the Rayleigh wave devices based on conventional $LiNbO_3$ based SAWs and thin film ZnO SAW devices.

### 5.3.1 Rayleigh SAW streaming

For experimental work for Rayleigh SAW streaming, $LiNbO_3$ based SAWs were used as the device. As with the Rayleigh wave SAW, the wave can be launched by applying an alternating electric field to the IDT. This wave then propagates along the interface between solid surface and gas (air), and changes its mode to leaky SAW when it reaches the liquid and solid boundary. This leaky SAW Rayleigh wave produces a longitudinal wave that attenuates within a few micrometres, depending on the liquid density and substrate material property, which in turn establishes an effective body force acting into the fluid medium [23]. The generated body force can create a significant acoustic streaming in the liquid and facilitate liquid mixing, stirring, vibrating, pumping, ejection and atomization [16], [67], [71], [147].

For the streaming experiments a SAW device ($LiNbO_3$) with an IDT with finger width of 16 µm, and an IDT aperture of 2000 µm was characterised. The fundamental frequency of the SAW device was measured as 61.92 MHz, this correlates well with calculated values of 61.24 MHz.

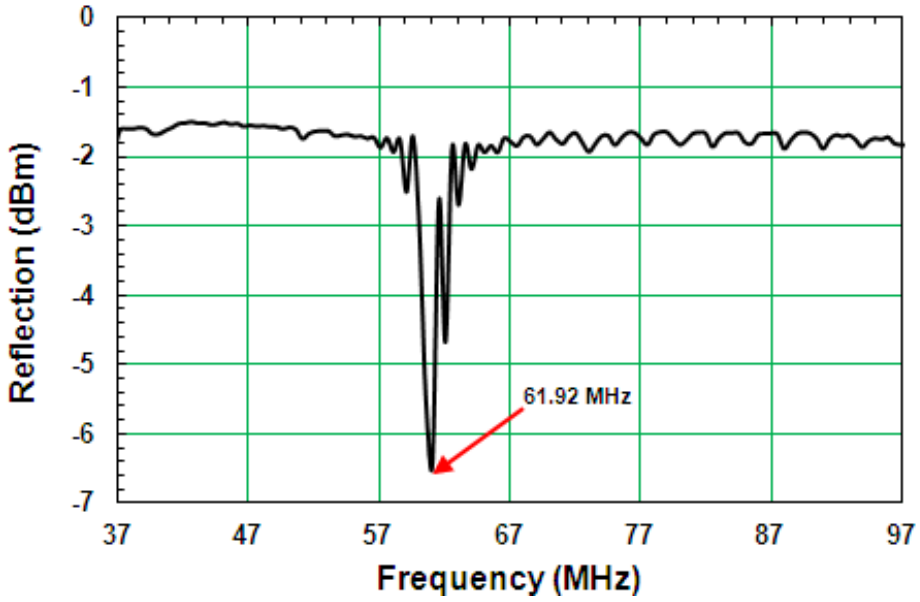


**Figure 5-42: The reflection signal of a 128° YX- black LiNbO3 SAW device with IDT's periodicity of 64 µm that measured using the network analyser; the red arrow indicates to the exact resonant frequency of the SAW device.**

Velocity was compared to droplet size for the Rayleigh wave, with a maximum velocity of 30mm/s observed for a power of 39 dBm (1W). As pervious discussed the velocity was seen to decrease with the increasing volume of the droplet.

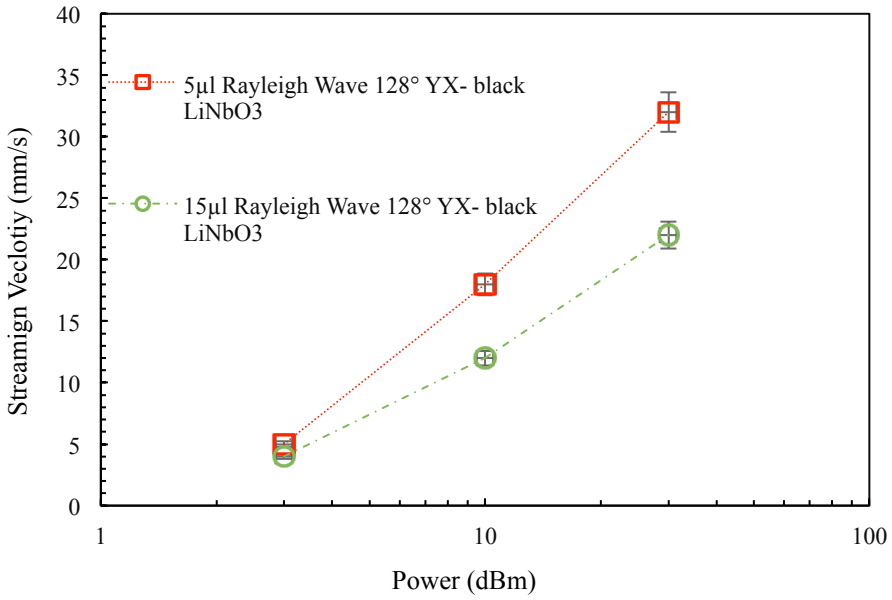


**Figure 5-43: Streaming velocity for droplet sizes 5µl and 15µl on 128° YX - Black $LiNbO_3$ substrate excited with Rayleigh wave for varying powers from 2 dBm – 12dBm.**

Alghane et al. investigated the flow patterns of the Rayleigh wave SAW using numerical CFD calculations, this simulated data will be used to analyse the streaming behaviour and discussed in the following section. Figure 5-44 shows the simulated streamlines of the SAW streaming with 3D circular flow patterns for a 30 µl water droplet at an RF power of 15.98 mW [10]. The simulation results show that the highest value of streaming velocity is located at the interaction area between the droplet and SAW because a higher momentum is delivered near the substrate surface (SAW-droplet interaction area), where the source of SAW force is more intense. This momentum source at the SAW-droplet interaction area establishes a flow field that drives the flow with a Rayleigh angle, resulting in a continuous flow within the droplet. Indeed, experimental observation using a high-speed camera revealed that the particles inside the droplet start to move from the bottom to the centre of the top surface of the droplet after SAW application, and this phenomenon of flow development was predicted accurately by current model numerical simulation results presented in Figure 5-45. When the moving liquid reaches the droplet boundary, the interaction between the liquid and the solid boundary induces a reverse flow at the both sides of droplet and the bottom liquid-solid boundary. When this reverse

flow goes back towards the IDT's, the driving flow due to a SAW force drives the reverse flows upwards to the top of the droplet.

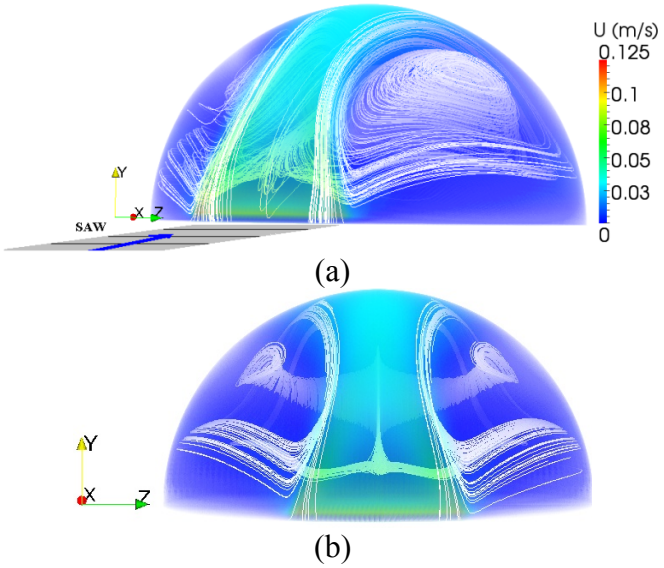


**Figure 5-44: Numerical 3D illustration showing the droplet SAW interaction leading to 3D complex flow patterns due to SAW energy attenuation and Reynolds stresses formation which in turn produces an effective steady force acting in the fluid body (30 µl droplet at the RF power of 15.98 mW); (a) tilted view, (b) direct view focusing through droplet centre [10].**

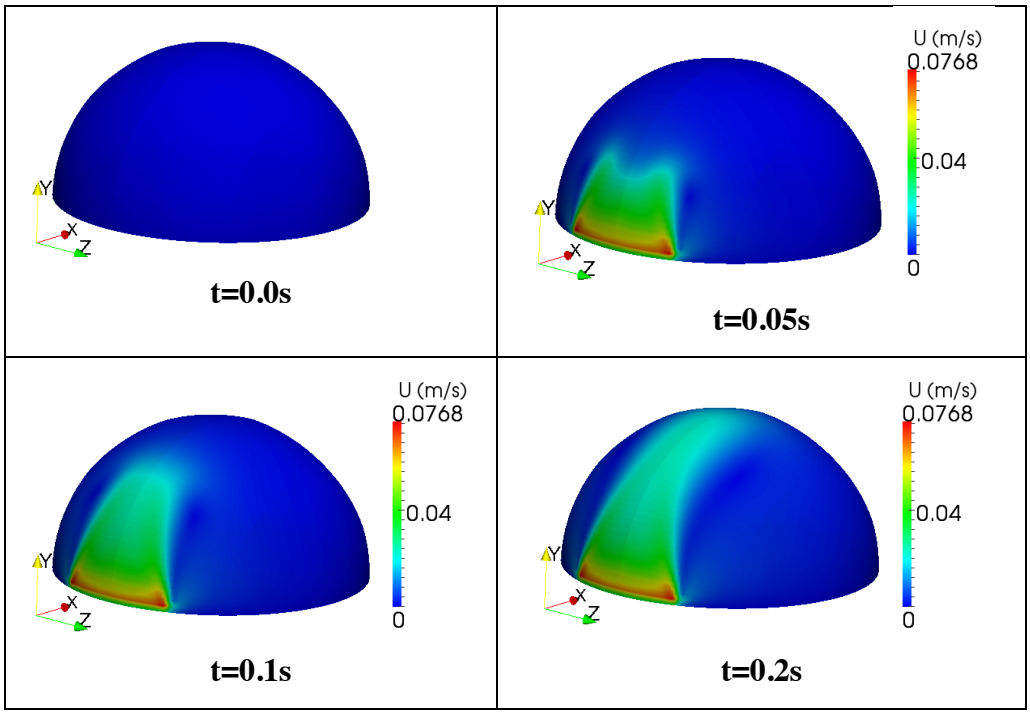


**Figure 5-45: Numerical results showing the progress of flow field after applying the RF power and SAW propagation (30 µl droplet at the RF power of 2.88 mW) [10].**

Eventually, the interaction between the reverse flow and the SAW driving flow produces a double vortex flow pattern that reaches a steady state within a few seconds, depending on the applied RF power, droplet size and fluid viscosity, as shown in Figure 5-44. The interaction between the two flows contributes to a decrease in the streaming velocity, especially at a high wave amplitude (i.e., a high RF power), where the progression flow is accelerated to a higher velocity and then decelerated to a steady velocity afterwards.

Viewing the side elevation of Navier-Stokes simulated droplet flow from Alghane et al. and those from the captured trajectory pictures of 6µl polystyrene particles were compared at the same SAW setup and droplet size. Figure 5-46 shows the side elevation for the Rayleigh weave streaming. These figures present comprehensive views of SAW streaming patterns within a microdroplet positioned centre on the SAW propagation direction, the driving flow and reverse flow are clearly visible. The Rayleigh angle of the leaky saw is clearly visible with a high droplet velocity at the base of the droplet creating the reverse flow.

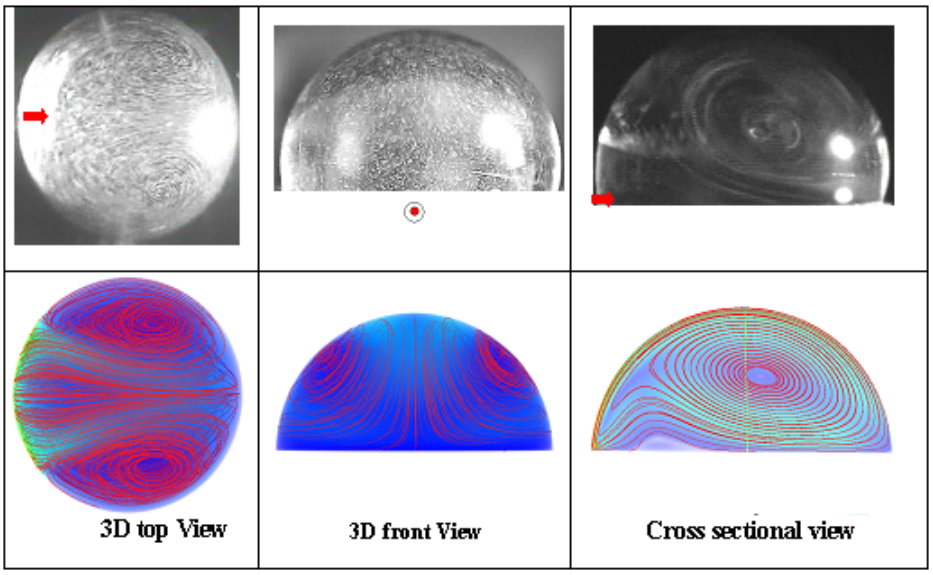


**Figure 5-46: Comparison of experimental and numerical modelling for a 30µl droplet positioned at the centre with the SAW propagation direction; the upper row shows pictures of particles trajectories; the bottom row shows the corresponding streaming patterns from numerical simulations. The red arrow indicates the SAW propagation direction. [10]**

### 5.3.2 Rayleigh SAW induced pumping

Rayleigh wave pumping was investigated next using thin film ZnO devices as the $LiNbO_3$ SAW devices were easily fractured and failed at a high powers. The as-deposited ZnO film is normally hydrophilic with a typical contact angle of 60~80°. Although the contact angle is reasonable large, the hydrophilic nature of the ZnO surface has the effect of

preventing water droplets for moving efficiently on the ZnO SAW device. With a low SAW power of about 50 to 100 mW at a frequency of 65.4 MHz (Rayleigh wave), a typical butterfly streaming pattern within the water droplet can be clearly observed. By increasing the input SAW power applied to the IDT's on a ZnO film, the water droplet becomes obviously deformed from its original shape (see Figure 5-47). The large SAW pressure excites and stirs the droplet, causing it to vibrate along with the propagating acoustic wave, and the significant internal streaming inside the droplet can be clearly observed as shown in Figure 5-47. Finally the droplet is pushed forward, spreading on the film surface, but due to the hydrophilic nature of the surface, the liquid droplet as a single unit could not be pumped away.

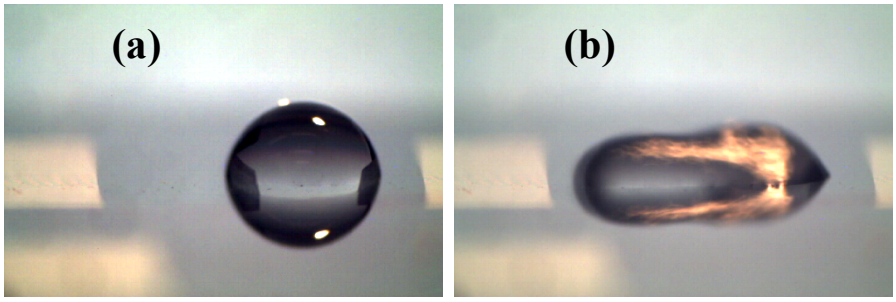


**Figure 5-47: Liquid droplet flow on untreated ZnO/diamond surface (the SAW propagates from right to the left) (a) original droplet; (b) droplet deformation and spreading with significant streaming inside.**

Pumping and jetting tests using the ZnO SAW device were performed using water droplets with various SAW powers. Figure **5-48** (a) to (c) shows examples of pumping movement of a droplet of 2 µl at an RF power of 4 W. The droplet has been deformed dramatically following the Rayleigh angle, and then pushed forward through sliding and rolling, which have been reported in details previously. The pumping speed increases significantly with the increase of RF power.

(a) (b) (c)

**Figure** 5-48**: Droplet pumping for a droplet of 2 µl at an RF power of 2 W at various durations after applying SAW (a) 0s; (b) 0.08s; (c) 0.16**

### 5.3.3 Rayleigh SAW Induced Jetting

For Rayleigh wave jetting the ZnO devices were used again. As-deposited ZnO film is hydrophilic with a contact angle of water droplet typically of 50~70°. The large acoustic energy dissipated into the droplet results in a large inertial pressure in the droplet to overcome the capillary force, causing the large deformation along the Rayleigh angle. However, due to its hydrophilic nature of the droplet on the surface, the droplet could not be continuously ejected from the surface, and the pinching of droplet easily occurs. Therefore, some small droplets have been ejected from the surface, and the remaining liquid was driven to spread on the surface. The pinch-off of droplets and the related drop sizes was found to be dependent on applied power and jetting velocity. According to Richards et al. [148], at a lower power, a force balance between surface tension, viscous, inertial, etc. will determine the final ejected drop volume, while at high power inducing the jetting, the jet stability dynamics determine the drop size.

For the devices spin-coated with CYTop, when the input SAW power applied to the one port IDT of the ZnO SAW device was above 2 W, the liquid droplet on the surface of the acoustic wave path was found to fully eject from the substrate surface. Large acoustic energy dissipated into the droplet results in a large inertial pressure in the droplet to overcome the capillary force, resulting in a coherent cylindrical liquid beam. Figure 5-40 shows the images captured from a movie taken at 1000 frames $s^{-1}$ showing jetting phenomena of a droplet of 2 µl induced by the leaky surface acoustic waves with an RF power of 15 W. The droplets have been ejected following the Rayleigh angle. The jetting angle was predicted using Snell's Law and wave propagation velocities of 4200 m/s (ZnO film) and 1495 m/s (water), $\theta = \sin^{-1}(C_{water}/C_{ZnO}) = 20.95^{o}$. The measured ejection angle varied from $13^{o}$ to $32^{o}$. The droplet was continuously ejected in such an elongated jetting beam until the entire water droplet has been consumed. The jet length is increased from ~5 mm to ~23 mm with the RF power increased from 5.6 W to 23 W for the 2 µl droplet of about 1.8 mm in diameter. Near to the end of jetting process, the elongated jet suffered from the classical Rayleigh-Plateau instability [149], [150] and breaks up into small droplets as shown in Figure 5-49. Some tiny droplets were ejected from the ZnO SAW surface, up to a maximum height of 30.7 mm at a power of 23 W.

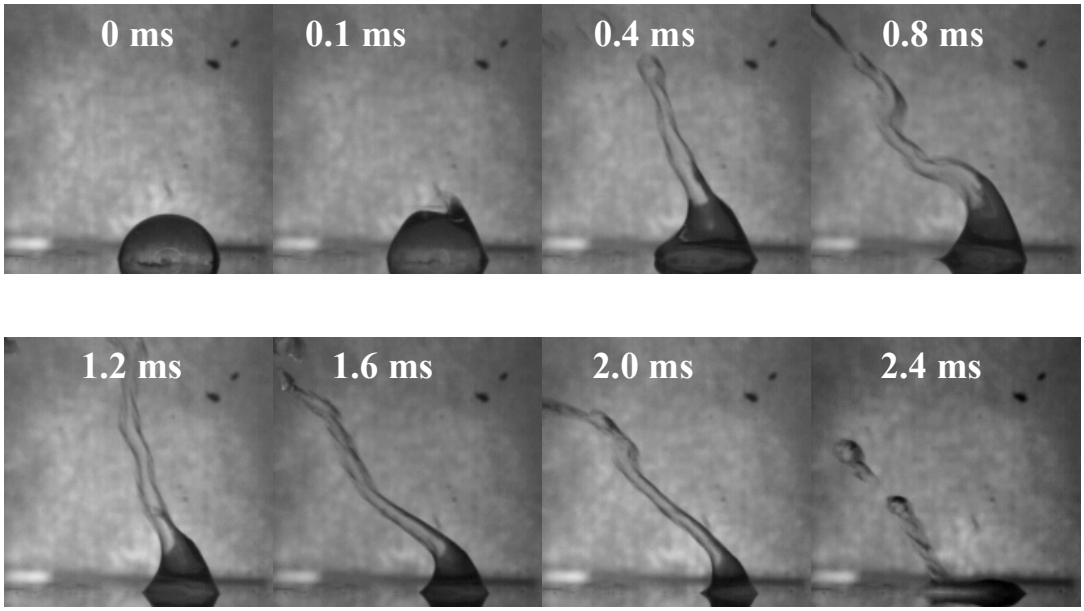


**Figure 5-49: Images captured from a movie taken at 1000 frames s-1 showing the jetting phenomenon for a droplet of 2 µl from the unbalanced force induced by surface acoustic waves on a ZnO substrate (input power of 50 W). The SAW generates from right to left.**

### 5.3.4 Rayleigh SAW induced Nebulisation

If the SAW power is high and the surface is hydrophilic, nebulisation can occur at a low frequency of 10 MHz to 50 MHz. Figure 5-50 shows a sequence of high speed images of nebulisation behaviour of a 0.5 µl water droplet driven by an RF power of ~8.6 W at a frequency of ~12.3 MHz. Figure 5-50, three stages of nebulisation process can be clearly identified.

(a) *Generation of capillary waves* (Figure 5-50 a).

As the leaky SAW propagates into the droplet, acoustic wave pressure drives the liquid droplet, and the surface vibrates significantly with the wave, forming capillary waves on the parent droplet surface (as shown in Figure 5-50 i and ii). The duration for this stage is dependent on the applied RF power and droplet size, and is significantly shortened with either decrease in the parent droplet size or increase in RF power. The higher the RF power, the larger the amplitude of the capillary waves was observed.

(b) *Generation of ejected droplets* (Figure 5-50 b).

Amplitudes of the capillary waves increase significantly, and the capillary wave quickly becomes unstable. The large amplitude capillary undulations on the free surface of the parent droplet result in whipping, pinch-off and jetting of satellite

droplets of about tens to hundreds of μm as shown in Figure 5-50 ii and iii, which have been reported in the $LiNbO_3$ SAW devices [78], [146]. Generation of these large satellite droplets is also attributed to the burst or spurious waves from the SAWs. This stage is generally very short followed by significant nebulisation process.

(b) *Significant nebulisation with formation of mist and satellite droplets before the consumption of the whole parent droplet* (Figure 5-50 c).

A higher magnification image shows that the mist is actually formed of different sizes of tiny droplets, ejected from the surface of the parent droplets at random directions (mostly vertical upwards as shown in Figure 5-50 iv to vi). Along with the significant formation and rising of the mist, many large satellite micro-droplets with estimated sizes of tens of μm are generated from the parent droplet as shown in Figure 5-50 v to vi. During the continuous nebulisation process, the mist rises up to a few centimetres in height. Some of the large jetted drops would be much heavier compared to mist, thus they tend not to be nebulised as high as the mist, and eventually fall to the surface as can be seen in Figure 5-50 viii. Other middle sized satellite droplets can be observed to flow away with the mist during the nebulisation process, but most of the tiny droplets within the mist are too small to be identified from the high speed images Figure 5-50 viii. At the edges of the nebulised droplet, the falling satellite droplets were attracted back by the atomised streams and then pushed up again along with the upward flow of the mist.

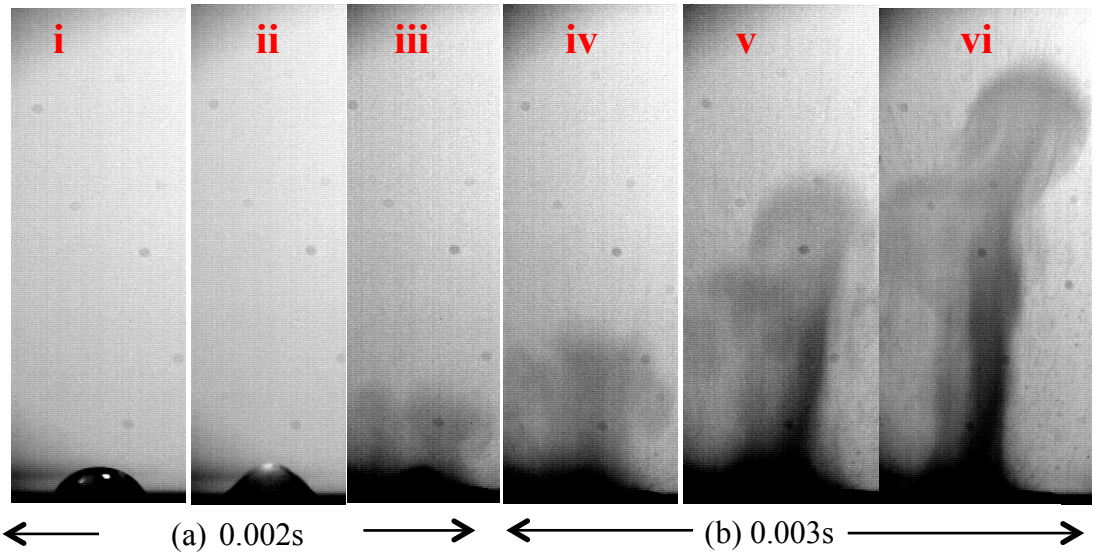

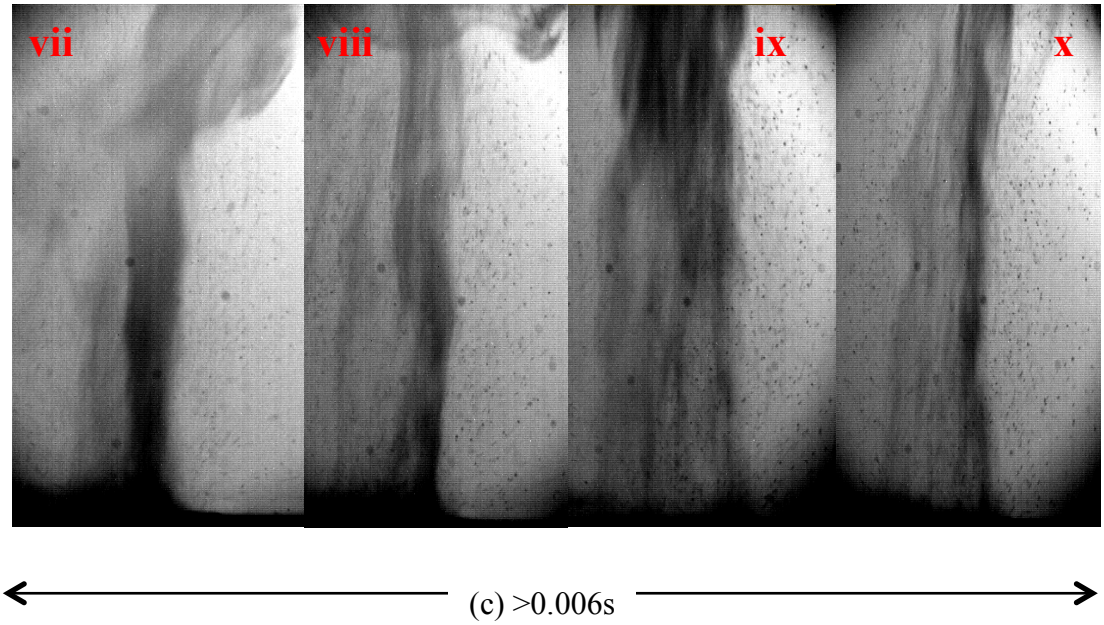


**Figure 5-50: Nebulisation morphology and sequences of the ZnO/Si SAW devices with 0.5µl droplet, IDT power of 12 W; (a) Capillary wave and ejection of droplet after ~0.002 sec; (b) Generation of droplets at ~0.003 sec; (c) Significant nebulisation (mist and satellite droplets) at ~0.006 sec. Individuate images are also notated with roman numerals for reference.**

## 5.4 Discussions on the Differences between Microfluidics from Rayleigh SAW and SH-SAW

With microfluidic function realised with both SH-SAW and Rayleigh wave leaky SAW, a comparison was made of the various physical mechanisms.

(a) Streaming:

Streaming behaviour with the Rayleigh wave is characterised by a longitudinal wave that attenuate rapidly in contact with the droplet at the Rayleigh angle. With the droplet aligned with the IDT a characteristic butterfly flow pattern is observed across a range of powers, droplets sizes and viscosities. The SH-SAW in contrast is generated by a shear wave which attenuates in the droplet causing viscous drag of the fluid creating an acoustic pressure wave either; by compressing against the liquid air boundary; or against static fluid outside of the IDT propagation path. For water droplets where the IDT aperture is wider than the droplet diameter a pattern similar to Rayleigh wave is formed but with a reverse flow direction, this is caused by boundary drag which forms a flow around the boundary of the droplet causing the flow reversal. Streaming observed with the SH-SAW wave was around 7 times lower in magnitude compared to the Rayleigh wave at small droplet volumes, but this was reduced to around 2 times at volumes great than 15

µl. With varying droplet volumes, viscosity and IDT apertures a range of flow regimes was observed with the SH-SAW. This is in contrast to the Rayleigh wave which is formed by a single vectors force creating consistent flow patterns.

(b) Pumping:

At a threshold of 4W, pumping with the Rayleigh wave was observed for a range of droplet sizes and IDT apertures. The mechanism for the Rayleigh wave pumping is a pressure gradient in the direction of the acoustic wave. For SH-SAW pumping, a narrow range of parameter was identified for pumping to occur. With an IDT aperture size of 0.2 times the droplet diameter or less, pumping was observed. The mechanism identified was different to the Rayleigh wave with a narrow IDT with high power creating a narrow streaming field due to viscous compression. This in turn creates a large rotation velocity in the droplet enabling pumping. The directional vector of pumping was observed with a high variance and distances were limited to 10 mm - 20 mm.

(c) Jetting:

For Rayleigh wave device, jetting was realised using thin film ZnO devices. The acoustic energy creates a large deformation in the Rayleigh angle direction following Snell's law. Ejection was achieved with a power of 5 W for a droplet size of 2 µl. For the SH-SAW wave, no Rayleigh angle was observed with the jetting with an almost vertical jet observed with lateral movement to the IDT. This correlates with the boundary theory indicating that the energy is distributed evenly through the whole droplet. Droplet separation occurred with the SH-SAW at 6.3 W and above.

(d) Nebulisation

With the Rayleigh wave nebulisation, capillary forces are seen to cause break-up of the surface tension of the free surface resulting in ejection of micro scale droplets. Deformation of the droplet is again observed in the propagation direction of the SAW wave. For the SH-SAW wave, the break-up of the surface

of the droplet was seen to occur on both sides of the droplet, thus resulting in nebulisation. This again correlates that the compression wave at the boundary of the droplet resulting in the capillary forces which then break up the surface tension.

## 5.5 Summary

The theoretical simulation of SH-SAW wave propagation within microfluidic droplets and the range of microfluidic functions realisable on with the 36ºYX $LiTaO_3$ crystal with the SH-SAW wave can be summarised as follows:

Theoretical and numerical analysis of SH-SAW:

- Theoretical analysis of the oscillating substrate by SH-SAW demonstrates that a thin layer will experience fluid drag with the dissipation depth driven by the frequency of oscillation.
- Numerical analysis of boundary oscillation, utilising Comsol, correlated with numerical analysis results and confirmed pervious correlation of Comsol with stokes second flow boundary oscillation theory.
- Coupled fluid-acoustic simulations as undertaken using Navier-Stokes and acoustic pressure theory showed a net acoustic wave generated at the fluid to air boundary for the fluid oscillation. Using wave superposition theory, comparison to experimental values showed good correlation.
- A simplified 2D model was able to model flow behaviours and correlate with patterns observed in experimental results, further validating the boundary oscillation theory.

Experiment analysis of SH-SAW microfluidic functions:

- Streaming was realised using the SH-SAW wave, and the flow within water droplets was seen to stream in a reverse pattern when compared to the Rayleigh wave flow. The streaming velocity was 7 times lower in magnitude compared to the Rayleigh wave at small droplet volumes, but this reduced to around 2 times at volumes great than 15 µl. Inline streaming of two droplets simultaneously was realised, confirming that the mechanism is different to Rayleigh wave streaming. Streaming velocity was characterised at various positions vertically above and below the IDT's, showing an exponential relationship for the reduction in streaming velocity.

- Pumping was realised using the SH-SAW wave with a power threshold of 4 W. Compared to Rayleigh wave pumping, SH-SAW pumping was only realised with a narrow aperture, 0.2 time of the droplet diameter. The mechanism of pumping was with a narrow IDT causing a large rotational force.
- Jetting with the SH-SAW wave was observed with no angle in the droplet compared to the Rayleigh wave jetting where an angle of 20.95° observed for a ZnO device. A threshold of 6.3 W was observed for droplet separation.
- Nebulisation was the final fluid function realised with the SH-SAW wave. For the SH-SAW wave, the nebulisation started from the sides of the droplet in contrast to the Rayleigh wave where the surface was deformed in the Rayleigh angle direction. This correlates well with the boundary layer theory where the high pressure field is expected at the droplet boundary.

A comprehensive analysis of the SH-SAW acoustic fluids physics has proposed for the first time a theory for the acoustic wave propagation based on boundary oscillation. A wide range of fluid functions can be realised on the SH-SAW, which is surprisingly given the different wave propagation mechanisms.

# Chapter 6. Thermal Analysis of SH-SAW Wave Propagation

This section discusses the thermal analysis for the SH-SAW wave propagation within sessile droplets placed on the 36ºYX $LiTaO_3$ crystal. Analysis of the Rayleigh wave effects on thermo acoustic heating has been investigated by several authors previously [81], [82], [151], but no investigation on the SH-SAW heating effect has been investigated to date. Experimental analysis of the thermo-acoustic behaviour was analysed for a single droplet and multiple droplets aligned in series. A numerical simulation for the convection behaviour in the droplets was presented. An analysis of the thermal behaviour of the droplet during nebulisation process was also studied.

### 6.1.1 Single Droplet Thermal Analysis

Measurements were undertaken using the experimental set-up outlined in Chapter 3. For the first analysis a single droplet was placed on the 36ºYX $LiTaO_3$ substrate and varying powers of 0.4 W - 12 W were applied. For the second experiment the droplet size was varied from 2 µl – 15 µl. Finally the two droplets placed in series were analysed.

Droplet internal streaming is typically characterised by Reynolds number and for heat transfer the Péclet number is used, i.e. $Pe_{TH}$, which is defined by the following equation:

$$Pe_{TH} = \frac{p \cdot c \cdot v \cdot L}{\kappa} \qquad 6\text{-}1$$

where $\rho$ is the liquid density (Kg/m$^3$); $v$ is the characteristic streaming velocity (m/s); $L$ is the characteristic length (m); $\kappa$ is the thermal conductivity (W/m·K) and $c$ is the specific heat capacity (J/Kg·K).

This Péclet number, $Pe_{TH,}$ enables us to understand the heat transfers mechanism in the bulk droplet. Indeed, the heat transfer within the droplet can take place by conduction (equivalent to diffusion for mass transfer), corresponding to $Pe_{TH}$ <<1 and/or forced convection (SAW streaming), corresponding to $Pe_{TH}$ >>1. Heat transfer by forced

convection is faster than by conduction. These two mechanisms may take place by either: (1) heating of the substrate by propagation of the SH-SAW wave, which will cause a net conductive heating force on the droplet, or (2) energy imparted by attenuation of the SH-SAW wave, which will cause a viscous heating convective force. Both mechanisms were measured and characterised.

### 6.1.2 Results and Discussion

Firstly, a single droplet of 0.2 µl was placed on the substrate and varying powers were applied and the temperature recorded. The temperature was seen to increase as a function of power, and a maximum temperature increase of 38ºC was realised with a SH-SAW power of 11 W (Figure 6-1). The rise of substrate temperature was seen to be around 4ºC at a power of ~14 W. Observing the thermal profile of the droplet, the temperature was seen to be a constant through the droplet except at its boundary. Indeed, the transferred energy within the droplet in the form of acoustic streaming, is the source of two concomitant phenomena. On one hand, internal flow takes place; on the other hand, energy dissipation by viscous friction leads to a liquid heating.

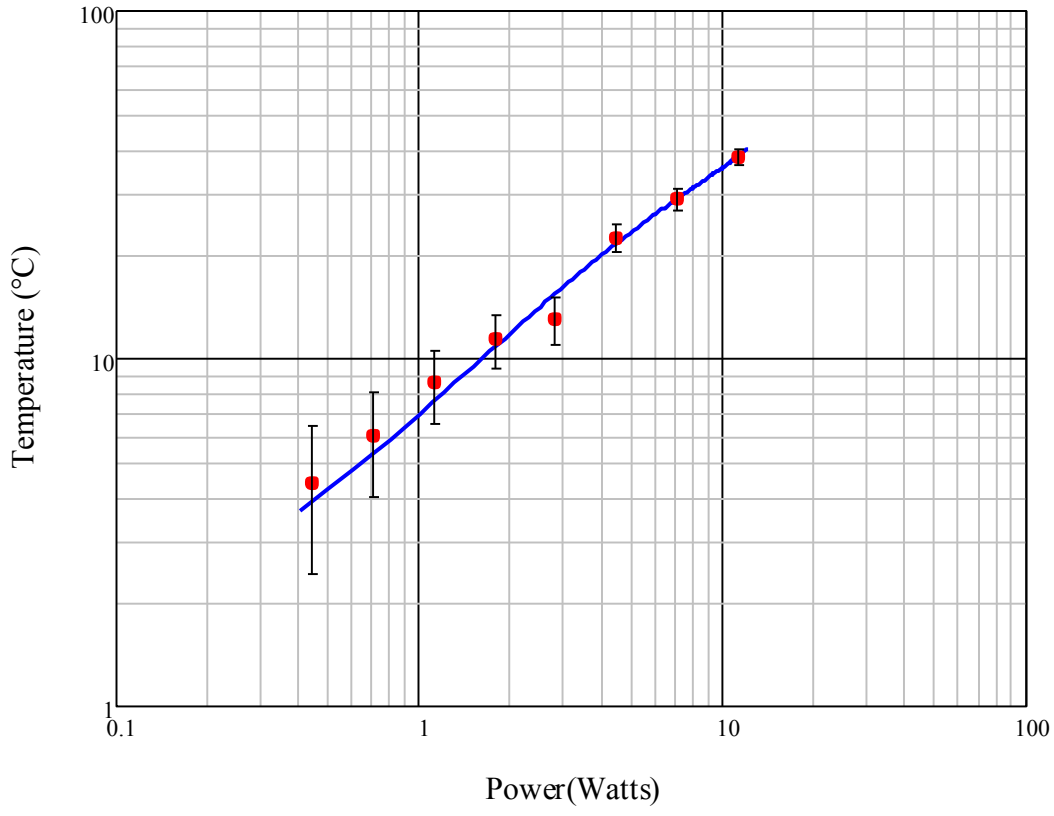


**Figure 6-1: Temperature increase from ambient for a 2µl droplet excited with a SH-SAW wave on 36ºYX $LiTaO_3$ crystal**

Analysing the time to reach thermal equilibrium at varying powers, the 2µl droplet was seen to reach a steady state temperature at 0.1 s for all cases (Figure 6-2). With increasing power, there is no associated increase in the time to reach an equilibrium showing that there must be an advective force driving the transport of heat.

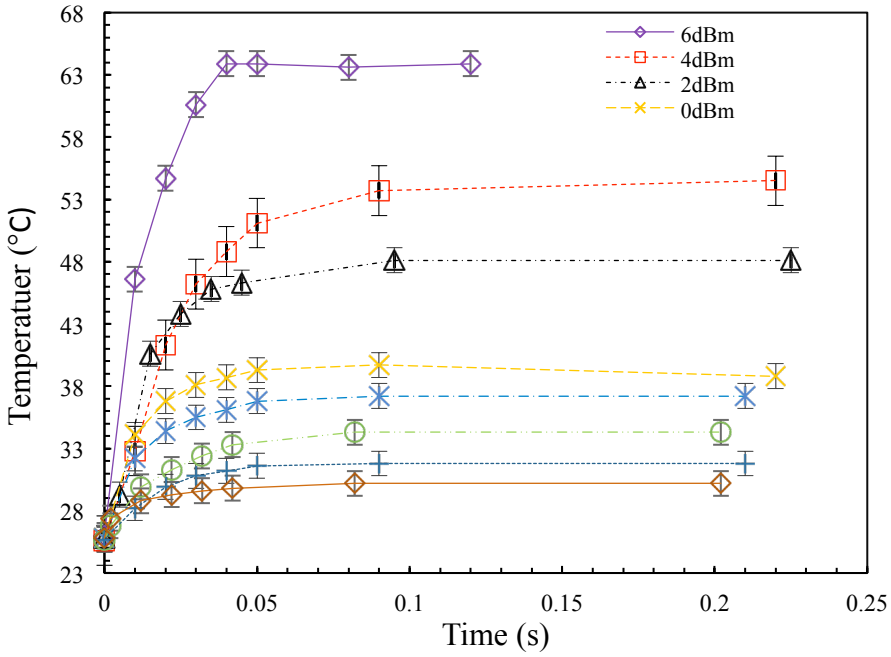


**Figure 6-2 : Transient plot of increase for a 2µl droplet excited with a SH-SAW wave on 36ºYX $LiTaO_3$ crystal**

Analysis of the advective behaviour was undertaken using Equation 6-1. For velocity analysis, data measurements from section 5.2.2 were used, and for the characteristic length, the diameter of the droplet was used assuming a wetting angle of 90º. Beyssen et al. showed there are four zones which can be identified using the Péclet number [82]: (1) for the first zone, a low advection conduction is predominant; (2) for the second zone, forced convection and conduction are both present; (3) for the third zone, forced convection is predominant with some conduction; and (4) for the final forth zone, only convection is present [82]. Calculating the Péclet number for the SH-SAW devices above 2 mW, heat transfer is predominantly forced convection, with only the 2µl droplet showing a possibility of mixed conduction heating (Figure 6-3). This correlates well with a time to reach a steady state temperature of 0.1 s. Comparatively, the Rayleigh wave excited on the 128° YX- black $LiNbO_3$ substrate was also shown at droplet volume of 5 µl, with powers less than 4 mW. It exhibits the forced convection and conduction heating, but at droplet volume of 15 µl, this has changed to a forced convection only. Comparing these two sets of data, it is apparent the SH-SAW wave shows higher Péclet numbers over

a range of droplet volumes, whereas the Rayleigh wave is more sensitive to volume change in the advection heating process.

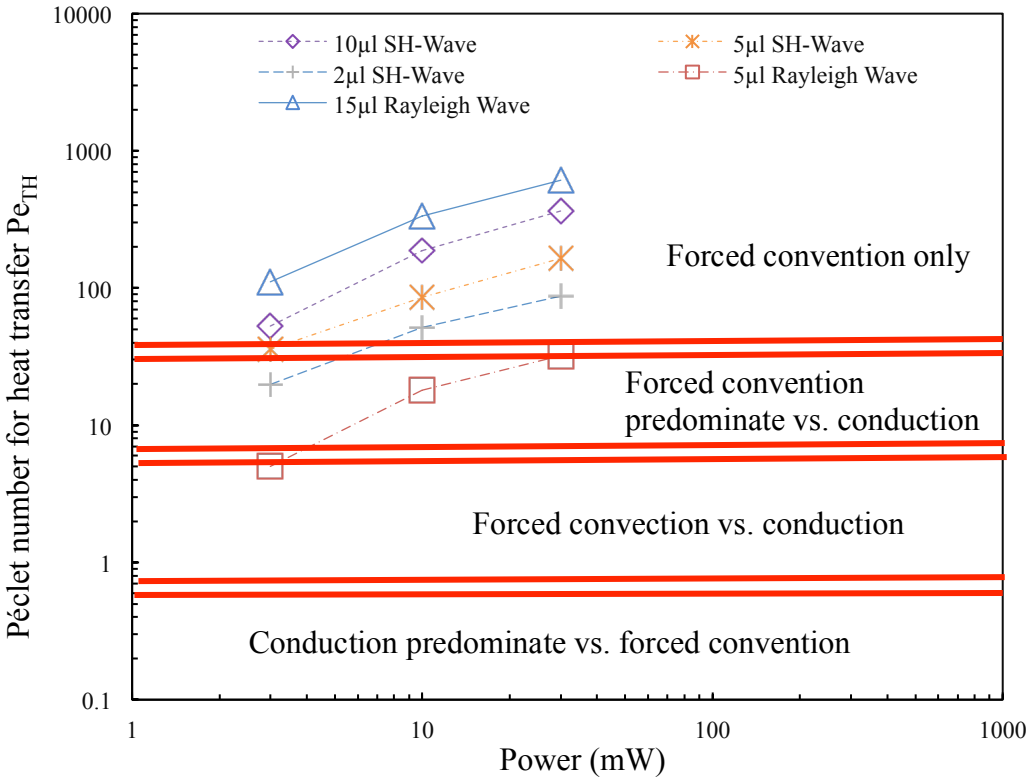


**Figure 6-3: Evolution of Péclet number for heat transfer and a function of $P_{IDT}$ (mW) and droplet size (µl) for pure water. Data is shown for thermal heating with SH-SAW wave on 36°YX $LiTaO_3$ crystal and Rayleigh wave on 128° YX- black $LiNbO_3$**

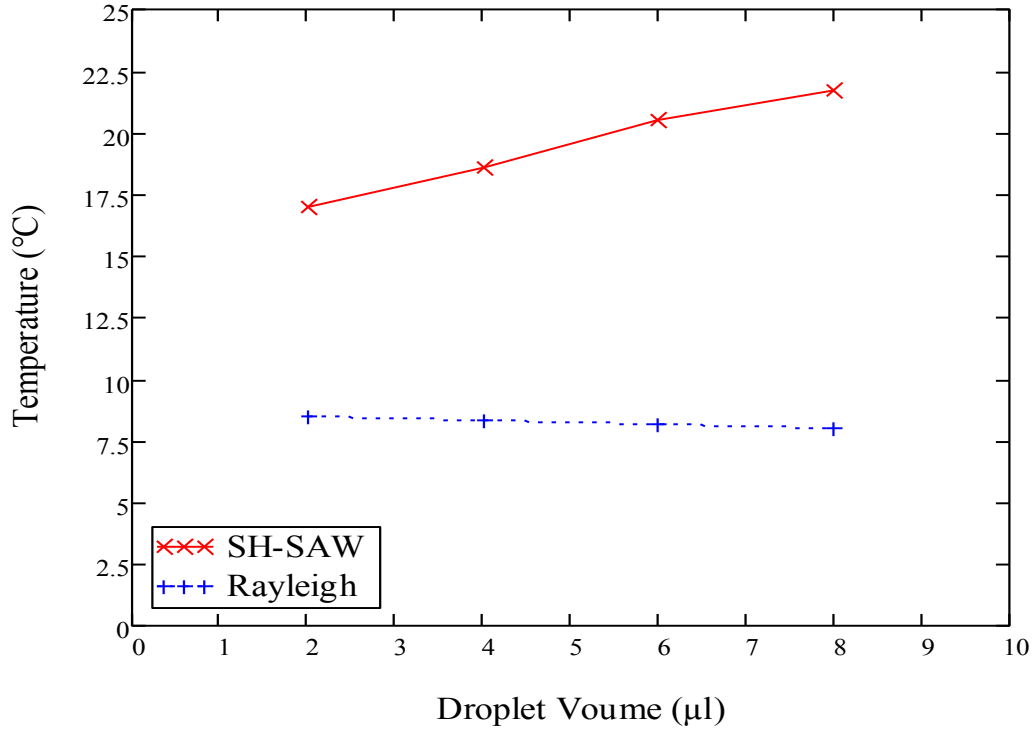


**Figure 6-4: Temperature increase from ambient for varying droplet volumes excited with $P_{IDT}$ =1W. Increase of SH-SAW and Rayleigh wave on 36°YX $LiTaO_3$ crystal**

Comparing the temperature increase as a function of the droplet size of the SH-SAW and Rayleigh wave on the 36ºYX $LiTaO_3$ crystal shows an increase in temperature as a function of increasing droplet size for the SH-SAW wave (Figure 6-4). For the Rayleigh wave no increase in temperature was observed with the increase in droplet volume. This correlates well with similar observations with the SH-SAW streaming data and modelling which indicates that the acoustic pressure is a function of the boundary dimensions.

## 6.2 Numerical Simulations

To verify the heat transfer mechanism within the droplet and prove or disprove if the forced convection is dominant, a numerical simulation was undertaken using the COMSOL Mulitiphysics.

### 6.2.1 Theory

The fundamental law governing all heat transfer is given by the first law of thermodynamics, which is commonly referred to the principle of conservation of energy. The basic law (written in terms of temperature of a fluid) results in the following heat equation:

$$\rho C_p \left(\frac{\partial T}{\partial t} + (u \cdot \nabla)T\right) = -(\nabla \cdot q) + \tau : S - \frac{T}{\rho}\frac{\partial p}{\partial T}\left(\frac{\partial p}{\partial t} + (u \cdot \nabla)\mathrm{p}\right) + Q \qquad 6\text{-}2$$

where $\rho$ is the density of the fluid, $C_p$ is the specific heat capacity at a constant pressure, $T$ is the absolute temperature, $u$ is the velocity vector, $q$ is the heat flux by conduction, $p$ is pressure, $\tau$ is the viscous stress tensor, $S$ is the strain rate tensor and $Q$ contains heat sources other than viscous heating.

Assuming Fourier's law of heat conduction, that states conductive hear flux, $q$, is proportional to temperature gradient, we can simplify the equation 6-2 into a more familiar form:

$$\rho C_p \frac{\partial T}{\partial t} + \rho C_p \mathrm{u} \cdot \nabla T = \nabla \cdot (\kappa \nabla \mathrm{T}) + Q \qquad 6\text{-}3$$

where κ is thermal conductivity.

### 6.2.2 Simulation Parameters:

A transient model was used to simulate the propagation of heat flux within the droplet. A 3D model was created for a 2 µl droplet, assuming a wetting angle of 90°, and the piezoelectric substrate of $LiTaO_3$ was modelled at 300 µm thick and an aluminium block was modelled to represent the socket. The following material properties were used:

**Table 6-1: Material Properties used for Thermal Simulations**

| Material | Heat Capacity (J/Kg·K) | Thermal Conductivity (W/m·K) | Density ($Kg/m^3$) |
|---|---|---|---|
| **Water** | 4.18 | 0.58 | 1000 |
| **$LiTaO_3$** | 0.43 | 46 | 7450 |
| **Aluminium** | 0.897 | 205 | 2700 |

The 3D domain was modelled as 10 mm wide by 100 mm high by 15 mm deep. Boundary conditions of 5 $W/m^2 \cdot K$ was applied to the fluid to air boundary for convective cooling and the 5 walls of the aluminium base were fixed at a temperature of 293.15K

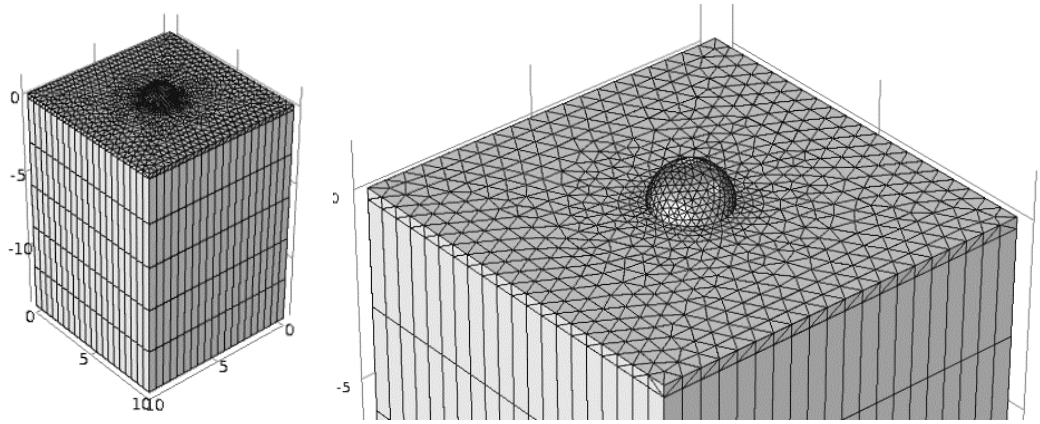


**Figure 6-5: Three dimensional (3-D) image of typical mesh used for thermal simulation. Mesh is approx. 34,000 DOF. Grid dimensions are shown in mm.**

General tetrahedral mesh elements were used for the fluid and piezoelectric substrate with quadrilateral elements used for the aluminium substrate (Figure 6-5). A mesh refinement zone was created around the droplet to allow for a smooth transition of the piezoelectric surface elements to the liquid elements. For the bulk aluminium 5 layers were used through the thickness as a minimal gradient is expected in this area.

### 6.2.3 Quantification of Péclet number Convective Cooling

A varying internal streaming velocity with one vector was applied to the droplet, defined as $u$ in Equation 6.3, as a boundary condition to analyse the effect of increasing Péclet number on the maximum temperature of the droplet. The thermal heating power, $q$, was set at 0.23 W. The diffusion rate was analysed using a transient simulation and measuring the time to reach a steady state. Visualisation of the Péclet number is shown in Figure 6-6.

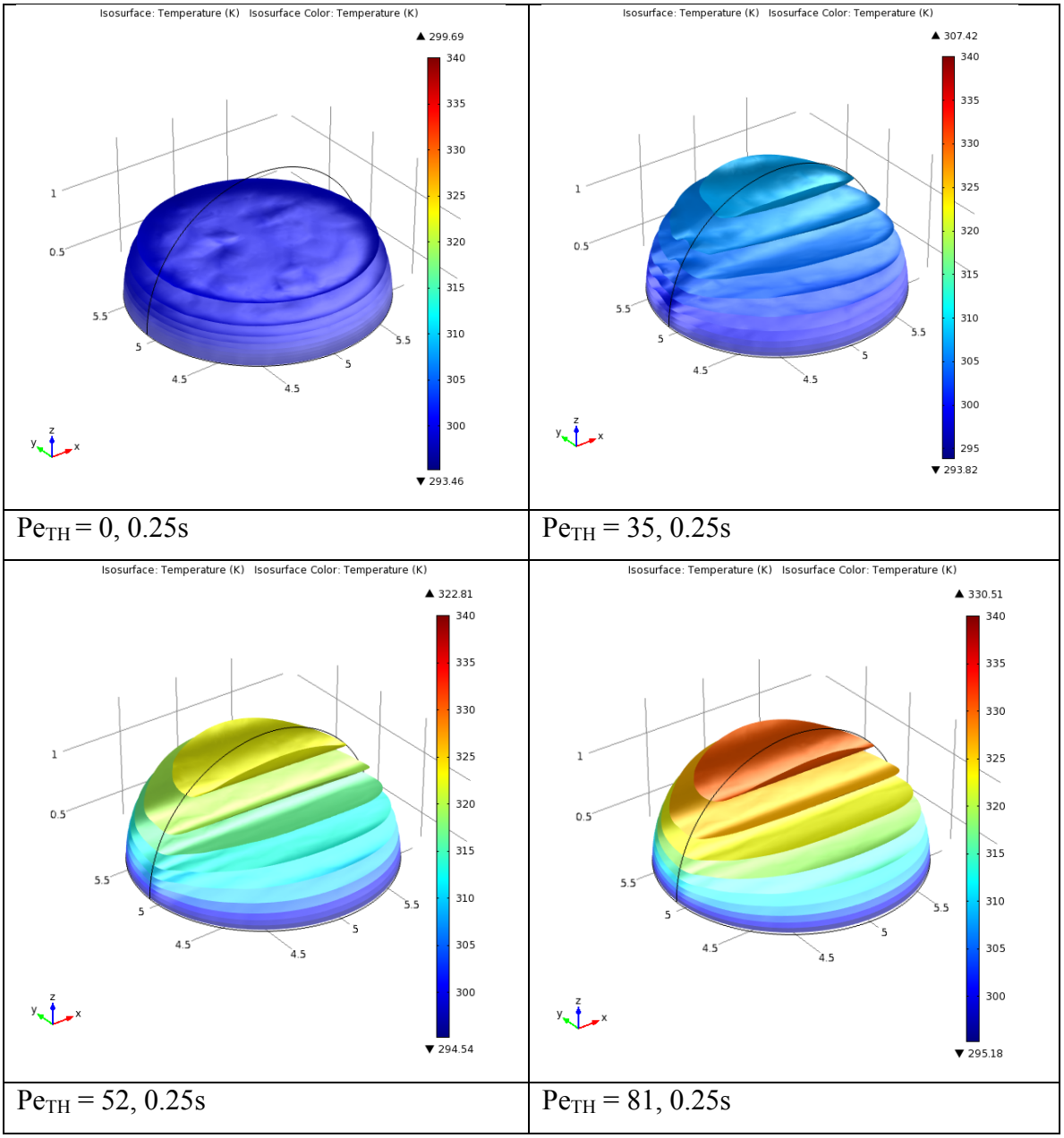


$Pe_{TH}$ = 0, 0.25s | $Pe_{TH}$ = 35, 0.25s

$Pe_{TH}$ = 52, 0.25s | $Pe_{TH}$ = 81, 0.25s

**Figure 6-6: Evaluation of droplet thermal gradient for increasing Péclet number for 0.2µl with thermal power of 0.23 W at 0.25 s.**

At a Péclet number of zero, only conduction exists; at t = 0.25 only a temperature rise of 7°C is observed. With increasing Péclet numbers, the time to reach a steady state

decreases and at $Pe_{TH}$ = 81, the droplet is seen to increase in temperature by 45°C at 0.05 s. Calculating the Péclet number from data in Figure 6-3 for a 45°C rise, the $Pe_{TH}$ value is 78, which is within 4% of the value obtained from simulation. Comparing the temperature rise to experimental data (Figure 6-7), we can see that there is close correlation to the time to reach a steady state between the simulated and experimental data. This data shows that forced convection is the predominant force, as only at a higher Péclet number, the simulation is shown to match experimental data. Since the Péclet number is directly linked to velocity, it is clear that the SAW streaming is the driving diffusion force, reducing the time for the droplet to reach a steady state. This shows that the SH-SAWs are able to thermally heat sessile droplets with high rates of diffusion, indicating that they can be used to accurately control the temperature in a sessile droplet with a rapid heating rate.

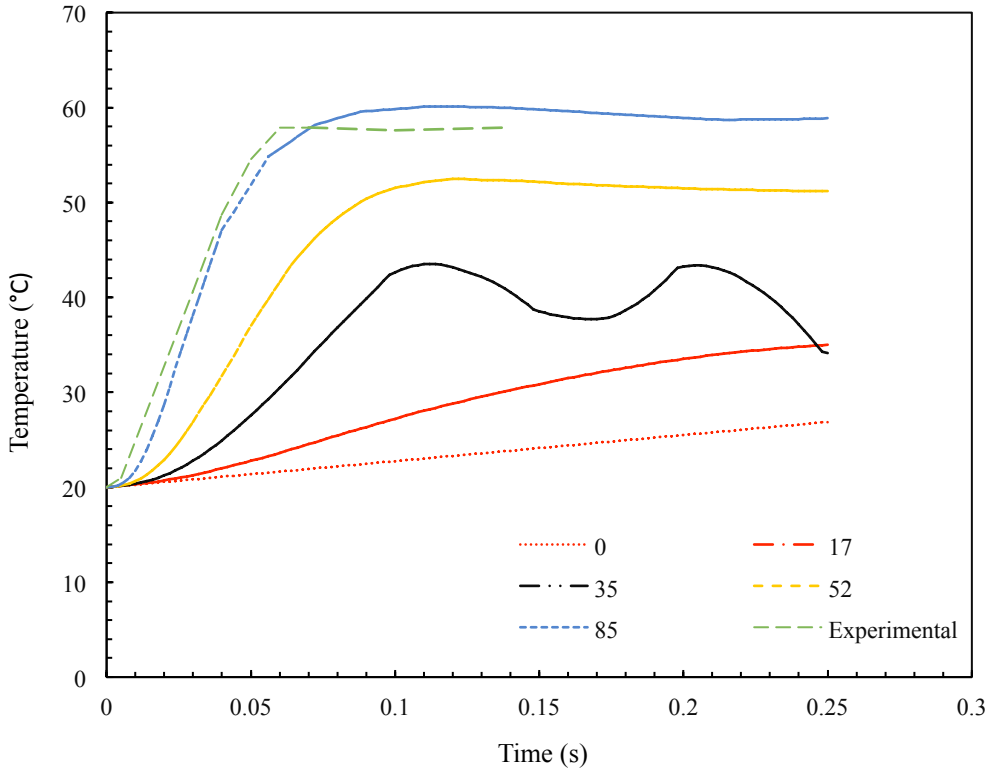


**Figure 6-7: Temperature increase in droplet for increasing Péclet numbers for 0.2 µl droplet with thermal power of 0.23 W. Simulation data is compared to experimental result.**

With a correlation between the thermal and experimental data, the thermal efficiency of SAW heating was analysed.

Using experimental data, an empirical relationship was derived between temperature increase, Péclet number and thermal power dissipated ($Q$). The power input was modelled

for the varying temperature rises for a droplet size of 2 µl using data shown in Figure 6-2. The efficiency of SAW streaming was calculated using the following relationship

$$\eta_{SAWTH} = \frac{P_{TH}}{P_{IDT}} \qquad 6\text{-}4$$

Where $P_{TH}$ is the thermal energy dissipated in the droplet and $P_{IDT}$ is the power applied to the IDT. Simulating the power required to give the associated temperature increase in 2 µl droplet, the SH-SAW wave was observed to have a thermal heating efficiency of between 2% - 6%. Higher efficiencies were observed at lower powers with the efficiency decreasing as a logarithmic function of power (Figure **6-8**). It is noted that the SH-SAW generally has a low efficiency. However, as this is the first report for a calculation has been made, there is limited data for a comparison.

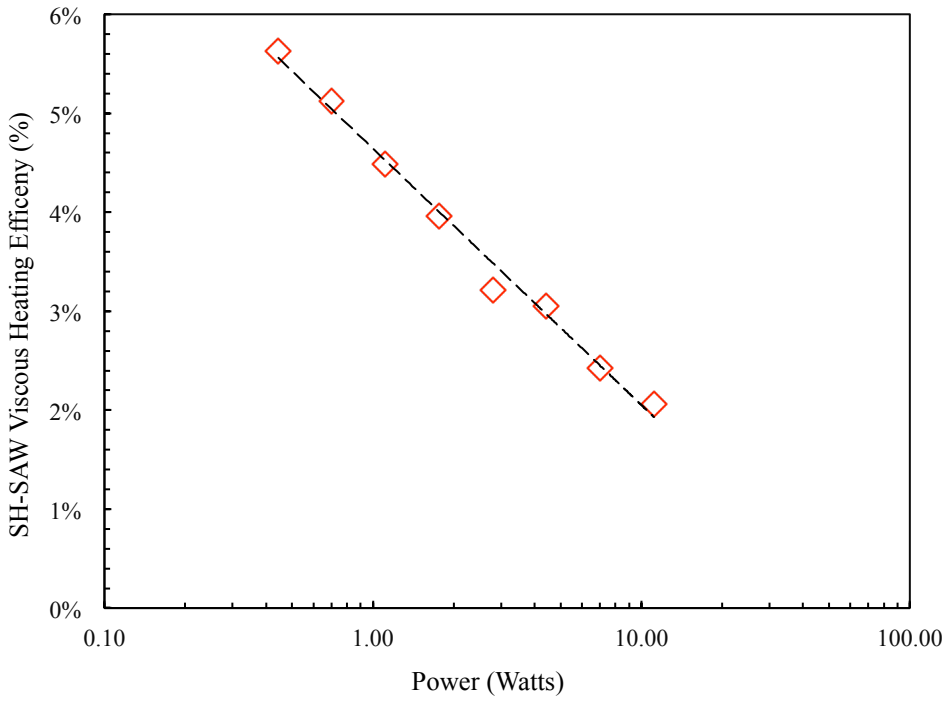


**Figure 6-8: Efficiency of thermal heating on 36°YX $LiTaO_3$ with a 2 µl droplet. Calculated input IDT power was varied from 0.2 W – 12 W.**

## 6.3 Dual Inline Droplet Analysis

For SAW streaming using the SH-SAW, it was observed that when droplets were placed in series, the same velocity is observed in both droplets with a minimal attenuation of the wave observed in the first droplet (Figure 6-9). A thermal analysis was undertaken to examine the thermal behaviour of the droplet in the same configuration.

Two droplets of 4 µl were pipetted onto the 36ºYX $LiTaO_3$ substrate with a distance of 5 mm between the droplets. A power of 1 W was applied until a steady state temperature was reached.

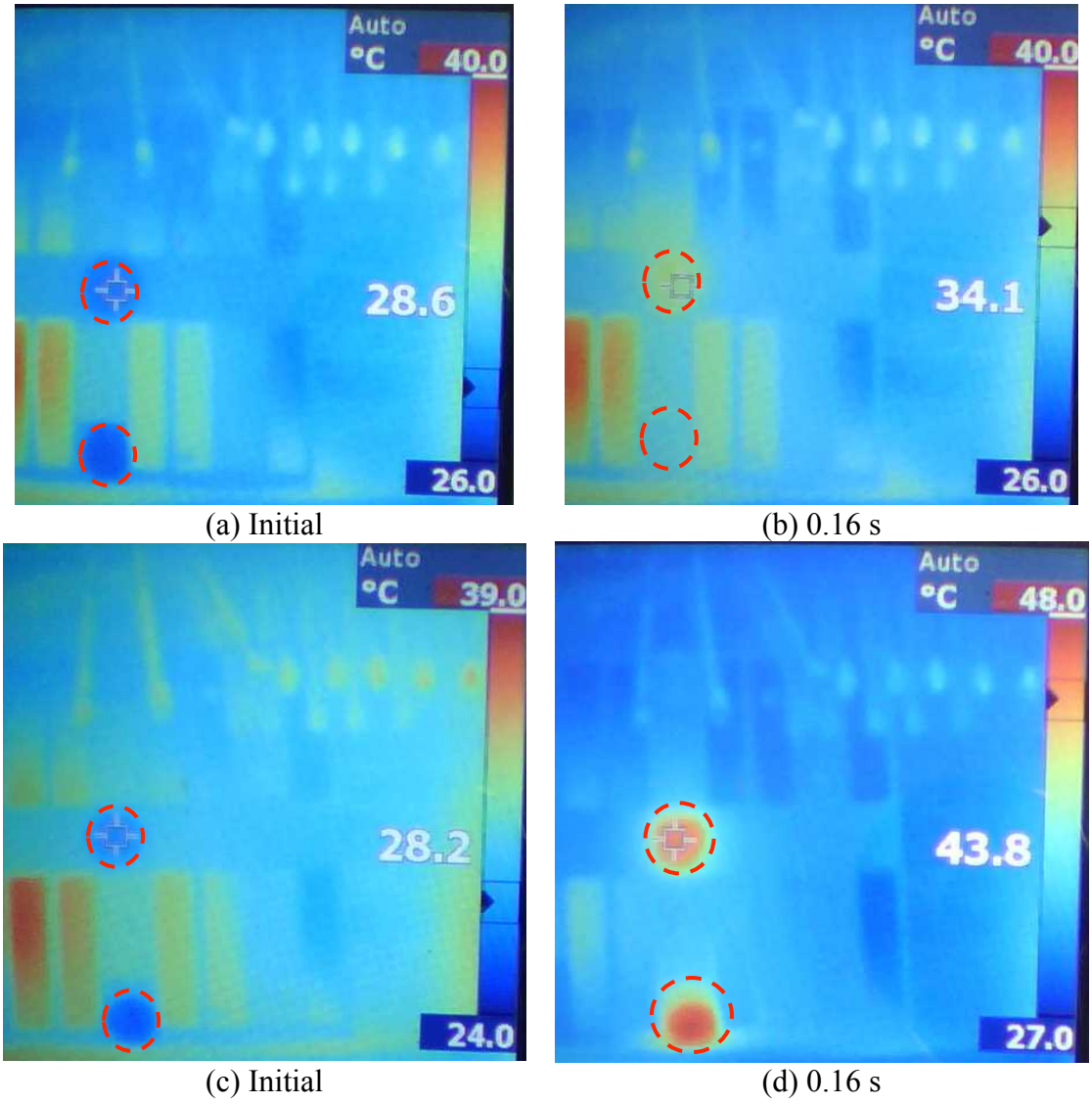


**Figure 6-9: Temperature increase in two droplets (4 µl) placed in series (a+c) on 36ºYX $LiTaO_3$, (b) temperature in both droplets at t = 0.16 s excited with Rayleigh Wave, (d) temperature in both droplets at t=0.16s excited with SH-SAW wave**

For the droplets excited with the SH-SAW wave, the temperature was observed to be within 1°C between both the droplets showing minimal attenuation in the first droplet. The thermal heating was also observed to be uniform between both the droplets. For the droplet excited with the Rayleigh wave, all the energy was observed to dissipate in the first droplet in the propagation direction of the SAW wave. Heating of less than 0.5°C was observed in the second droplet. This correlates well with the high attenuation of the Rayleigh wave.

## 6.4 Thermal Analysis of Droplet Nebulisation and Atomisation

Whist nebulisation and atomisation is observed with the SH-SAW wave (results presented in Chapter 5) the mechanism of atomisation & nebulisation were not verified. Kondoh et al. previously used thermal analysis techniques to verify that atomisation with a Rayleigh wave was a result of the leaky wave propagation and not heating [151].

In order to verify the mechanism of atomisation and nebulisation, the thermal set-up was used to measure the temperature of the droplet under a SH-SAW propagation. For the experiment, the 36ºYX $LiTaO_3$ substrate was excited with $P_{IDT}$ = 4 W & 12 W, and the temperature was recorded using the FLIR thermal camera. This was repeated with a 2 µl droplet placed on the substrate.

At $P_{IDT}$ = 4W, nebulisation was seen to occur at 0.22 s, at which the temperature of the droplet was recorded at 48.4°C, with a decrease of 2°C during the nebulisation process. Measuring the surface temperature of the device without any droplet, within the same time frame, a temperature of 30.5°C was recorded (Figure 6-10). It is clear that the nebulisation under the action of the SH-SAW is not caused by the acoustic wave heating effect or boiling.

Nebulisation was observed at $P_{IDT}$ > 12 W, and the experiment was repeated with this power and the results recorded. Atomisation was seen to occur at 0.12 s with a maximum temperature of 64.6°C for about one minute. Measuring the substrate temperature at the same power and time, a temperature of 38.0°C was recorded. Correlating with the nebulisation results it is clear that atomisation occurs without boiling.

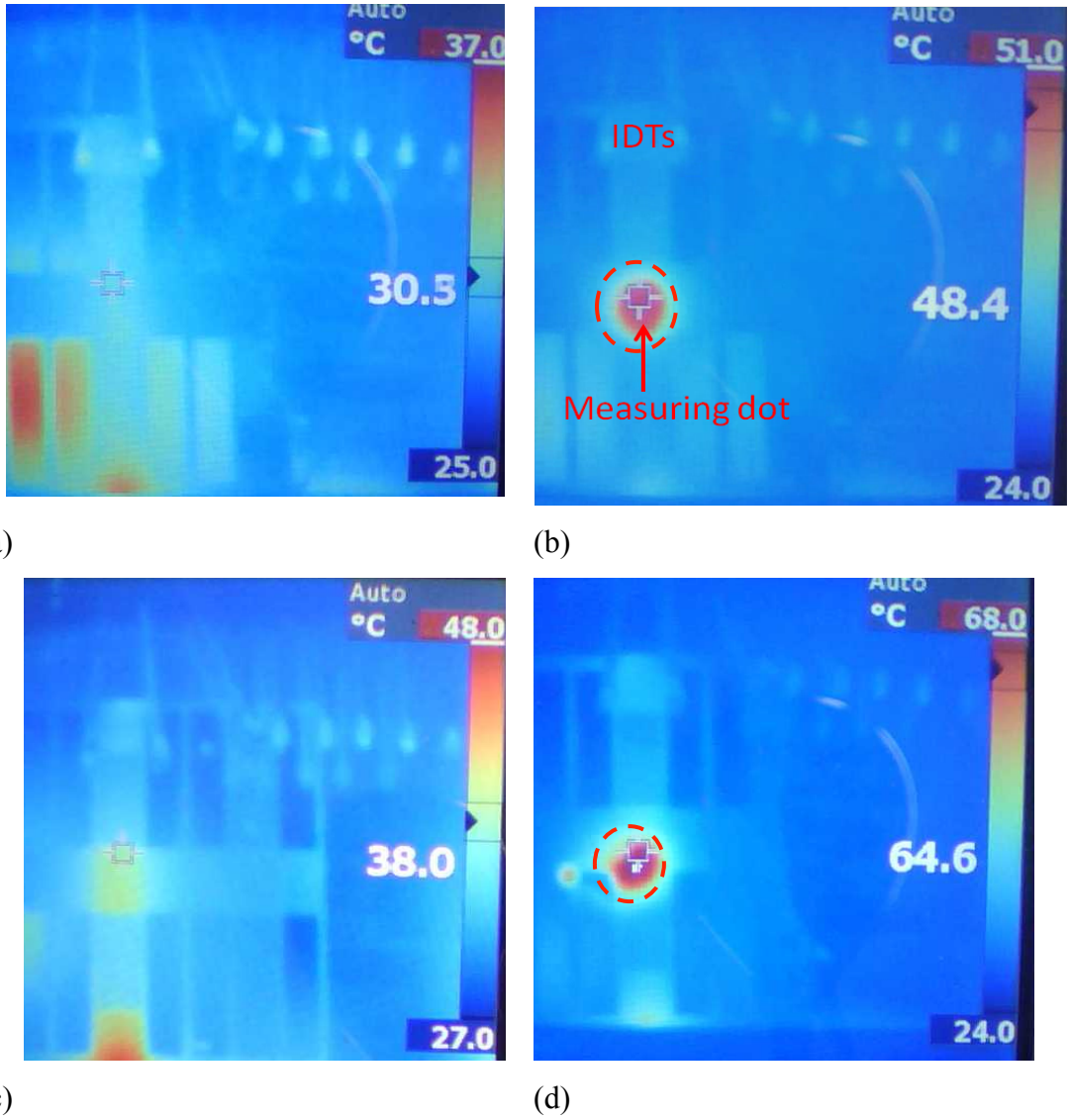


**Figure 6-10: (a) 36°YX $LiTaO_3$ substrate temperature with no droplet, $P_{IDT}$=4 W (b) 36°YX $LiTaO_3$ substrate with droplet in situ at start of atomisation process, $P_{IDT}$=4 W. (c) 3 6°YX $LiTaO_3$ substrate temperature with no droplet, $P_{IDT}$=12 W (d) 36°YX $LiTaO_3$ substrate with droplet in situ at start of nebulisation process, $P_{IDT}$=12 W**

Acoustic heating is a common phenomenon in SAW based devices, which will affect the performance of acoustic streaming, pumping and nebulisation. Increasing surface temperature could shift the resonant frequency of a SAW device, which is normally treated as a constant during SAW microfluidic/sensing experiments. Increasing the surface temperature could also cause slight changes in the surface contact angles of the sessile droplet on the SAW device surface, thus influencing the nebulisation processes. In order to evaluate the acoustic heating effect on the nebulisation process in this study, the surface temperature of a water droplet of 2 µL, on the surface of the SAW device, were recorded using an IR camera within a duration of one minute at different SAW frequencies and powers. The temperature was observed to increase at the initial period, but gradually reached a saturated value. The higher the RF power applied, the higher the

maximum temperature. The maximum temperature recorded was approximately 70$^{o}$C at a high power of 30 W after several minutes.

## 6.5 Summary

Reviewing the thermal analysis of the SH-SAW propagation within sessile droplets placed on the 36ºYX $LiTaO_3$ crystal, following conclusions can be summarised:

- Temperature within a droplet, excited by SH-SAW wave inducing viscous heating, varied as a linear function of power.
- Maximum temperature rise of 38°C observed in 2µl droplet with SH-SAW wave at a power of 12W.
- Comparison of droplet heating vs. droplet size for Rayleigh and SH-SAW wave demonstrated that for increasing droplet sizes, with the SH-SAW wave, the internal temperature was seen to increase. No increase was observed for the Rayleigh wave.
- For powers from 0 dBm to 6 dBm the time to reach thermal equilibrium for a 2µl droplet was observed to be less than 0.1 s for all cases.
- Calculation of Péclet number for droplet sizes of 2µl -15µl indicated that forced convection was the dominant method for thermal advection with SH-SAW and Rayleigh wave excited droplets.
- FEA numerical simulations developed to model convection with SAW streaming correlated with experimental data showing convection as dominate advection mechanism.
- Using numerical model efficiency of SAW heating determined to be 2% - 6% for the SH-SAW wave.
- For droplets placed in-line, Rayleigh wave attenuates in first droplet correlating with acoustic streaming results. For SH-SAW both droplets were observed to reach temperatures within 1°C, this again correlates with streaming measurements where minimal damping was observed.

Thermal analysis of nebulisation and atomisation can be summarised as follows:

- Maximum temperature observed during nebulisation of 48.4°C, $P_{IDT}$ = 4W, demonstrating nebulisation is not an effect of droplet boiling for the SH-SAW wave.

- At higher powers of > 12W maximum temperature of 64.6°C recorded. This is below the point at which any second order effects or phase change may occur.

In conclusion, thermal analysis of the SH-SAW heating showed that the SH-SAW wave is suitable for heating droplets exhibiting high rates of advection. This linear control and high temperatures show applicability of the SH-SAW for PCR (Polymerase Chain Reaction); in which the temperature is periodically controlled with a profile of $50^{o}C \rightarrow 95^{o}C \rightarrow 60^{o}C$ [152]. In contrast to the Rayleigh wave, high temperatures may be achieved with the SH-SAW due to the high power threshold for pumping. In-line analysis identified that multiple reactions may be undertaken by a single IDT.

# Chapter 7. SH-SAW Lab-on-chip for Bio-Sensing

With fluid manipulation and thermal heating of sessile droplets outlined in Chapter 5 and 6 respectively, this section will describe experiments related to sensing with the SH-SAW and integrating with fluid handling and management on a single substrate.

## 7.1 SH-SAW Mass and Bio-Sensing

Bio-sensing and mass loading sensing has been investigated using both Rayleigh wave and SH-SAW modes [153]. Sensing occurs by attenuation of the wave by mass loading, causing small changes in resonance frequencies which can be detected by the frequency change of the SAW device [18], [53], [56], [62], [154], [155]. As previous described in Chapter 2 the Love mode SH-SAW devices have been shown to the most promising for bio-sensing applications. For a Love Mode device a waveguide layer, consisting of a dielectric material, is deposited on the surface where acoustic energy is attenuated in this layer. The mass sensitivity ($S_m$) of acoustic wave sensors, and more specifically Love mode sensors, is defined as the relative change in the frequency due to the mass loading divided by the surface density of the deposited mass:

$$S_m = \lim_{m \to 0} \left( \frac{\frac{\Delta f}{f_0}}{\frac{\Delta m}{A}} \right) \tag{7-1}$$

where $\Delta f$ is the frequency change, $f_0$ the operating frequency and $\Delta m/A$ the deposited mass per unit area [156]–[159].

For calculating thin layers first-order perturbation theory can be used to calculate the change of the operational frequency. Thus the change in frequency is given by [56]:

$$\Delta f = -\frac{V}{4} f_o \rho d \left[ 1 - \left( \frac{V}{V_{S2}} \right)^2 \right] \tag{7-2}$$

The frequency shift depends on the acoustic phase velocity in the media (V), the operational frequency $f_0$, $\rho d$ which represent the mass loading per unit area. The following term 1- ($V / V_{s2}$) represents a reduction in mass sensitivity with the increase of the thickness of the layer.

### 7.1.1 Characterisation of 36°YX $LiTaO_3$ Sensitivity to Mass Loading

With numerical simulation in Chapter 4 showing that bio-sensing and mixing may be obtained on the 36ºYX $LiTaO_3$ crystal, the perturbation of the sensing signal will be investigate to understand the feasibility of combining the two microfluidic functions on a single substrate.

To characterise the mass loading effect on the crystal an initial experiment was undertaken to investigate the frequency change with mass loading due to various droplets. IDT design 3 was used (as described in Chapter 3) with a fundamental frequency of 63 MHz and IDT aperture of 1.0 mm was used. The oscillator loop, as described in Chapter 3, was used to measure the frequency change with the respective mass loading of the droplets. Droplets of deionised water with the following volumes: 0.1µl, 0.5 µl, 1µl, l.5µl, 2µl, 3µl, 5µl, 8µl, 10µl, 12µl, 14µl and 16 µl were loaded onto the surface and the relative frequency change was measured.

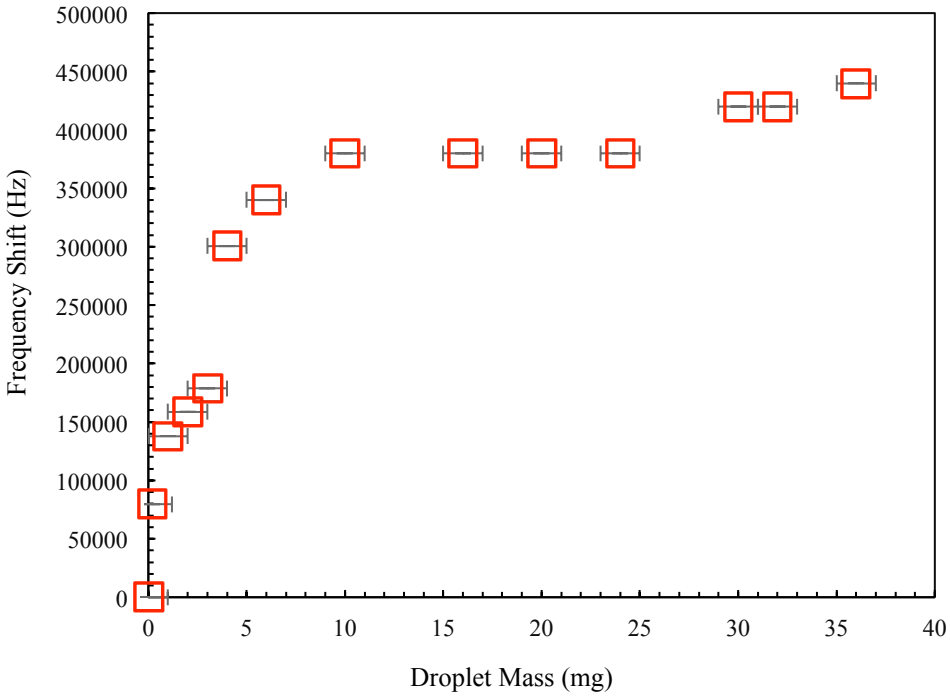


**Figure 7-1: Mass loading vs. frequency change of various water droplets from 0.1 µl – 16 µl deposited on 36ºYX $LiTaO_3$ substrate.**

A non-linear relation was observed for the change in frequency with the mass loading from the various droplet volumes. At 5 mg and below a frequency shift of 350 kHz was observed. From 5mg to 35 mg a frequency shift of only 350 kHz to 450 kHz was recorded (Figure 7-1). It is known that the SH-SAW devices that the wave only

attenuates within 1-2 wavelengths of the surface therefore mass loading of the device will only occur within a thin layer. Mass loading based on the attenuation will be insensitive to droplet volume and dependent on the wetted surface area.

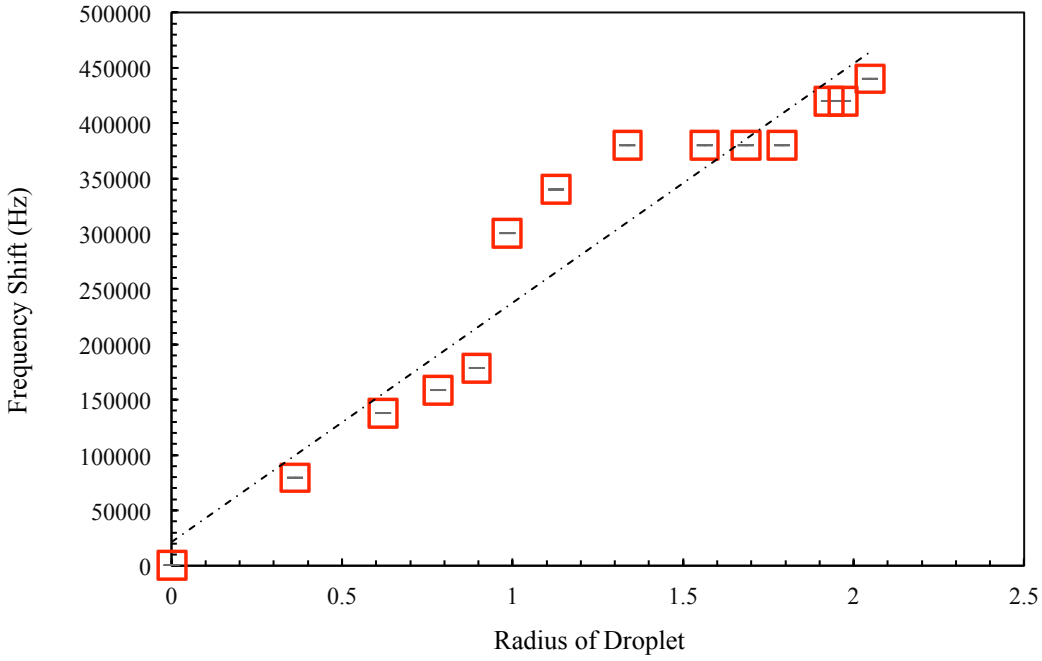


**Figure 7-2: Radius of Droplet vs. frequency change of various water droplets from 0.1 µl – 16 µl deposited on 36°YX $LiTaO_3$ substrate.**

Plotting the frequency change against the droplet radius we can observe there is a linear relationship, confirming that the wave is attenuating in a thin layer. For Love mode devices the mass sensitivity has been reported as varying between 0.4 – 4 $cm^2/ng$ [156]–[159]. Calculating the sensitivity, (Eqn. 7.1) based on the bulk droplet mass, the range is $5.096 \times 10^{-5}$ $cm^2/ng$ to $4.9 \times 10^{-5}$ $cm^2/ng$, and clearly this is below the expected reported values. Calculating the decay length of the wave with Eqn. 5-5, we can estimate the SH-SAW wave should attenuate within 70 µm of the surface of the substrate. Assuming a 70 µm thick disc of the droplet fluid loaded on the surface, we can now calculate the sensitivity, which is in the range of 0.175 $cm^2/ng$ – 0.923 $cm^2/ng$. This value correlates well with published values, and previous modelling in Chapter 5, that the shear wave attenuates within a thin layer described by Eqn. 5-5.

### 7.1.2 Shear Wave Bio-Sensing and Streaming

Bio-sensing using Love mode sensors has been reported by numerous authors, a limitation identified of bio-sensing performance is the diffusion of analytes near the sensing surface [71]. Methods investigated to improve diffusion of the analyte by pervious authors include electro-thermal stirring and more recently authors have proposed using Rayleigh wave SAW to induce micro-stirring and diffusion [75]. Whilst the mechanics of the diffusion effects of the SAW steaming have been well characterised, improving the binding interaction for a streptavidin\biotin system by 2 times [160], no method has been proposed to simultaneously combine SAW streaming and bio-sensing on a single substrate.

Numerical investigations in Chapter 4 identified that simultaneous bio-sensing and mixing may be possible using Euler angle (0,36,0) for sensing and a weak Rayleigh wave component for streaming in the direction (90,36,0). To investigate if streaming and bio-sensing simultaneously can be realised; the following SAW devices were fabricates with 4 IDT's aligned with Euler angles (0,36,0) and (90,36,0). As previously described in Chapter 3 a network analyser and signal generator were used with a 4 IDT SAW design. One pair of IDT's were used for the bio-sensing (0,36,0) whilst a third orthogonal IDT was used to excite the droplet to invoke mixing (90,36,0). The frequency shift was monitored continuously to detect any perturbation of the signal, due to the active mixing and droplet displacement. The set-up used is shown below in Figure 7-3.

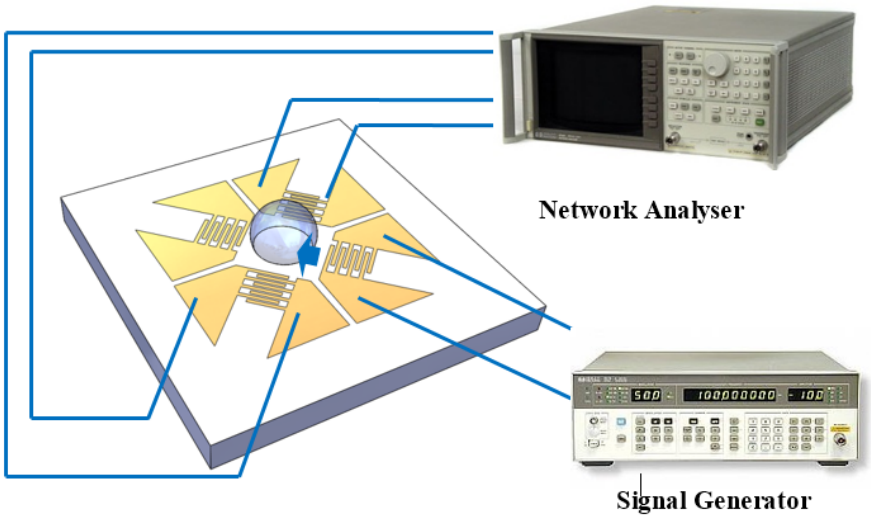


**Figure 7-3: *In Situ* biosensing and mixing using Euler angle for sensing (0,36,0) and the streaming direction utilised was (90,36,0). Arrow indicates streaming direction.**

The frequency was observed to shift by 20 kHz when a 1 µl droplet was placed on the surface. A power of 0.2 W was applied to the streaming IDT, with a frequency 97 MHz, and a streaming velocity of 5 mm/s was recorded with a weak Rayleigh wave mode observed. This correlates with modelled FEA data in Chapter 4, where a weak Rayleigh wave mode is predicted at Euler angle was (90,36,0).

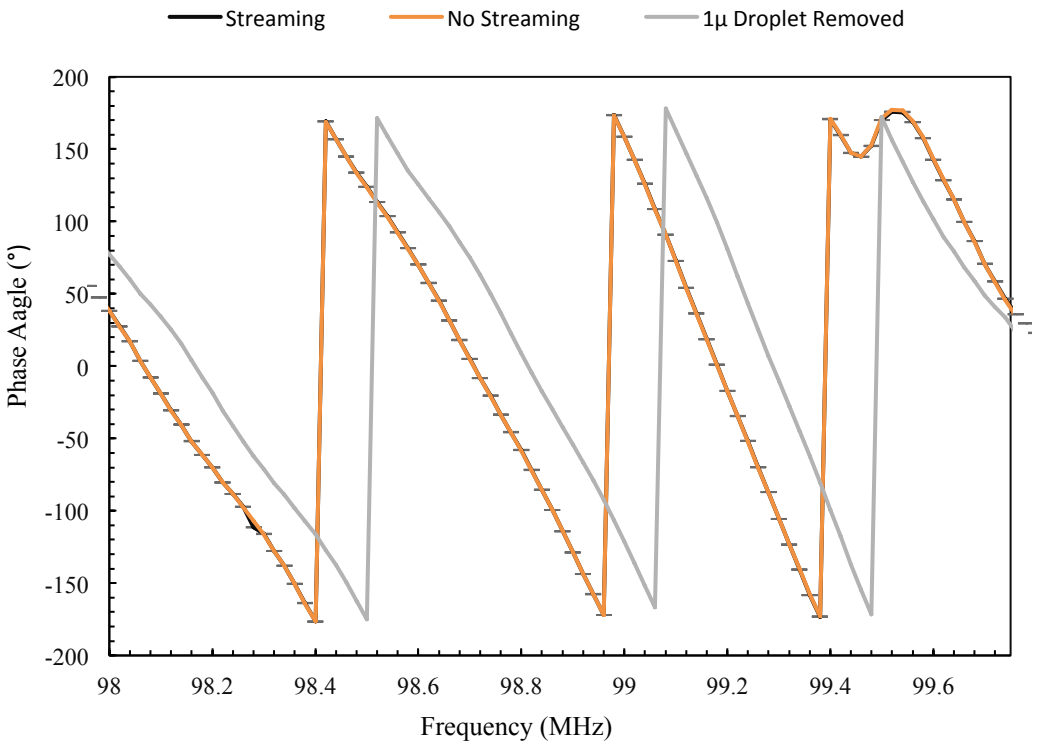


**Figure 7-4: Phase angle change for 36ºYX $LiTaO_3$ with and without 1 µl droplet and with acoustic streaming at 23 dBm.**

Minimal frequency shift was observed with the streaming velocity of 5 mm with only a 200 Hz change in frequency observed. Using Equation 5-5 we can estimate this to be a loss of $2.9 \times 10^{-5}$ $cm^2/ng$ in sensitivity, which is below the normal level of detectable mass.

These results show that Love mode sensing and streaming are possible on a single device utilising the 36ºYX $LiTaO_3$ crystal. Minimal change to the in-situ sensing performance was observed providing the opportunity to increase binding and reaction time of bio-sensing with SAW devices.

## 7.2 Droplet Manipulation Integration on Shear Wave SAW Sensor

Various methods of integration of bio-sensing with fluid kinetics and handling have been investigated, including integration with fluidic channels and using SAW Rayleigh wave for pumping [161], [162]. One of the most promising areas of fluid integration is the use of electro-wetting-on-dielectrics (EWOD). EWOD devices generally consist of electrode arrays covered by a dielectric insulation material and a thin layer of a hydrophobic material such as Teflon-AF or CYTOP. By applying a DC voltage to an electrode, which attracts charges to the liquid-dielectric interface, the hydrophobic surface is changed to hydrophilic, thus attracting micro-droplets onto the addressed electrode [85], [86], [163]–[165]. Whilst Rayleigh wave mode devices have been shown to be effective at fluid manipulation the waves are rapidly attenuated in the liquid media and this makes them unsuitable for use as bio-sensing elements. Though pumping was realised with the SH-SAW the ability to move droplets was still limited by the complex wave propagation of the SH-SAW. Fortunately, electro-wetting on dielectric (EWOD) can be integrated with SAW to efficiently pre-position droplets, which overcomes the problem that there may not be sufficient force available from the SAW to move the droplet in a stable and precise manner.

Devices were fabricated using design A of the SAW mask outlined in Chapter 3, with the 36ºYX $LiTaO_3$ wafer. In addition to the standard SAW lift-off process the dielectric stack was fabricated using the anodic $Ta_2O_5$ for low voltage EWOD operation. The additional process steps were: before lift-off; deposition of 0.45 µm thick layer of $Ta_2O_5$; after lift-off anodisation of EWOD electrodes and finally a layer of hydrophobic CYTOP is spin-coated and cured Figure 7-5.

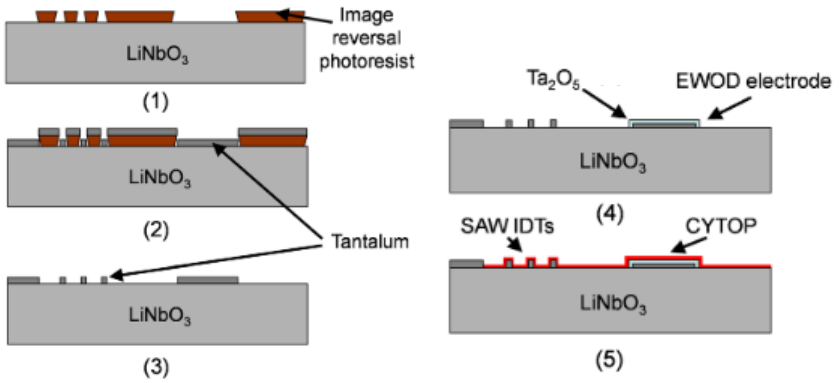


**Figure 7-5: EWOD lift-off process for integration with SH-SAW**

To demonstrate the possible integration of EWOD and SH-SAW sensing function, the possibility of sensing droplet position was investigated. As previously shown the SAW devices is able to accurately detect not only if the droplet is present but an estimation of the droplet volume based of the attenuation of the SH-SAW wave.

For position and mass sensing, the SH-SAW device was used as a resonator in an oscillator circuit connected to an RF amplifier. The IDT's with an aperture of 2500 µm, precocity of 16 µm (64.33Mhz SH-SAW) and 30 pairs were used. A frequency counter was used to monitor the oscillation frequency. This set-up is described in Chapter 3 and shown in Figure 3-11 and Figure 3-12. The change of the resonant frequency was used as the sensing signal, which is sensitive to the mass loading, elasticity, viscosity, permittivity, and conductivity change on the SH-SAW surface. A 5 µl DI water droplet was applied to the 1st EWOD electrode (a) and 60 V was applied to the middle electrode which resulted in a change of wetting force "attracting" the droplet. The voltage was then switched off and 60 V was applied to the third electrode moving the droplet to the final position.

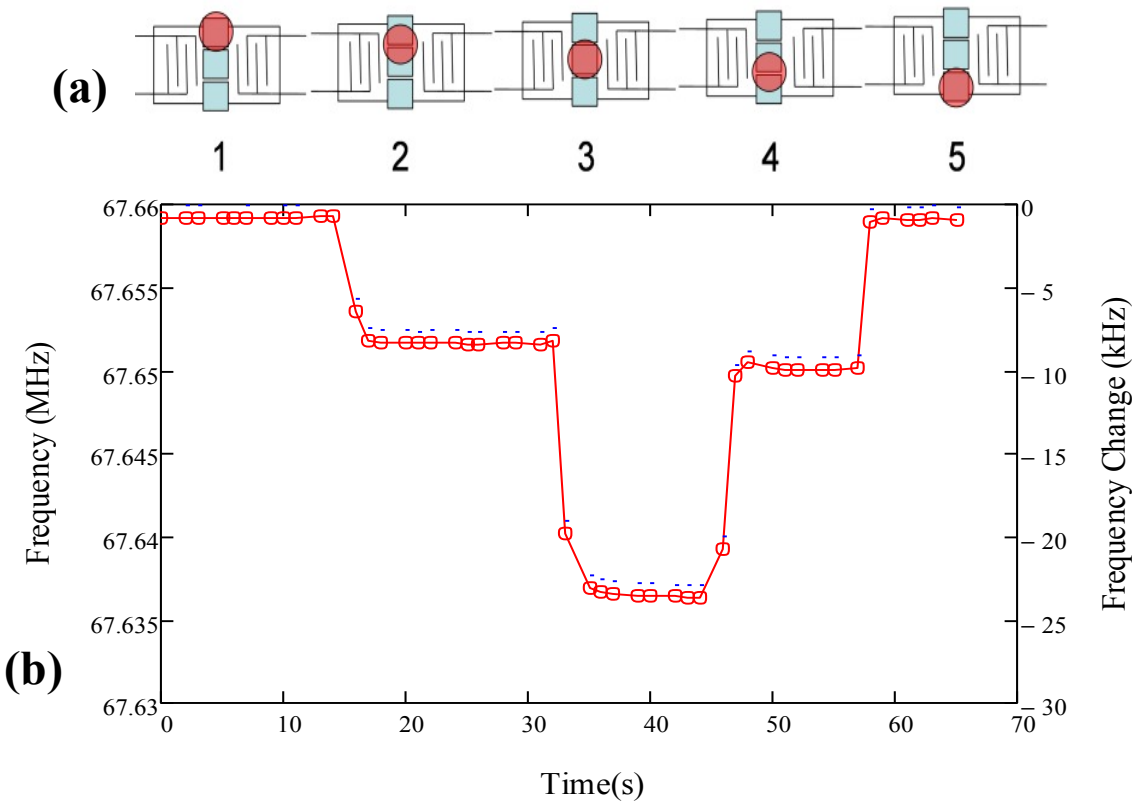


**Figure 7-6: (a) Location of droplet with (b) measured frequency when the droplet is located at different positions. 1 & 5 droplet out of SAW propagation path, 2 & 4 at the side of the SAW wave, 3 at the centre of the SAW wave.**

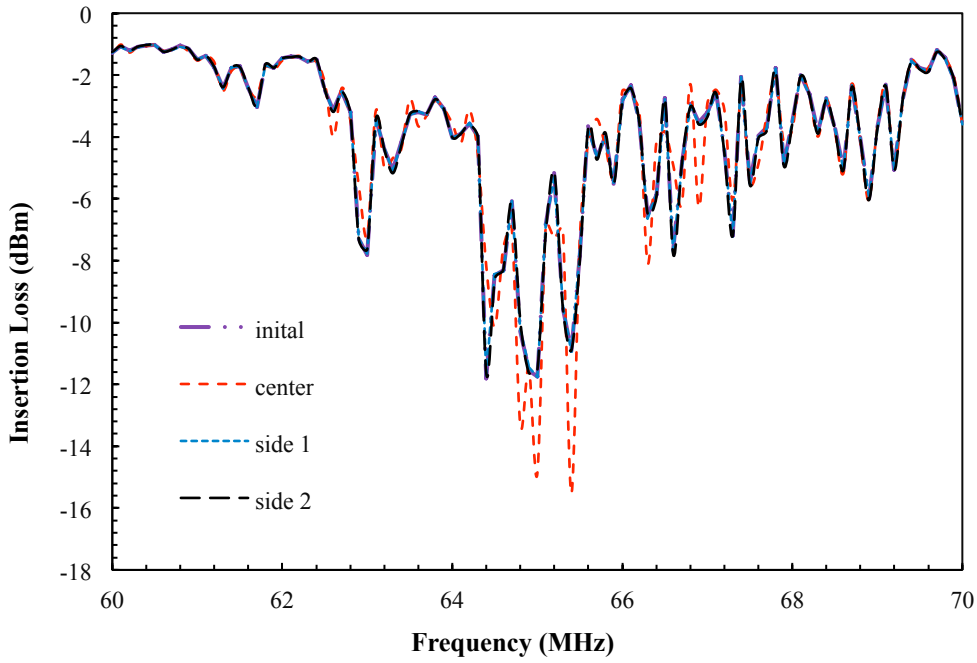


**Figure 7-7: Insertion Loss Measurement at droplet locations on 36°YX $LiTaO_3$ Substrate**

Measuring transmission between the two IDT's and the frequency change in the oscillator loop circuit the following results are obtained in Figure 7-6 (b): position 1 - 2 a change of 8.5 kHz is observed; from position 2 – 3 a change of 14.7 kHz is observed; from position 3 – 4 only a change of 13 kHZ is observed showing the droplet stability had changed with a slightly higher mass remaining on the middle electrode; from position 4 - 5 the frequency shift is seen to return to the initial position. It is evident that using the oscillator loop configuration position sensing of the droplet using the SH-SAW wave can be clearly determined. Knowing the distance, velocity can easily be determined providing an effective way to measure the spatial location of droplets and if droplets are present. Some initial characterisation of the SAW device may also enable the mass of droplet on the surface to be calculated providing the ability to measure nebulisation, ejection and evaporation processes.

A comparison was made to the insertion loss measurements as an alternative method for position sensing. A clear change in attention can be observed at the primary resonance mode around 65Mhz of around 4dBm between the centre position and the two side IDT's with the centre position shown high attention due to the droplet loading. Whilst this method can be used it lacks the time information which reduce the usefulness of the data.

## 7.3 Summary

Reviewing the bio-sensing and mass sensing properties of the SH-SAW devices the conclusions can be summarised as follows:

- SH-SAW device shown to be suitable for detection of mass loading from varying droplet volumes, to date only bio-detection has been reported.
- Linear relationship shown to exist between droplet radius and frequency shift, enabling the possibility to accurately predict droplet size on surface.
- SH-SAW seen to attenuate within a 70μm thin layer in the droplet. This compares well to modelled data of mass loading sensitivity values, assuming the thin layer of attenuation. Comparison to published values at 0.175 $cm^2/ng$ – 0.923 $cm^2/ng$ shows good correlation of this method.
- Simultaneous in-situ and sensing were realised on the 36ºYX $LiTaO_3$ with two IDT's rotated at 90°. The main propagation direction was Euler angle (0,36,0) and the streaming direction utilised was (90,36,0).
- With a streaming velocity of 5mm/s a calculated sensitivity change of $2.9 \times 10^{-5}$ $cm^2/ng$ was observed. This is insignificant compared to normal detectible values for mass loading of biological agents.
- Integration of SH-SAW and EWOD on a single device was realised with EWOD digital manipulation combined with the SH-SAW device to sense mass loading.
- Digital droplet position detection was possible with the ability to sense the spatial location and velocity of the droplet using the SH-SAW device in an oscillator loop. Droplet position was also determined with insertion loss measurements but without any time information provided less meaningful data and requires more post process.

In conclusion, the SH-SAW was shown to effectively measure the mass loading from various droplets with a relationship determined for the prediction of droplet volume. In-sit mixing showed that bio-sensing and mixing can be realised using the SH-SAW on a single substrate. Finally integration with EWOD provides a method for digital fluidics droplet sensing showing that the SH-SAW in an oscillation loop is an optimal method for droplet location detection.

# Chapter 8. Conclusions

Motivated by the desire to develop cost-effective and integrated lab-on-chip solution for rapid diagnostic of pathogens, this work describes the investigation of the SH-SAW wave propagation on piezoelectric substrates and various microfluidic functions that can be realised. The main conclusions can be classified into four categories.

1. ***Numerical Modelling of SH-SAW Wave Propagation:***
   (1) A finite element model was developed of the SH-SAW wave propagation on the Y cut 36ºYX $LiTaO_3$ crystal and accuracy verified against experimental data.
   (2) Only a weak vertical component of the SH-SAW was found, less that 4% of the shear wave component, excluding the possibility of any fluidic functions from the vertical wave.
   (3) Linear relationship was established for wave amplitude and input power, showing the applicability for tuneable microfluidic functions.
   (4) Simulation of the Rayleigh wave mode showed a mixed vertical component which indicated that this lower order mode would be suitable for microfluidic functions.
   (5) For bio-sensing the Euler angle (0,36,0) was determined to be the optimum cut for mass detection. Analysis of the (90,36,0) direction, where IDT's are patterned at 90° to the optimum cut, exhibited two Rayleigh wave modes which indicates mixing and diffusion may be realised whilst sensing on a single substrate.
2. ***Development of Numerical and Theoretical Model for SH-SAW Acoustic Propagation:***
   *(1)* An initial theory was proposed for SH-SAW acoustic streaming mechanism based on fluid oscillation at the boundary interface between the droplet and piezo-electric substrate. Entrapped fluid of a few tens of nanometres compressing against the air/water interface was proposed for the mechanism of acoustic streaming.
   (2) Investigation of the streaming behaviour was undertaken using a mixed physics model, solving both Navier-Stoke equation and acoustic propagation, showed a clear dispersion of an acoustic wave within the droplet which is comparable to experimental streaming velocities.

(3) A simplified 2D model was able to model flow behaviours and correlate with patterns observed in experimental results, further validating the boundary oscillation theory.

(4) In contrast to Rayleigh wave, the SH-SAW wave was seen to have higher streaming velocities with larger volume droplets, this can only be explained with a non-damped wave which is acting on the boundary. This behaviour demonstrates the difference in the wave propagation compared with the Rayleigh wave, where a vertically polarised wave is damped when it contacts a droplet. This results in a fixed streaming power which is relatively independent across droplet sizes with larger droplets exhibiting reduced streaming for the same power. Since the SH-SAW wave acts across the boundary of the droplet, larger droplet will have higher energy transfer with increased streaming velocities. This mechanism shows that the SH-SAW will provide more configurable streaming behaviour over a range of droplet sizes.

***3. Fluidic Functions Enabled with SH-SAW Wave:***

(1) A wide range of fluidic functions were realised on the 36ºYX $LiTaO_3$ crystal including, streaming, pumping, nebulisation/atomisation, ejection and thermal heating.

(2) Streaming observed with the SH-SAW wave was around 7 times lower in magnitude compared to the Rayleigh wave at small droplet volumes but this reduced to around 2 times at volumes greater than 15 µl. This result shows the applicability of the SH-SAW wave for streaming in mesofluidics. Comparing the Rayleigh wave to the shear wave, it was noted that droplets can be streaming inline due to the low attenuation of the wave enabling the possibility of serial fluidics with a single IDT.

(3) Nebulisation was observed with the SH-SAW wave with a maximum rate of 0.2 µl /s at a power of 6.7 W. The nebulisation characteristics with the SH-SAW were substantially different to the Rayleigh wave mechanism with nebulisation of the droplet possible at a distance of greater than 5 mm from the IDT as where Rayleigh wave droplets only showed nebulisation in the direct propagation path. Thermal characterisation of the process showed that the droplet reached a maximum temperature of 64ºC at 12 W demonstrating that nebulisation and atomisation are due to the break-up of surface tension by the acoustic wave rather than by any boiling phenomenon.

(4) Ejection was observed with the SH-SAW at powers great than 5 W on a hydrophobically treated surface. Comparing to Rayleigh wave ejection, no pumping occurred and the ejection angle was lateral to the IDT's in contrast to the Rayleigh wave devices where ejection occurs at an angle of 22.6$^{o}$ towards the SAW propagation direction. Interesting was the different mechanism of wave propagation due to the boundary oscillation.

(5) Thermo-acoustic heating of droplet was also realised with the SH-SAW with large temperature rises observed before any nebulisation occurred. Analysis of the heating behaviour showed that the thermal heating is driven by thermal advection with conductive forces during the rapid thermal heating of less than 0.05 seconds for droplets of up to 10 µl. Numerical modelling quantified the efficiency of the heating at between 2% - 6%, where high efficiencies were observed at lower powers. Comparing the SH-SAW to Rayleigh wave heating, it was found to be more applicable to the PCR where higher temperatures were achievable without streaming or nebulisation occurring.

***4. Integration of Bio-Sensing and Fluidic Functions on a Single Substrate***

(1) Integration of SH-SAW with EWOD device was realised with EWOD digital manipulation combined with the SH-SAW device to sense mass loading. Digital droplet position detection was possible with the ability to sense the spatial location and velocity of the droplet.

(2) Simultaneous in-situ and sensing were realised on the 36ºYX $LiTaO_3$ with two IDT's rotated at 90°, and the main propagation direction was used with Euler angle (0,36,0) and the streaming direction utilised was (90,36,0).

To summarise, the author concludes that SH-SAW wave acoustic streaming is driven by a different physical mechanism than Rayleigh wave streaming. As shown, a range of fluidic operations can be realised with the SH-SAW wave, which offers a possibility to realise new and novel microfluidic devices and functions on a single integrated substrate. The next chapter will discuss the proposed expansion of this research to a more thorough characterisation the SH-SAW.

# Chapter 9. Future work

This thesis has presented an initial numerical analysis and simulation of the acoustic wave propagation. The analysis considered only a 2D domain and only low viscosity fluids, such as water. For a more comprehensive analysis, the research could be expanded as follows:

a. Development of 3D fluidic model with base oscillation using a decaying function derived from SH-SAW wave propagation as a boundary condition;
b. Expansion of the model to include mixed physical modelling of piezoelectric substrate displacement coupled with fluidic model to analyse full streaming behaviour. Due to size of model a significant computing resource would be required to model a 5 µl droplet;
c. Coupling of fluid streaming with thermal analysis for higher accuracy simulation of Péclet numbers and advection.

For experimental analysis of the SH-SAW wave, currently only low viscosity fluids were analysed, expanding this to a range of high viscosity fluids may lead to new behaviours and observation of the wave propagation. Higher viscosity fluids would provide interesting for a deep analysis of the effects of low Péclet numbers.

A second area of expansion on this research is to integrate all the microfluidic functions, identified with the SH-SAW device, into a single device which can undertake multiple fluidic applications on a single substrate. The aim would be to analyse a blood sample for pathogen detection. An example of a possible device is shown in Figure 9-1 (right) which would have an integrated syringe and with multiplexing could possibly analyse a blood sample for 6 pathogens in a single package.

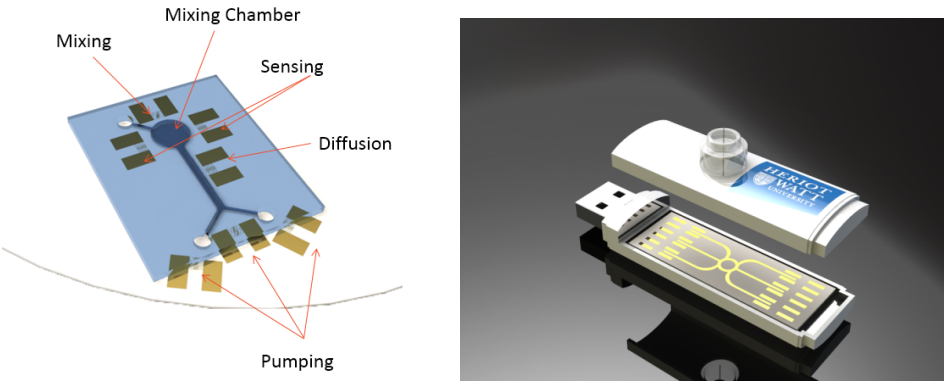


**Figure 9-1: (left) Integrated SH-SAW device (right) Lab-On-USB Shear Wave concept device**

Additionally, expanding the SH-SAW wave to interaction with fluidic channels (Figure 9-1 (left)) would give the possibility of observing the effects of the SH-SAW wave on particles. Due to the high power achievable, the analysis of surface cleaning for bio-fouling may yield interesting results.

Utilising the ability of the SH-SAW to evenly distribute energy through multiple droplets using a single IDT, specifically thermal energy, a multiplexing SAW device could be realised. An example device that could be investigate is shown in Figure 9-2 which is called a "Loss-Less" acoustic mixer. This device could be used to mix microfluidic samples in similar method to Rayleigh wave commercial devices but with reduced IDT count and higher efficiency. Additionally, as observed, the devices could be investigated for thermal heating of droplets in series and a quantification of the achievable energy that can be realised from a single IDT.

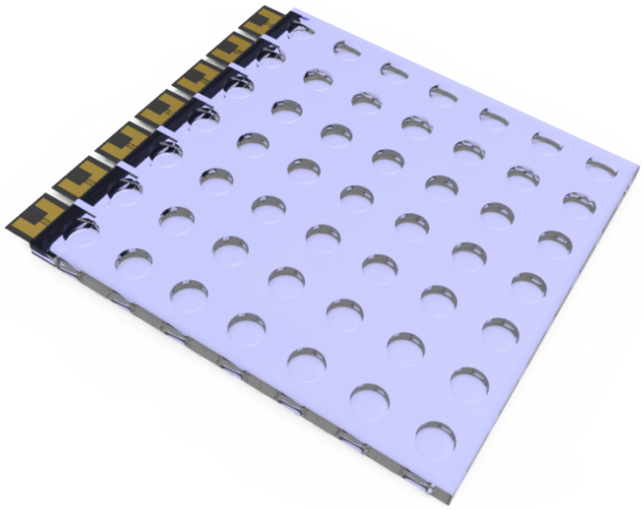

**Figure 9-2: Loss-Less Acoustic Mixing / Thermal Heating for SH-SAW**

In addition to thermal heating of the droplets, another promising areas for thermal heating and streaming is analysing the thermal mixing with the PCR process. The mixed advection and SAW streaming may provide an improve rate of the replication process providing an interesting areas for further research. With the substantial existing research of Rayleigh wave fluidics the discovery of SH-SAW fluidics may lead to many interesting research opportunities.

# Appendix 1: Euler Angle Transforms

Transformation cosines and sines:

$$\alpha_1 := \cos(\psi)\cos(\phi) - \cos(\theta)\cdot\sin(\phi)\cdot\sin(\psi)$$

$$\alpha_2 := -\sin(\psi)\cos(\phi) - \cos(\theta)\cdot\sin(\phi)\cdot\cos(\psi)$$

$$\alpha_3 := \sin(\theta)\sin(\phi)$$

$$\beta_1 := \cos(\psi)\sin(\phi) + \cos(\theta)\cdot\cos(\phi)\cdot\sin(\psi)$$

$$\beta_2 := -\sin(\psi)\sin(\phi) + \cos(\theta)\cdot\cos(\phi)\cdot\cos(\psi)$$

$$\beta_3 := -\sin(\theta)\cos(\phi)$$

$$\gamma_1 := \sin(\psi)\cdot\sin(\theta)$$

$$\gamma_2 := \cos(\phi)\cdot\sin(\theta)$$

$$\gamma_3 := \cos(\theta)$$

Transformation Matrices:

$$V := \begin{pmatrix} \alpha_1 & \beta_1 & \gamma_1 \\ \alpha_2 & \beta_2 & \gamma_2 \\ \alpha_3 & \beta_3 & \gamma_3 \end{pmatrix}$$

$$Q := \begin{pmatrix} \alpha_1^2 & \beta_1^2 & \gamma_1^2 & 2\cdot\beta_1\cdot\gamma_1 & 2\cdot\gamma_1\cdot\alpha_1 & 2\cdot\alpha_1\cdot\beta_1 \\ \alpha_2^2 & \beta_2^2 & \gamma_2^2 & 2\cdot\beta_2\cdot\gamma_2 & 2\cdot\gamma_2\cdot\alpha_2 & 2\cdot\alpha_2\cdot\beta_2 \\ \alpha_3^2 & \beta_3^2 & \gamma_3^2 & 2\cdot\beta_3\cdot\gamma_3 & 2\cdot\gamma_3\cdot\alpha_3 & 2\cdot\alpha_3\cdot\beta_3 \\ \alpha_2\cdot\alpha_3 & \beta_2\cdot\beta_3 & \gamma_2\cdot\gamma_3 & \beta_2\cdot\gamma_3 + \beta_3\cdot\gamma_2 & \gamma_2\cdot\alpha_3 + \gamma_3\cdot\alpha_2 & \alpha_2\cdot\beta_3 + \alpha_3\cdot\beta_2 \\ \alpha_3\cdot\alpha_1 & \beta_3\cdot\beta_1 & \gamma_3\cdot\gamma_1 & \beta_1\cdot\gamma_3 + \beta_3\cdot\gamma_1 & \gamma_1\cdot\alpha_3 + \gamma_3\cdot\alpha_1 & \alpha_1\cdot\beta_3 + \alpha_3\cdot\beta_1 \\ \alpha_1\cdot\alpha_2 & \beta_1\cdot\beta_2 & \gamma_1\cdot\gamma_2 & \beta_1\cdot\gamma_2 + \beta_2\cdot\gamma_1 & \gamma_1\cdot\alpha_2 + \gamma_2\cdot\alpha_1 & \alpha_1\cdot\beta_2 + \alpha_2\cdot\beta_1 \end{pmatrix}$$

Original elastic matrix for $LiTaO_3$

$$C := \begin{pmatrix} 2.3966 & 0.468904 & 0.802342 & -0.110267 & 0 & 0 \\ 0.468904 & 2.3966 & 0.802342 & 0.110267 & 0 & 0 \\ 0.802342 & 0.802342 & 2.75364 & 0 & 0 & 0 \\ -0.110267 & 0.110267 & 0 & 0.938995 & 0 & 0 \\ 0 & 0 & 0 & 0 & 0.938995 & -0.110267 \\ 0 & 0 & 0 & 0 & -0.110267 & 0.938995 \end{pmatrix}$$

Transformed matrix for 36ºYX $LiTaO_3$

$$C_{transform} := Q \cdot C \cdot Q^T = \begin{pmatrix} 2.397 & 0.479 & 0.792 & 0.124 & 0 & 0 \\ 0.479 & 2.705 & 0.722 & 0.073 & 0 & 0 \\ 0.792 & 0.722 & 2.605 & 0.131 & 0 & 0 \\ 0.124 & 0.073 & 0.131 & 0.859 & 0 & 0 \\ 0 & 0 & 0 & 0 & 1.044 & -0.034 \\ 0 & 0 & 0 & 0 & -0.034 & 0.834 \end{pmatrix}$$

Original permittivity matrix for $LiTaO_3$

$$E := \begin{pmatrix} 0 & 0 & 0 & 0 & 2.59576 & -1.58923 \\ -1.58923 & 1.58923 & 0 & 2.59576 & 0 & 0 \\ 0.0821598 & 0.0821598 & 1.88197 & 0 & 0 & 0 \end{pmatrix}$$

Transformed matrix for 36ºYX $LiTaO_3$

$$E_{transform} := V \cdot E \cdot Q^T = \begin{pmatrix} 0 & 0 & 0 & 0 & 3.034 & 0.24 \\ -1.237 & 3.253 & -0.812 & 0.541 & 0 & 0 \\ 1.001 & -1.493 & 2.148 & 0.665 & 0 & 0 \end{pmatrix}$$

Original piezoelectric coupling matrix for $LiTaO_3$

$$\underset{\sim}{e} := \begin{pmatrix} 40.9 & 0 & 0 \\ 0 & 40.9 & 0 \\ 0 & 0 & 43.3 \end{pmatrix}$$

Transformed matrix for 36ºYX $LiTaO_3$

$$e_{transform} := V \cdot e \cdot V^T = \begin{pmatrix} 40.9 & 0 & 0 \\ 0 & 41.729 & 1.141 \\ 0 & 1.141 & 42.471 \end{pmatrix}$$

The transformed material properties were used in the FEA model.

# Appendix 2: Power Conversion Values

| [dBm] | [Watts] | [Volts]rms | [Volts]p | [Volts]pp |
|---|---|---|---|---|
| **0** | 0.001 | 223.607 mV | 316.180 mV | 632.360 mV |
| **1** | 0.00126 | 250.891 mV | 354.760 mV | 709.520 mV |
| **2** | 0.00158 | 281.504 mV | 398.047 mV | 796.094 mV |
| **3** | 0.002 | 315.853 mV | 446.616 mV | 893.232 mV |
| **4** | 0.00251 | 0.354 V | 0.501 V | 1.002 V |
| **5** | 0.00316 | 0.398 V | 0.562 V | 1.125 V |
| **6** | 0.00398 | 0.446 V | 0.631 V | 1.262 V |
| **7** | 0.00501 | 0.501 V | 0.708 V | 1.416 V |
| **8** | 0.00631 | 0.562 V | 0.794 V | 1.588 V |
| **9** | 0.00794 | 0.630 V | 0.891 V | 1.782 V |
| **10** | 0.01 | 0.707 V | 1.000 V | 2.000 V |
| **11** | 0.0126 | 0.793 V | 1.122 V | 2.244 V |
| **12** | 0.0158 | 0.890 V | 1.259 V | 2.517 V |
| **13** | 0.02 | 0.999 V | 1.412 V | 2.825 V |
| **14** | 0.0251 | 1.121 V | 1.585 V | 3.169 V |
| **15** | 0.0316 | 1.257 V | 1.778 V | 3.556 V |
| **16** | 0.0398 | 1.411 V | 1.995 V | 3.990 V |
| **17** | 0.0501 | 1.583 V | 2.238 V | 4.477 V |
| **18** | 0.0631 | 1.776 V | 2.512 V | 5.023 V |
| **19** | 0.0794 | 1.993 V | 2.818 V | 5.636 V |
| **20** | 0.1 | 2.236 V | 3.162 V | 6.324 V |
| **21** | 0.126 | 2.509 V | 3.548 V | 7.095 V |
| **22** | 0.158 | 2.815 V | 3.980 V | 7.961 V |
| **23** | 0.2 | 3.159 V | 4.466 V | 8.932 V |
| **24** | 0.251 | 3.544 V | 5.011 V | 10.022 V |
| **25** | 0.316 | 3.976 V | 5.623 V | 11.245 V |
| **26** | 0.398 | 4.462 V | 6.309 V | 12.617 V |
| **27** | 0.501 | 5.006 V | 7.078 V | 14.157 V |
| **28** | 0.631 | 5.617 V | 7.942 V | 15.884 V |
| **29** | 0.794 | 6.302 V | 8.911 V | 17.822 V |
| **30** | 1 | 7.071 V | 9.998 V | 19.997 V |
| **31** | 1.26 | 7.934 V | 11.218 V | 22.437 V |
| **32** | 1.58 | 8.902 V | 12.587 V | 25.175 V |
| **33** | 2 | 9.988 V | 14.123 V | 28.246 V |
| **34** | 2.51 | 11.207 V | 15.847 V | 31.693 V |
| **35** | 3.16 | 12.574 V | 17.780 V | 35.560 V |
| **36** | 3.98 | 14.109 V | 19.950 V | 39.899 V |
| **37** | 5.01 | 15.830 V | 22.384 V | 44.768 V |
| **38** | 6.31 | 17.762 V | 25.115 V | 50.230 V |
| **39** | 7.94 | 19.929 V | 28.180 V | 56.359 V |
| **40** | 10 | 22.361 V | 31.618 V | 63.236 V |
| **41** | 12.6 | 25.089 V | 35.476 V | 70.952 V |
| **42** | 15.8 | 28.150 V | 39.805 V | 79.609 V |
| **43** | 20 | 31.585 V | 44.662 V | 89.323 V |
| **44** | 25.1 | 35.439 V | 50.111 V | 100.222 V |
| **45** | 31.6 | 39.764 V | 56.226 V | 112.451 V |
| **46** | 39.8 | 44.615 V | 63.086 V | 126.172 V |
| **47** | 50.1 | 50.059 V | 70.784 V | 141.568 V |
| **48** | 63.1 | 56.168 V | 79.421 V | 158.842 V |
| **49** | 79.4 | 63.021 V | 89.112 V | 178.223 V |
| **50** | 100 | 70.711 V | 99.985 V | 199.970 V |

## References


[1] G. Magnus, *The Age of Aging: How Demographics are Changing the Global Economy and Our World*. Wiley, 2008.

[2] R. J. Rosati, "Evaluation of Remote Monitoring in Home Health Care," in *International Conference on eHealth, Telemedicine, and Social Medicine, 2009. EMED'09*, 2009, pp. 151–153.

[3] N. R. Chumbler, B. Neugaard, R. Kobb, P. Ryan, H. Qin, and Y. Joo, "An observational study of veterans with diabetes receiving weekly or daily home telehealth monitoring," *Journal of telemedicine and telecare*, vol. 11, no. 3, p. 150, 2005.

[4] P. S. Dittrich, K. Tachikawa, and A. Manz, "Micro Total Analysis Systems. Latest Advancements and Trends," *Analytical Chemistry*, vol. 78, no. 12, pp. 3887–3908, Jun. 2006.

[5] A. Arora, G. Simone, G. B. Salieb-Beugelaar, J. T. Kim, and A. Manz, "Latest Developments in Micro Total Analysis Systems," *Analytical Chemistry*, vol. 82, no. 12, pp. 4830–4847, Jun. 2010.

[6] Muck, J. Wang, M. Jacobs, G. Chen, M. P. Chatrathi, V. Jurka, Z. Výborný, S. D. Spillman, G. Sridharan, and M. J. Schöning, "Fabrication of Poly(methyl methacrylate) Microfluidic Chips by Atmospheric Molding," *Anal. Chem.*, vol. 76, no. 8, pp. 2290–2297, Apr. 2004.

[7] B. Romanowicz, "Surface Waves," in *Encyclopedia of Solid Earth Geophysics*, H. K. Gupta, Ed. Springer Netherlands, 2011, pp. 1406–1419.

[8] G. S. Calabrese, H. Wohltjen, and M. K. Roy, "Surface acoustic wave devices as chemical sensors in liquids. Evidence disputing the importance of Rayleigh wave propagation," *Anal. Chem.*, vol. 59, no. 6, pp. 833–837, Mar. 1987.

[9] M. J. Vellekoop, "Acoustic wave sensors and their technology," *Ultrasonics*, vol. 36, no. 1–5, pp. 7–14, 1998.

[10] M. Alghane, Y. Q. Fu, B. X. Chen, Y. Li, M. P. Y. Desmulliez, and A. J. Walton, "Streaming phenomena in microdroplets induced by Rayleigh surface acoustic wave," *Journal of Applied Physics*, vol. 109, no. 11, p. 114901, Jun. 2011.

[11] X. Y. Du, M. E. Swanwick, Y. Q. Fu, J. K. Luo, A. J. Flewitt, D. S. Lee, S. Maeng, and W. I. Milne, "Surface acoustic wave induced streaming and pumping in 128° Y-cut LiNbO3 for microfluidic applications," *J. Micromech. Microeng.*, vol. 19, no. 3, p. 035016, Mar. 2009.

[12] X. Y. Du, Y. Q. Fu, J. K. Luo, A. J. Flewitt, and W. I. Milne, "Microfluidic pumps employing surface acoustic waves generated in ZnO thin films," *Journal of Applied Physics*, vol. 105, p. 024508, 2009.

[13] S. Alzuaga, S. Ballandras, F. Bastien, W. Daniau, B. Gauthier-Manuel, J.-F. Manceau, B. Cretin, P. Vairac, V. Laude, and A. Khelif, "A large scale XY positioning and localisation system of liquid droplet using SAW on LiNbO 3," in *Ultrasonics, 2003 IEEE Symposium on*, 2003, vol. 2, pp. 1790–1793.

[14] J. K. Luo, Y. Q. Fu, Y. Li, X. Y. Du, A. J. Flewitt, A. J. Walton, and W. I. Milne, "Moving-part-free microfluidic systems for lab-on-a-chip," *Journal of Micromechanics and Microengineering*, vol. 19, no. 5, p. 054001, 2009.

[15] H. Jin, J. Zhou, X. He, W. Wang, H. Guo, S. Dong, D. Wang, Y. Xu, J. Geng, and J. K. Luo, "Flexible surface acoustic wave resonators built on disposable plastic film for electronics and lab-on-a-chip applications," *Scientific reports*, vol. 3, 2013.

[16] J. Friend and L. Y. Yeo, "Microscale acoustofluidics: Microfluidics driven via acoustics and ultrasonics," *Reviews of Modern Physics*, vol. 83, no. 2, p. 647, 2011.

[17] Y. Q. Fu, J. K. Luo, X. Y. Du, A. J. Flewitt, Y. Li, G. H. Markx, A. J. Walton, and W. I. Milne, "Recent developments on ZnO films for acoustic wave based bio-sensing and microfluidic applications: a review," *Sensors and Actuators B: Chemical*, vol. 143, no. 2, pp. 606–619, Jan. 2010.
[18] D. W. Branch and S. M. Brozik, "Low-level detection of a Bacillus anthracis simulant using Love-wave biosensors on 36°YX LiTaO3," *Biosensors and Bioelectronics*, vol. 19, no. 8, pp. 849–859, Mar. 2004.
[19] G. Lindner, "Sensors and actuators based on surface acoustic waves propagating along solid–liquid interfaces," *J. Phys. D: Appl. Phys.*, vol. 41, no. 12, p. 123002, Jun. 2008.
[20] P. Gravesen, J. Branebjerg, and O. S. Jensen, "Microfluidics-a review," *Journal of Micromechanics and Microengineering*, vol. 3, p. 168, 1993.
[21] D. R. Reyes, D. Iossifidis, P.-A. Auroux, and A. Manz, "Micro Total Analysis Systems. 1. Introduction, Theory, and Technology," *Analytical Chemistry*, vol. 74, no. 12, pp. 2623–2636, Jun. 2002.
[22] B. D. Iverson and S. V. Garimella, "Recent advances in microscale pumping technologies: a review and evaluation," *Microfluid Nanofluid*, vol. 5, no. 2, pp. 145–174, Feb. 2008.
[23] A. Wixforth, "Acoustically driven planar microfluidics," *Superlattices and Microstructures*, vol. 33, no. 5–6, pp. 389–396, Jun. 2003.
[24] L. Rayleigh, "On waves propagated along the plane surface of an elastic solid," *Proceedings of the London Mathematical Society*, vol. 1, no. 1, p. 4, 1885.
[25] M. K. Tan, J. R. Friend, and L. Y. Yeo, "Surface acoustic wave driven microchannel flow," in *16th Australasian Fluid Mechanics Conference (AFMC)*, 2007, pp. 790–793.
[26] A. Gubaidullin and O. Kuchugurina, "Rayleigh Waves in Porous Media Saturated with Liquid," in *IUTAM Symposium on Theoretical and Numerical Methods in Continuum Mechanics of Porous Materials*, 2001, pp. 179–186.
[27] D. Royer and E. Dieulesaint, *Elastic Waves in Solids I: Free and Guided Propagation*. Springer, 2000.
[28] G. W. Farnell, "Properties of elastic surface waves," *Physical acoustics*, vol. 6, pp. 109–166, 2012.
[29] W. R. Smith, "Basics of the SAW interdigital transducer," in *(European Workshop on the Computer-Aided Design of Surface Acoustic Wave Devices, Bologna, Italy, Apr. 7-9, 1976.) Wave Electronics, vol. 2, July 1976, p. 25-63.*, 1976, vol. 2, pp. 25–63.
[30] C. Campbell, *Surface acoustic wave devices for mobile and wireless communications*. New York: Academic Press, 1998.
[31] T.-T. Wu and W.-S. Wang, "An experimental study on the ZnO/sapphire layered surface acoustic wave device," *Journal of applied physics*, vol. 96, no. 9, pp. 5249–5253, 2004.
[32] M. Benetti, D. Cannata, F. Di Pietrantonio, and E. Verona, "Growth of AlN piezoelectric films on diamond for high frequency SAW devices," in *Ultrasonics, 2003 IEEE Symposium on*, 2003, vol. 2, pp. 1738–1741.
[33] M. Benetti, D. Cannata, F. Di Pictrantonio, and E. Verona, "Growth of AlN piezoelectric film on diamond for high-frequency surface acoustic wave devices," *Ultrasonics, Ferroelectrics and Frequency Control, IEEE Transactions on*, vol. 52, no. 10, pp. 1806–1811, 2005.
[34] S. Fujii, S. Kawano, T. Umeda, M. Fujioka, and M. Yoda, "Development of a 6GHz resonator by using an AlN diamond structure," in *Ultrasonics Symposium, 2008. IUS 2008. IEEE*, 2008, pp. 1916–1919.
[35] A. D'amico and E. Verona, "SAW sensors," *Sensors and Actuators*, vol. 17, no. 1–2, pp. 55–66, 1989.

[36] D. G. Buerk, *Biosensors: Theory and Applications*, 1st ed. CRC Press, 1995.
[37] L. C. Clark Jr and C. Lyons, "Electrode systems for continuous monitoring in cardiovascular surgery," *Annals of the New York Academy of Sciences*, vol. 102, no. Automated and Semi-Automated Systems in Clinical Chemistry, pp. 29–45, 1962.
[38] B. R. Eggins, *Biosensors: An Introduction*. Wiley, 1997.
[39] P. M. Wolny, J. P. Spatz, and R. P. Richter, "On the Adsorption Behavior of Biotin-Binding Proteins on Gold and Silica," *Langmuir*, vol. 26, no. 2, pp. 1029–1034, Jan. 2010.
[40] J. E. Pearson, A. Gill, and P. Vadgama, "Analytical aspects of biosensors," *Ann Clin Biochem*, vol. 37, no. 2, pp. 119–145, Mar. 2000.
[41] Y. Hur, J. Han, J. Seon, Y. E. Pak, and Y. Roh, "Development of an SH-SAW sensor for the detection of DNA hybridization," *Sensors and Actuators A: Physical*, vol. 120, no. 2, pp. 462–467, May 2005.
[42] Y. Inoue, Y. Kato, and K. Sato, "Surface acoustic wave method for in situ determination of the amounts of enzyme substrate complex formed on immobilized glucose oxidase during catalytic reaction," *Faraday Trans.*, vol. 88, no. 3, p. 449, 1992.
[43] H. Wohltjen and R. Dessy, "Surface acoustic wave probe for chemical analysis. I. Introduction and instrument description," *Analytical Chemistry*, vol. 51, no. 9, pp. 1458–1464, 1979.
[44] H. Wohltjen and R. Dessy, "Surface acoustic wave probes for chemical analysis. II. Gas chromatography detector," *Analytical Chemistry*, vol. 51, no. 9, pp. 1465–1470, 1979.
[45] H. Wohltjen and R. Dessy, "Surface acoustic wave probes for chemical analysis. III. Thermomechanical polymer analyzer," *Analytical Chemistry*, vol. 51, no. 9, pp. 1470–1475, 1979.
[46] J. W. Grate and G. C. Frye, "Acoustic Wave Sensors," *Sensors Update*, vol. 2, no. 1, pp. 37–83, Oct. 1996.
[47] J. E. Roederer and G. J. Bastiaans, "Microgravimetric immunoassay with piezoelectric crystals," *Anal. Chem.*, vol. 55, no. 14, pp. 2333–2336, Dec. 1983.
[48] H. Wohltjen, "Mechanism of operation and design considerations for surface acoustic wave device vapour sensors," *Sensors and Actuators*, vol. 5, no. 4, pp. 307–325, Jul. 1984.
[49] S. Shiokawa and T. Moriizumi, "Design of SAW sensor in liquid," *Jpn. J. Appl. Phys*, vol. 27, pp. 142–144, 1988.
[50] A. E. H. Love, "Some Problems of Geodynamics," 1911. [Online]. Available: http://adsabs.harvard.edu/abs/1911spge.book.....L. [Accessed: 21-Sep-2010].
[51] Z. Wang, C. K. Jen, and J. D. N. Cheeke, "Mass sensitivity of two-layer shear horizontal plate wave sensors," *Ultrasonics*, vol. 32, no. 3, pp. 209–215, May 1994.
[52] K. Yamanouchi, K. Iwahashi, and K. Shibayama, "Temperature dependence of Rayleigh waves and piezoelectric leaky surface waves in rotated Y-cut LiTaO3 and SiO2/LiTaO3 structures," *Wave Electronics*, vol. 3, pp. 319–333, 1979.
[53] N. Moll, E. Pascal, D. H. Dinh, J.-P. Pillot, B. Bennetau, D. Rebière, D. Moynet, Y. Mas, D. Mossalayi, J. Pistré, and C. Déjous, "A Love wave immunosensor for whole E. coli bacteria detection using an innovative two-step immobilisation approach," *Biosensors and Bioelectronics*, vol. 22, no. 9–10, pp. 2145–2150, Apr. 2007.
[54] E. Gizeli, N. J. Goddard, C. R. Lowe, and A. C. Stevenson, "A Love plate biosensor utilising a polymer layer," *Sensors and Actuators B: Chemical*, vol. 6, no. 1–3, pp. 131–137, Jan. 1992.
[55] G. Kovacs, G. W. Lubking, M. J. Vellekoop, and A. Venema, "Love waves for (bio) chemical sensing in liquids," in *Ultrasonics Symposium*, 1992, p. 281.

[56] K. Kalantar-Zadeh, W. Wlodarski, Y. Y. Chen, B. N. Fry, and K. Galatsis, "Novel Love mode surface acoustic wave based immunosensors," *Sensors and Actuators B: Chemical*, vol. 91, no. 1–3, pp. 143–147, Jun. 2003.
[57] F. Herrmann, M. Weihnacht, and S. Büttgenbach, "Properties of shear-horizontal surface acoustic waves in different layered quartz–SiO2 structures," *Ultrasonics*, vol. 37, no. 5, pp. 335–341, 1999.
[58] Y. Xia, "Whitesides. G.M.:'Soft lithography,'" *Angew. Chem., Int. Ed. Engl*, vol. 37, pp. 550–575, 1998.
[59] K. Mitsakakis, A. Tsortos, J. Kondoh, and E. Gizeli, "Parametric study of SH-SAW device response to various types of surface perturbations," *Sensors and Actuators B: Chemical*, vol. 138, no. 2, pp. 408–416, May 2009.
[60] K. Mitsakakis, A. Tserepi, and E. Gizeli, "SAW device integrated with microfluidics for array-type biosensing," *Microelectronic Engineering*, vol. 86, no. 4–6, pp. 1416–1418, April.
[61] K. Mitsakakis, A. Tserepi, and E. Gizeli, "Integration of Microfluidics With a Love Wave Sensor for the Fabrication of a Multisample Analytical Microdevice," *Microelectromechanical Systems, Journal of*, vol. 17, no. 4, pp. 1010–1019, 2008.
[62] O. Tamarin, C. Déjous, D. Rebière, J. Pistré, S. Comeau, D. Moynet, and J. Bezian, "Study of acoustic Love wave devices for real time bacteriophage detection," *Sensors and Actuators B: Chemical*, vol. 91, no. 1–3, pp. 275–284, Jun. 2003.
[63] V. Raimbault, D. Rebière, C. Dejous, M. Guirardel, and V. Conedera, "Acoustic Love wave platform with PDMS microfluidic chip," *Sensors and Actuators A: Physical*, vol. 142, no. 1, pp. 160–165, Mar. 2008.
[64] K. Länge, G. Blaess, A. Voigt, R. Götzen, and M. Rapp, "Integration of a surface acoustic wave biosensor in a microfluidic polymer chip," *Biosensors and Bioelectronics*, vol. 22, no. 2, pp. 227–232, Aug. 2006.
[65] L. A. Francis, J.-M. Friedt, C. Bartic, and A. Campitelli, "An SU-8 liquid cell for surface acoustic wave biosensors," in *MEMS, MOEMS, and Micromachining*, Strasbourg, France, 2004, vol. 5455, pp. 353–363.
[66] H. Li, J. R. Friend, and L. Y. Yeo, "A scaffold cell seeding method driven by surface acoustic waves," *Biomaterials*, vol. 28, no. 28, pp. 4098–4104, Oct. 2007.
[67] T. A. Franke and A. Wixforth, "Microfluidics for miniaturized laboratories on a chip," *Chemphyschem*, vol. 9, no. 15, pp. 2140–2156, Oct. 2008.
[68] Y. Q. Fu, X. Y. Du, J. K. Luo, A. J. Flewitt, W. I. Milne, D. S. Lee, N. M. Park, S. Maeng, S. H. Kim, and Y. J. Choi, "SAW streaming in ZnO surface acoustic wave micromixer and micropump," in *Sensors, 2007 IEEE*, 2007, pp. 478–483.
[69] G. Zhang, Y. Li, J. Zhang, C. Yang, and J. Liu, "Micro mixer based on surface acoustic wave driving," 2010, vol. 7544, p. 75441O–75441O–6.
[70] S. Ito, M. Sugimoto, Y. Matsui, and J. Kondoh, "Study of Surface Acoustic Wave Streaming Phenomenon Based on Temperature Measurement and Observation of Streaming in Liquids," *Jpn. J. Appl. Phys.*, vol. 46, no. No. 7B, pp. 4718–4722, Jul. 2007.
[71] R. Shilton, M. K. Tan, L. Y. Yeo, and J. R. Friend, "Particle concentration and mixing in microdrops driven by focused surface acoustic waves," *Journal of Applied Physics*, vol. 104, no. 1, pp. 14910–14910, 2008.
[72] R. V. Raghavan, J. R. Friend, and L. Y. Yeo, "Particle concentration via acoustically driven microcentrifugation: microPIV flow visualization and numerical modelling studies," *Microfluid Nanofluid*, vol. 8, no. 1, pp. 73–84, May 2009.
[73] W. K. Tseng, L. Lin Jr, W. C. Sung, S. H. Chen, and G. B. Lee, "Active micro-mixers using surface acoustic waves on Y-cut 128° LiNbO3," *Journal of Micromechanics and Microengineering*, vol. 16, p. 539, 2006.

[74] K. Sritharan, C. J. Strobl, M. F. Schneider, A. Wixforth, and Z. Guttenberg, “Acoustic mixing at low Reynold’s numbers,” *Appl. Phys. Lett.*, vol. 88, no. 5, p. 054102, 2006.
[75] O. Ducloux, E. Galopin, F. Zoueshtiagh, A. Merlen, and V. Thomy, “Enhancement of biosensing performance in a droplet-based bioreactor by in situ microstreaming,” *Biomicrofluidics*, vol. 4, no. 1, p. 011102, 2010.
[76] A. Renaudin, P. Tabourier, V. Zhang, J. C. Camart, and C. Druon, “SAW nanopump for handling droplets in view of biological applications,” *Sensors and Actuators B: Chemical*, vol. 113, no. 1, pp. 389–397, Jan. 2006.
[77] M. Cecchini, S. Girardo, D. Pisignano, R. Cingolani, and F. Beltram, “Acoustic-counterflow microfluidics by surface acoustic waves,” *Appl. Phys. Lett.*, vol. 92, no. 10, p. 104103, 2008.
[78] M. K. Tan, J. R. Friend, and L. Y. Yeo, “Interfacial Jetting Phenomena Induced by Focused Surface Vibrations,” *Phys. Rev. Lett.*, vol. 103, no. 2, p. 024501, Jul. 2009.
[79] A. Qi, L. Y. Yeo, and J. R. Friend, “Interfacial destabilization and atomization driven by surface acoustic waves,” *Physics of Fluids (1994-present)*, vol. 20, no. 7, p. 074103, 2008.
[80] J. Ho, M. K. Tan, D. B. Go, L. Y. Yeo, J. R. Friend, and H.-C. Chang, “Paper-based microfluidic surface acoustic wave sample delivery and ionization source for rapid and sensitive ambient mass spectrometry,” *Analytical chemistry*, vol. 83, no. 9, pp. 3260–3266, 2011.
[81] H. Jagannathan, G. G. Yaralioglu, A. S. Ergun, and B. T. Khuri-Yakub, “Acoustic heating and thermometry in microfluidic channels,” in *Micro Electro Mechanical Systems, 2003. MEMS-03 Kyoto. IEEE The Sixteenth Annual International Conference on*, 2003, pp. 474–477.
[82] D. Beyssen, T. R.-M. I. Perry, and F. Sarry, “Correlation of Rayleigh-SAW streaming and thermal effect for prediction of heat transfer mechanism(s) within microdroplet.”
[83] L. Y. Yeo, H.-C. Chang, P. P. Chan, and J. R. Friend, “Microfluidic devices for bioapplications,” *small*, vol. 7, no. 1, pp. 12–48, 2011.
[84] R. B. Fair, A. Khlystov, T. D. Tailor, V. Ivanov, R. D. Evans, P. B. Griffin, V. Srinivasan, V. K. Pamula, M. G. Pollack, and J. Zhou, “Chemical and biological applications of digital-microfluidic devices,” *Design & Test of Computers, IEEE*, vol. 24, no. 1, pp. 10–24, 2007.
[85] S. K. Cho, H. Moon, and C. J. Kim, “Creating, transporting, cutting, and merging liquid droplets by electrowetting-based actuation for digital microfluidic circuits,” *Microelectromechanical Systems, Journal of*, vol. 12, no. 1, pp. 70–80, 2003.
[86] Y. Li, B. W. Flynn, W. Parkes, Y. Liu, Y. Feng, A. D. Ruthven, J. G. Terry, L. I. Haworth, A. Bunting, J. T. M. Stevenson, and others, “The integration of EWOD and SAW technologies for improved droplet manipulation and mixing,” in *Solid State Device Research Conference, 2009. ESSDERC’09. Proceedings of the European*, 2009, pp. 371–374.
[87] I. D. Avramov, “Analysis and design aspects of SAW-delay-line-stabilized oscillators,” in *Second International Conference on Frequency Control and Synthesis, 1989*, 1989, pp. 36–40.
[88] H. Antil, A. Gantner, R. H. . Hoppe, D. K\öster, K. Siebert, and A. Wixforth, “Modeling and simulation of piezoelectrically agitated acoustic streaming on microfluidic biochips,” *Domain Decomposition Methods in Science and Engineering XVII*, pp. 305–312, 2008.
[89] T. Frommelt, D. Gogel, M. Kostur, P. Talkner, P. Hanggi, and A. Wixforth, “Flow patterns and transport in Rayleigh surface acoustic wave streaming: combined finite element method and raytracing numerics versus experiments,” *Ultrasonics,*

*Ferroelectrics and Frequency Control, IEEE Transactions on*, vol. 55, no. 10, pp. 2298–2305, 2008.

[90] Z. Guttenberg, A. Rathgeber, S. Keller, J. O. Rädler, A. Wixforth, M. Kostur, M. Schindler, and P. Talkner, "Flow profiling of a surface-acoustic-wave nanopump," *Phys. Rev. E*, vol. 70, no. 5, p. 056311, Nov. 2004.

[91] A. Gantner, R. H. W. Hoppe, D. Köster, K. Siebert, and A. Wixforth, "Numerical simulation of piezoelectrically agitated surface acoustic waves on microfluidic biochips," *Comput. Visual Sci.*, vol. 10, no. 3, pp. 145–161, Nov. 2006.

[92] S. K. R. Sankaranarayanan, S. Cular, and V. R. Bhethanabotla, "Finite Element modeling of hexagonal surface acoustic wave biosensor based on LiTaO3," in *Sensors, 2008 IEEE*, 2008, pp. 514–517.

[93] J. J. Campbell and W. R. Jones, "A method for estimating optimal crystal cuts and propagation directions for excitation of piezoelectric surface waves," *IEEE Transactions on Sonics and Ultrasonics*, vol. 15, no. 4, pp. 209–217, Oct. 1968.

[94] D.-J. Yao and H.-C. Hao, "Biosensor and method using the same to perform a biotest," US20110236877 A1, 29-Sep-2011.

[95] V. P. Plessky and C. S. Hartmann, "Characteristics of leaky SAWs on 36-LiTaO3 in periodic structures of heavy electrodes," in *Ultrasonics Symposium, 1993. Proceedings., IEEE 1993*, 1993, pp. 1239–1242 vol.2.

[96] A. Abdollahi, Z. Jiang, and S. Arabshahi, "Evaluation on mass sensitivity of SAW sensors for different piezoelectric materials using finite-element analysis," *IEEE Trans. Ultrason., Ferroelect., Freq. Contr.*, vol. 54, no. 12, pp. 2446–2455, Dec. 2007.

[97] S. Zhgoon, D. Tsimbal, A. Shvetsov, and K. Bhattacharjee, "3D finite element modeling of real size SAW devices and experimental validation," in *Ultrasonics Symposium, 2008. IUS 2008. IEEE*, 2009, pp. 1932–1935.

[98] S. J. Ippolito, K. Kalantar-Zadeh, D. A. Powell, and W. Wlodarski, "A 3-dimensional finite element approach for simulating acoustic wave propagation in layered SAW devices," in *Ultrasonics, 2003 IEEE Symposium on*, 2004, vol. 1, pp. 303–306.

[99] Y. L. Rao and G. Zhang, "Enhancing the sensitivity of SAW sensors with nanostructures," *Current Nanoscience*, vol. 2, no. 4, pp. 311–318, 2006.

[100] G. Scheerschmidt, K. J. Kirk, and G. McRobbie, "Resonance modes of magnetically generated surface waves in acoustic wave guide systems," *Journal of Magnetism and Magnetic Materials*, vol. 322, no. 9–12, pp. 1628–1630, May.

[101] R. Krishnan, H. B. Nemade, and R. Paily, "Simulation of a One-Port SAW Resonator using COMSOL Multiphysics," in *Excerpt from the Proceedings of the COMSOL Users Conference*, 2006.

[102] R. Singh, V. R. Bhethanabotla, and S. K. R. . Sankaranarayanan, "A novel three dimensional fluid-structure interaction finite element model of wave propagation in SAW device: Application to biosensing & microfluidics," in *Sensors, 2009 IEEE*, 2010, pp. 1061–1064.

[103] B. A. Auld, *Acoustic fields and waves in solids*. R.E. Krieger, 1990.

[104] G. Kovacs, M. Anhorn, H. E. Engan, G. Visintini, and C. C. W. Ruppel, "Improved material constants for LiNbO 3 and LiTaO 3," in *IEEE 1990 Ultrasonics Symposium, 1990. Proceedings.*, 1990, pp. 435–438.

[105] J. Kushibiki, I. Takanaga, M. Arakawa, and T. Sannomiya, "Accurate measurements of the acoustical physical constants of LiNbO3 and LiTaO3 single crystals," *Ultrasonics, Ferroelectrics and Frequency Control, IEEE Transactions on*, vol. 46, no. 5, pp. 1315–1323, 2002.

[106] A. H. Fahmy and E. L. Adler, "Transformation of tensor constants of anisotropic materials due to rotations of the co-ordinate axes," *Electrical Engineers, Proceedings of the Institution of*, vol. 122, no. 5, pp. 591–592, 1975.

[107] Holm A., Sturzer Q., Xu Y., and Weigel R., "Investigation of surface acoustic waves on LiNbO3, quartz, and LiTaO3 by laser probing," *Microelectronic Engineering*, vol. 31, no. 1, pp. 123–127, 1996.
[108] A. Holm, R. Weigel, P. Russer, and W. Ruile, "A laser probing system for characterization of SAW propagation on LiNbO3, LiTaO3, and quartz," in *Microwave Symposium Digest, 1996., IEEE MTT-S International*, 1996, vol. 3, pp. 1541–1544 vol.3.
[109] K. Nakamura, M. Kazumi, and H. Shimizu, "SH-Type and Rayleigh-Type Surface Waves on Rotated Y-Cut LiTaO3," in *Ultrasonics Symposium, 1977*, 1977, pp. 819–822.
[110] L. Y. Yeo and J. R. Friend, "Ultrafast microfluidics using surface acoustic waves," *Biomicrofluidics*, vol. 3, no. 1, pp. 012002–23, Mar. 2009.
[111] A. J. Slobodnik, "Surface acoustic waves and SAW materials," *Proceedings of the IEEE*, vol. 64, no. 5, pp. 581– 595, May 1976.
[112] Y. Kwon and Y. Roh, "Development of SH-SAW sensors for underwater measurement," *Ultrasonics*, vol. 42, no. 1–9, pp. 409–411, Apr. 2004.
[113] Z. Li, Y. Jones, J. Hossenlopp, R. Cernosek, and F. Josse, "Design considerations for high sensitivity guided SH-SAW chemical sensor for detection in aqueous environments."
[114] F. Zhou, Z. Li, L. Fan, S. Zhang, and X. Shui, "Experimental study of Love-wave immunosensors based on ZnO/LiTaO3 structures," *Ultrasonics*, vol. 50, no. 3, pp. 411–415, Mar. 2010.
[115] G. Xu, "Direct finite-element analysis of the frequency response of a YZ lithium niobate SAW filter," *Smart materials and structures*, vol. 9, p. 973, 2000.
[116] F. M. White, *Viscous fluid flow*. New York, NY: McGraw-Hill Higher Education, 2006.
[117] H. L. Bandey, S. J. Martin, R. W. Cernosek, and A. R. Hillman, "Modeling the Responses of Thickness-Shear Mode Resonators under Various Loading Conditions," *Analytical Chemistry*, vol. 71, no. 11, pp. 2205–2214, Jun. 1999.
[118] G. McHale, M. I. Newton, M. K. Banerjee, and J. A. Cowen, "C : Acoustic wave–liquid interactions," *Materials Science and Engineering*, vol. 12, no. 1–2, pp. 17–22, Aug. 2000.
[119] V. K. Sin and I. K. Wong, "Numerical Study of Stokes' Second Flow Problem," in *Computational and Information Sciences, International Conference on*, Los Alamitos, CA, USA, 2010, vol. 0, pp. 242–245.
[120] P. Brunet, M. Baudoin, O. B. Matar, and F. Zoueshtiagh, "Droplet displacements and oscillations induced by ultrasonic surface acoustic waves: a quantitative study," *Physical Review E*, vol. 81, no. 3, p. 036315, 2010.
[121] D. Köster, "Numerical Simulation of Acoustic Streaming on Surface Acoustic Wave-driven Biochips," *SIAM J. Sci. Comput.*, vol. 29, no. 6, p. 2352, 2007.
[122] M. K. Tan, L. Y. Yeo, and J. R. Friend, "Rapid fluid flow and mixing induced in microchannels using surface acoustic waves," *EPL (Europhysics Letters)*, vol. 87, no. 4, p. 47003, 2009.
[123] S. K. Sankaranarayanan, R. Singh, and V. R. Bhethanabotla, "Acoustic streaming induced elimination of nonspecifically bound proteins from a surface acoustic wave biosensor: Mechanism prediction using fluid-structure interaction models," *Journal of Applied Physics*, vol. 108, no. 10, p. 104507, 2010.
[124] M. K. Tan, J. R. Friend, O. K. Matar, and L. Y. Yeo, "Capillary wave motion excited by high frequency surface acoustic waves," *Physics of Fluids (1994-present)*, vol. 22, no. 11, p. 112112, 2010.
[125] M. Schindler, P. Talkner, and P. Hänggi, "Computing stationary free-surface shapes in microfluidics," *Physics of Fluids (1994-present)*, vol. 18, no. 10, p. 103303, 2006.

[126] H. Antil, R. Glowinski, R. H. Hoppe, C. Linsenmann, T.-W. Pan, and A. Wixforth, "Modeling, simulation, and optimization of surface acoustic wave driven microfluidic biochips," *J. Comp. Math*, vol. 28, pp. 149–169, 2010.
[127] J. Vanneste and O. Bühler, "Streaming by leaky surface acoustic waves," *Proc. R. Soc. A*, p. rspa20100457, Dec. 2010.
[128] S. Shiokawa, Y. Matsui, and T. Ueda, "Liquid streaming and droplet formation caused by leaky Rayleigh waves," in *Ultrasonics Symposium, 1989. Proceedings., IEEE 1989*, 1989, pp. 643–646 vol.1.
[129] W. Nyborg, *Physical Acoustics: Principles and Methods*, vol. II B. New York: Academic Press, 1965.
[130] M. K. Aktas and B. Farouk, "Numerical simulation of acoustic streaming generated by finite-amplitude resonant oscillations in an enclosure," *The Journal of the Acoustical Society of America*, vol. 116, no. 5, pp. 2822–2831, Nov. 2004.
[131] M. Alghane, B. X. Chen, Y. Q. Fu, Y. Li, J. K. Luo, and A. J. Walton, "Experimental and numerical investigation of acoustic streaming excited by using a surface acoustic wave device on a 128° YX-LiNbO $_3$ substrate," *J. Micromech. Microeng.*, vol. 21, no. 1, p. 015005, Jan. 2011.
[132] C. K. Campbell, *Surface Acoustic Wave Devices for Mobile and Wireless Communications*, 1st ed. New York: Academic Press, 1998.
[133] T. I. Browning, M. F. Lewis, and R. F. Milsom, "Surface Acoustic Waves on Rotated Y-Cut LiTaO3," in *1978 Ultrasonics Symposium*, 1978, pp. 586–589.
[134] H. L. Bertoni and T. Tamir, "Unified theory of Rayleigh-angle phenomena for acoustic beams at liquid-solid interfaces," *Appl. Phys.*, vol. 2, no. 4, pp. 157–172, Oct. 1973.
[135] M. I. Newton, M. K. Banerjee, T. K. H. Starke, S. M. Rowan, and G. McHale, "Surface acoustic wave–liquid drop interactions," *Sensors and Actuators A: Physical*, vol. 76, no. 1–3, pp. 89–92, Aug. 1999.
[136] S. Shiokawa, Y. Matsui, and T. Moriizumi, "Experimental Study on Liquid Streaming by SAW," *Japanese Journal of Applied Physics*, vol. 28S1, no. Supplement 28–1, pp. 126–128, 1989.
[137] S. Shiokawa, Y. Matsui, and T. Ueda, "Study on SAW Streaming and its Application to Fluid Devices," *Japanese Journal of Applied Physics*, vol. 29S1, no. Supplement 29–1, pp. 137–139, 1990.
[138] S. J. Martin, A. J. Ricco, T. M. Niemczyk, and G. C. Frye, "Characterization of SH acoustic plate mode liquid sensors," *Sensors and Actuators*, vol. 20, no. 3, pp. 253–268, Dec. 1989.
[139] S. K. Yang, H. Y. Lee, C. Y. Shen, and Ro, "Effects of conducting liquid loadings on propagation characteristics of surface acoustic waves," *Proceedings of the National Science Council Republic of China Part A Physical Science and Engineering*, vol. 25, pp. 131–136, 2001.
[140] S. Ballandras, A. Reinhardt, A. Khelif, M. Wilm, V. Laude, W. Daniau, and V. Blondeau-Patissier, "Theoretical analysis of damping effects of guided elastic waves at solid/fluid interfaces," *J. Appl. Phys.*, vol. 99, no. 5, p. 054907, 2006.
[141] S. K. R. S. Sankaranarayanan and V. R. Bhethanabotla, "Design of efficient focused surface acoustic wave devices for potential microfluidic applications," *J. Appl. Phys.*, vol. 103, no. 6, p. 064518, 2008.
[142] D. Beyssen, L. Le Brizoual, O. Elmazria, P. Alnot, I. Perry, and D. Maillet, "6I-2 Droplet Heating System Based on SAW/Liquid Interaction," in *IEEE Ultrasonics Symposium, 2006*, 2006, pp. 949–952.
[143] K. Chono, N. Shimizu, Y. Matsui, J. Kondoh, and S. Shiokawa, "Development of novel atomization system based on SAW streaming," *Japanese journal of applied physics*, vol. 43, no. 5S, p. 2987, 2004.

[144] K. Chono, N. Shimizu, Y. Matsui, J. Kondoh, and S. Shiokawa, "Novel atomization method based on SAW streaming," in *Ultrasonics, 2003 IEEE Symposium on*, 2003, vol. 2, pp. 1786–1789.
[145] J. R. Friend, L. Y. Yeo, D. R. Arifin, and A. Mechler, "Evaporative self-assembly assisted synthesis of polymeric nanoparticles by surface acoustic wave atomization," *Nanotechnology*, vol. 19, no. 14, p. 145301, 2008.
[146] J. Friend, M. Tan, and L. Yeo, "Unraveling interfacial jetting phenomena induced by focused surface acoustic waves," in *Ultrasonics Symposium (IUS), 2009 IEEE International*, 2009, pp. 811–814.
[147] L. Y. Yeo and J. R. Friend, "Surface Acoustic Wave Microfluidics," *Annual Review of Fluid Mechanics*, vol. 46, pp. 379–406, 2014.
[148] J. R. Richards, A. M. Lenhoff, and A. N. Beris, "Dynamic breakup of liquid–liquid jets," *Physics of Fluids (1994-present)*, vol. 6, no. 8, pp. 2640–2655, 1994.
[149] J. P. Plateau, "Recherches expérimentales et théorique sur les figures d'équilibre d'une masse liquide sans pesanteur.," *Mémoires de l'Académie Royale des Sciences, des Lettres et des Beaux-Arts de Belgique*, vol. 23, p. 1, 1849.
[150] Lord Rayleigh, "On the Capillary Phenomena of Jets," *Proc. R. Soc. Lond.*, vol. 29, no. 196–199, pp. 71–97, Jan. 1879.
[151] J. Kondoh, N. Shimizu, Y. Matsui, and S. Shiokawa, "Liquid heating effects by SAW streaming on the piezoelectric substrate," *IEEE Transactions on Ultrasonics, Ferroelectrics and Frequency Control*, vol. 52, no. 10, pp. 1881–1883, Oct. 2005.
[152] V. Miralles, A. Huerre, F. Malloggi, and M.-C. Jullien, "A Review of Heating and Temperature Control in Microfluidic Systems: Techniques and Applications," *Diagnostics*, vol. 3, no. 1, pp. 33–67, 2013.
[153] K. Länge, B. Rapp, and M. Rapp, "Surface acoustic wave biosensors: a review," *Analytical and Bioanalytical Chemistry*, vol. 391, no. 5, pp. 1509–1519, Jul. 2008.
[154] T. M. A. Gronewold, U. Schlecht, and E. Quandt, "Analysis of proteolytic degradation of a crude protein mixture using a surface acoustic wave sensor," *Biosensors and Bioelectronics*, vol. 22, no. 9–10, pp. 2360–2365, Apr. 2007.
[155] N. Barie, H. Sigrist, and M. Rapp, "Development of immunosensors based on commercially available surface acoustic wave (SAW) devices," *Analusis*, vol. 27, no. 7, pp. 622–629, 1999.
[156] E. Gizeli, F. Bender, A. Rasmusson, K. Saha, F. Josse, and R. Cernosek, "Sensitivity of the acoustic waveguide biosensor to protein binding as a function of the waveguide properties," *Biosensors and Bioelectronics*, vol. 18, no. 11, pp. 1399–1406, 2003.
[157] D. A. Powell, K. Kalantar-zadeh, and W. Wlodarski, "Numerical calculation of SAW sensitivity: application to ZnO/LiTaO3 transducers," *Sensors and Actuators A: Physical*, vol. 115, no. 2–3, pp. 456–461, Sep. 2004.
[158] Z. Wang, J. D. N. Cheeke, and C.-K. Jen, "Perturbation method for analyzing mass sensitivity of planar multilayer acoustic sensors," *IEEE Transactions on Ultrasonics, Ferroelectrics and Frequency Control*, vol. 43, no. 5, pp. 844–851, Sep. 1996.
[159] S. W. Wenzel and R. M. White, "Flexural plate-wave gravimetric chemical sensor," *Sensors and Actuators A: Physical*, vol. 22, no. 1–3, pp. 700–703, Jun. 1989.
[160] L. Y. Yeo, D. Lastochkin, S.-C. Wang, and H.-C. Chang, "A New ac Electrospray Mechanism by Maxwell-Wagner Polarization and Capillary Resonance," *Phys. Rev. Lett.*, vol. 92, no. 13, p. 133902, Apr. 2004.
[161] T. Franke, A. R. Abate, D. A. Weitz, and A. Wixforth, "Surface acoustic wave (SAW) directed droplet flow in microfluidics for PDMS devices," *Lab Chip*, vol. 9, no. 18, p. 2625, 2009.

[162] L. Schmid and T. Franke, “Miniaturisation for chemistry, physics, biology, materials science and bioengineering,” *Lab Chip*, vol. 13, no. 1691, pp. 1691–1694, 2013.

[163] Y. Li, R. Y. Fu, D. Winters, B. W. Flynn, B. Parkes, D. S. Brodie, Y. Liu, J. Terry, L. I. Haworth, and A. S. Bunting, “Test Structures for Characterizing the Integration of EWOD and SAW Technologies for Microfluidics,” *Semiconductor Manufacturing, IEEE Transactions on*, vol. 25, no. 3, pp. 323–330, 2012.

[164] Y. Li, W. Parkes, L. I. Haworth, A. A. Stokes, K. R. Muir, P. Li, A. J. Collin, N. G. Hutcheon, R. Henderson, B. Rae, and A. J. Walton, “Anodic Ta2O5 for CMOS compatible low voltage electrowetting-on-dielectric device fabrication,” *Solid-State Electronics*, vol. 52, no. 9, pp. 1382–1387, Sep. 2008.

[165] Y. Li, Y. Q. Fu, S. D. Brodie, M. Alghane, and A. J. Walton, “Integrated microfluidics system using surface acoustic wave and electrowetting on dielectrics technology,” *Biomicrofluidics*, vol. 6, no. 1, pp. 012812–012812–9, Mar. 2012.